Quantitative studies of the nucleation of recrystallization in metals utilizing microscopy and X-ray diffraction

Larsen, Axel Wright

Publication date:
2005

Document Version
Publisher's PDF, also known as Version of record

RISØ

Risø-PhD-9(EN)

Quantitative studies of the nucleation of recrystallization in metals utilizing microscopy and X-ray diffraction

Axel Wright Larsen

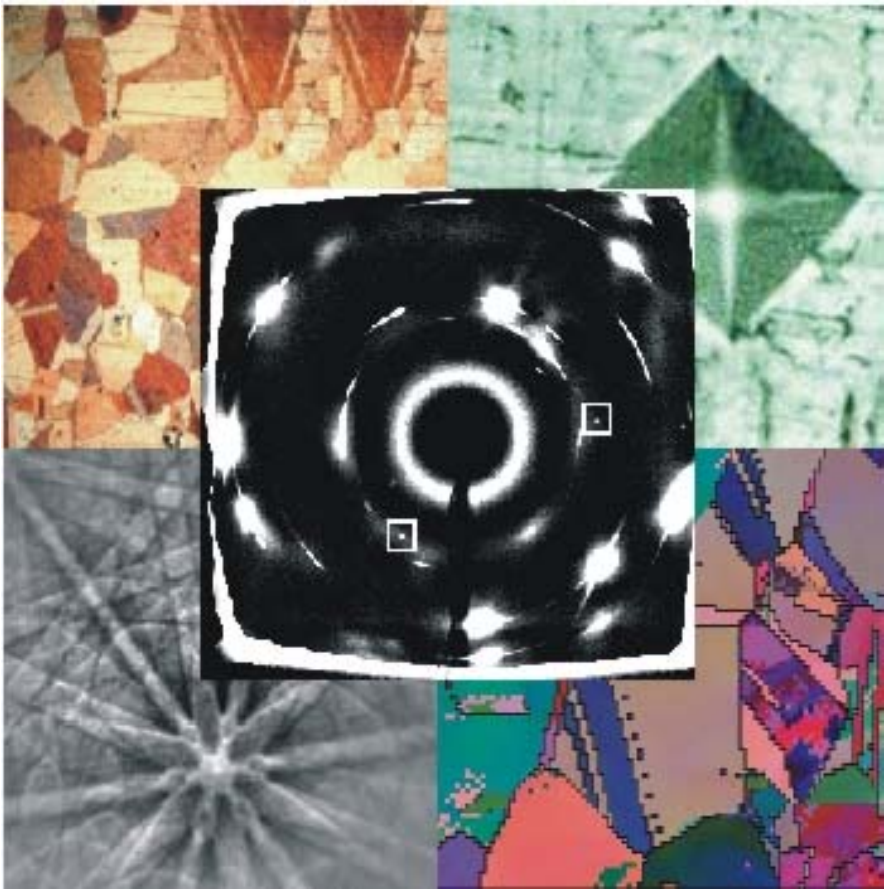

Risø National Laboratory
Roskilde
Denmark
September 2005

Risø-PhD Thesis

Author: Axel Wright Larsen
Title: Quantitative studies of the nucleation of recrystallization in metals utilizing microscopy and X-ray diffraction
Department: Materials Research Department

This thesis is submitted in partial fulfilment of the requirements for the Ph.D. degree at the University of Copenhagen and Risø National Laboratory

Abstract :
This thesis covers three main results obtained during the project:
A reliable method of performing serial sectioning on metal samples utilizing a Logitech polishing machine has been developed.
Serial sectioning has been performed on metal samples in 1 µm steps utilizing mechanical polishing, and in 2 µm steps when electrochemical polishing was needed.
A method by which reliable EBSP line scans may be performed by scanning three parallel lines has been developed. This method allows lines of the order of 1 cm in length to be characterized with a 1 µm or better spatial resolution. The method is proven to be a good way of determining microstructural parameters, which are important when studying recrystallization dynamics.
The nucleation of recrystallization at triple junctions has been studied by 3 dimensional X-ray diffraction (3DXRD), allowing for the first time the deformed and recrystallized microstructures to be compared at a given nucleation site in the bulk of a metal sample. From an experiment three nuclei were identified, their respective crystal orientations were determined, and growth curves were obtained for two of them.

Resume :
Denne afhandling dækker tre resultater opnået i løbet af projektet:
En pålidelig metode til at udføre seriel sektionering på metalprøver vha. en Logitech poleringsmaskine er blevet udviklet. Seriel sektionering er blevet udført på metalprøver i 1 µm skridt ved brug af mekanisk polering og i 2 µm skridt hvor elektropolering var nødvendigt.
En metode hvormed pålidelige EBSP-linieskans kan udføres ved at skanne tre parallelle linjer er blevet udviklet. Denne metode tillader linjer, med længder af størrelsesorden 1 cm, at blive karakteriseret med en rumlig opløsning på 1 µm. Metoden er blevet påvist at være en god metode til at bestemme de mikrostrukturelle parametre, som er vigtige ved studier af dynamikken i rekrystallisation.
Kimdannelse ved tripelgrænser er blevet studeret vha. 3 dimensional røntgendiffraktion, hvilket for første gang tillod de deformerede- og rekrystalliserede mikrostrukturer at blive sammenlignet ved et kimdannelsessted i det indre af en metalprøve. Tre kim blev identificeret i et eksperiment, deres respektive krystalorienteringer blev bestemt, og vækstkurver blev bestemt for to af dem.

Risø-PhD-9(EN)
September 2005

ISBN 87-550-3417-9

Cover :
The images on the cover show respectively:
(centre) a typical X-ray diffraction image obtained from a deformed sample, but including two reflections from a nucleus;
(top left) an image obtained from copper by optical microscopy utilizing polarized light;
(top right) a single Vickers hardness indentation;
(bottom left) EBSP from silicon; and
(bottom right) an EBSP orientation image map of a sample for X-ray studies.

Pages: 133/193
Tables: 8
Figures: 45
References: 119

Risø National Laboratory
Information Service Department
P.O.Box 49
DK-4000 Roskilde
Denmark
Telephone +45 46774004
bibl@risoe.dk
Fax +45 46774013
www.risoe.dk

Abstract

This thesis covers three main results obtained during my Ph.D. project:

A reliable method of performing serial sectioning on metal samples utilizing a Logitech PM5D polishing machine has been developed. Serial sectioning has been performed on metal samples in 1 μm steps utilizing mechanical polishing, and in 2 μm steps when electrochemical polishing was needed, such as for electron backscatter pattern (EBSP) studies. It is proven possible to polish down from the sample surface to a pre–specified target depth with an accuracy of 1–2 μm, and in all cases, the height difference across the sample surface was not more than 1–2 μm.

A method by which reliable EBSP line scans may be performed by scanning three parallel lines has been developed. This method allows lines of the order of 1 cm in length to be characterized with a 1 μm or better spatial resolution, in the same time that it takes to acquire a standard EBSP map consisting of 173×173 data points, thus drastically improving the sampling statistics. The method is proven to be a good way of determining the microstructural parameters: the volume fraction recrystallized; the free surface area density separating recrystallized and deformed material; and the mean intercept length of the recrystallized grains, which are important when studying recrystallization dynamics.

The nucleation of recrystallization at triple junctions has been studied by 3 dimensional X–ray diffraction (3DXRD), allowing for the first time the deformed and recrystallized microstructures to be compared at a given nucleation site in the bulk of a metal sample. From an experiment three nuclei were identified, their respective crystal orientations were determined, and growth curves were obtained for two of them. Two nuclei were found to exhibit orientations corresponding to 1st order twins of one of the deformed grains. The third nucleus was however found to appear with a new orientation, neither present in any of the deformed grains associated with the triple junction or 1st order twin–related to any of them.

The images on the cover show respectively:
(centre) a typical X–ray diffraction image obtained from a deformed sample, but including two reflections from a nucleus; *(top left)* an image obtained from copper by optical microscopy utilizing polarized light; *(top right)* a single Vickers hardness indentation [1]; *(bottom left)*; EBSP from silicon [2]; and *(bottom right)* an EBSP orientation image map of a sample for X–ray studies.

Abstract in Danish

Denne afhandling dækker tre resultater opnået i løbet af mit ph.d.-projekt:

En pålidelig metode til at udføre seriel sektionering på metalprøver vha. en Logitech PM5D poleringsmaskine er blevet udviklet. Seriel sektionering er blevet udført på metalprøver i 1 μm skridt ved brug af mekanisk polering og i 2 μm skridt hvor elektropolering var nødvendigt, som f.eks. ved studier vha. EBSP. Det er blevet bevist, at det er muligt at polere ned fra prøveoverfladen til en prædefineret dybde med en nøjagtighed på 1-2 μm, og i alle tilfælde har højdeforskellen henover overfladen ikke overskredet 1-2 μm.

En metode hvormed pålidelige EBSP-linieskans kan udføres ved at skanne tre parallelle linjer er blevet udviklet. Denne metode tillader linjer, med længder af størrelsesorden 1 cm, at blive karakteriseret med en rumlig opløsning på 1 μm eller bedre på den samme tid, som det tager at optage et standard EBSP-kort bestående af 173x173 datapunkter, og derved drastisk forbedre målestatistikken. Metoden er blevet påvist at være en god metode til at bestemme de mikrostrukturelle parametre: volumenbrøkdelen af rekrystalliseret materiale; densiteten af frit areal, som adskiller deformeret og rekrystalliseret materiale; samt den gennemsnitlige interceptlængde af de rekrystalliserede korn, som er vigtige ved studier af dynamikken i rekrystallisation.

Kimdannelse ved tripelgrænser er blevet studeret vha. 3 dimensional røntgendiffraktion, hvilket for første gang tillod de deformerede- og rekrystalliserede mikrostrukturer at blive sammenlignet ved et kimdannelsessted i det indre af en metalprøve. Tre kim blev identificeret i et eksperiment, deres respektive krystalorienteringer blev bestemt, og vækstkurver blev bestemt for to af dem. To kim blev fundet med orienteringer, der svarede til førsteordens tvillinger af en af de deformerede korn, og det tredje kim havde en ny orientering, der hverken svarede til orienteringen af en af de deformerede korn ved en triplegrænse og heller ikke var førsteordens tvillingerelateret til nogen dem.

Billederne på forsiden viser respektivt:
(midten) et typisk røntgendiffraktionsbillede optaget af en deformeret prøve, men som også inkluderer to reflekser fra et krystalkim; *(øverst t.v.)* billede optaget af kobber vha. optisk mikroskopi med polariseret lys; *(øverst t.h.)* et enkelt Vickers hårdhedsindtryk [1]; (nederst t.v.) EBSP fra silicium [2]; og *(nederst t.h.)* et EBSP orienteringskort af en prøve brugt til røntgenstudier.

Preface

This thesis is submitted in partial fulfilment of the requirements for obtaining the Ph.D. degree at the University of Copenhagen. The research presented here was carried out within the Center for Fundamental Research: Metal Structures in Four Dimensions (Metals–4D center), at Risø National Laboratory, under the supervision of Jens Als–Nielsen at the University of Copenhagen, and Dorte Juul Jensen and Henning Friis Poulsen both at the Metals–4D center.

The work presented here was done during the period from September 1. 2001 until August 31. 2004, and included are six publications (including a technical report) by the author, of which four have the author as first author.

The author gratefully acknowledges the Danish Research Foundation for supporting the Center for Fundamental Research: Metal Structures in Four Dimensions, within which this work was performed. This work was also partly supported by the Danish Natural Science Research Council (via Dansync), and the ESRF is acknowledged for provision of beamtime.

The author wishes to thank everyone associated with the Metals–4D center for ideas, help, discussions, and simply for making the time spent on this PhD–project a pleasant one. Dorte Juul Jensen in particular is thanked for her guidance, support, trust, and general wonderful personality, which has been a great source of inspiration.

The author would also like to thank Jørgen Bilde–Sørensen and Christian Mammen for many good discussions on respectively electron microscopy and X–ray physics, and Kristofer Hanneson for his contributions to developing the serial sectioning technique.

Lastly, a special thank you must go to the three technicians Preben Olesen, Palle Nielsen, and Helmer Nilsson, who have been of tremendous help during this PhD project, and with whom I have shared many a good laugh.

Contents

List of Tables

List of Figures

List of Abbreviations

3DXRD	Three–dimensional X–ray diffraction
AI	Area of Interest
bcc	body centered cubic
BF	Bormann fan
CCD	Charge–Coupled–Device
CMS	Centre of Mass
EBSP	Electron Backscatter Patterns
ECD	Equivalent Circle Diameter
EM	Electron Microscopy
ESRF	European Synchrotron Radiation Facility
fcc	face centered cubic
FWHM	Full–Width–at–Half–Maximum
HAGB	High Angle Grain Boundary
LAGB	High Angle Grain Boundary
ML	Multilayer
ND	Normal direction (rolling geometry)
ODF	Orientation Distribution Function
OFHC	Oxygen–Free High Conductivity
OIM	Orientation Image Map
OM	Optical Microscopy
PSN	Particle Stimulated Nucleation
RD	Rolling direction (rolling geometry)
SEM	Scanning Electron Microscope
SFE	Stacking Fault Energy
SIBM	Strain–Induced Boundary Migration
TD	Transvers direction (rolling geometry)
TEM	Transmission Electron Microscope

Chapter 1

Introduction

This PhD thesis deals with the nucleation of recrystallization, which is the initial step of discontinuous recrystallization (see section 1.1). The aim of the PhD project was to spatially and crystallographically characterize nucleation in metals using various experimental techniques (see section 1.3).

This thesis is divided into 5 chapters:

1. a general introduction to the nucleation of recrystallization, including nucleation theories, and the relevant experimental techniques;
2. an introduction to stereology, a stereological technique (LSGRAINS) developed by the author, and scientific results obtained using this technique;
3. an introduction to microscopical techniques (both optical and electron), with special detail given to the electron backscatter pattern technique;
4. an introduction to 3 Dimensional X–Ray Diffraction (3DXRD), followed by the *in situ* study of nucleation of recrystallization, which was performed using this technique, will be covered in detail;
5. an overall conclusion based on the results obtained in the previous three chapters, as well an outlook on their potential impact.

This chapter includes an introduction to the thesis, as well as three sections dealing with respectively: (i) an introduction to basic metallurgy relevant for the nucleation of recrystallization; (ii) an introduction to current nucleation theories; (iii) and an introduction to experimental techniques used to study recrystallization, as well as the ones used in this PhD project.

Typically, it is assumed that the nuclei (the new grains when they initially appear) are formed from cells in the deformed/recovered structure, which grow especially fast, i.e., that the nuclei have the same crystallographic orientation as the deformed microstructure they nucleate from. However, new experimental results have indicated that nuclei can form with orientations not observed in the deformed microstructure [3, 4, 5, 6, 7, 8], and therefore that simple growth mechanism models are inadequate to fully describe the nucleation process. Examples of such models are given in references [9, 10].

Nucleation of recrystallization is not an easy process to study, as the size of nuclei are of the order of $\sim$1 μm (samples are sized 10^3–10^4 μm), the nuclei may be heterogeneously distributed within the material, and as the nuclei grow into a deformed grain they consume the parent microstructure, thereby "erasing" any trace of it, and thus making it impossible to determine which physical mechanism resulted in the creation of the nuclei, because we, so to speak, have only half the picture.

One reason why precise incontrovertible experimental data of the nucleation of recrystallization is so difficult to obtain is because it has so far been impossible to characterize both a bulk nucleus and its parent microstructure in a nucleation event. Either dynamic information has been obtained from the surface, which can not necessarily be viewed as representative of the bulk kinetics and there is also the uncertainty of whether the nucleus grew up to the surface from the sample bulk below [3, 11], or nuclei have been located on polished sections, where it is not possible to determine the exact microstructure, which was previously present at the nucleation sites [8].

In recent years, a new technique utilizing high energy X–rays has been developed, which allows studies of exactly the desired nature (see section 1.3) [4]. The main focus of this PhD project was to design and perform an experiment, which allowed *in situ* studies bulk of nucleation before, during, and after annealing. However, this PhD project also involved other experimental methods relevant for studying recrystallization.

1.1 Metallurgical background

The vast majority of metal components used for industrial purposes are polycrystalline. That is, they are typically conglomerates of crystal grains with a size of the order of 1–1000 μm, which can be considered as individual single crystals with a low mosaic spread[1], and each with its own crystallographic orientation[2] [13, 14]. For a general overview of metallurgy the reader is referred to the following references [10, 15, 16, 17].

When a metal or alloy is plastically deformed at a relatively low temperature microstructural changes occur (see figure 1.1) [18]:

- the grain shape is deformed, according to the imposed deformation.
- point defects (mainly vacancies) are generated from jogs on the dislocation lines.
- line defects (dislocations) are generated and pile up, creating boundaries in cell–forming metals.

This results in an increase of stored energy, and changes the mechanical properties of the metal or alloy. In recent years, much knowledge of these processes has been gleaned, particularly from studies of the build up of dislocation structures by electron microscopy [19, 20].

When the plastically deformed metal or alloy is subsequently heated (annealed), the energy stored by the deformation processes is released in three (usually overlapping) processes.

Recovery is the process, which occurs first at lower temperatures, and according to Cotterill & Mould it refers to all the various annealing phenomena, which occur during annealing, but *prior* to the appearance of new strain–free grains [22]. It is dominated by the removal of excess vacancies to [23]: free surfaces; grain boundaries; and dislocation, which leads to climb, and the sharpening of the dislocation substructure, often referred to as polygonization. After the onset of recovery, it is more correct to speak of the deformed microstructure as the *recovered* microstructure. The energy released during recovery generally represents less than 10% of the total stored energy.

[1]The *mosaic spread* of a single crystallite corresponds to its spread of crystal orientations, the so–called mosaic distribution [12].

[2]In this context crystallographic orientation is understood as: the orientation of the crystal lattice of the grain with respect to the main axis of deformation imposed on the metal sample (see appendix A).

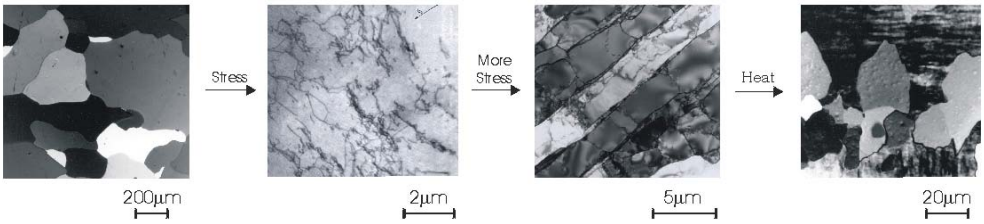

Figure 1.1: *Micrographs showing the microstructure during different stages of thermomechanical processing. In the figure on the left the microstructure is fully recrystallized. It is subsequently deformed and dislocation tangles are seen to appear, and after additional deformation the microstructure is subdivided into distinct cells. Lastly, during annealing new strain–free grains nucleate and grow [21].*

In terms of rising temperature, the next process to occur is recrystallization, of which two types can be identified [24]:

- Continuous recrystallization, where the recovered dislocation substructure keeps on coarsening. It is a homogeneous type–I Gibbs process.
- Discontinuous recrystallization (the most common, and the case of interest in this study), where a new set of strain–free grains nucleate and grow, and thereby consume the deformed/recovered microstructure. It is a heterogeneous type–II Gibbs process.

Recrystallization begins at an ill–defined temperature, which is referred to as the *recrystallization temperature*. This temperature also distinguishes the cold work region (of interest in this study), which takes place below the recrystallization temperature [25, 26, 27]. The recrystallization temperature is affected by the initial stored energy that is in the metal, and the amount of recovery that has taken place prior to recrystallization — it is in fact possible to recover samples so much that recrystallization will not set in at *any* temperature [22].

The process of discontinuous recrystallization (simply referred to as recrystallization from now on) is divided into two steps: (i) critical embryos, present in the deformed/recovered microstructure, that nucleate as new grains; and (ii) the new grains that grow until they impinge upon each other and thus consume all the deformed/recovered material in the microstructure (the micrograph on the right in figure 1.1 shows a partially recrystallized microstructure).

The final annealing process to take place is *grain growth*, also called grain coarsening. When the entire deformed/recovered microstructure has been consumed by the recrystallizing grains, large grains generally continue to grow at the expense of smaller grains, which increases the mean grain size, and leads to a reduction in the total grain boundary area and therefore the total grain boundary energy [28]. Once again, homogeneous coarsening may be thought of as a type–I Gibbs process.

This study is concerned with the fundamentals of the nucleation of recrystallization. It is however important to note the industrial/commercial importance of recrystallization, because the recrystallized grains determine to a large extent the properties of the annealed metal or alloy, and it is therefore of great importance to understand the nucleation of recrystallization, both from a scientific as well as from an applied point–of–view. Thus in forming car body steel sheet from a cast billet or aluminium sheet stock many of tens of recrystallization steps may be involved.
The recrystallization process (often repeated): a) controls the crystallographic texture of the metal (see appendix B), which is important e.g. to obtain an isotropic deformation when bodies are stamped from sheet material; b) breaks up segregation within the casting and homogenizes the chemistry. This is because migrating grain boundaries are able to redistribute solutes over very large distances compared with bulk diffusion; c) removes any undesirable columnar grain structure and replaces it with the more desirable equiaxed grain shape; d) allows a suitable grain size to be selected.
For most applications, a fine grain size is preferable, giving high strength ($\sigma \propto$(grain size)$^{-1/2}$), high fatigue strength, toughness and corrosion resistance. However, where good creep properties are required, a coarse–grained microstructure (or even large single crystals) may be grown by a process referred to as the "strain–anneal" method, where repeated critical strains (deformations) and anneals are given to selectively reduce the number of recrystallization nuclei which form [22].

In essence, discontinuous recrystallization is a solid state phase transition, where there is no change of composition or crystal lattice [29]. However, there is a significant difference between this type of phase transition and other phase transitions, such as the liquid–to–solid phase transition, precipitation within a solid, or the change from one phase to another, eg. the austinite–to–ferrite transition in iron, where the crystal structure changes from the *fcc* to the *bcc* lattice. In the other cases the nucleus size is relatively small, involving a few tens of atoms, and this can be formed (homogenously and

heterogeneously) by statistical fluctuations within the system [29, 24]. This is not the case for the nucleation of recrystallization, where calculations show that a critical nucleus has a size in the micrometre range [24, 30].

1.2 Nucleation theories

In this section we will focus on what is known about the nucleation process, and the most common nucleation theories will be summarized. Nucleation is a process, where small regions, known as critical embryos, nucleate as new strain–free grains in the deformed/recovered microstructure. The nuclei are typically heterogeneously distributed within the bulk of the material. Nucleation is also a rare event considering that the size of a critical embryo is $\sim$1 μm, and if the material is allowed to fully recrystallize with an average grain size of $\sim$100 μm, this estimate hints that much material must be characterized in order to locate nuclei early in the nucleation process.

In single–phase materials[3] it has been shown that the critical embryo size cannot be achieved by atom–by–atom construction through thermal fluctuations [24]. It is instead accepted that nuclei grow from subgrains in the deformed structure through a thermally activated process, and that in order to become a nucleus a subgrain *must* have a minimum size and a high angle boundary (HAGB) of high mobility [7, 30]. Also, the number of successful nucleation events increases with increasing stored energy, and the nucleation rate increases with increasing temperature above the recrystallization temperature.

1.2.1 Strain–induced boundary migration

One mechanism by which nucleation is thought to proceed is strain–induced boundary migration (SIBM). It involves a part of a pre-existing high angle boundary bulging, and leaving a relatively dislocation–free region behind the migrating boundary (see figure 1.2). This region will become a nucleus if the bulge is sufficiently large. Two different scenarios can occur, in which either multiple subgrains make up the bulge (fig. 1.2b), or a single large subgrains makes up the bulge (fig. 1.2c). An interesting point about the SIBM mechanism is that it appears to have no incubation time if a suitably

[3] *single–phase* is defined as a material consisting of one chemical species or compound (eg. NaCl) without concentration gradients (i.e., a constant crystal lattice).

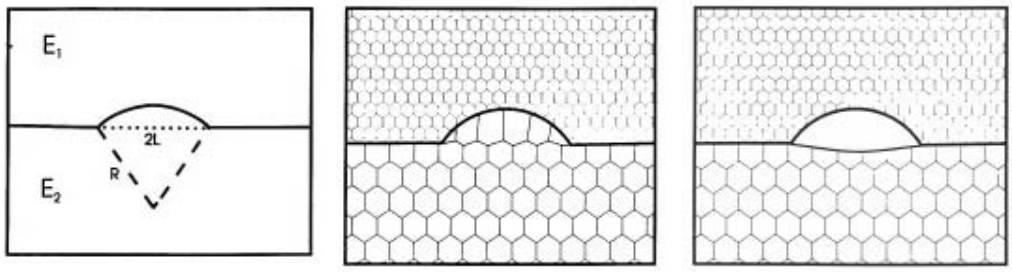

(a) (b) (c)

Figure 1.2: *Critical embryo creation by strain–induced boundary migration (SIBM). A part of the HAGB bulges out into the grain with the higher stored energy (E_1>E_2), and if the driving force is big enough it will keep bulging until it reaches the size of a critical embryo.* ***(a)*** *Initial bulge on a HAGB;* ***(b)*** *multiple subgrain SIBM; and* ***(c)*** *single subgrain SIBM [11].*

sized subgrain is available at a grain boundary at the start of annealing, as opposed to other recovery driven nucleation mechanisms. If however a subgrain of suitable size must first be produced by other recovery mechanisms there is of course an incubation time [22].

The driving force is the difference in stored energy at the two sides of the HAGB ($E_V = E_1 - E_2$). The boundary energy of a spherical bulge with radius R, and boundary energy γ_B [J/m^2] is [11]:

$$E_B = 4\pi R^2 \gamma_B \quad \Longrightarrow \quad \frac{dE_B}{dR} = 8\pi R \gamma_B \tag{1.1}$$

In the early stages of bulging, i.e., before the dislocation density drops within the bulge, the driving force is given by the energy difference E_V between the microstructures:

$$\frac{dE}{dR} = 4\pi R^2 E_V \tag{1.2}$$

In order for the bulge to grow we must have $\frac{dE}{dR} > \frac{dE_B}{dR}$, and if the critical point is taken to be when the bulge is a hemisphere (R=L), then from equations 1.1 and 1.2, which contain the conditions for a HAGB bulge developing

into a nucleus:

$$\frac{dE}{dR} > \frac{dE_B}{dR} \implies$$
$$R > \frac{2\,\gamma_B}{E_V} \implies L > \frac{2\,\gamma_B}{E_V} \tag{1.3}$$

By inserting typical values ($\gamma_B \approx 0.5$ Jm^{-2}, and $E_V \approx 10^6$ Jm^{-3}) into eq. 1.3 we find the minimum radius of an embryo to be $L \approx 1$ μm, which is in concurrence with what is observed experimentally [11].

1.2.2 Subgrain coalescence

Subgrain coalescence is a mechanism that allows two or more subgrains in the deformed microstructure to merge into one larger subgrain, which may then be a potential embryo (see figure 1.3). It is based on the rotation of a subgrain, so as to reduce the grain boundary energy of a low angle subgrain boundary (LAGB) separating two subgrains.

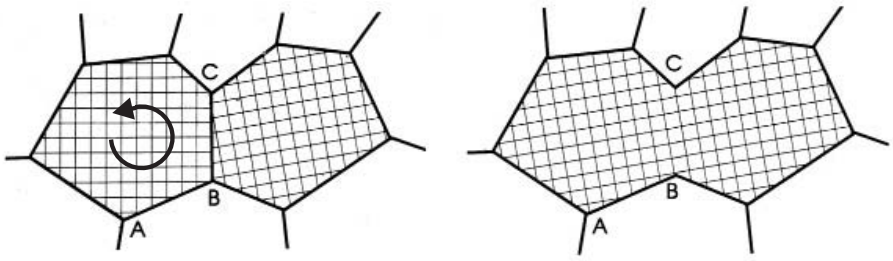

(a) (b)

Figure 1.3: *Embryo creation by subgrain coalescence. The LAGB (B to C) disappears due to the rotation of a subgrain:* ***(a)*** *Two subgrains divided by a LAGB;* ***(b)*** *The subgrains have coalescenced into one bigger subgrain (embryo) [11].*

For a low angle tilt boundary with a misorientation angle θ, the boundary energy γ may readily be calculated from the Read–Shockley equation [11]:

$$\gamma(\theta) = \gamma_m \frac{\theta}{\theta_m}\left[1 - \ln\left(\frac{\theta}{\theta_m}\right)\right] \tag{1.4}$$

where the parameters γ_m and θ_m are respectively the energy and misorientation as the boundary becomes a high angle boundary (HAGB). θ_m is typically set to 15°.

The rate by which subgrain reorientation can occur by dislocation climb of a single tilt boundary has been studied, first by Li and later by Doherty & Szpunar, who arrived at an expression for the rate of subgrain rotation [31, 32]:

$$\frac{d\theta}{dt} = \frac{3\gamma_m \theta B b}{L^2 \theta_m} \ln\left(\frac{\theta_m}{\theta}\right) \tag{1.5}$$

where L is the height of the boundary, b is the Burger's vector of the dislocations, and B is the mobility of the dislocations.

During a coalescence event in a recovered microstructure, the reorientation of a subgrain affects *all* of the N ($\sim$12) surrounding subgrain boundaries. The total driving force for reorientation of a subgrain is the contributions from all its boundaries [11]:

$$F = \sum_{i=1}^{N} L_i^2 \frac{d\gamma}{d\theta} = \sum_{i=1}^{N} L_i^2 \frac{\gamma_m}{\theta_m} \ln\left(\frac{\theta_m}{\theta}\right) \tag{1.6}$$

From eq. 1.6 it is evident that the largest driving force will come from the boundary with the smallest θ and the largest L, which from eq. 1.5 will have the lowest rate of rotation. It can therefore be argued that the lowest rate of rotation is to a first approximation the controlling rate of rotation of the entire subgrain. It should be noted that θ and L refer not to the average properties of the subgrain, but to the largest value of $(L^2 \ln\{\frac{\theta_m}{\theta}\})$, which means that to determine the kinetics of subgrain rotation we need to know the initial distribution of subgrain sizes and orientations, and also how these parameters evolve as the coalescence event progresses. The usual modelling method is to equate θ with the mean misorientation between subgrains, and to assume that all subgrains with a diameter less than L have coalesced at the time t, so that L^2 is proportional to t [11].

The limited experimental evidence of subgrain coalescence is inconclusive. Direct evidence of subgrain rotation has been observed , but this was from *in situ* transmission electron microscopy heating experiments, where surface effects could not be ruled out, and at a temperature close to the melting temperature ($T \approx 0.9\, T_m$) [11], which is a much higher temperature than the recrystallization temperature. So far, all bulk experiments have been *post*

mortem experiments, where it is not possible to distinguish between whether a LAGB is forming or disappearing. However, *post mortem* studies have shown that the subgrain size adjacent to HAGB is larger than in the interior of the grain, which correlates well with simulation data that predicts that coalescence is roughly 2.5 times more likely to occur adjacent to a HAGB than within the interior of a recovered grain (see fig. 1.2) [11].

1.2.3 Subgrain coarsening

Subgrain coarsening is an alternative mechanism by which neighboring subgrains may merge into a critical embryo. The mechanism is believed to be the migration of a LAGB, which can then be absorbed in another grain boundary (see figure 1.4).

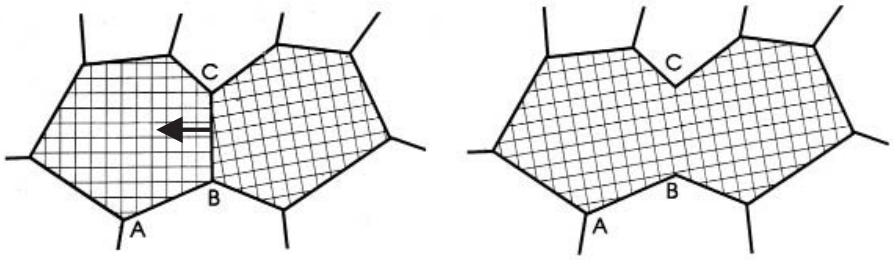

(a) (b)

Figure 1.4: *Embryo creation by subgrain coarsening: The LAGB (line from B to C) moves (see arrow) through the left subgrain, eventually being absorbed in the left boundary.* ***(a)*** *Two subgrains divided by a LAGB;* ***(b)*** *The two subgrains have coarsened into one bigger subgrain (embryo) by LAGB migration [11].*

Experimental evidence suggests that this process occurs primarily within regions with large orientation gradients. In such regions statistical studies show an increase in the mean misorientation across boundaries, and an increase in the mean subgrain size with annealing time [11].

1.2.4 Inverse Roland

The inverse Roland nucleation mechanism has been proposed to explain the strong 'cube' annealing texture (i.e., {100}<001>) in cold rolled face centered cubic (*fcc*) material specimens (see appendix A and B). Experimental evidence indicates invariably that the 'cube' texture forms during recrystallization when the rolling texture is of the 'copper'–type (i.e., {112}<111>).

The proposed mechanism was that twins produced during deformation, could coalesce by cooperative glide on <111>–planes, i.e., glide of partial dislocations, and the proposed twin orientations were of the {112}<111> orientation [33]. In the absence of large (>1 μm) interstitial particles within the microstructure (see section 1.2.6), the inverse Roland mechanism is the only proposed nucleation mechanism, which predicts nuclei forming with orientations, which are *not* already present in the parent microstructure.

However, this mechanism is not thought to work for high stacking fault energy (SFE) metals, such as aluminium, which is also known to produce the 'cube' texture. Also, several materials that where predicted to produce strong 'cube' texture failed to do so during investigations, which has generally caused the inverse Roland nucleation mechanism to be rejected [33]. Instead, experimental evidence suggests that the 'cube' annealing texture should be explained by 'cube' grains having a higher growth rate [34]. In general, there has been a very long argument about the relative importance of oriented nucleation vs. oriented growth (eg. Lücke vs. Verbraak), which has yet to be fully resolved [35, 36, 37].

A stacking fault is a rigid translation of a portion of the crystal lattice by the $\left(\frac{\mathbf{a}}{6}[11\bar{2}]\right)$–vector, where $\mathbf{a}$ is a crystal lattice vector. This can be produced by plastic glide during deformation or a growth accident during grain growth [38]. The stacking fault energy (SFE) is the energy associated with a stacking fault on a {111} plane, and it depends on the specific volume of the metal, and the atomic bonding. For further details, the author refers to Haasen [15]. A short list of the SFE of various common metals is given in table 1.1:

Ag	Co	Au	Cu	Ni	Al	Zn
20	25	40	60	130	200	250

Table 1.1: *Stacking fault energy of various common metals. The values are in mJ/m^2, at a temperature of 300 K, and for the stable microstructure [39].*

1.2.5 Twinning

Twinning is not a proposed nucleation mechanism in its own right, but rather it is a process, by which recrystallizing grains may develop orientations not previously present in the parent microstructure [8, 39]. Twinning consists of a 60° rotation of the crystal lattice about a {111}–axis (equivalent to forming a coincidence site lattice with $\sum 3$), which is envisaged to occur via a growth accident on a {111}–plane (see fig. 1.5), and it produces orientations *not* previously present in the parent microstructure. The possible new orientations produced by a twinning event are discussed in appendix A.1. During recrystallization of certain materials, particularly in *fcc* metals with

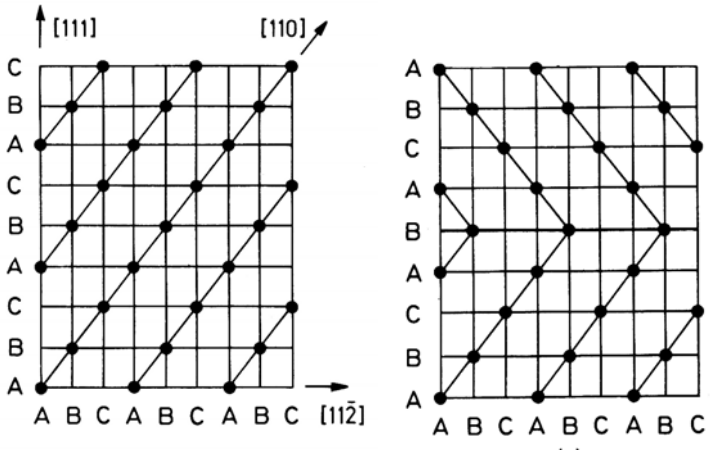

(a) (b)

Figure 1.5: *A stacking fault in an* fcc *lattice leading to twinning. The perfect* fcc *ABC/ABC/...stacking of* **(a)** *is turned into* **(b)** *if a stacking fault occurs, such that an expected C layer becomes an A layer instead [38].*

low–to–medium SFE such as copper, annealing twins are formed.

A proposed model for the formation of annealing twins in low–to–medium SFE metals, which is what would be seen after nucleation events, is based on the nucleation of Shockley partial dislocation loops on consecutive {111}–planes by growth accidents on moving {111}–steps on a migrating grain boundary [40]. In short, the model only predicts twinning in low–to–medium SFE metals, because the Shockley partial dislocation loops are stable there. Furthermore, the probability of growth accidents occurring rises with increas-

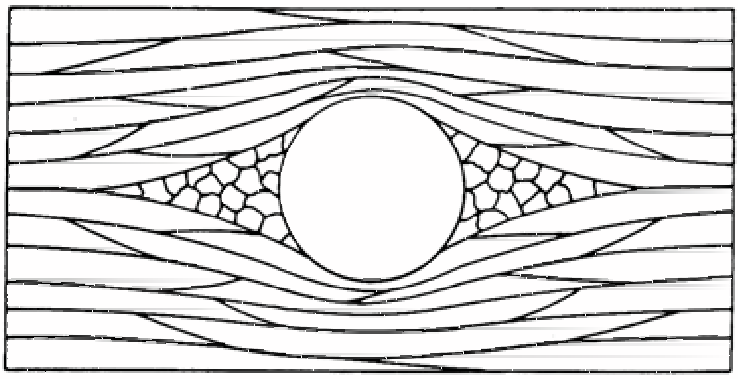

Figure 1.6: *Strained and misoriented zone around a rigid interstitial particle. The zone extends ∼2d around a particle of diameter d [41].*

ing grain boundary mobility, so alloying elements have a role too, since they both lower the SFE and lower the grain boundary mobility in general.

1.2.6 Particle stimulated nucleation

Interstitial rigid particles within the microstructure can have one of two effects on the nucleation behavior. If the particles are present as a fine dispersion of fine particles (∼0.1 μm), they will actually retard the nucleation process, as the fine particles act as inhibitors to the movement of both dislocations and grain boundaries.

If however, the particles are sized d>1 μm they can give rise to high local concentrations of stored energy and large misorientations in the surrounding microstructure when the particle–containing material is deformed (see fig. 1.6), and can thus act as favorable nucleation sites. These zones of high stored energy tend to extend $\sim 2d$ from the particle itself, which means that the size of the zone is determined by the size of the particle [41]. There is experimental evidence that the microstructure tends to rotate around the particles when the particle–containing material is deformed, which depending on strain, can create a local misorientation of 10° or higher to the surrounding microstructure.

Thus if the strained region, which depends on the particle size, is larger than the critical nucleus size, nuclei can form in these strained regions and immediately start growing due to the misorientation to the surrounding mi-

crostructure. For elongated particles, the misorientations are greatest at the ends of the particles, which means that any nucleation is likely to occur there [41]. This can then give rise to nuclei with orientations not previously present in the deformed grains away from the particles. However, truly new orientations are not created, as the nuclei are envisaged to grow from the highly misoriented subgrains within the strained region around the particles [23, 25, 41, 42].

1.3 Experimental techniques

A wide variety of experimental techniques have been applied to study the processes involved in annealing and recrystallization. Macroscopically, since recovery largely involves elimination of vacancies, the recovery process as well as the recrystallization process may be followed by monitoring the change in *electrical resistivity* [22]. The main hardness changes taking place during the regime of recrystallization can be studied directly by *hardness indentation* (see section 1.3.1) [43], and since the whole annealing process involves the release of stored energy, *calorimetry* can be used to good effect throughout all three stages of annealing [22].

Many forms of microscopy have been employed in studying recrystallization (see section 1.3.3), and much of what is known about the detailed mechanisms of recrystallization has been gleaned from studies using transmission electron microscopy (TEM). This has been particularly useful in following the evolution of dislocation substructures from the cold worked state to the recovered state and then on to the nucleation of recrystallization [44]. *Optical microscopy* (especially using polarized light for enhanced contrast) has been used to identify nucleation sites. Until 20 years ago *scanning electron microscopy* has had only a minor role to play in recrystallization studies, but with the advent of channelling diffraction [45], and more recently automatic characterization of electron backscatter patterns [46, 47], one has a technique well suited to recrystallization studies of the surfaces of metals.

X–ray and neutron diffraction have also long been used in metallurgy, but their use has always been limited by various factors. The penetration depth of X–rays generated by a copper or molybdenum anode is of the order of μm, which has severely limited their usefulness for bulk studies, and in the case of neutrons, the mm spatial resolution has limited studies to mostly strain and texture analysis [17, 48, 49]. However, with the advent of synchrotron

X–ray sources, higher fluxes and energies have become available, and it has thus become possible to perform non–destructive *in situ* experiments on *bulk* single–phase metal and alloy samples using X–ray diffraction, due to the massive increase in penetration depth, which is now of the order of *mm* (see section 1.3.4) [50].

In order to perform a study of the nucleation of recrystallization, of the form described in the introduction, it is necessary to characterize the deformed microstructure within a suitably large *volume*, so as to be reasonably sure that at least one nucleation event will take place within that given volume during recrystallization. Also, the characterization of the deformed microstructure must be non–destructive, so as to not effect the subsequent mechanism of the nucleation event(s). This basically means that we must be able to non–destructively probe volumes sized up to 1 mm^3 within a reasonable amount of time and still be able to detect and characterize new nuclei sized $\sim$1 μm^3, which translates as being able to detect volume fractions down to 10^{-9}.

The choice was made to study nucleation (recrystallization) using both well tested metallurgical techniques (hardness indentation, optical and electron microscopy), and a newly–developed technique (3 Dimensional X–Ray Diffraction). The classical approaches are to study the polished surface, or very thin sections of samples using optical or electron microscopy. This allows a wealth of information to be obtained, but only from the surface or thin section, and if heating experiments are involved, it is not possible to rule out surface effects. The new technique is to use high energy synchrotron radiation to non–destructively characterize the bulk of a sample before, during and after heating, and thus follow nucleation *in situ*.

1.3.1 Hardness indents

A classical way of studying recrystallization is by hardness indents, which gives a direct measure of the recrystallization–induced softening in the material. A hardness test measures the resistance of a material to penetration by a harder test body. Many different hardness tests exist, but they mainly differ in the shape of the object, which is pressed into the sample. For this PhD project, the Vickers hardness indentation test was used [43].

A Vickers hardness test consists of pressing a pyramidal diamond indentor with an apex angle of 136° into the sample surface with an accurately controlled load (see fig. 1.7a) for a specific dwell time (typically 10–15 s). After

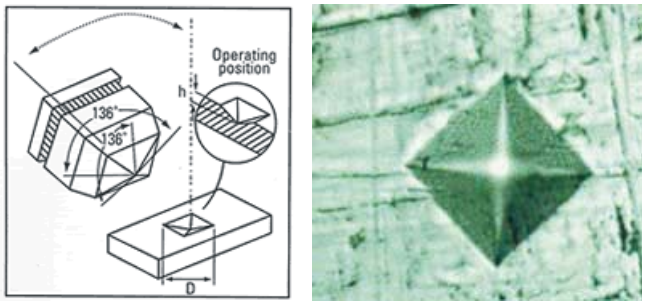

(a) (b)

Figure 1.7: *Vickers hardness indents.* ***(a)*** *the Vickers hardness indentation system [1];* ***(b)*** *a single Vickers hardness indentation seen from above [51].*

the pyramid is removed an indentation is left in the surface, which appears square shaped (see fig. 1.7b). Its size is determined optically by measuring the two square diagonals of the indentation. Because the indentation size is measured optically, the sample surface must be pre–polished in order to get an accurate measurement of the diagonals. The Vickers hardness H_V [N/m^2] is a function of the test load divided by the surface area of the indentation, which is calculated from the mean of the two diagonals. Thus H_V is given by [1, 15]:

$$H_V = C_1 \times \frac{\text{test force}}{(\text{indent diagonal})^2} \tag{1.7}$$

where C_1 is a function of the pyramid geometry, and the units of load and diagonal. It is usually tabulated for a given hardness indentor. Generally, the mean width of several indentions are used to calculate the hardness.

By annealing samples at different temperatures and for different lengths of time, the resulting hardness curve allows one to determine at which temperature material softening (eg., recrystallization) sets in, and how quickly it progresses. This is possible because the flow stress of a metal is the sum of the flow stress of all its constituents, so a dramatic softening corresponds to the transformation of the harder deformed/recovered material into softer recrystallized material.

Thus from Hansen &Ṽandermeer [52]:

$$\sigma_f - \sigma_0 = \sigma_r V_V + \sigma_d(1 - V_V) \tag{1.8}$$

where V_V is the volume fraction recrystallized of material, σ_f, σ_0, σ_r, and σ_d are respectively the flow stress, the lattice friction stress, the flow stress of the recrystallized material, the flow stress of the deformed/recovered material.

1.3.2 Optical microscopy

Optical microscopy consists of studying back–reflected light from polished (and often chemically etched) surfaces of metal samples. By using polarized light, after anodization of the polished surface, it is often possible to clearly distinguish between regions of different crystallographic orientation. The size, shape, and location of individual grains or groups of grains may be determined, but the crystallographic orientation of the individual grains is *not* determined directly.

1.3.3 Electron microscopy

Scanning electron microscopy (SEM) has been used extensively to characterize the microstructure of metal samples in this thesis. In SEM an electron beam impinges upon the *surface* of a sample, and information is obtained from the backscattered electrons as well as the emitted X–ray photons. In modern scanning electron microscopes, the spatial resolution may be as good as ∼10 nm.

The microscopy technique of choice during this PhD project has been the electron backscatter patterns (EBSP) technique, where the electron beam is diffracted according to Bragg's law (see eq. 2.1). It is a technique by which a scanning electron microscope may be used to characterize the microstructure of a sample based on crystallographic analysis, and it is based on analyzing the electrons elastically scattered, from different crystal planes, onto a 2D detector. A beautiful example of an EBSP image can be seen on figure 1.8.

It is a quantitative technique that reveals grain size, grain boundary character, grain orientation, texture, and phase identity from the polished surface of metallurgical, ceramic, and geological samples. Depending on the scanning electron microscope used, the technique enables analysis of up to cm–sized

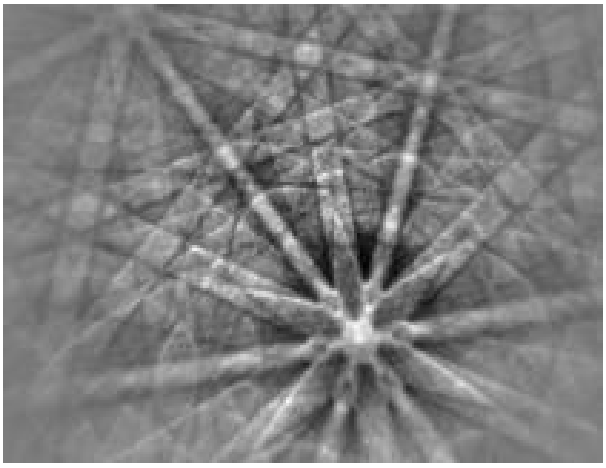

Figure 1.8: *High–quality EBSP image from silicon [2].*

samples with grains varying in size from the nm to mm range, and the angular resolution can be as good as $\sim 0.5^\circ$ [47, 53]. For an overview of the EBSP technique the author refers to the following references [46, 47, 54, 55, 56].

1.3.4 X–ray diffraction

3 dimensional X–ray diffraction (3DXRD) has been used for *in situ* studies of nucleation. 3DXRD is a technique developed in recent years by the synchrotron group within the *Center for Fundamental Research: Metal Structures in Four Dimensions*[4] (Metals–4D center) [21, 57].

It is based on diffraction of high energy (40–100 keV) X–rays. Within this energy range, kinematical scattering theory (i.e., X–rays are only scattered *once* within the sample) generally applies. Furthermore a 10% transmission through metal samples is possible in *mm*–sized samples (see figure 1.9), which is generally the minimum acceptable transmission in order to perform scattering experiments on bulk samples [58].

[4] http://www.metals4d.dk

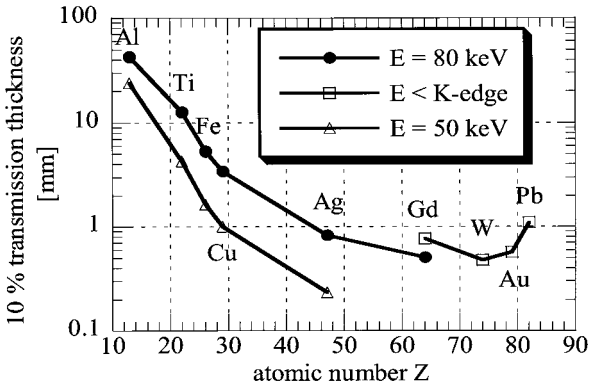

Figure 1.9: *10% transmission of X–rays through matter at 50 keV and 80 keV for selected elements. The penetration data for elements symbolized by □ refer to the use of an X–ray energy just below the absorption K–edge of the element [58].*

Since X–ray diffraction is a non–destructive technique, 3DXRD allows us to non–destructively probe the bulk of metal samples, and thus follow bulk kinetics *in situ*. For an overview of X–ray diffraction and absorption the author refers to the following references [12, 21, 38, 49, 59, 60].

A considerable number of different studies have so far been performed using the 3DXRD microscope including strain analysis, grain boundary mapping, 3D grain maps, deformation studies, grain growth during recrystallization, subgrain growth, recovery, phase transformations, and spatial and crystallographic characterization of single grains [4, 50, 61, 62, 63, 64, 65, 66, 67, 68, 69].

3DXRD microscopy is perfectly suited for *in situ* studies of nucleation, which is a "needle–in–the–haystack" problem, as the fractional volume detection limit can be as low as 10^{-9}, which would allow the detection of a 1 μm^3 nucleus within the bulk of a 1 mm^3 volume.

Chapter 2

Techniques employing microscopies of various kinds

Optical microscopy (OM) and electron microscopy (EM) of polished surfaces have been instrumental in studying metal microstructures since the beginning of modern metallurgy. Both have been used extensively during this PhD project.

This chapter is divided into three parts: an introduction to optical microscopy; an introduction to the electron backscatter patterns (EBSP) technique; and lastly, an introduction to serial sectioning, as well as results obtained.

2.1 Optical microscopy

Optical microscopy (OM) amounts to studying samples in a microscope under visible light. Preparing surfaces for optical microscopy is a much simpler process than for electron microscopy (see section 2.2), and much larger areas may be observed. However, the best achievable theoretical spatial resolution is limited by the wavelength of visible light ($\sim$0.5 μm), and the crystal orientation of the observed grains is not determined directly.

OM has been used for many studies were it was not important to know the crystal orientations within the sample. It is typically also an important step in sample preparation, as the sample surface is inspected by optical microscopy after each polishing step.

The optical microscope used was a Leitz Aristomet reflection microscope. It had a choice of six objective lenses, which together with the ocular gave a magnification range of ×10 to ×1583, which allows the distance between lines (on a scale inserted into the microscope) to be as small as 1 μm. Halogen or zenon light (top or bottom incidence) was available, as well as a polarizing filter, phase contrast, and darkfield imaging. A Leica DC300 V2.0 CCD–camera controlled by Leica IM500 framegrabber software, is installed on the microscope.

2.2 Electron microscopy

The electron microscopy (EM), which has been performed during this PhD project has almost exclusively been scanning electron microscopy (SEM), where the technique of choice has been the electron backscatter pattern (EBSP) technique, which will be described below. A short overview of EBSP will be given here, but for further reading the following references are recommended [53, 70, 71]. The set–up of a typical EBSP system can be seen in figure 2.1.

In the SEM, the electron beam is brought to impinge on the specimen surface at a sharp angle ∼20°. The primary electrons from the electron beam penetrate into the sample and are subject to diffuse inelastic scattering in all directions, and in a crystalline sample a fraction of these electrons will have an angle of incidence to the atomic planes, which satisfies Bragg's law:

$$n\lambda = 2\, d_{hkl} \sin\theta \tag{2.1}$$

where n (positive integer) is the order of the reflection, λ is the electron wavelength, d_{hkl} is the distance between crystal lattice planes with Miller indices {hkl}, and θ is the diffraction angle. The energy loss of the electrons due to the inelastic scattering is negligible (of the order of 100 eV), so we may to a first approximation assume that the energy of the electrons is unchanged, and thus the wavelength of the electrons is given by the de Broglie wavelength [17, 38]:

$$\lambda = \frac{h}{mv} \approx \frac{12.3}{\sqrt{V + 10^{-6}V^2}} \tag{2.2}$$

where λ is the wavelength (in Å), h is Planck's constant, m is the electron mass, v is the electron speed, and V is the accelerating voltage (in V). Thus,

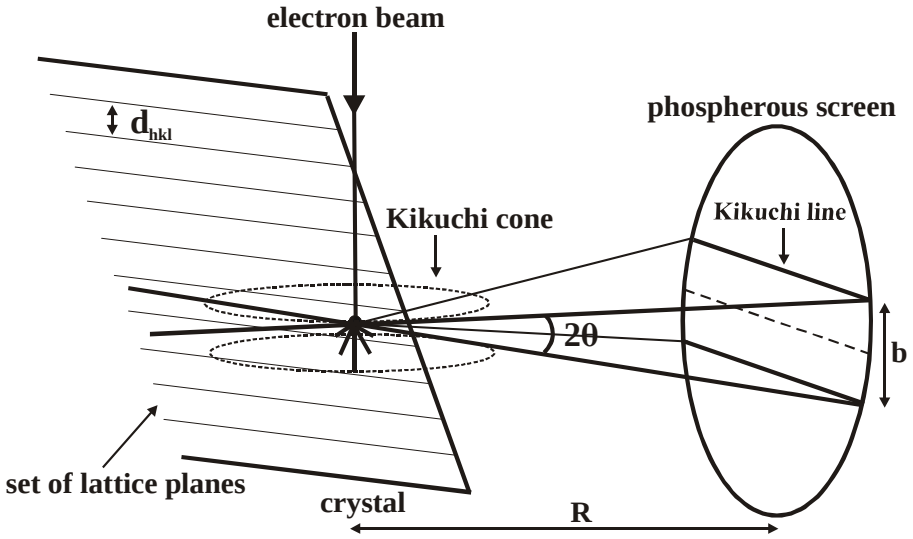

Figure 2.1: *Illustration of the geometry of a typical EBSP system.* 2θ *is the opening angle of a Kikuchi band,* d_{hkl} *is the distance between the crystal lattice planes,* R *is the sample to screen distance,* b *is the distance between two Kikuchi lines from the same band, and the dashed line is the intersection of the crystal lattice plane with the screen [70].*

for an accelerating voltage of 20 kV, the electrons will have a wavelength of 0.085 Å, and from eq. 2.1 we see that diffraction angles are of the order of 1°.

Since the electrons initially exhibit all directions, the diffraction from a set of parallel planes will have a fixed angle θ to the planes and therefore be in the form of the two Kikuchi cones emitted from the diffracting volume (see fig. 2.1). Because of the low Bragg angles ($\sim$1°), the two cones will appear as a pair of Kikuchi lines (also called a band) on the screen instead of as hyperbolas.

Each pair of lines are the result of electrons being diffracted from one particular set of atomic planes in the crystal, and the intersection of the plane with the screen is a line, which is located very close to the center between the two Kikuchi lines. The distance b between two Kikuchi lines on the screen is roughly proportional to the diffraction angle θ and the sample–to–screen distance R ($b = 2R\sin\theta \approx 2R\theta$), which readily allows the {hkl}–family of the diffracting plane to be determined from equation 2.1. Also, the intensity of a particular band relative to the intensities of the other bands can be predicted

from the structure factor of the material ($I \propto |F_{hkl}|^2$), which is used along with the diffraction angle when assigning Miller indices (hkl) to the observed Kikuchi bands in the EBSP.

Experimentally, a video camera or a CCD–detector is coupled to the phosphorous screen, generating a digitized EBSP image. The EBSP are extracted from the images by an image analysis technique known as the Hough transform [72]. If several sets of bands are obtained and indexed (i.e., their (hkl)–values are determined) from the same spot, it is possible to determine the crystal orientation of the volume struck by the electron beam. In order to reliably determine the crystal orientation of a volume by the use of successfully indexed Kikuchi bands, experience dictates that at least 5 out of 8 eight detected bands are successfully indexed with the same orientation [72].

The electrons forming the EBSP originate from a small volume below the surface, where its depth below the surface is of the order of 20 nm for an accelerating voltage of 20 kV, so the information obtained is basically from the surface region. This thin layer must be clean and with a relatively low dislocation density, which requires the surface to be mechanically polished, and often electrochemically polished as well, to remove any surface deformation. By scanning over the surface of the sample it is possible to produce 2 dimensional crystallographic orientation image maps [73], which clearly show the surface microstructure of the sample (see fig. 3.1). This technique is a "workhorse" in modern metallurgy, where the EBSP data is often complimented by energy dispersive spectroscopy, where characteristic X–ray peaks are generated by the interaction of the electron beam with the sample and the relative intensities of the peaks gives the concentrations of each element in the material being studied. These systems, coupled to computer materials data bases, can be used to yield phase maps of inspected samples [47].

2.3 Serial sectioning

Serial section is a method by which 3 dimensional microstructures may be reconstructed from data obtained by surface techniques, such as OM and EBSP. This is important, because the structures (eg. grains) are really 3 dimensional objects, which are generally studied by microscopy on 2 dimensional surfaces. In serial sectioning, stacks of closely–spaced parallel surfaces (sections) are inspected by microscopy, and by using purpose–written software, it is possible to layer the sections on top of one another and thus reconstruct the 3D microstructure [74, 75, 76].

The biggest challenge in performing serial sectioning is in producing polished sections, which are parallel enough and where the distance between sections is small and constant enough. Typically, the required flatness and depth control is 1–2 μm [77, 78]. It was the task of the author to device a system, which could satisfy these criteria, as well as polish a sample down to any target depth with the same precision. The polishing system of choice was the 'Logitech PM5D polishing and lapping system', who's construction guaranteed the sample flatness, and which included the 'PSM1 position sample monitor' that determines the amount of material removed during lapping [79]. The user manual, written by the author, is inclosed in this thesis as reference [A3].

It has been proven possible to polish samples down to a pre–specified target depth with an accuracy of 1–2 μm and the same degree of flatness, and it has also been proven possible to consistently serial section samples in 2 μm steps. After electrochemical polishing the resulting surfaces have then been suitable for EBSP studies. However, flawless mirror–like surfaces have been somewhat harder to obtain through mechanical polishing alone, due to the fact that the Logitech PM5D is placed in a normal laboratory, and contamination of the polishing surface by hard particles can therefore be a problem.

Sectioning of copper samples at an early stage of recrystallization has shown that volumes around triple junctions are the dominant nucleation sights in non–particle containing metals, which is also supported by the literature [3, 11, 30]. Sectioning of aluminium samples has shown that nucleation kinetics might vary slightly near the surface from that in the bulk [A5].

Serial sectioning and EBSP 2D mapping with a group of students from Roskilde University has created 3D grain maps [80]. This work was a successful preliminary study, which has lead to a direct mapping of the same microstructure by both EBSP and 3DXRD [81].

Also, the author has collaborated with a European group studying precipitates in supercooled liquids containing 58% Cu and 42% Co [82]. The author's task was to instruct and supervise S. Curiotto, a PhD student from the University of Turin, Italy, who performed serial sectioning on Cu–Co samples. Optical microscopy was used to observe the structures, which consisted of Co spheres and dendrites.

Chapter 3

Recrystallizing microstructures studied by stereology

Stereology is an efficient tool for *statistical* studies of recrystallization kinetics, based on traditional techniques employing microscopy on polished surfaces. "Stereology is a mathematical science, which deals with inferring (n+1) dimensional information from observation at the n'th level" [83], or in other words, it establishes 3-dimensional properties of a material from 0, 1, or 2–dimensional measurements performed on polished planar surfaces (eg. volume fractions, grain size, grain shape etc.) [84].

Recrystallization kinetics can be studied by studying the polished surfaces of samples, cut from the bulk of a series of specimens and heat treated to various fractions of recrystallization. From these surfaces, critical microstructural properties can be determined stereologically:

V_V — the volume fraction recrystallized;

S_V — the interfacial area (grain boundary) density separating recrystallizing grains from deformed volumes;

$<\lambda>$ — the mean recrystallized grain intercept length.

These properties are of special interest, because the average growth rate of the recrystallizing grains may be determined by using for example the Cahn–Hagel method (see section 3.1) [85]. Also, it may be possible to determine the nucleation rate as a function of time using microstructural growth path modelling [86, 87].

The properties are often determined by the linear intercept method (see section 3.1), and if EBSP (see section 2.2) is used, the properties of the individual texture components may be determined. Generally, EBSP studies have been performed by experts using subjective means to distinguish between different recrystallized grains, and the deformed material [34]. Also, previously an automatic technique based on EBSP, utilizing line scans consisting of *one* scanned line was found to yield a precise determination of V_V, but S_V was typically an order of magnitude off [88]. A new automatic technique based on EBSP has been envisaged, and developed by the author [A1]. It is based on quasi–line scans consisting of 3 *parallel* lines of equal length, and with a mutual distance equal to the line scan step size. This method has the advantages of only scanning lines (short measuring times, and good statistics), while being automatic (i.e., objective) and making use of the principle of connectivity to avoid errors [89]. An other advantage of scanning random lines is that this takes microstructural anisotropies into account.

Another line scan method for quantifying recrystallization using EBSP has recently been published [90]. It is based on measuring the fractional changes of the HAGB–fraction of boundaries along a line through the microstructure. It can be used to determine V_V, but no information is provided about S_V and $<\lambda>$.

The chapter is divided up into three parts and is largely based on reference A1. The first part deals with how critical parameters, which describe the recrystallizing microstructure, may be determined by line scans through the microstructure. The second part describes the automatic line scan method, which was developed by the author. It consists of an alternative way of performing line scans, and a data analysis program called LSGRAINS, which interprets the experimental data. The third part deals with the validation of the 3–line technique, and various results obtained using it.

3.1 Studies of recrystallizing microstructures

An efficient way of studying the microstructural properties described in the previous section by stereology, is by scanning the microstructure along random lines through the microstructure, using the linear intercept method. Random lines are drawn through the microstructure, and the intersections between different recrystallized grains, and between grains and the deformed microstructure are noted. An example of this can be seen on figure 3.1, which is an EBSP orientation image map (OIM) [73].

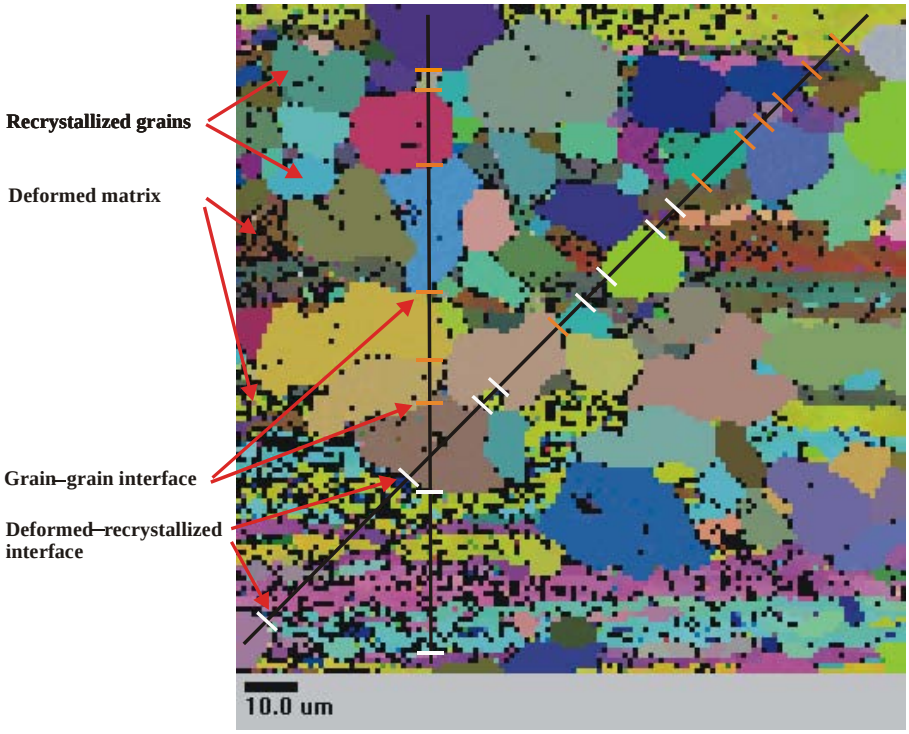

Figure 3.1: *EBSP OIM showing a partially recrystallized microstructure with two random lines drawn through it. Examples of recrystallized and deformed grains are identified by the red arrows, and where the drawn lines cross an interface this is marked:* ***orange*** *for a recrystallized–recrystallized interface, and* ***white*** *for a deformed–recrystallized interface. The colour of the individual grains corresponds to their crystal orientation [A1].*

With the linear intercept method it is easy to determine the three parameters V_V, S_V, and $<\lambda>$, described in the previous section, which are important when studying recrystallizing microstructures [34]:

$$V_V = \frac{L_{rex}}{L} \tag{3.1}$$

$$S_V = \frac{2 \times n_{int}}{L} \tag{3.2}$$

$$<\lambda> \equiv \frac{1}{N} \sum_{i=1}^{N} \lambda_i \tag{3.3}$$

where L is the total length of the scanned line, L_{rex} is the total length of

the line in recrystallized material, n_{int} is the number of interfaces between recrystallized and deformed material crossed by the line, N is the number of grains intersected by the line, and λ_i is the intersect length of the i'th recrystallized grain.

If these parameters are determined for a series of samples, annealed for different periods of time at the same temperature, it is possible to study the recrystallization kinetics at that temperature. Following the work of Cahn & Hagel, the overall deformed–to–recrystallized material transformation rate may be written as [85]:

$$\frac{\mathrm{d}V_V}{\mathrm{d}t} = <G> \cdot S_V \tag{3.4}$$

where $<G>$ is the average growth rate of the recrystallizing grains ($G = dR/dt$), and R is their radius. If the recrystallized grains are distinguished based on which crystallographic texture component they belong to (see appendix B), as is possible by EBSP, the average growth rate for the texture components is also determined [34].

The main difficulty related to using the linear intercept method is insufficient statistics, since ideally hundreds of *different* grains scattered over a large area must be probed in order for the approach to be statistically viable. The demand for different grains is often a problem, since the typical approach is to perform a 2 dimensional scan, and then trace random lines across it while noting down changes in the microstructure. However, the number of sampled grains remains relatively low. This difficulty is aggravated when individual texture components are studied, because doing so only uses a fraction of all the intercepted grains.

Line scans can be performed by optical microscopy on polished surfaces, which may be photographed, and the linear intercept method may be applied with a ruler and a pencil. However, the crystal orientations of the intercepted grains are not determined directly. An alternative way, is by using the EBSP system in a SEM (see section 2.2). The EBSP are monitored on the computer screen while the sample is translated beneath the electron beam. This form of data acquisition is slow, subjective, and tiresome in the extreme, but the crystal orientation is also determined. A fast, automatic, and objective method, which consisted of a data acquisition procedure, and a corresponding analysis program, was developed by the author (see section 3.2).

3.2 LSGRAINS

The automatic method, which will be denoted as the LSGRAINS method, for obtaining quantitative recrystallization parameters, is a line scan method based on the EBSP technique, scanning not one but three parallel lines, with a mutual separation equal to the line scan step size. Examples of the form of 3–line scans can be seen in figure 3.2a–c.

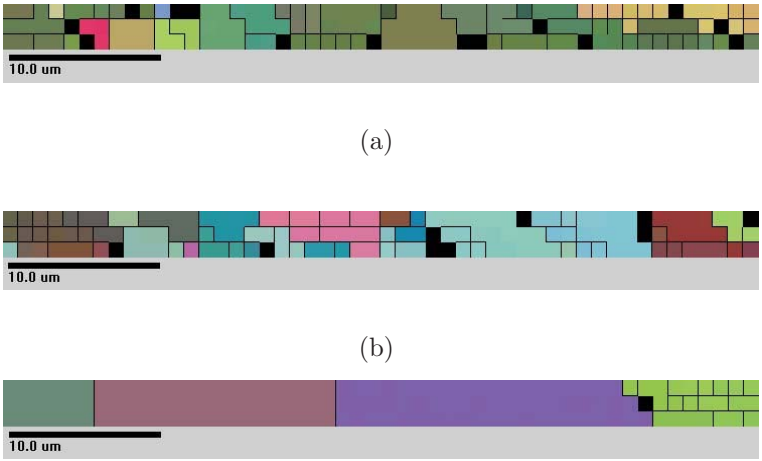

(a)

(b)

(c)

Figure 3.2: *Orientation image map of 3–line scans (3×50 steps, 1 μm step size) of AA1050–aluminium sample at various annealing times. The black lines indicate misorientations θ with θ≥1.0° between neighboring data points, and black spots are "bad" data points. The colour of the individual grains corresponds to their crystal orientation. The samples were annealed in an oil bath at 250° C for respectively:* ***(a)*** *300;* ***(b)*** *2,000; and* ***(c)*** *28,000 s [A1].*

The method has the advantage of scanning lines (i.e., short measuring time, or alternatively good statistics), while making use of the principle of *connectivity*, where adjacent data points of the same crystal orientation are grouped together into grains, to avoid errors [89]. Two adjacent data points are considered connected if their orientations are equivalent, i.e., their misorientation θ is lower than some cut–off angle, which is usually set to the resolution of the EBSP system (normally $\theta \leq 1°$). The 3–line data is interpreted by the computer program LSGRAINS, which was developed specifically for 3–line EBSP scans. The LSGRAINS algorithm is described in detail in article A1, but in this section an overview of the most important concepts will be given.

The LSGRAINS algorithm interprets EBSP data in the form of 3–line scans, and the central line is the main source of data, while the upper and lower lines are auxiliary lines, which assist the computer algorithm in calculating which parts of the microstructure are recrystallized and which are deformed, based on data point connectivity. The data points on the *central* line are compared to all their surrounding data points (see the arrows on figure 3.3), and comparisons between data points are used to group data into recrystallized grains and deformed material. When the data points have finally been grouped into individual recrystallized grains and deformed regions, the recrystallization parameters are calculated using eq. 3.1–3.3, giving a reliable and time–efficient measuring technique.

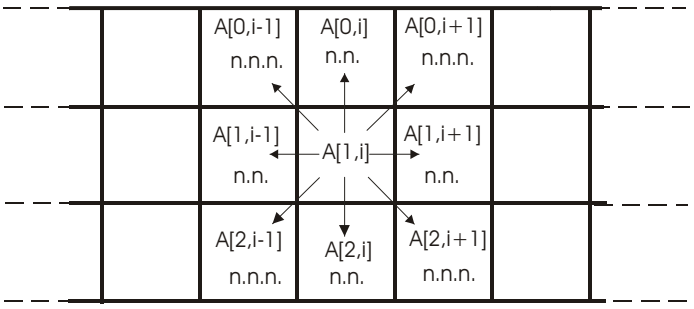

Figure 3.3: *Connectivity around the i'th data point on the central line. The arrows indicate which neighboring data points are compared with the i'th data point. If the i'th and (i-1)'st data points are both recrystallized and of the same orientation, then they are connected, and both data points thus belong to the same grain. nn and nnn are respectively the nearest and next nearest neighboring data points adjacent to the i'th data point [A1].*

More specifically, the algorithm runs through a series of iterations (see fig. 3.4), which test for/implement the various criteria that recrystallized grains *must* fulfill, as set down by the operator of the program. The algorithm has been made to run with all the routines, but some may be omitted at the discretion of the operator (see sec. 3.3.1a). From figure 3.4 it is seen that the data is run through some of the iterations more than once, which constitutes a refining process of the microstructure derived from the experimental data.

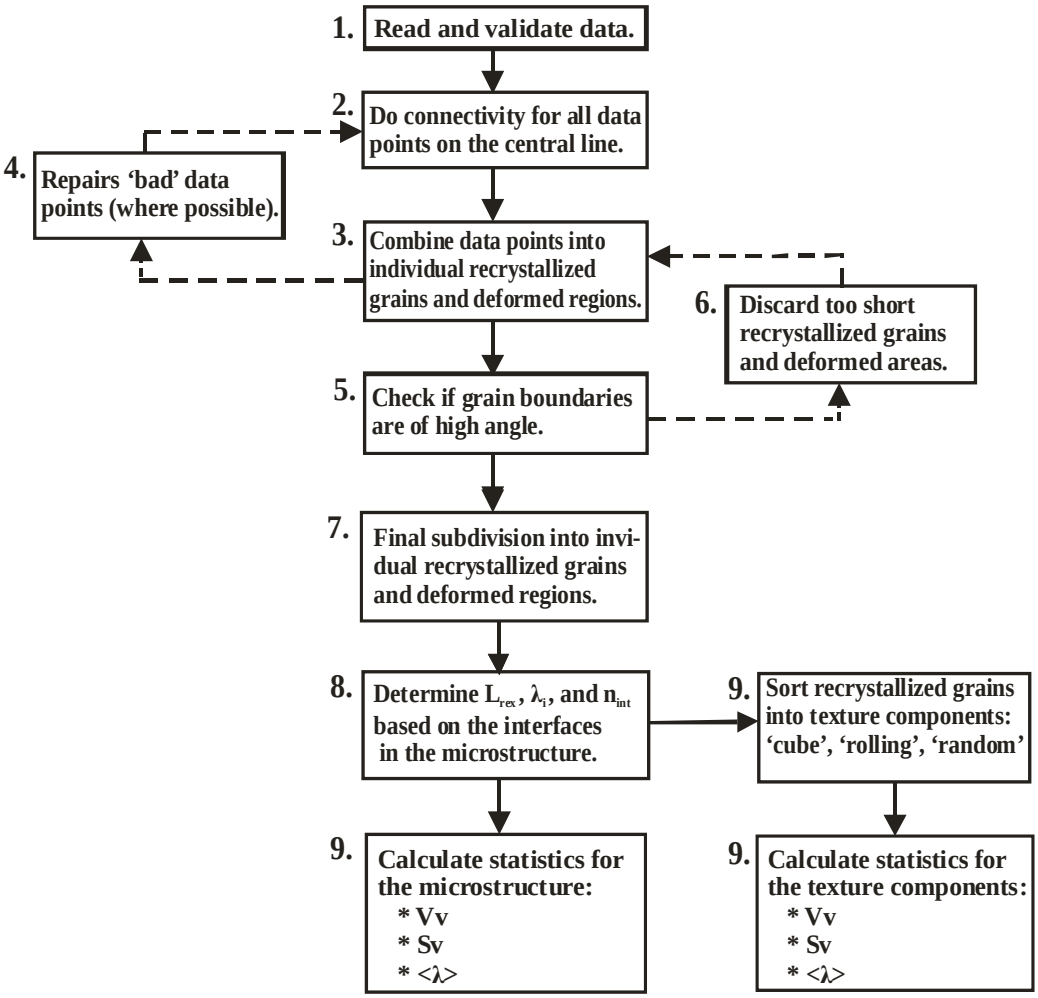

Figure 3.4: *Flow diagram of the LSGRAINS algorithm. The iterations are numbered for easy reference.*

1. Initially, the EBSP data is read from a long string file and ordered into an array with dimensions $(3 \times n_{points})$, and every data point is checked to see if it satisfies the minimum acceptable successfully indexed EBSP Kikuchi bands (normally 5). Those that do are considered indexed and are termed "good", while those that do not are considered non–indexed and are termed "bad". The first and the last data point on the lines are not used!

2. All "good" data points (see above) are checked for equivalence with all their neighboring data points (see arrows in fig. 3.3). Data points, which have the acceptable minimum number of neighbors (normally 4), are considered as belonging to a recrystallized grains ("rex"), and those that do not are considered as belonging to the deformed matrix ("def"). Every data point is then given an ID–number to define its status: "rex" (positive integer), "def" (-1), or "bad" (0). Note that when iteration 2 is run again after the repair routine (iteration 4, see below), only "good" data points exist (i.e., "rex" or "def").

3. "rex" data points (positive ID–number) are combined into recrystallized grains if they are adjacent to each other *and* their orientations are equivalent (i.e., the misorientation is smaller than $\sim 1°$), while data points with ID–number equal to -1 and 0 are grouped into deformed regions between the recrystallized grains. This gives a first rudimentary picture of the microstructure.

4. This iteration attempts to repair every "bad" data point (ID–number=0) on the central line, by allocating a new good orientation to the data point, with preference to the orientation of a neighboring grain. This is done by using the rudimentary picture of the microstructure from iteration 3. If a dominant orientation exists around a "bad" data point (see arrows in fig. 3.3), the "bad" data point assumes this orientation and becomes a "good" data point (ID–number=positive integer). In order to be able to define a dominant orientation surrounding the "bad" data point, a minimum number of neighboring data points with the same orientation (normally 2) must exist. If this is not the case, the "bad" data point becomes a "def" data point (ID–number=-1).

5. This iteration checks the boundaries of each grain to ascertain if *at least* one them is of high angle (normally, $\theta \geq 15°$ for grain–deformed or $\theta \geq 2°$ for grain–grain boundaries). A grain that does not satisfy this criteria is rejected as a large sub–grain, and the data points of the grain are relabelled to ID–number=-1.

6. To limit fictitious interfaces arising from small grains and deformed regions, which are considered too small (normally smaller than 3 times the scan step size), are relabelled. Based on mutual misorientations (normally, if θ <2°) small grains are joined into larger grains or relabelled as deformed, and small deformed regions are added to the adjacent grains. This iteration is necessary to avoid adding fictitious grain–grain and grain–deformed interfaces to the microstructure, which is a critical parameter for calculating S_V and $<\lambda>$.

7. The final subdivision into recrystallized grains and deformed regions is determined in the same fashion as in iteration 3. From this the location and nature of all the boundaries of the grains are determined, as well as which of the texture components 'cube', 'rolling', or 'random' the grains belong to (see appendix B).

8. The nature and location of the grain boundaries are used to calculated the number of grain–grain and grain–deformed interfaces, the number of grains, as well as the intercept length of each grain, and the total summed length of the recrystallized grains.

9. Lastly, from equations 3.1–3.3 the recrystallization parameters V_V, S_V, and $<\lambda>$ are calculated for the full microstructure and for each of the texture components, as well as grain contiguity, grains size distribution, and a distribution of the length of deformed material between recrystallized grains.

The following are the user–set parameters in the algorithm. These parameters have default settings, but the parameters need to be set and tested for each series of experiments if a different material is used. This can be done by comparing the algorithm's results with what is obtained from inspecting the OIM of a 3–line scan (see section 3.3.1). Below is a list of the parameters, their capital letter codes, and their default values for aluminium:

***M* — *min indexed bands*:** minimum number of correctly indexed Kikuchi bands from the EBSP required for a data point to be "good" (default: M=5).

***C* — *min data point connectivity*:** minimum number of equivalent data points around and including data point $A[1, i]$ required for a data point to be termed "rex" (default: C=5).

***D* — *max misorientation*:** maximum allowed point–to–point misorientation between data points of the same orientation (default: D=1.0°).

***X & Y* — *min boundary misorientation*:** minimum accepted misorientation across a 'high' angle boundary (default: X=15.0° for grain–deformed, and Y=2.0° for grain–grain boundaries).

***L* — *min grain intercept length*:** minimum accepted intercept length in data points of a recrystallized grain *along* the line (default: L=3 for 1 μm steps).

***I* — *min deformed region intercept length*:** minimum accepted intercept length in data points of a deformed region *along* the line (default: I=3 for 1 μm steps).

***N* — *min equivalent neighbors*:** minimum number of neighboring data points of equivalent orientation needed to repair a 'bad' data point (default: N=2 data points).

***R* — *repair*:** should LSGRAINS try to repair 'bad' data points (default: R=YES).

***B* — *check boundaries*:** should LSGRAINS check the grain boundaries of each grain to see if it has at least one is of high angle (default: B=YES).

In general, the stricter the requirements that are placed on data to be accepted as coming from recrystallized grains, the lower V_V will of course be. Discarding grains may cause S_V to go either up or down, generally depending on the degree of recrystallization in the scanned material. This is because the number recrystallized–deformed interfaces depends on the local microstructure around the discarded grains, so discarding a grain may do anything in between removing or creating two interfaces. $<\lambda>$ generally goes up with stricter requirements because only bigger and more developed grains are likely to satisfy stricter criteria.

3.3 Results and discussion

In this section the 3–line technique, with its corresponding analysis program LSGRAINS, is validated by comparison with three different techniques (see section 3.3.1). Also included is an experimental investigation of recrystallization kinetics at the surface and in the bulk, which was performed using LSGRAINS (see section 3.3.2) [A6].

3.3.1 Validation of the LSGRAINS technique

The automatic LSGRAINS line scan technique was validated by comparing the results obtained using the LSGRAINS method with results obtained by using other and significantly slower manual scanning methods, who's results are considered correct, on the same specimens. One–to–one comparisons, and the resulting graphs were used to determine whether the automatic method gives viable results.

The material used in the validation studies was AA1050–aluminium (99.5% pure), and was chosen because it had previously been used for extensive characterization and modelling [91]. In cases (a) and (c), the material was cold rolled 90%, and then annealed in a 250°C oil bath for 300, 2,000, 11,000, 20,000, 28,000, 38,000, 55,000, 72,000, and 86,400 seconds. In case (b), the aluminium was cold rolled 60%, and then annealed for 1 hour in an air furnace at 550°C, producing a fully recrystallized sample.

After annealing the RD–ND surface (see appendix A) of the samples was mechanically and electrochemically polished to produce a surface suitable for EBSP measurements. For long scans (length=1000+ μm), the flatness of the sample surface is critical, as a non–flat surface may move out of focus in the SEM. The samples were therefore mechanically lapped and polished on a Logitech PM5D lapping and polishing machine, giving a height difference of only 1–2 μm across the sample surface. Finally, the samples were electrochemically polished for 40 seconds at 12 V. The sample was used as anode, aluminium was used as cathode, and an A2–solution was used as electrolyte[1] before they were studied by EBSP [92, 93]. In all cases a JEOL–840 scanning electron microscope with a LaB_6–filament was used to collect the EBSP data. The working distance was 22 mm, the electron beam current was 280 μA, and the voltage was 20 kV.

[1] A2: 12% H_2O, 70% ethanol, 10% ethylene glycol monobutyl ether, and 7.8% HCl.

Three different comparisons were performed to validate LSGRAINS:

(a) To test that the LSGRAINS algorithm performed as required, short (200 steps) scans were performed on samples annealed for 300, 2,000, and 28,000 seconds. Their OIMs were plotted on paper, and misorientations with $\theta \geq 1^\circ$ were marked by black lines (see figure 3.2). Other plots were made with lines drawn for misorientations greater than 2° and 15° so as to allow high angle boundaries to be identified. The identification of recrystallized grains could then be performed both by the algorithm, and by visually performing the same calculations, as the algorithm would do, on the OIM. Diagonal data point connectivity is very difficult to visually discern on OIMs, so it was chosen to omit repair of bad data points, and not to ignore short deformed regions. This ensured that exactly the same criteria were used to define a recrystallized grain with the two procedures. The results of the comparison show excellent agreement (see table 3.1). The very slight scatter in V_V and $<\lambda>$ comes from the slight uncertainty when measuring longer grain lengths on the paper printouts. Also, only grains intersected by all *three* lines were indexed by the algorithm as recrystallized grains. This indicates that the chance of accidentally indexing cells within the deformed matrix as recrystallized grains is very low.

Time (s)	$V_{V\ vis}$	$V_{V\ auto}$	$S_{V\ vis}$	$S_{V\ auto}$	$<\lambda>_{vis}$	$<\lambda>_{auto}$
300	0.05	0.04	0.05	0.05	3.5	4.0
2,000	0.04	0.04	0.04	0.04	3.5	4.0
28,000	0.66	0.67	0.11	0.11	14.6	14.8

Table 3.1: *Short line scans* — 3×200 *data point line scans with a step size of 1 μm were performed on the 300; 2,000; and 28,000 s samples. The chosen parameters were: M=5, D=1.0°, C=5, L=3, I=1, R=NO, B=YES, Y=2°, X=15° [A1].*

(b) Two 3–line scans were extracted from a large 2 dimensional EBSP map, which was performed on a fully recrystallized microstructure, where it was possible to identify the recrystallized grains by direct visual inspection of the OIM. This allowed a more direct comparison than in (a), and importantly allowed a test of how well the method handled samples with V_V=1.0 and S_V=0.0 (fully recrystallized). The results generated by the algorithm were compared directly with the results of the visual inspection (see table 3.2), and the results again show excellent agreement.

(c) For the chosen material (see below), a previous stereological study had supplied values for V_V, S_V, and $<\lambda>$ for a large range of annealing times

Scan	$V_{V\ OIM}$	$V_{V\ auto}$	$S_{V\ OIM}$	$S_{V\ auto}$	$<\lambda>_{OIM}$	$<\lambda>_{auto}$
middle	0.98	0.99	0.01	0.01	48.2	45.8
top	1.00	1.00	0.00	0.00	59.6	59.6

Table 3.2: *Extracted line scans — 3×169 data point line scans with a step size of 5 μm were performed on the 300; 2,000; and 28,000 s samples. The chosen parameters were: M=5, D=1.0°, C=5, L=1, I=2, R=YES, B=YES, Y=2°, X=15° [A1].*

using the manual line scan method [91]. The corresponding parameter values obtained with the LSGRAINS technique therefore needed to be statistically viable to allow a comparison between the two methods. For practical reasons, the criteria for a statistically viable data set was set to 100+ detected recrystallized grains. When single scans did not yield a 100+ grains, additional scans were performed, and the weighted average of the scans was used (based on the scan length for V_V and S_V, and the number of grains for $<\lambda>$). The results of the automatic method on the same specimen were compared to the results of the manual scans (see table 3.3 and fig. 3.5).

Time (s)	$V_{V\ man}$	$V_{V\ auto}$	$S_{V\ man}$	$S_{V\ auto}$	$<\lambda>_{man}$	$<\lambda>_{auto}$
300	0.02	0.03	0.02	0.02	2.6	3.7
2,000	0.07	0.05	0.05	0.03	3.5	4.3
11,000	0.22	0.22	0.09	0.08	5.8	7.1
20,000	0.60	0.89	0.06	0.05	14.2	12.8
28,000	0.21	0.43	0.05	0.09	6.9	8.5
38,000	0.37	0.43	0.05	0.08	13.5	14.5
55,000	0.78	0.93	0.03	0.03	23.8	16.7
72,000	0.96	0.64	0.02	0.10	18.1	13.1
86,400	0.87	0.89	0.05	0.05	16.7	15.2

Table 3.3: *Long line scans — 3×1000+ data point line scans with a step size of 1 μm were performed on all the samples. The table shows the automatic vs. the manual results. The automatic results were based on the following choice of parameters: M=5, D=1.0°, C=5, L=3, I=3, R=YES, B=YES, Y=2°, X=15° [A1].*

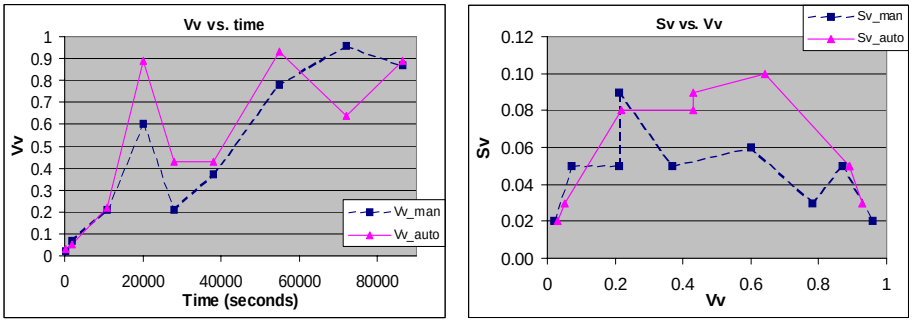

(a) (b)

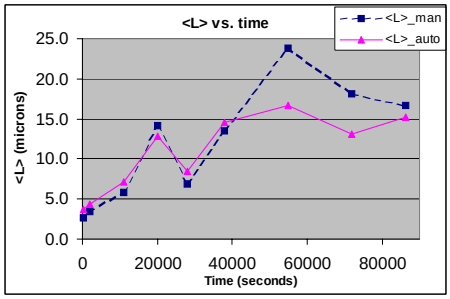

(c)

Figure 3.5: *The results from comparing long manual and automatic scans.* ***(a)*** *V_V vs. time;* ***(b)*** *S_V vs. V_V;* ***(c)*** *$<\lambda>$ vs. time. Parameters were: M=5, D=1.0°, C=5, L=3, I=3, R=YES, B=YES, Y=2°, X=15° [A1].*

3.3.2 Depth–dependent nucleation kinetics

The 3–line scanning technique has been used in studies of possible differences between nucleation close to the surface and in the bulk of 90% cold rolled Al–2S aluminium [A6].

The V_V and $<\lambda>$ curves were identical in both samples. However, in the bulk microstructure samples, the maximum of the S_V vs. V_V curve was located at V_V=0.47, and in the surface microstructure samples, it was found that the maximum of the S_V vs. V_V curve was located at about V_V=0.5 (see fig. 3.6). The difference between a maximum in S_V at a V_V–value of 0.47

and 0.5 may not be significant, or it might perhaps suggest that there is a slight difference in the nucleation kinetics at the surface and in the bulk, as a maximum S_V at lower V_V generally implies *clustered* nucleation, whereas a V_V value near 0.5 is typical for a *random* distribution of the nuclei. This could indicate that the nuclei in the bulk are clustered, while the nuclei at the surface are more randomly distributed.

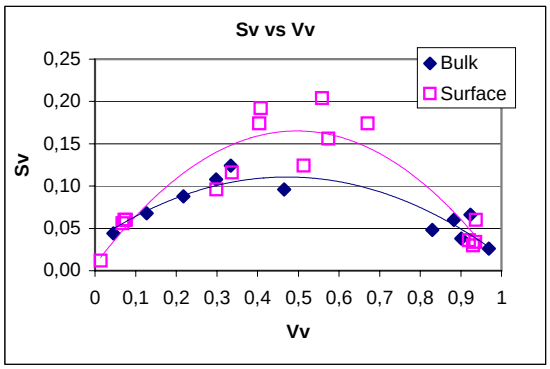

Figure 3.6: *S_V vs. V_V curve from article A5. The large scatter in the data, due to limited sampling statistics, is quite normal in metallurgy. The solid lines indicates fits to the data. The maximum of S_V is located at respectively 0.47 and 0.5 in the bulk and surface microstructure samples [A6].*

Chapter 4

Nucleation of recrystallization studied by X–ray diffraction

This chapter on 3 dimensional X–ray diffraction (3DXRD) studies is divided into four main sections. The first deals with the general properties of the 3DXRD microscope. The second deals with the nucleation experiment, which was carried out by the author, and where the primary weight of this PhD project lies. The third deals with the results obtained from the nucleation experiment, and the fourth contains a discussion of the results obtained.

In this thesis no distinction will be made between the terms diffraction spot and reflection. Also, the term pole will often be used in short for a diffraction spot/reflection arising from one of the deformed parent grains. When dealing with Miller indices, the following notation is traditionally applied and will be used here [68]: (hkl) is a specific direction; {hkl} is a set of equivalent lattice planes; and <hkl> is a set of equivalent directions.

3DXRD is based on the rotational diffraction method, where the sample is irradiated by a monochromatic X–ray beam, which is diffracted as it passes through the sample [21, 38]. The sample is rotated around an axis perpendicular to the X–ray beam (the vertical axis), and at each angular position, the sample is oscillated around the rotation axes while a diffraction image is collected on a 2 dimensional detector oriented perpendicular to the beam (see fig. 4.1). Using the in–house software GRAINDEX [94], the individual crystal orientations of up to thousands of crystal grains may be determined at the same time (see section 4.2.3.5). Due to the high X–ray

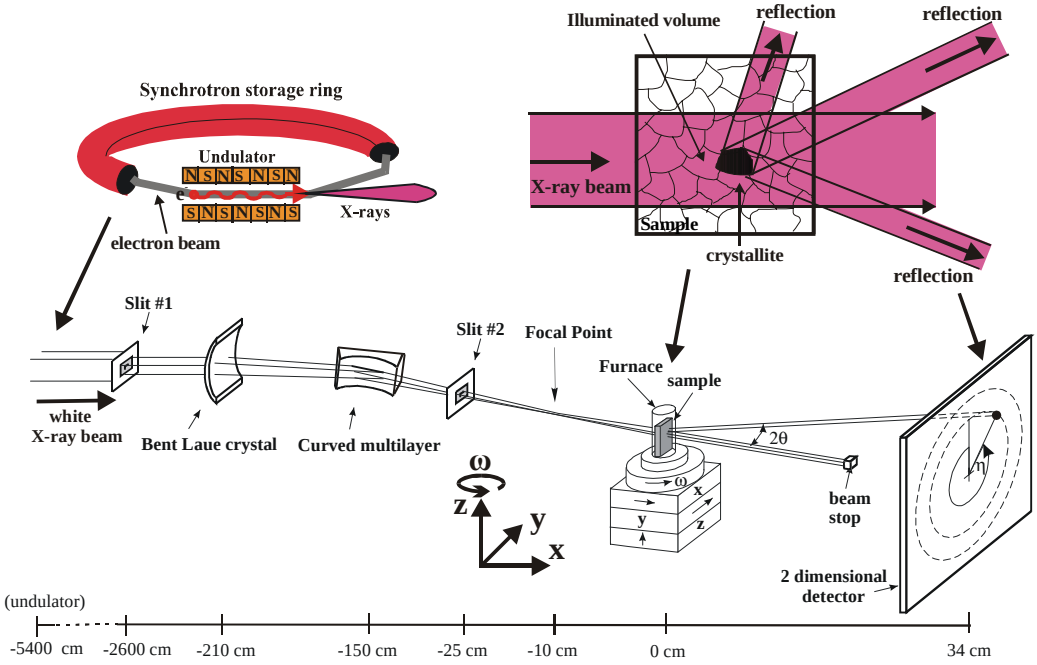

Figure 4.1: *The 3DXRD microscope. The white beam was monochromated and focused vertically by a bent Laue-crystal, and then focused horizontally by a curved graded multilayer. In the experiment, the beam focus was in front of the sample and the beam profile was defined by slit # 2.*

energies, kinematical scattering theory[1] may be used, even in mm–sized bulk samples, and because the scattering angles are small, it is possible to obtain sufficient structural information for most experiments with a fixed position of a flat detector.

The experimental data from 3DXRD is very similar to that obtained from X–ray powder diffraction (see figure 4.2a–c). Each crystal grain gives rise to a set of reflections, and since a polycrystal is essentially a coarse powder fused together, the reflections from the differently–oriented grains produce a basic powder diffractogram (see fig. 4.2a), but which is made up of discrete discernable diffraction spots (see fig. 4.2c). If the sample is deformed, the mosaic spread of the grains increases and the diffraction spots spread out

[1]In *kinematical* scattering theory, individual X–rays are assumed to be scattered only once within the sample [12].

(a) (b) (c)

Figure 4.2: *Example of experimental 3DXRD data. Diffraction images showing the six first* fcc *Debye–Scherrer rings:* ***(a)*** *drawn Debye–Scherrer rings;* ***(b)*** *reflections from a heavily deformed sample lying on the powder rings; and* ***(c)*** *individual reflections from strain free grains lying on the powder rings.*

over the rings, but without filling them completely (see fig. 4.2b). In the case of a material with a face centered cubic (*fcc*) structure this is much simplified, and only the first five powder rings, which are allowed in the *fcc*–structure, are normally necessary to determine the crystal orientation of a grain: {111}, {200}, {220}, {311}, and {222}.

As already mentioned in chapter 1, the big challenge in studying nucleation of recrystallization is the fact that it is not possible to predict *exactly* where a new grain will nucleate, which means that large volumes must be characterized with a spatial resolution of at least 1 μm in order to properly characterize all possible nucleation sites before annealing. This same volume must then be characterized post–annealing, so that the before and after microstructure at a nucleation site can be compared. Ideally, the "birth" and subsequent growth of a nucleus should be followed *in situ*, so that the nucleation mechanism can be identified. Lastly, the microstructures and nuclei studied should be away from the sample surfaces, so as to avoid possible surface effects.

The criteria placed on a suitable experimental technique for studying bulk nucleation *in situ*, exclude all techniques based on microscopies of various kinds, as they either study the surface or thin sections. 3DXRD, which has a penetration power of the order of *mm* in most metals (see fig. 1.9), and the ability to detect volumes sized $\sim$1 μm^3 within volumes sized up to 1 mm^3,

on the other hand satisfies all these criteria, and it would seem that this technique is the natural technique for studying *in situ* bulk nucleation.

The primary motivation for performing the experiment was to perform a feasibility study to determine whether it was possible to study bulk nucleation *in situ* in suitable detail using 3DXRD, and what information could actually be gleaned from such an experiment. It was for example known that we would only be able to detect nuclei, which appeared with orientations on the tails of the orientation spread of a deformed grain or with a completely new orientation. Whether such nuclei would actually appear was not known prior to the experiment, even though copper's tendency to produce annealing twins, with new and detectable orientations, made this more likely (see section 1.2.5).

4.1 The 3DXRD microscope

The 3DXRD microscope is an unique instrument, located in the second experimental station at beamline ID11 at the European Synchrotron Radiation Facility (ESRF), which is a 6 GeV third generation X–ray source located in Grenoble, France [95]. The experimental hutch is 10 m long and is centered at 56 m from the undulator source. The lead shielding provides sufficient radiation protection to allow 1 mm^2 of the white beam to be accepted into the hutch [58]. With *white* beam we mean the quasi–monochromatic X–ray beam, which is emitted by the undulator (see fig. 4.4). The experiments are remotely controlled from the outside using 'SPEC' control software, and 'Image Pro' image processing software is used to capture the diffraction images. The specific parameters of the undulator, the monochromating–focusing optical elements, and the 2D detector can be found in appendix C.

4.1.1 Governing equations and scattering geometry

In the tilted coordinate system, within which the 3DXRD microscope operates (see Appendix A.2), the governing equation is Bragg's law (see eq. 4.1), which relates the diffraction angle to the spacing between the diffracting lattice planes, and the wavelength of the X–rays for elastic coherent scattering from a periodic lattice [12, 59]:

$$n\lambda = 2\, d_{hkl} \sin\theta \tag{4.1}$$

where n is an integer number, λ is the wavelength, d_{hkl} is the spacing of the diffracting lattice planes, and θ is the diffraction angle. Also [12]:

$$\lambda = \frac{hc}{E_{photon}} = \frac{12.398}{E_{photon}\,[\mathrm{keV}]} \tag{4.2}$$

where E_{photon} is the photon energy, and λ is in Å. Further:

$$d_{hkl}(\mathrm{cubic}) = \frac{a}{\sqrt{h^2+k^2+l^2}} \tag{4.3}$$

where a is the lattice vector, and $\{hkl\}$ are the Miller indices of the lattice plane. Please note that in this thesis only *cubic* lattices will be dealt with, and only *kinematical* scattering will be assumed.

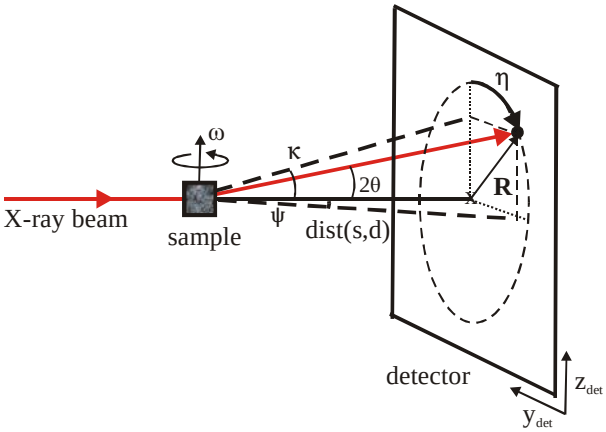

Figure 4.3: *3DXRD scattering geometry. The X–ray beam is along the x–axis, and is scattered with an angle* 2θ*, the azimuthal angle is* $\eta \in [0°, 360°]$*, the sample–to–detector distance is* $dist(s,d)$*, the horizontal scattering angle is* $\psi = (2\theta \sin\eta)$*, the vertical scattering angle is* $\kappa = (2\theta \cos\eta)$*, and* $R = \mathrm{dist(s,d)} \tan(2\theta)$*.* y_{det} *and* z_{det} *are respectively the y and z–coordinates on the detector.*

4.1.2 X–ray source

The radiation source for beamline ID11 is either an in–vacuum undulator (U23) or a wiggler[2] [12], where the in–vacuum undulator is used for experiments with the 3DXRD microscope (see table C.1 for specifics).

A wiggler/undulator is a device that is inserted into the electron beam on a straight section of a storage ring. It consists of powerful magnets of alternating polarity, which causes the electrons to move in a sinusoidal manner while in the device. Since radiation is emitted when a charged particle is accelerated, radiation is emitted at each sinusoidal "wiggle", and if the dimensions of the insertion device are constructed such that the radiation emitted at one wiggle is in phase with the radiation emitted from the other wiggles, the insertion device is called an "undulator", which is currently the most intense X–ray source available to man.

It should be noted that the spectrum produced by the ID–11 undulator (see fig. 4.4) is somewhat different from what is expected from ideal circumstances, and that which can be modelled by undulator spectrum simulation software such as XOP (available at ESRF) [96].

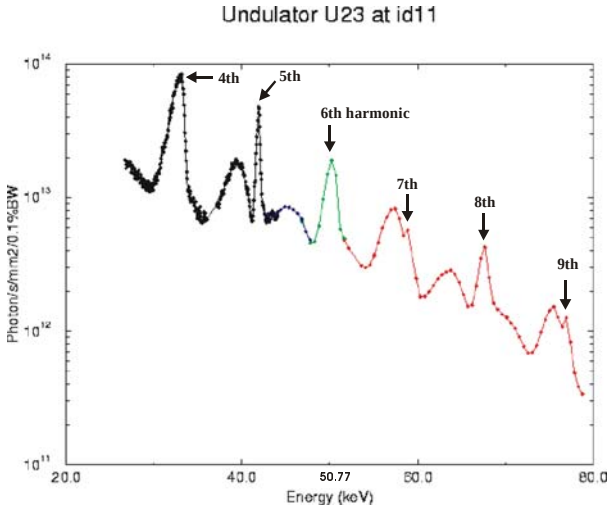

Figure 4.4: *Example of ID–11 undulator spectrum. A complete undulator spectrum is* only *available for a motor gap of* 8 mm. *This is shown here including the locations of the various harmonics. Note the non–ideal shape of the undulator spectrum [97, 98].*

[2]http://www.esrf.fr/exp_ facilities/ID11/handbook/welcome.html

The spectrum is instead fitted with a beamline ID–11 in–house program, which gives a quadratic fit to the gap motor position. A user defines which X–ray energy he or she wishes to work at, and the program calculates which gap motor positions correspond to which harmonics. For the experiment, a motor gap of 7.219 mm was used, placing the energy 50.77 keV in the 7th harmonic [98], which would place the *ideal* fundamental energy at 7.25 keV (λ=1.7 Å). The beam divergence was 0.5 mrad at the sample position.

4.1.3 High energy X–ray focusing

The quasi–monochromatic white X–ray beam is generated in the undulator (see section 4.1.2), passes slit#1 (see fig. 4.1), and then enters the experimental hutch, where the 3DXRD microscope is located, through a $1 \times 1\,\mathrm{mm}^2$ pinhole.

The 3DXRD microscope is constructed to operate in the energy range of 40–100 keV (λ=0.12–0.31 Å), and two optical elements are used to monocromate and focus the X–beam. These are an asymmetrically cut cylindrically bent perfect silicon (Si) crystal in transmission mode, and an elliptically shaped laterally graded W/B_4C–multilayer in reflection mode (see figure 4.1 and 4.5) [58].

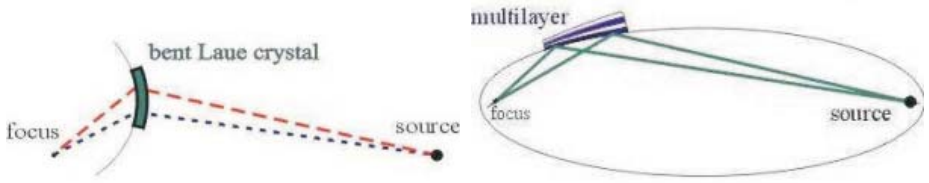

(a) (b)

Figure 4.5: *The X–ray monochromating and focusing optical elements:* ***(a)*** *Vertical: asymmetrically cut cylindrically bent Si[111]–Laue crystal;* ***(b)*** *Horizontal: elliptically shaped and laterally graded* W/B_4C*–multilayer [58].*

The sample phases are generally known in 3DXRD experiments, and the angular resolution may therefore be relatively relaxed compared to other condensed matter studies, such as structural determination, and reciprocal space mapping. Hence, by focusing in two dimensions, and increasing the

energy bandwidth to $\Delta E/E \sim 1$ %, a flux increase for micrometre–sized beams of the order of 10^6 can be obtained (10^2 from the increased bandwidth, and 10^4 from the focusing) compared to 'standard' X–ray optics, where the beam is monocromated by two flat Si crystals, and subsequently narrowed to the required size by slits.

For experiments with the 3DXRD microscope, three different X–beam cross sections are generally used: a *box* beam, where the cross section is much larger than the structural elements (5×5 μm^2 to 1×1 mm^2); a *line* beam, where the cross section is confined as much as possible to the ω–plane (1×1000 μm^2); and a *pencil* beam, where the beam is confined in both directions to dimensions smaller than the structural elements (2×5 μm^2) [21].

When a *box* beam is required, such as for the nucleation experiment described in section 4.2, the X–ray focus is located *in front* of the sample. From experience, the most homogeneous box–like beams, where the tails are very small and the maximum intensity variation across the beam is $\frac{\Delta I}{I} \sim 10\%$, are obtained when the focus is placed in front of the sample, and the beam size itself is defined by slits placed between the focusing optics and the focus point (see figure 4.6). It could be argued that even better results could be obtained by placing the slits between the focus point and the sample, but this option is not practical due to space restrictions.

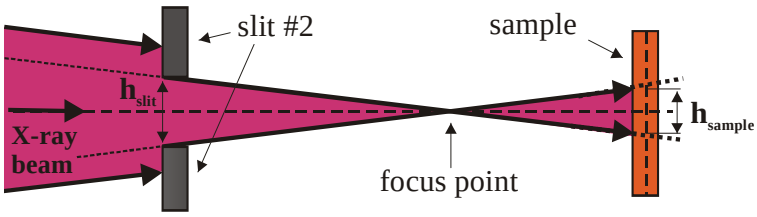

Figure 4.6: *Setup with focus point in front of the sample. Slit #2 was 15 cm in front the focus point, which was 10 cm in front of the sample, and the beam divergence was 0.5 mrad.*

4.1.3.1 Focusing by a bent Laue crystal

The incident X–ray beam is monocromated and focused in the *vertical* direction by reflection from the [111]–plane of an asymmetrically cut cylindrically bent perfect Si–crystal in transmission mode (a Laue crystal). In

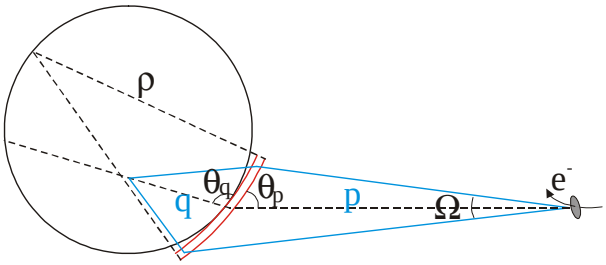

Figure 4.7: *Rowland circle for focusing with bent Laue crystal. The X–ray beam is incident on the convex side of the bent crystal.* θ_p *is the angle of incidence,* θ_q *is the exiting angle, and both are related through* $|\theta_q - \theta_p| = 2\theta_B$*, where* θ_B *is the Bragg angle.* $\Omega (\approx K/\gamma\sqrt{N})$ *is the opening angle of the undulater, and* ρ *is the bending radius of the crystal lattice planes [100].*

this geometry, the X–ray beam is nearly perpendicular to the surface of the Si(111)–crystal, which gives a small footprint on the crystal, limits the beam absorption, crystal heating, and necessary crystal size.

Only a brief introduction to the focusing mechanisms will be given here, and for a more detailed account the author refers to the following references [58, 99, 100], which the following introduction is based on. Focusing with a bent Laue crystal corresponds to solving the lens equation for a geometrically focusing crystal (see fig. 4.7), which is [101]:

$$\frac{2}{\rho} = \frac{\sin\theta_q}{q} + \frac{\sin\theta_p}{p} = \frac{1}{f} \tag{4.4}$$

where q is the geometric focus to crystal distance, p is the source to crystal distance, ρ is the radius of curvature of the lattice planes, and f is the focal length of the crystal (for $p \to \infty$), which is seen to be half that of the radius of curvature. The big difference from normal optical focusing is that the paths of the X–rays are changed by Bragg reflection, and not by refraction.

It is however not that simple, as the polychromatic X–ray beam propagates through the bent crystal, rays of different energies follow different trajectories inside an area known as the "Borrmann fan" (BF). This causes the different energies to be spread out over the BF at the exit surface (see figure 4.8). Due to the concave curvature of the inner crystal surface, these rays will all meet in one point known as the polychromatic focus q_{poly}, which in general does not coincide with the geometric focus q_{geom} (see figure

4.8). However, for a given energy, these foci can be brought to coincide by giving the diffracting planes of the crystal a specific angle to the surface normal, known as the asymmetry angle χ. Different energies therefore require different asymmetry angles [99].

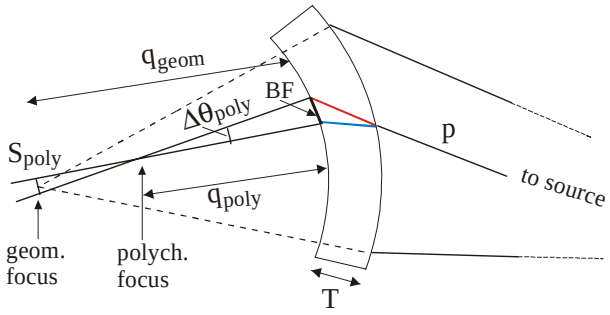

Figure 4.8: *Schematics of focusing with a bent Laue crystal. p is the source to crystal distance, q_{geom} is the geometric focal length, and the polychromatic focus q_{poly} is where all wavelengths of the Bormann fan (BF) coincide [102].*

Bending a perfect crystal entails an (often dramatic) increase in its angle of acceptance. This is due to changing reciprocal lattice vector orientations, as well as variations in d_{hkl}–spacing and asymmetry angle. For a cylindrically bent asymmetrically cut Laue crystal, the angular acceptance is increased by [99]:

$$\begin{aligned}\Delta\theta_{geom} &= \pm\left(\frac{T\tan\chi}{\rho\cos^2\theta_B}\right)\left(\frac{\cos(\chi\mp\theta_B)}{\cos(\chi\pm\theta_B)}\right)^{1/2} \times \\ &\left\{1+\frac{1}{2}(\cos(2\chi)+\cos(2\theta_B))\left[1-\frac{s_{13}+s_{15}\cot\chi}{s_{11}}\right]\right\} \quad (4.5)\end{aligned}$$

where T and ρ are respectively the thickness and bending radius of the crystal, θ_B is the Bragg angle, s_{ij} are the elastic compliances for the given crystal orientation, and χ is the asymmetry angle. The lower sign of the $\pm/\mp$ corresponds to a X–ray beam incident *between* the surface normal and the lattice plane. In the hard X–ray range, the intrinsic angular acceptance of the crystal (the absolute Darwin width) is of the order of 10^{-6} radians, which is negligible compared to the geometric acceptance, so we may take:

$$\Delta\theta_0 = \left(\Delta\theta_{DW}^2+\Delta\theta_{geom}^2\right)^{1/2} \approx \Delta\theta_{geom} \quad (4.6)$$

The total angle of acceptance is the result of the geometric as well as the polychromatic focusing $\Delta\theta_{poly}$, which is [99]:

$$\Delta\theta_{poly} = \left(1 + \frac{\cos(\chi \mp \theta_B)}{\cos(\chi \pm \theta_B)}\right) \Delta\theta_0 + \frac{\mathrm{BF}}{\rho} \tag{4.7}$$

where $\Delta\theta_0$ is the rocking–curve width of the crystal, and BF is the length of the Borrmann fan. Via the differential Bragg's law (see eq. 4.8), this directly gives the energy bandwidth of the bent Laue crystal:

$$\frac{\Delta E}{E} = \frac{\Delta\theta_{poly}}{\tan\theta_B} \tag{4.8}$$

The bandwidth of an asymmetrically cut bent Si[111]–Laue crystal ($\sim 10^{-2}$) is considerably larger than the natural bandwidth of a perfect Si[111]–crystal (the relative Darwin width: $\sim 10^{-4}$), which allows focusing and greatly increases flux. The geometric and the polychromatic focal lengths are given by [99]:

$$q_{geom} = \frac{\rho\,|\cos(\chi \mp \theta_B)|}{2 - \rho\,\cos(\chi \pm \theta_B)/p} \tag{4.9}$$

$$q_{poly} = \frac{BF}{\Delta\theta_{poly}} \cos(\chi \mp \theta_B) \tag{4.10}$$

and these may be brought to coincide for a suitable choice of χ.

In practice, the energy tunability of a Si[111]–Laue crystal is only about 10%, because the geometric and the polychromatic foci must be brought to coincide appreciably to obtain a good result. The 3DXRD microscope therefore has *two* identical focusing set–ups, with nominal energies of 50 keV and 80 keV, which allows most of the 40–100 keV energy range to be covered. For specifics on the two crystals, see table C.3.

4.1.3.2 Multilayer focusing

After the beam has been monocromated and focused in the vertical direction by the bent Laue crystal, it is focused in the *horizontal* direction by a 30 cm long elliptically shaped and laterally graded periodic W/B_4C–multilayer (ML), used in reflection mode at grazing angle (see figure 4.5b, and table C.4 for specifics).

In the 3DXRD setup, the ML is used solely to focus the X–ray beam in the horizontal plane. The reason for using a graded ML, as opposed to a curved mirror, is that the ML may be made considerably shorter, especially at higher energies, where the angle of total reflection is impractically small ($\alpha_c \sim$mrad) for mirrors. This is due to the fact that while mirrors work by total specular reflection, while a ML works by Bragg reflection from the *periodic* layers, which works at much higher angles of incidence, thus reducing the length necessary to accommodate the footprint of the X–ray beam on the surface.

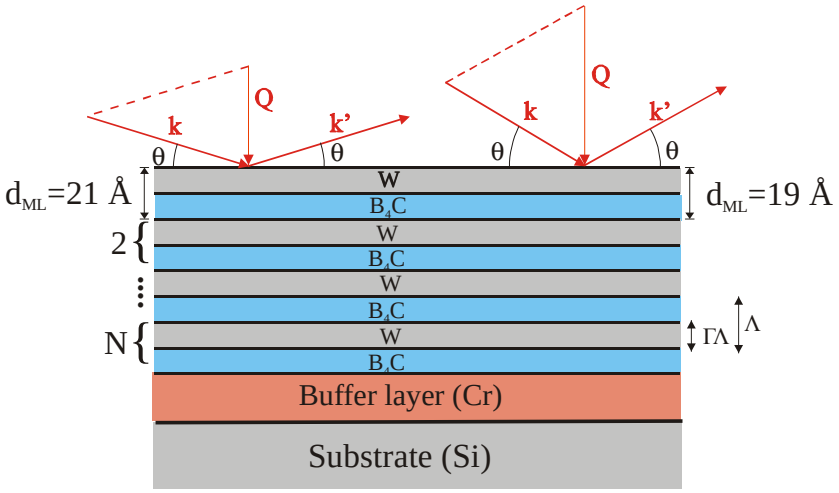

Figure 4.9: *Reflection from a multilayer mirror. The reflection angle θ varies with the periodic layer spacing d_{ML}, through equation 4.11. Λ is the thickness of one bilayer, $\Gamma\Lambda$ is the thickness of one W-layer, k and k' are respectively the wavevectors of the incident and reflected beams, and Q is the wavevector transfer. The two reflected beams shown have the* same *energy, but different incident angles.*

Periodic multilayers are stacks of alternating periodic layers of materials of high and low electron density, which are grown on highly polished substrates. At each layer interface a fraction of the incident intensity is reflected and large reflectivities are obtained when the Bragg condition is fulfilled (see fig. 4.9):

$$n\lambda = 2\, d_{ML} \sin\theta_B \tag{4.11}$$

where λ is the X–ray wavelength, n is the order of the reflection, d_{ML} is the periodic layer spacing, and θ_B is the corresponding Bragg angle. Due to eq. 4.11, ML may also be used as monochromators.

Focussing is obtained by giving the surface an elliptical shape, where the source and focus points coincide with the focal points of an ellipse (see fig. 4.5b). In elliptical geometry, the incidence angle of the X–ray beam changes along the the footprint, and the periodic layer thicknesses are therefore changed correspondingly to prevent a further increase of the bandwidth [58]. The energy bandwidth of periodic multilayers is of the order of 1%, which is of the same order as the bandwidth of the bent Laue crystal (see tables C.3 and C.4) [58, 97].

The multilayer consists of 100 consecutive layers of W and B_4C, with a Γ–factor (W/B_4C–thickness ratio) of 0.1455. They are deposited on a polished Si–substrate, with a 100 Å chromium–buffer layer. The elliptical curvature of the multilayer corresponds to a major radius of 25 m, and the periodic spacing d_{ML} at the centre of the multilayer is 20 Å, and this spacing falls from 21 Å at the edge furthest from the focal point to 19 Å at the edge closest to the focal point (see figure 4.5). The substrate dimensions are 30×4×1.5 cm.

4.1.4 Detectors

For the 3DXRD experiment, two different types of detectors was used:

A solid state silicon pin diode was used to align the experimental setup and characterize the X–ray beam. The active area of the diode is 20×20 mm, and the detector efficiency as a function of X–ray energy is known.

Diffraction images were recorded on an ESRF–developed 14–bit 2D Frelon CCD detector with anti–blooming coupled by an image intensifier to a fluorescence screen of area 160×160 mm^2 (see table C.2 for specifics). The X–rays strike a spherical phosphorous screen, where some are absorbed and generate visible light, which is then reflected up onto a CCD–chip (Charge Coupled Device) with 1024×1024 pixels. The CCD–chip has a dynamic range of 14 bits, which means that it saturates at 2^{14} (∼16,000) counts, where counts is the number of detected photons within the exposure time. Anti–blooming limits electrical charge 'seeping' from intense to less intense areas on the CCD–chip, but also lowers the maximum dynamic range of the chip to about 14,000 counts.

The spatial resolution of a detector depends mainly on the thickness of the fluorescence screen, where a thinner screen gives a better resolution. However, for too thin screens, the absorption becomes small, which is detrimental to the detector efficiency. The Frelon detector has a relatively high efficiency,

but also a large point spread function (the size of a perfectly collimated infinitely thin beam on the detector) of 200–300 μm, which means that the Frelon detector does not have a high spatial resolution, and therefore does not preserve the shape of the diffracting volumes. The spatial resolution is therefore defined by the volume illuminated by the X–ray beam, and the diffraction images are solely used to determine the crystallographic orientation and size of the individual diffracting volumes (see fig. 4.1). Due to the relatively large size of the detector, it can be placed at some distance to the sample, and a good angular resolution ($\sim$0.1°) is obtained.

4.1.5 The furnace

The furnace used in the experiment can provide a maximum stable temperature of 500°C. It is mounted on the sample stage, and can be rotated 360° around the ω–axis (see figure 4.1). The sample is mounted in a groove on a copper sample stub and fastened with a screw, and a thermocouple is in direct contact with the bottom of the sample through a hole drilled in the sample stub.

The sample is surrounded by a quartz cylinder with an *outer* diameter of 20 mm, which allows sample sizes up to 1 cm. The quartz cylinder has been chemically etched down to a thickness of approximately 0.1 mm, thereby giving rise to negligible absorption and minimizing diffuse scattering. The furnace allows a controlled atmosphere.

The furnace temperature is controlled by a 'EuroTherm' control box, which is controlled by the computer interface 'iTools' and the 'Set Point Editor' software[3]. This software allows very quick heating up to a target temperature without overshooting. Please note that this requires that a comparable sample is initially used to calibrate the temperature set points of the EuroTherm–furnace system.

[3]Manuals can be found at http://www.risoe.dk/afm/synch/furnace.htm

4.2 The nucleation experiment

This section is concerned with the design and carrying out of the 3DXRD experiment. It follows and elaborates on what is written in publications [A2,A5,A7], and is divided up into three subsection covering the following topics:

4.2.1 the choice of sample material and the sample preparation.

4.2.2 the preliminary studies carried out before the 3DXRD experiment.

4.2.3 the 3DXRD experiment.

It was decided to limit our X–ray study of nucleation to triple junctions of grains (i.e., where three grains meet) within the material. Previous investigations [3, 30, 74], as well as a study by optical microscopy (see section 2.3) had shown that triple junctions are preferred nucleation sites in light to moderately deformed large particle–free single–phase metals.

4.2.1 Samples used for the 3DXRD study

The sample material was oxygen–free high conductivity (OFHC) copper 99.995% pure, which was relatively free of large interstitial particles. The Metals–4D center has considerable experience in working with aluminium, but copper was chosen for the 3DXRD experiment, because we wanted to focus on nucleation at triple junctions, which requires a material relatively free from large particles in order to avoid particle stimulated nucleation (see section 1.2.6). We chose not to use high purity aluminium because it recrystallizes at very low temperatures, thus making it impossible to characterize the deformed state in the 3DXRD microscope. Additional advantages when using copper for the experiment is that copper recrystallizes at relatively low strains, and has a X–ray scattering power, which is greater than that of aluminium, allowing us to detect smaller volumes (see section 4.2.3.2). Also, copper routinely produces annealing twins (see section 1.2.5), which greatly improves the chances of a nucleus appearing with an orientation not present in the parent grains, and therefore facilitates its detection significantly. However, we must also bear this in mind when comparing the orientation of nuclei with the available parent grains (see section 4.2.3.6). It should be noted that on a timescale of months the OFHC copper was found to recover at room temperature. This was however not deemed a problem, since all studies were

performed within 1–2 weeks of cold rolling, and here no dramatic recovery effects were observed.

In a previous study by Poulsen *et al.* [4], it was observed that an aluminium single crystal, channel die deformed to 78% reduction in thickness at room temperature, fills 30–40% of the orientation space available in a {200}–pole figure (see appendix B), which contains the {hkl}–family of lowest multiplicity (m_{200}=6). From this it is clear that a smaller deformation must be used in order to characterize the microstructure at triple junctions, where it must be possible to distinguish the reflections of *at least* three grains at the same time, and some free orientation space must also be present to allow nuclei with new orientations to be detected. At low to moderate deformation (10–40%), pre–existing grain boundaries should act as the dominant nucleation sites [30], and reduce the number of potential nucleation events [103].

The chosen solution was to use a moderately deformed material (20% deformed) with a relatively large grain size, and to limit spot–overlap (overlap of diffraction spots from different grains) as much as possible, it was chosen to polish the sample down to a small thickness (0.3 mm), so that the surface grains would generally continue throughout the thickness of the sample. It was then deemed that there was good chance that only three grains would be irradiated by the X–ray beam as it penetrated the samples at a triple junction, and as the sample thickness was two orders of magnitude larger than the average cells in the deformed microstructure (see section 4.2.2.3), as well as the expected initial size of the nuclei (see section 1.2), the nucleation dynamics were therefore expected to exhibit *bulk* properties.

It should be noted that the sample thickness was *not* chosen to maximize the diffracted flux $I(x)$ from the full thickness of the sample, which is [12]:

$$I(x) = xe^{-\mu x} \implies \tag{4.12}$$

$$I_{max} = I(x{=}\frac{1}{\mu}) \tag{4.13}$$

where x is the thickness of the sample, and μ is the linear absorption coefficient. From eq. 4.13, the total diffracted intensity from the sample is at maximum for a thickness of 0.43 mm (at 50 keV)[4], and at a thickness of 0.3 mm, 95% of the maximum possible diffracted intensity is obtained.

[4]The linear absorption coefficient of copper at 50 keV is: $\mu = 2.31\,\mathrm{mm}^{-1}$ [104].

The starting material was annealed for 2 hours in an air furnace at 600°C, then cold rolled 20%, and lastly, annealed for 8 hours at 700°C. This resulted in a grain size distribution with an average grain size of about 500 μm. This starting material was then additionally cold rolled to a 20% reduction in thickness — from a thickness of 32.0 mm to 25.6 mm (see figure A.1a). During cold rolling, where the roll radius was 170 mm, the L/h–ratio was 1.2 (see eq. 4.14), and the deformation is therefore expected to be uniform throughout the thickness of the material [105]:

$$\frac{L}{h} = \frac{\sqrt{r(h_0 - h_1)}}{(h_0 - h_1)/2} \tag{4.14}$$

where r is the radius of the rolls, h_0 and h_1 are respectively the specimen thickness before and after rolling, $L{=}|\widehat{AB}|{\approx}|\overline{AB}|{=}\sqrt{r(h_0 - h_1)}$ is the contact length between the rolls and the specimen, and $h{=}(h_0 - h_1)/2$ is the average thickness of the specimen.

From this material thin $10 \times 10\,mm^2$ RD–ND (see appendix A) sections were cut out. The sections were mechanically lapped (with 9 and 3 μm Al_2O_3) and polished (with colloidal silica) down to a thickness of 0.3 mm. The lapping and polishing was performed on both sides using a Logitech PM5D polishing and lapping machine with a PSM1 sample monitor [A3]. Additionally, to remove any remaining surface deformation or sub–micrometre scratching (i.e., surface nucleation sites), the samples were electrolytically polished for 5 seconds at a voltage of 10 V. The sample was used as anode, platinum was used as cathode, and a D2–solution[5] was used as electrolyte [92, 93].

[5]D2: $500\,ml\,H_2O$, $250\,ml$ H_3O_4P, $500\,ml$ ethanol, $50\,ml$ propanol, $5\,g$ (crystalline uric acid), and $2\,ml$ *'Dr. Vogels Sparbeize'* :
'Dr. Vogels Sparbeize' is a chemical solution, who's exact recipe is unknown. It acts as an inhibitor that allows electrochemical polishing of copper surfaces without corrosion. Known contents are: $\leq$ 20% H_2SO_4, $\leq$ 1% H_3PO_4, 40–50% 1–methoxy–2–propanol, 5–7% nonylphenol–ethoxylate, 3–5% thio–uric acid.

4.2.2 Preliminary studies

Several preliminary studies were performed with various experimental techniques prior to the 3DXRD nucleation experiment. These studies were essential in order to maximize the probability of the experiment being a success.

Firstly, it was necessary to ascertain whether the diffraction spots from three large grains located at a triple junction in a 20% cold deformed sample could be distinguished from each other, and whether they left enough free space in the diffraction images for any new diffraction spots, which might appear, to be observed. Also, several studies were performed on the sample material using hardness indentations and microscopies of various kinds, so as to determine the approximate recrystallization temperature, whether triple junctions were the dominant nucleation sites, and the surface positions of triple junctions suitable for study by 3DXRD on the samples used in the experiment.

4.2.2.1 3DXRD feasibility study

At an earlier beamtime, a short feasibility study was performed at the 3DXRD microscope on a sample identical with those used in the actual experiment. This was done in order to confirm that the reflections from three adjacent grains, cold deformed 20%, would not completely fill all of orientation space, which would make the experiment impossible to perform with the chosen amount of deformation.

Before the X–ray study, an area of the surface was characterized by optical microscopy, so as to determine the surface location of all triple junctions suitable for 3DXRD study. This feasibility study confirmed that spot–overlap was at an acceptable level for the deformed grains at a triple junction, and that there was still plenty of available space in the diffraction images.

4.2.2.2 Vickers hardness testing

The recrystallization temperature (see section 1.1) was estimated by annealing several identical samples at different temperatures for 1 hour, and then performing Vickers hardness tests on them. The Vickers hardness vs. annealing temperature curve (see figure 4.10a) was used to estimate the minimum temperature for the onset of nucleation. The recrystallization temperature was estimated to be around 290°C, and this was chosen for the experi-

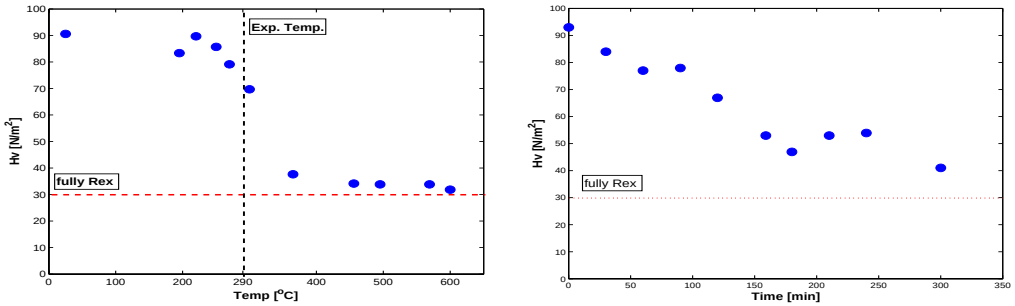

(a) (b)

Figure 4.10: *Vickers hardness tests on the copper sample material. The material was cold rolled 20%, the samples were heated in an air furnace, and the test load was 5 kg.* ***(a)*** *samples were annealed for 1 hour at different temperatures;* ***(b)*** *samples were annealed at 300° C for different periods of time.*

ment, to make sure that the softening was not caused solely by recovery and that nucleation would occur from the onset of annealing (see section 1.1).

A series of samples were annealed at 300°C, which was slightly above the recrystallization temperature, for varying periods of time to ascertain how fast recrystallization proceeds at this temperature. The resulting hardness curve can be seen on figure 4.10b). The hardness curve shows that recrystallization does not occur very rapidly at 300°C, taking more than 5 hours to be complete, which indicated that it would be possible to follow the kinetics of a growing nucleus if one was identified in the experiment. From the large scatter in hardness, it could also be concluded that not all regions of the sample material would initially recrystallize at an experimental temperature of 290°C.

4.2.2.3 Investigations by microscopy

Previously a detailed TEM study of pure copper had been performed by Huang *et al.* [106]. In this study it was found that the minimum distance between cell boundaries with a misorientation of 1° or greater was 1–2 μm in pure copper deformed 17% by cold rolling and 36% in tension. According to Huang, the minimum subgrain size within the sample material should therefore be 1–2 μm [107]. This may be compared with the *classical* critical nucleus size that can be determined from equation 4.15 [30]:

$$R_C > \frac{2\gamma}{E_S} \tag{4.15}$$

where R_C is the classical critical radius of curvature, which allows a nucleus to grow, γ is the boundary energy, and E_S is the stored energy of cold work. For copper we have γ=0.625 Jm^{-2} [11], and for copper 20% cold deformed we have E_S=2.20·10^6 Jm^{-3} [108]. By inserting these into equation 4.15, we find ECD_C=2R_C>1.14 μm.

After electrochemical polishing, a $1.820 \times 1.800\, mm^2$ area on each sample was inspected by EBSP, with a step size of $20\,\mu m$. From this an OIM was produced to allow easy identification of all triple junctions within that surface area. Figure 4.11 shows an example of the area on the samples characterized by EBSP — the upper right edge of the inspected area was 2 mm below the top edge, and 2 mm left of the right edge (see also fig. 4.12–4.14). A JEOL JSM–840 scanning electron microscope, with a LaB_6–filament was used to collect the EBSP data. The working distance was 22 mm, the electron beam current was 270 μA, and the accelerating voltage was 20 kV.

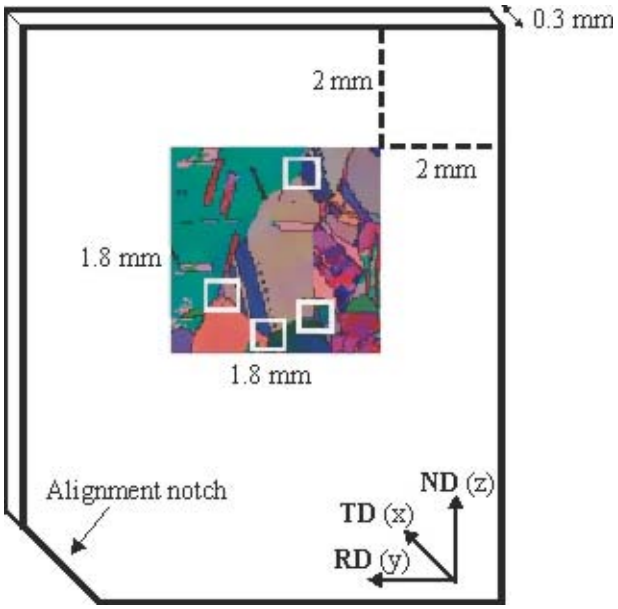

Figure 4.11: *X–ray sample geometry. Note that the relative size of the OIM has been slightly exaggerated to make the microstructure more easily discernable. The white squares indicate the surface locations of selected triple junctions, and the alignment notch was made to ensure that the the sample was mounted correctly in the X–ray study.*

4.2.3 The 3DXRD experiment

An X–ray energy of 50.77 keV (λ=0.2442 Å) was used for the 3DXRD experiment, thus giving a transmission of 50% through the 0.3 mm thick copper samples. This energy was not chosen specifically for the experiment, but was to be used for an experiment directly following the one described in this section. However, using this energy was not a drawback. During the experiment, the synchrotron ring was in 16–electron bunch mode, giving a maximum synchrotron ring current of 90 mA, and a maximum monochromated flux[6] of $3.6 \cdot 10^6$ photons/s at 50.77 keV was measured with the pin diode behind the multilayer, which corresponds to a flux of the order of 10^{10} photons/s [98].

[6]Should be corrected for Si–diode efficiency at the X–ray energy.

For the experiment, a 800×800 μm^2 sized white X–ray beam was monochromated and focused onto the sample. The focal point was located 10 cm in front of the sample, and the beam dimensions were defined by using slit #2 (see fig. 4.6). The resulting X–ray *box* beam had a flat profile ($\frac{\Delta I}{I} \leq 10\%$) and a size of 49×49 μm^2 at the sample position. The X–ray beam size, defined as the full width at half maximum (FWHM) at the sample position, was determined by scanning the Si–diode through the beam. While it is possible to focus the X–ray beam down to a size of roughly 2×5 μm on the sample (see tables C.3 and C.4), a considerably larger beam was used in order to characterize a relatively large volume in a reasonable amount of time.

It should be noted that specific details pertaining to the setup and alignment have been omitted from this section, except where doing so has been deemed of great importance. Also, before performing the actual experiment, the calibration data utilized in sections 4.2.3.1 and 4.2.3.2 was collected.

To characterize the microstructure of a volume, defined by the beam size and the sample thickness, diffraction images were obtained by CCD exposures made for a number of equally spaced values of the rotation axis ω, equal to the angular range in degrees. To ensure an even sampling of integrated intensities, the sample was rotated by $\pm 0.5^\circ$ during each exposure, which lasted for 1 second. To further increase the volume characterized by the X–ray beam, exposures were made at a set of sample positions. For all samples this corresponded to an (y, z)–grid, where the distance between grid nodes was 40 μm.

The experiment could basically be divided into two parts. First, a volume (grid area × sample thickness) centered on a suitable triple junction was characterized in the deformed state at room temperature (25°C). Secondly, the sample was heated to 290°C in a helium atmosphere (1.3 bar), and once at temperature, the same volume was continually characterized, so as to follow the nucleation kinetics. The same volume was located again in the hot sample by utilizing its (y, z)–distance to the upper right sample corner, who's change with heating was negligible on the length scales and precision of the experiment.

Three samples (A, B, and C) were studied during the experiment, and on each sample a grid, of varying size and centered on a triple junction, was characterized as described below. Figures 4.12–4.14 show the X–ray grid superimposed on the EBSP OIMs obtained from the preliminary study (see section 4.2.2.3). The samples were characterized in the following order:

Sample A: a 2×2 grid centered at a triple junction, with (y, z)–motor positions = (0.769, 138.460), was characterized within an ω–range of [-10°,11°]. The sample was subsequently heated to 290°C, and upon reaching temperature, an identical 2×2 grid was then continually characterized with a time resolution of ≈6 minutes. During annealing a reflection originating from a nucleus was identified in the diffraction images, and it was therefore decided to quench the sample back to room temperature after only 45 minutes of annealing, in order to determined the exact (x, y, z)–position of the nucleus, as well as to increase the ω–range, to determine the crystal orientation of the nucleus with greater accuracy. The exact position of the nucleus was determined, and the nucleus was subsequently translated into the centre of rotation, allowing exposures to be made for an ω–range of [-45°,46°] without risk of the nucleus moving out of the X–ray beam as the sample was rotated. Afterwards, the sample was once again heated to 290°C, and the growth kinetics of the nucleus were followed.

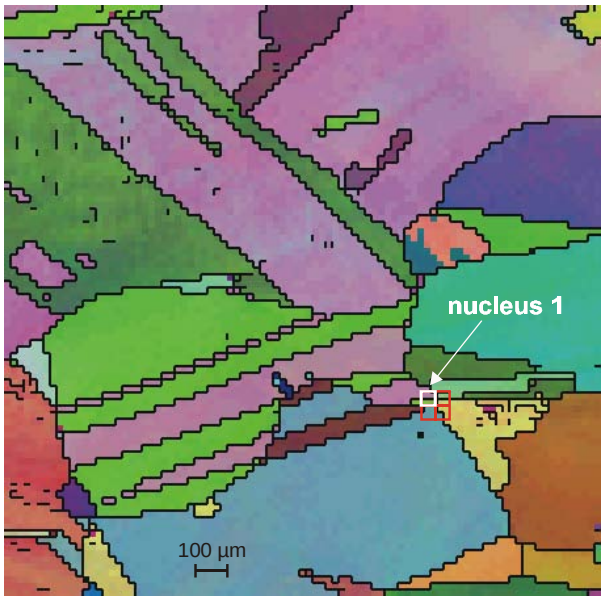

Figure 4.12: *Sample A: OIM of the surface microstructure and the location of the X–ray grid (marked in red). A 2×2 grid was characterized, within the ω–range of [-10°,11°], in the deformed state and continuously during annealing with a time resolution of ≈6 minutes. A nucleus (nucleus 1) was detected in the white grid area.*

Sample B: a 2×2 grid centered at a triple junction, with (y, z)–motor positions = (1.431, 138.806), was characterized within an ω–range of [-20°,21°]. However, to increase the sensitivity of the characterization of the deformed microstructure, the exposure time was increased to 15 seconds and the ω steps between exposures was reduced to 0.5°, giving a sampling rotation of ±0.25°. This increased the intensity diffracted into a given reflection during an exposure by a factor of 30 (see eq. 4.17). After the initial high sensitivity characterization, the sample was heated to 290°C, and upon reaching temperature, an identical 2×2 grid with an ω–range of [-20°,21°] was continually characterized during annealing, which lasted for 11.1 hours. Note that the exposures made during annealing were made with normal sensitivity (i.e., 1° ω–steps, rotated ±0.5° for 1 second), giving a time resolution of ≈8.5 minutes.

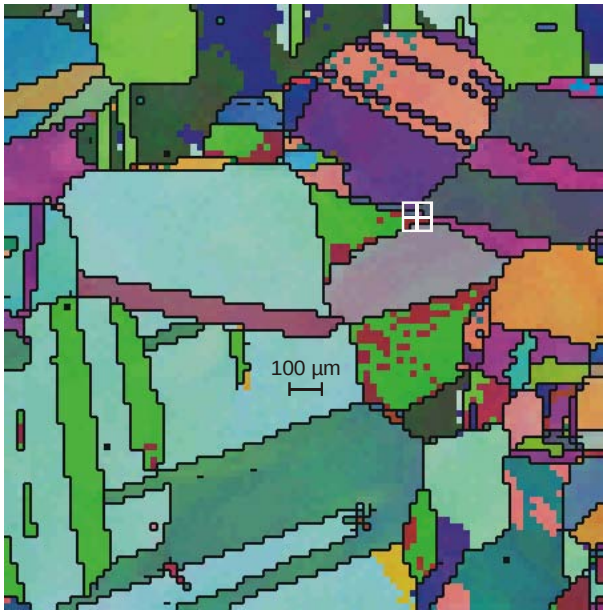

Figure 4.13: *Sample B: OIM of the surface microstructure and the location of the X–ray grid (marked in white). A 2×2 grid was characterized, within the ω–range of [-20°,21°], before and continuously during annealing with a time resolution of ≈8.5 minutes. No nuclei were identified in this sample.*

Sample C: a grid centered at a triple junction, with (y, z)–motor positions = (0.776, 138.646), was characterized within an ω–range of [-20°,21°]. For this sample it was chosen to expand the grid into a 4×4 grid, in order to increase the probability of a nucleation event occurring within the characterized volume. The deformed sample was characterized with the 4×4 grid described above, after which the sample was heated to 290°C. Once the sample had reached the desired temperature, the central 2×2 grid areas of the 4×4 grid were continually characterized within an ω–range of [-20°,21°] during annealing with a time resolution of ≈8.5 minutes. Towards the end of annealing (after 3–3.5 hours), the grid was once again expanded into a 4×4 grid, so as to characterize the same volume as was initially characterized within the deformed sample.

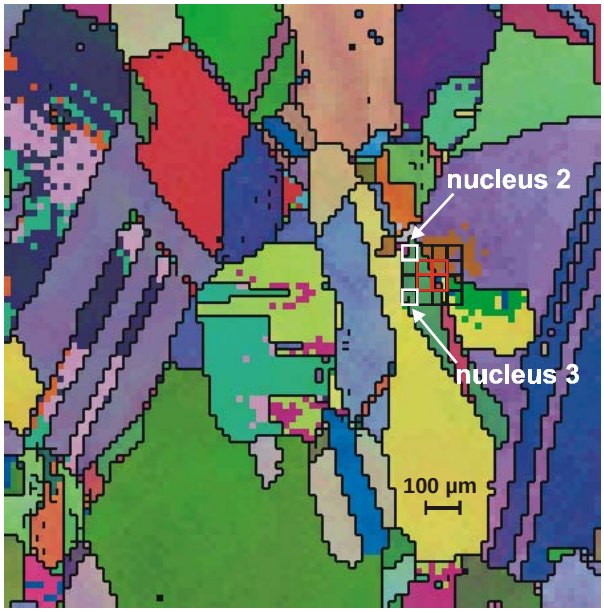

Figure 4.14: *Sample C: OIM of the surface microstructure and the location of the X–ray grid (marked in black). The 4×4 grid was characterized before and at the end of annealing, within the ω–range of [-20°,21°]. During annealing the red 2×2 grid was characterized continuously with a time resolution of ≈8.5 minutes. Two nuclei (nucleus 2 and nucleus 3) were detected in respectively the top and bottom white grid areas. Nucleus 2 was also faintly observed in the top left red grid area.*

4.2.3.1 Image processing

The 2D Frelon detector produces raw digital images in the .EDF–format, roughly 2 MByte in size. Before the images can be used for quantitative crystallographic analysis, the background intensity must be subtracted and the images must be spatially corrected.

Background subtraction

The typical background subtraction method, is to record X–ray images without the sample present (raw background image), and without any X–rays (darkfield image). The darkfield image (the internal noise in the CCD–chip, which is only exposure–time dependant) is initially subtracted from both the diffraction and the background image, which are then scaled to the same synchrotron current (i.e., the same X–ray flux), and the background image is then subtracted from the diffraction image.

However, in this case a considerable effort was made to obtain a low volume detection limit (i.e, an intense X–ray beam), so the reflections from the large deformed grains gave rise to high intensities, which subsequently saturated the Frelon detector, which saturates at ∼14,000 counts (see section 4.1.4). Even with anti–blooming on the detector (see section 4.1.4), some charge from intense poles was seen to leak out onto the surrounding areas of the CCD–chip, and thus to surrounding areas of the diffraction image. This leakage can be seen as the streaks on figure 4.15a.

It was chosen to use the background subtraction method developed by Bowen *et al.* [109]. In the algorithm, an image is divided up into a grid, and each grid area is further subdivided into more subgrid areas. The standard deviation of the intensity in each subgrid area is calculated, and those in which the standard deviation is above a specified limit are ignored, while those that are below are used to interpolate the background intensity of the full grid area, which is in turn used to interpolate the background intensity of the entire image. The results were very good, with the pixel intensity often falling to zero between the Debye–Scherrer rings. Note that this procedure is performed on *every* single diffraction image, and that the calculated background is valid for that image only.

Figure 4.15 shows examples of diffraction images before and after background subtraction using the Bowen *et al.* method. Due to the nature of the interpolation function, the background is not subtracted from the outer edge of the image.

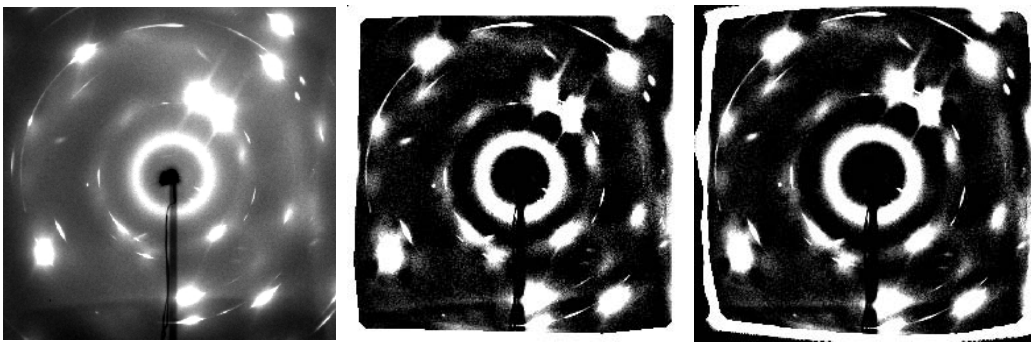

(a) (b) (c)

Figure 4.15: *Background subtraction using the Bowen et al. method. Diffraction images showing respectively:* ***(a)*** *a raw image;* ***(b)*** *a background subtracted image; and* ***(c)*** *a background subtracted, and spatially corrected image (see below). Note that* ***(a)*** *and* ***(b)****&****(c)*** *are not on the same intensity scale.*

Spatial correction

Because the diffraction cones are not scattered onto a flat surface (the phosphorous screen is spherical), the diffraction images are distorted and must be spatially corrected. This is done by mounting a flat 1.5 mm thick copper plate, with a regular grid of 65×65 holes, on the front surface of the detector. The holes have a diameter of 1.5 mm, and the centre–to–centre distance is 2.5 mm. Using the recorded transmission image of this grid (see figure 4.16b) and the software package 'FIT2D'[7] [110], it is possible to produce a spline function, which corrects the spatial distortion on the diffraction images (see figures 4.15c and 4.16c) [111].

The specifics of the scattering geometry (eg. sample–to–detector distance, detector tilt angle, effective detector pixel size, etc.), which are necessary to create the spline function, are determined by placing a LaB_6–powder sample in the beam and recording diffraction images from this. LaB_6 is used because it produces *many* well defined powder rings (see figure 4.16a), which allows an accurate fitting of the scattering geometry to be performed in FIT2D, using a fitting routine specifically developed for LaB_6–powder. This fitting is carried out twice. First, with the distorted raw LaB_6–image, which then

[7] http://www.esrf.fr/computing/expg/subgroups/data_analysis/FIT2D/

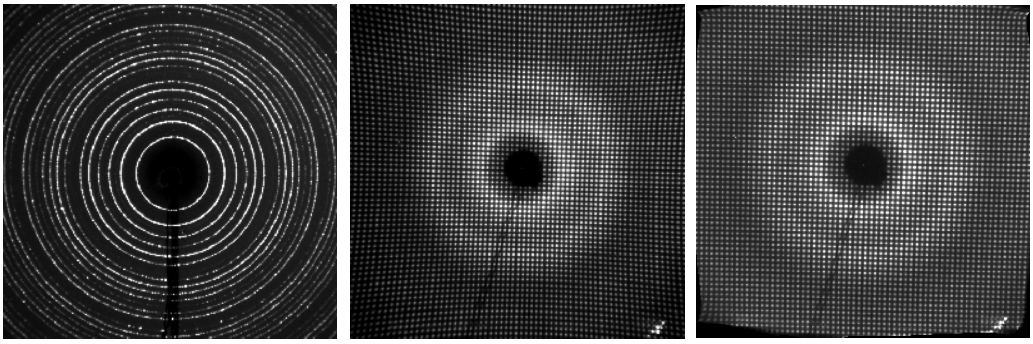

(a) (b) (c)

Figure 4.16: *Spatial correction of 2D diffraction images. Diffraction images showing respectively:* ***(a)*** *the* LaB_6*–powder rings (distorted);* ***(b)*** *image of grid (spatially distorted); and* ***(c)*** *image of grid (spatially corrected).*

yields rough parameters for the scattering geometry. These parameters are then used to produce a first spline function, which is then applied to the raw LaB_6–image. The resulting corrected parameters are subsequently used to determine the final spline function.

The spatial correction of the images using the spline function was also carried out using FIT2D, and the transmission images of the grid before and after the spatial correction has been applied can be seen on figure 4.16b–c. During image processing, the background subtraction was performed *before* the spatial correction, due to strict mathematical requirements imposed on the dimensions of the image file by the Bowen *et al.* background subtraction method.

4.2.3.2 Volume calibration

In this investigation of nucleation, the size of the nuclei was of interest, as well as their the crystal orientations. This is because if the size of the nuclei can be determined at different annealing times, it is possible to follow the growth kinetics of the nuclei. Also, of great importance was to determine the smallest detectable diffracting volume (the detection limit), because this determines with what sensitivity the deformed microstructure could be characterized, and the smallest nuclei that could be detected.

In 3DXRD, the size of a diffracting volume is determined by scaling the scattered intensity from the volume with the scatter from an accurately known volume of known scattering factor. By scaling the intensity of a reflection from a diffracting volume to the intensity of the known volume, the size of the diffracting volume may thus be determined.

An aluminium foil of 53 μm thickness and random texture was placed in the X–ray beam, with surface normal parallel to the beam, thus illuminating a channel through the foil, with a volume equal to the beam area $\times$ the foil thickness ($49 \times 49 \times 53\,\mu m^3$). The foil produced a powder diffraction pattern, and the total intensity of the {200} Debye–Scherrer ring was integrated, giving an intensity–to–volume conversion factor (see below). This conversion factor can readily be applied to other materials, but must then be corrected for differences in scattering factors and diffraction angles.

By placing aluminium attenuators in the X–ray beam, it was possible to perform long exposures without saturating the Frelon detector. 1 second counts with the Si–diode gave respectively 2059 counts and 389,000 counts for respectfully the attenuated and unattenuated X–ray beam, giving an attenuation factor of $I_{atten}/I_0 \approx 1/189$. Diffraction images were obtained at 20 adjacent y–positions. For each image, the exposure time was 4 seconds, and the sample was rotated by $\pm 5^\circ$, so as to achieve an even sampling and as homogeneous a powder diffraction image as possible.

The intensity of these 20 images was averaged using FIT2D, and from this average image, the average integrated intensity of the {200}–ring, and the average background were determined. The true intensity of the {200}–ring was determined by subtracting the average background (255 photons/pixel/4s) $\times$ the area covered by the ring (42,000 pixels). Scaling this intensity to 1 second exposures, and multiplying by the attenuation factor ($\approx$189), the total diffracted intensity of the {200}–ring was found to be $18.4 \cdot 10^6$ photons/s at a synchrotron ring current of 77.2164 mA.

We may also calculate this from Warren [59], where (for a monochromatic X–ray beam) the total energy scattered into a {hkl}–Debye–Scherrer ring by a perfect texture–free powder of volume V is given by:

$$E_{powder} = \frac{I_0\, t}{4}\, r_0^2\, \frac{\lambda^3\, |F^{u.c.}(hkl)|^2\, V\, m_{hkl}}{(v^{u.c.})^2}\, \frac{1}{\sin\theta\, \sin 2\theta} \tag{4.16}$$

where I_0 is the intensity of the X–ray beam, λ is the X–ray wavelength, $r_0 = 2.82 \cdot 10^{-5}$ Å is the electronic scattering cross section, $F^{u.c.}(hkl)$ is the structure factor of the atomic unit cell, $v^{u.c.}$ is the volume of the unit cell,

t is the integration time, V is the volume of the illuminated powder, θ and η are defined on fig. 4.3, and m_{hkl} is the multiplicity of the {hkl}–family.

This must be related to the intensity of a *single* reflection, which we may also calculate from Warren [59], where (for a monochromatic X–ray beam) the energy scattered by a crystallite of size δV into a *single* (hkl)–reflection is:

$$E_{single} = \frac{I_0}{\Delta\omega}\, r_0^2\, \frac{\lambda^3\, |F^{u.c.}(hkl)|^2\, \delta V}{(v^{u.c.})^2}\, \frac{P}{\sin 2\theta\, |\sin\eta|} \tag{4.17}$$

where $\Delta\omega$ is the rate of rotation of the crystallite in the X–ray beam, and P is the polarization factor.

By determining the intensity of a single reflection, and the intensity of a full powder ring, it is possible to find the ratio of E_{single} to E_{powder} by dividing eq. 4.17 by eq. 4.16. Note that if the same X–ray wavelength is used in both cases, there is no need to know the absolute value of I_0, or the detector efficiency for that matter. Below, the subscripts s and p refer to respectively a *single* reflection from a crystallite, and a full *powder* ring, so that comparisons between different materials may be made:

$$\frac{E_{single}}{E_{powder}} = \frac{4}{\Delta\omega\, t}\, \frac{\delta V}{V\, m_{hkl}}\, \frac{|F_s^{u.c.}(hkl)|^2}{|F_p^{u.c.}(hkl)|^2}\, \frac{(v_p^{u.c.})^2}{(v_s^{u.c.})^2}\, \frac{P\, \sin\theta_p\, \sin 2\theta_p}{\sin 2\theta_s\, |\sin\eta_s|} \tag{4.18}$$

By isolating δV in eq. 4.18, we obtain an equation for δV, based on the illuminated volume of the powder, and the ratio of E_{single} to E_{powder}, which may be substituted by the ratio of I_{single} to I_{powder}, and thus:

$$\delta V = \frac{\Delta\omega\, t}{4}\, \frac{I_s}{I_p}\, V\, m_{hkl}\, \frac{|F_p^{u.c.}(hkl)|^2}{|F_s^{u.c.}(hkl)|^2}\, \frac{(v_s^{u.c.})^2}{(v_p^{u.c.})^2}\, \frac{\sin 2\theta_s\, |\sin\eta_s|}{P\, \sin\theta_p\, \sin 2\theta_p} \tag{4.19}$$

Specifically for the experiment, the synchrotron X–ray beam was horizontally polarized, i.e., P=$\cos^2\psi_s$ [12], where ψ_s=$2\theta\, \sin\eta_s$ (see figure 4.3). From eq. 4.17 we can deduce that E_{single} is at minimum for η_s=90°, and therefore the "worst–case" detection limit is also to be found there. The angular rotation rate, and the integration time were respectively set to $\Delta\omega$=1° and t=1 s, which were used in the experimental exposures. From the diffraction images the signal–to–noise limit (the minimum detectable scatter) from an aluminium {200}–reflection at η=90° was estimated to 400 photons/s This signal–to–noise limit counts for every pixel, so the minimum detectable scatter corresponds to 400 photons/s on a *single* pixel.

Furthermore, we had V_{foil}=49×49×53 μm^3, and the multiplicity (i.e., the number of reflections of the {hkl}–family) was m_{200}=6. Aluminium and copper both have the *fcc*–structure, so instead of comparing the scattering factors of their respective lattices $|F^{u.c.}(hkl)|^2$ (given in eq. 4.20), it is enough to compare the scattering factors f_{atom} of the two elements [12]:

$$F^{u.c.}_{fcc}(hkl) = \begin{cases} 4 \cdot f_{atom} & \text{if all } (hkl) \text{ are even or odd.} \\ 0 & \text{otherwise.} \end{cases} \tag{4.20}$$

$$f_{atom} = f(\mathbf{Q})\, e^{-M(T)} \tag{4.21}$$

where $|\mathbf{Q}| = \left(\frac{4\pi}{\lambda}\right) \sin\theta$ is the wavevector transfer, $f(\mathbf{Q})$ is the atomic scattering factor, and $e^{-M(T)}$ is the temperature dependent Debye–Waller factor. The values of $f(\mathbf{Q})$ were obtained from appropriate tables [104], and the Debye–Waller factors were calculated by the method of Als–Nielsen & McMorrow [12]. Thus:

$$M = B_T \left(\frac{\sin\theta}{\lambda}\right)^2 \tag{4.22}$$

$$B_T[\mathring{\mathbf{A}}^2] = \frac{11,492\ T[K]}{A\,\Theta^2[K^2]} \cdot \phi(\Theta/T) + \frac{2,873}{A\,\Theta[K]} \tag{4.23}$$

$$\phi(x) = \frac{1}{x} \int_0^x \frac{\xi}{e^\xi - 1} d\xi \tag{4.24}$$

where λ is the wavelength, θ is the scattering angle, T is the temperature (in Kelvin), A is the atomic weight (A_{Al}=27.0, and A_{Cu}=63.5), Θ is the Debye temperature (Θ_{Al}=394 K, Θ_{Cu}=343 K [112]), and $x = \Theta/T$.

The scattering factors at 25°C (298 K) were respectively found to be f_{Al}=7.9, and f_{Cu}=20.0. The lattice parameters are respectively a_{Al}=4.05 Å, a_{Cu}=3.61 Å [112], which directly gives the volumes of the respective unit cells $v^{u.c.}_{Al}$=(4.05 Å)^3 and $v^{u.c.}_{Cu}$=(3.61 Å)^3. Lastly, the wavelength was λ=0.2442 Å, which gave the respective Bragg angles (see eq. 4.1): θ_{Al}=3.46°, and θ_{Cu}=3.88°. Entering all the above parameter values into equation 4.19, we obtain an

equation for the minimum detectable scattering *copper* volume $\delta V'_{min}$ at 25°C:

$$\begin{aligned}
\delta V'_{min} &= \frac{\Delta\omega\, t}{4}\,\frac{I_{min}}{I_p\{200\}}\,V_{foil}\,m_{200}\,\frac{f_{Al}^2}{f_{Cu}^2}\,\frac{(v_{Cu}^{u.c.})^2}{(v_{Al}^{u.c.})^2}\,\frac{\sin 2\theta_s\,|\sin\eta_s|}{\cos^2\psi_s\,\sin\theta_p\,\sin 2\theta_p} \qquad (4.25)\\
&= \frac{\pi}{720}\,\frac{400\,\mathrm{phot/sec}}{18.4\cdot 10^6\,\mathrm{phot/sec}}\,(49\times 49\times 53\,\mu m^3)\cdot 6\left(\frac{7.9}{20.0}\right)^2\left(\frac{3.61\,\text{Å}}{4.05\,\text{Å}}\right)^6\\
&\qquad\times\ \frac{\sin(2\cdot 3.88^\circ)\,|\sin(90^\circ)|}{\cos^2((2\cdot 3.88^\circ)\sin(90^\circ))\,\sin(3.46^\circ)\,\sin(2\cdot 3.46^\circ)}\\
&= 0.107\,\mu m^3
\end{aligned}$$

For equation 4.25 to yield the correct value in any situation, three corrections must be applied to the volume determined from the integrated intensity: Firstly, there may be a change in the synchrotron ring current I_{SC}, to which the X–beam flux is proportional: $I = I_0 \times (I_{SC}/I_{SC,0})$, where $I_{SC,0}$=77.2164 mA is the reference current.
Secondly, the Debye-Waller factor in the atomic scattering factor decreases with increasing temperature: $f(T) = f(T_0) \times (e^{-M(T)}/e^{-M(T_0)})$, where $M(T)$ is given by eq. 4.22, and T_0=25°C and T=290°C are respectively the cold and hot experimental temperatures.
Thirdly, the diffracted beam is attenuated as it travels the distance x through the sample, which is approximately equal to the sample thickness, and the attenuation is: $I_{Cu} = I_{Al} \times (e^{-\mu_{Cu}x_{Cu}}/e^{-\mu_{Al}x_{Al}})$, where the linear attenuation lengths are μ_{Al}=0.09 mm^{-1} and μ_{Cu}=2.31 mm^{-1} at E≈50 keV [58], and the sample thicknesses are x_{Al}=53 μm and x_{Cu}=300 μm.
We may correct for these three effects, by scaling the volume determined from eq. 4.25 correspondingly with the parameters given above (see eq. 4.26):

$$\delta V_{min} = \delta V'_{min}\,\frac{I_{SC,0}}{I_{SC,M}}\left(\frac{e^{-M(T_0)}}{e^{-M(T)}}\right)^2\frac{e^{-\mu_{Al}x_{Al}}}{e^{-\mu_{Cu}x_{Cu}}} = \begin{cases} 0.183\,\mu m^3 & \text{at } 25^\circ\mathrm{C}\\ 0.223\,\mu m^3 & \text{at } 290^\circ\mathrm{C}\end{cases} \qquad (4.26)$$

where the maximum synchrotron ring current $I_{SC,M}$=90 mA has been used. Please note, that there exists a 'cold' and a 'hot' value for δV_{min}, but to simplify things δV_{min} is defined to be at 25°C.

Using δV_{min} and I_{min}, we may scale the intensity of any given copper {hkl}–reflection, with scattering angle θ' and azimuthal angle η', to a volume:

$$V = \delta V_{min} \frac{I}{I_{min}} \frac{\cos^2(2\theta' \sin\eta')}{\cos^2(2\theta)} \frac{\sin(2\theta)}{\sin(2\theta')|\sin\eta'|} \frac{I_{SC,M}}{I_{SC}} \left(\frac{e^{-M(T_0)}}{e^{-M(T)}} \right)^2 \quad (4.27)$$

The structure factor for all non–vanishing reflections from an *fcc*–lattice is $F^{u.c.}=4 \cdot f_{atom}$, so no extra term is needed.

Due to the large point spread function of the Frelon detector (see section 4.1.4), it is not possible to determine the shape of the nucleus. However, based on the volume of the nucleus, we may define an *equivalent circle diameter* (ECD), which is the diameter of a spherically shaped nucleus of volume V. Here the diameter is used, because this is what is measured with other microscopy techniques. Thus:

$$ECD = 2 \times \left[\left(\frac{3}{4\pi} \right) V \right]^{1/3} \implies \quad (4.28)$$

$$ECD_{min} = \begin{cases} 0.70\,\mu m & \text{at } 25^\circ\text{C} \\ 0.75\,\mu m & \text{at } 290^\circ\text{C} \end{cases} \quad (4.29)$$

which gives the smallest length that can be detected within the microstructure, and ECD_{min} is therefore defined as the *detection limit* of the experiment.

For sample B, the characterization of the deformed microstructure was performed with a lower detection limit. This was achieved by decreasing the sample rotation rate to $\Delta\omega$=0.5°s^{-1}, and increasing the integration interval to t=15 seconds. Assuming Poisson statistics, where the noise level is equal to $\sim\sqrt{I}$, this gave an increase in volume resolution of $\times\sqrt{30} \approx \times 5.5$. Thus giving a minimum detectable volume of δV_{min}=0.033 μm^3, which is equal to ECD_{min}=0.40 μm.

An important observation to make is that even at the highest volume detection limit of the experiment (i.e., $I_{SC}\approx$62 mA and T=290°C), $ECD_{min}\approx$0.85 μm was still smaller than the size of the smallest subgrains observed in the deformed microstructure (see section 4.2.2.3). We may therefore conclude that, at no time during the experiment were we unable to detect the volume of the smallest subgrains.

4.2.3.3 Identifying nuclei

This was the single biggest challenge of the experiment, and was by no means a guarantied success. Sections 4.2.1 and 4.2.2 described all the steps taken to improve the chances of observing nuclei in their early stages of growth. Due to the high intensity of the large reflections from the deformed parent grains, any diffraction spots originating from the nuclei within the *central* regions of the poles will not be detectable. Only intense diffraction spots on the tails of the poles, or completely removed from them will be detectable (see fig. 4.17).

In practice, finding the diffraction spots originating from a nucleus is very much a "needle–in–the–haystack" problem. As of yet, no automatic method has been developed, which would be 100% certain of finding all nuclei in the diffraction images. The solution was to manually inspect each diffraction image for spots, which could be diffraction spots originating from a nucleus, Unlike the deformed/recovered parent grains, the nuclei exhibit only very limited mosaic spread, and the diffraction from the nuclei appear as distinct spots, as opposed to the broad reflections originating from the deformed grains. During data acquisition, the diffraction images were continually monitored on the computer screen in order to detect the nuclei during the *in situ* annealing. This was of course also done post–experiment.

During the *in situ* annealing of sample A, one nucleus was identified. This allowed us to follow the growth kinetics of the nucleus (see section 4.2.3.7). No nuclei were identified in sample B during annealing or the post–experiment data analysis. However, one important detail was gleaned from the images obtained from the deformed state of this sample — no reflections were observed outside the large poles, even with a detection limit of ECD_{min}=0.40 μm. No nuclei were identified in sample C during annealing, but two nuclei were identified in the post–experiment data analysis.

4.2.3.4 Determining the exact position of the nuclei

Determining the 3 dimensional positions of the nuclei was of high importance, since it was critical to the following discussion of the results, whether the nucleation events had occurred in the sample bulk or at the surface. The (x, y, z)–directions can be seen on figure 4.11, and the coordinate values are defined as follows: x is zero at the sample surface struck by the X–ray beam; and the (y, z)–coordinates are set equal to their corresponding motor positions. Positions are given in mm, and (y, z) are accurate to within 0.001 mm.

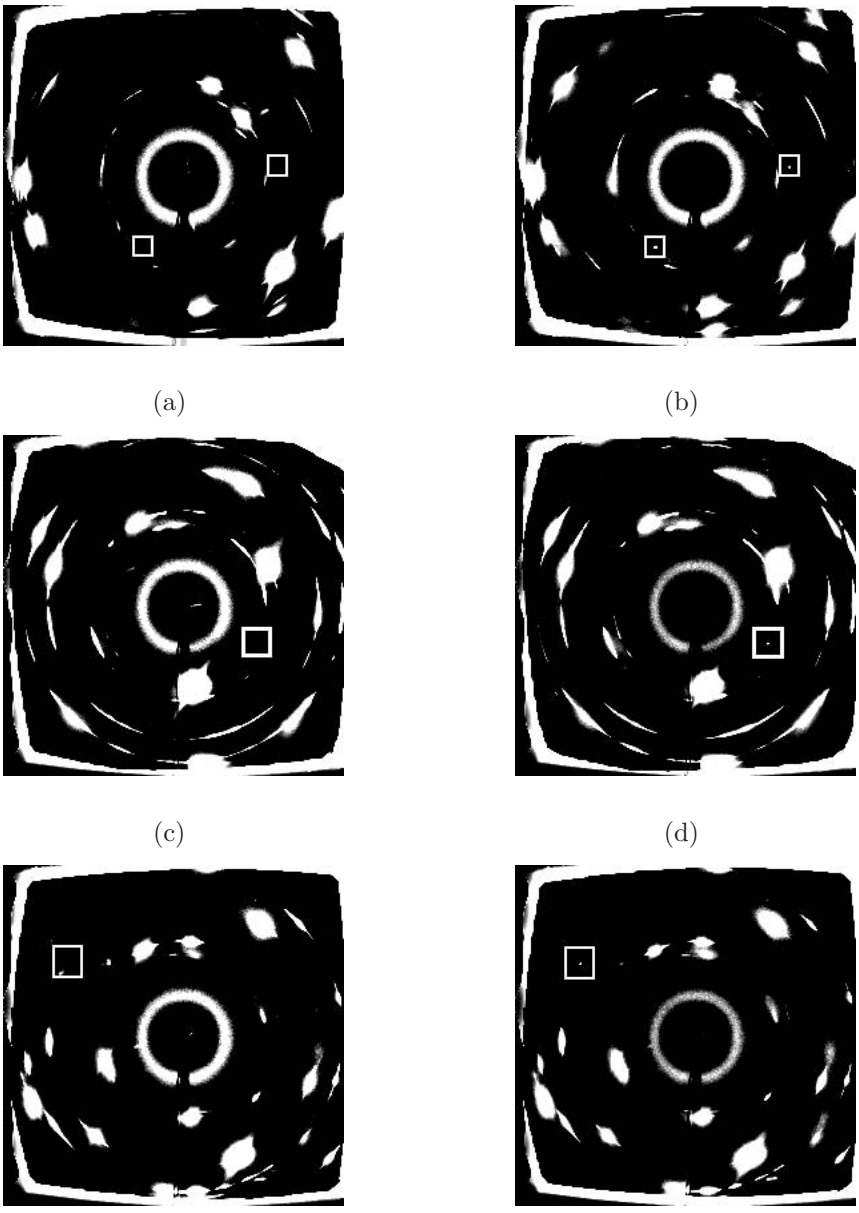

(a) (b)

(c) (d)

(e) (f)

Figure 4.17: *Nuclei detected in the diffraction images. The nuclei reflection appeared within the white squares (intensity≥400):* ***(a)&(b)*** *nucleus 1 — the deformed and annealed sample;* ***(c)&(d)*** *nucleus 2 — the deformed and annealed sample;* ***(e)&(f)*** *nucleus 3 — the deformed and annealed sample.*

Here we have to distinguish between the two different degrees of available experimental information. The nucleus in sample A was identified *during* the experiment, which allowed a much more precise determination of its position, whereas the two nuclei in sample C were identified during the post–experiment data analysis (see section 4.2.3.3), and no special effort could be made to determine their positions.

Nucleus in sample A

In the case of sample A, a nucleus (called nucleus 1) was located during the annealing part of the experiment, and it was therefore possible to perform a *superscan* (see below) in the y, z, and ω–directions to determine it's exact location in these directions, after the sample had been quenched back down to room temperature.

A superscan consists of defining an area of interest (AI) in Image Pro around a reflection with little or no mosaic spread, and scanning the intensity of the AI in small steps between two motor positions for one motor at a time, which allows the centre–of–mass (CMS) position of a grain to be determined for the motors scanned (i.e., y, z, and ω). During superscans, the slits are generally narrowed to increase precision, so that the beam size is ideally smaller than or at least comparable with the size of the grain being scanned.

By performing superscans on two different reflections, their (y, z)–positions as well as their ω–angles are determined. With these sets of coordinates, it is possible to perform a triangulation in the (x, y)–plane to determine the distance from the nucleus to the centre–thickness of the sample, which is 150 μm from the surface, and whether it in front of or behind the centre line. This, in turn, yields the 3 dimensional position of the nucleus. The triangulation geometry is visualized on figure 4.18, and based on this, the following equation can be used to determine the maximum distance R from the nucleus to the sample centre–thickness in the (x,y)–plane:

$$\begin{aligned} |y_2 - y_1| &= |R\sin\omega_2 - R\sin\omega_1| \iff \\ R &= \left|\frac{y_2 - y_1}{\sin\omega_2 - \sin\omega_1}\right| \end{aligned} \tag{4.30}$$

where R (defined to be positive) is the nucleus–to–centre thickness distance.

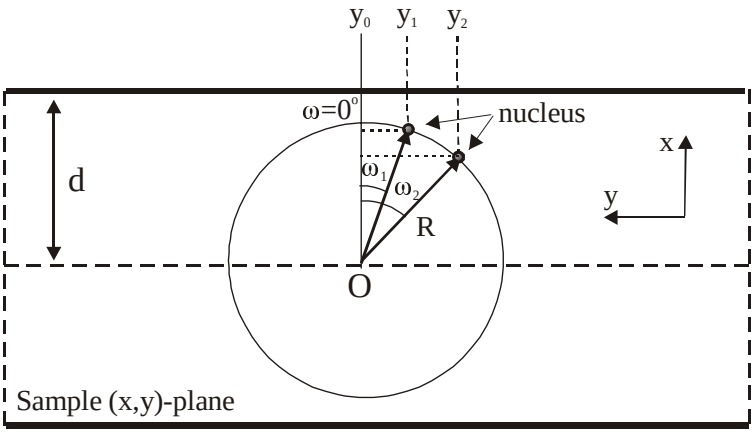

Figure 4.18: *Sample A nucleus location triangulation geometry in the (x,y)–plane of the sample: y_0, y_1, and y_2 are the y–coordinates of the nucleus, and 0°, ω_1, and ω_2 are the corresponding ω–angles. d is the half–thickness of the sample, O is the x-coordinate of the half–thickness, and R is the distance from the nucleus to O in the (x, y)–plane.*

Nuclei in sample C

The two nuclei in sample C (called nucleus 2 and nucleus 3) were identified post–experiment, and it was therefore *not* possible to perform superscans on them to determine their precise (x, y, z)–positions within the sample. Their positions must instead be inferred from the grid area, where they gave rise to diffraction spots, and the maximum distance the nuclei can have to the sample centre–thickness in order to still give rise to the *observed* reflections. We may therefore confine the (y, z)–position of the nuclei within a grid area (40×40 μm^2) on the sample surface, and the x–position within a distance R from the centre–thickness. However, due to the fact that the actual beam size (49×49 μm^2) used in the experiment was *accidentally* larger than the grid areas (40×40 μm^2), the nuclei in sample C gave rise to reflections in diffraction images from more than one grid area. The grid areas, where the nuclei were located, were taken to be the ones, where the integrated intensity of the reflections from the nuclei were highest.

The triangulation from sample A was not possible, but there is an alternative method of determining whether the nuclei nucleated in the sample bulk or at the surface. Since every observed reflection from the nuclei originated from within the volume illuminated by the X–ray beam, we can use the rota-

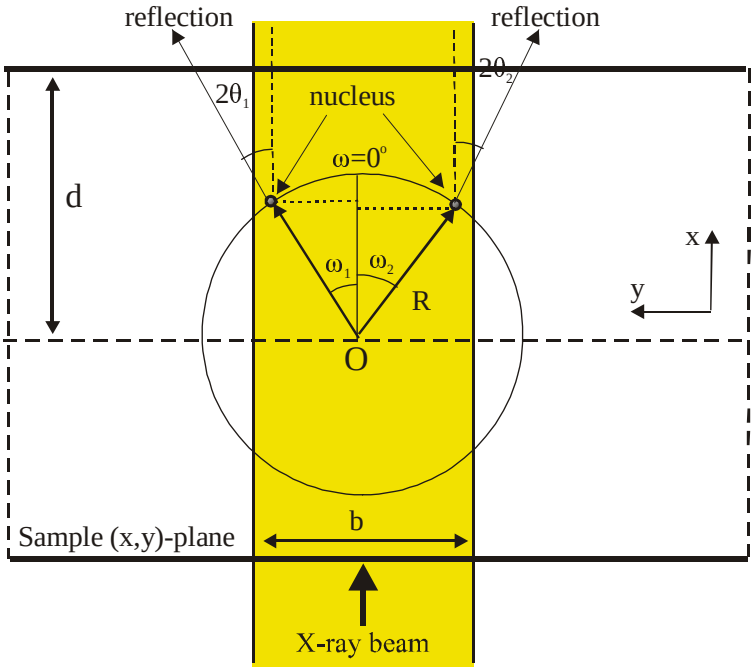

Figure 4.19: *Sample C nucleus location triangulation geometry in the (x,y)–plane of the sample: ω_1 and ω_2 are respectively the maximum negative and positive ω–values ($\omega \in [-20°, 21°]$), which give rise to observed reflections.*

tion angle between reflections to calculate the *maximum* distance R, which the nucleus may be from the centre–thickness in the (x, y)–plane in order for it not to rotate out of the X–ray beam when the sample is rotated. When the ω–values of the outermost reflections are known, the y–offset they represent may be used to calculate the maximum distance R, which the nucleus can be from the sample centre–thickness (see figure 4.19):

$$\begin{aligned} b &< |R\sin\omega_1| + |R\sin\omega_2| \iff \\ R &< \frac{b}{|\sin\omega_1| + |\sin\omega_2|} \end{aligned} \tag{4.31}$$

where b=49 μm is the horizontal width of the X–ray beam, R is the maximum distance from the centre–thickness, and ω_1 and ω_2 are respectively the maximum (negative and positive) ω–values, which give rise to *observed* reflections.

4.2.3.5 Determining the crystal orientations of the nuclei

The crystallographic orientations of the nuclei were determined using GRAINDEX, which is an in–house general–purpose multi–grain indexing routine for powder and polycrystalline samples [94], running on the Windows platform. It utilizes the commercial software *Image Pro Plus* for visualization and some image analysis tasks. Especially the 'Spot Finder', where individual diffraction spots are identified on the diffraction images, is used. In order to utilize only real diffraction spots, the minimum accepted intensity, the min/max accepted spot size, and the maximum accepted (y, z) aspect–ratio of a spot must be defined.

By rotating the sample around its vertical axis and recording diffraction images on a 2D detector at several ω–values (typically one image per 1° rotation), it is possible to locate several reflections from each grain, and using GRAINDEX, the individual crystal orientations of up to 5,000 bulk grains within a sample may be determined from the same data set. GRAINDEX works by assigning Miller indices (hkl) to the identified reflections, and fitting them to different crystal orientations, i.e., different grains. It is assumed that the crystal structural type (eg. *fcc*), such as may be determined by powder diffraction, is known prior to using GRAINDEX.

The accuracy of this indexing is dependant on the size of the ω–range, within which the diffraction images were obtained, and it is also *very* dependent on how much the sample has been deformed. This is because the mosaic spread of the grains increases with increasing deformation, and quickly leads to the diffraction spots from different grains overlapping for even moderate plastic deformation (10+%) [67]. However, for an *undeformed* powder sample, the data was good enough to allow Schmidt *et al.* to successfully perform structural refinement on a single Al_2O_3–grain [67].

The orientations of nucleus 1 and nucleus 2–3 were determined from respectfully ω–ranges of $\omega \in [-45°, 46°]$ and $\omega \in [-20°, 21°]$ with $\Delta\omega$=1°. For all nuclei, some of the expected reflections were hidden behind the poles, but where this was not the case, it was possible to locate the reflections from the nucleus with the GRAINDEX 'spot finder', using the following settings: the minimum accepted diffraction spot intensity was 600 counts (ignores noise); the maximum diffraction spot area was 500 pixels (ignores the large reflections from the parent grains); and the maximum diffraction spot aspect–ratio was 2 (the nucleus reflections were generally circular in shape).

4.2.3.6 Nucleus–to–parent grain orientation relationships

The reflections of the deformed grains all had a mosaic spread in the range of ±5–20° on either side of a diffraction peak (measured in the azimuthal direction). Calculating the misorientation between the orientation of a given nucleus, and the mean orientation of the grains in the deformed microstructure, was therefore not sufficient to prove whether the nucleus emerged with an orientation previously present in the deformed microstructure, a 1st order twin orientation of an orientation in the microstructure, or a new orientation entirely.

Consideration was given to generating orientation distribution functions (ODFs) for the deformed microstructure, as is possible from 3 pole figures (see appendix B.2), and plotting the orientations of the nuclei into the ODFs for a direct comparison. Unfortunately, this was impossible due to the saturation of the poles in the diffraction images, so another way of comparing the orientations of the nuclei and those of the deformed microstructure had to be envisaged.

Using pole figures was also considered (see appendix B.1), but was rejected as being too inaccurate. Pole figures, however, are a very good way of showing the orientations. Figures 4.24–4.26 show the orientations of a nucleus and its 1st order twins superimposed on the orientations present in the deformed microstructure. The pole figures were obtained by first using FIT2D to extract the azimuthal variations in intensity (intensity vs. η–angle) for the {111}, {200}, and {220} Debye–Scherrer rings for every diffraction image obtained from the deformed microstructure. The pole figures were then calculated by the method of Mishin *et al.* [113].

The chosen method of comparing the orientations of the nuclei with their possible parent orientations was to simulate the diffraction spots of the nuclei directly onto the diffraction images recorded from the deformed microstructure before annealing. On figure 4.20 the methodology of the simulation can be seen, as well as examples of spots lying within and outside the orientation spread of the deformed microstructure. The procedure was to run through the diffraction images obtained from the full ω–interval obtained from the deformed sample one orientation at a time, i.e., one time for the nucleus orientation, and one time for each of its four 1st order twin orientations. In order for an orientation to lie within the orientations of the deformed microstructure, no simulated diffraction spots for a given nucleus or twin orientation were allowed to lie outside the poles of the deformed grains in the diffraction images.

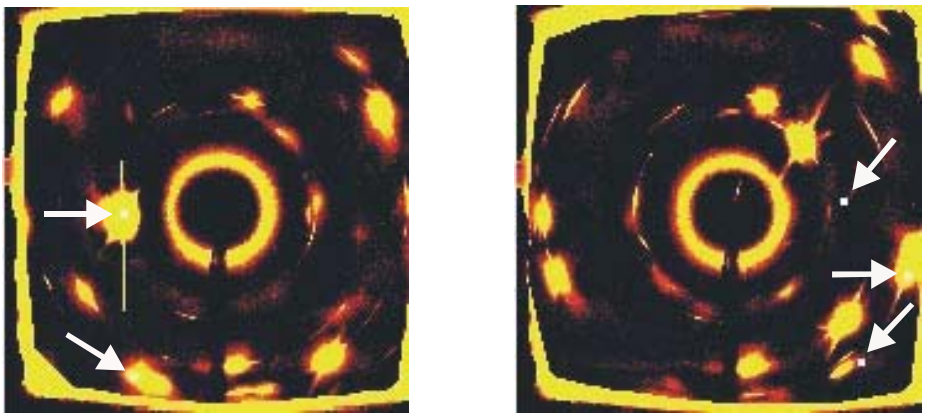

(a) (b)

Figure 4.20: *Diffraction spots simulated and plotted on images from the deformed microstructure. The diffraction image is colour scaled to intensity (black to yellow), and the white squares (indicated by arrows) are the simulated diffraction spots:* ***(a)*** *orientation* within *the poles of the deformed grains;* ***(b)*** *orientation* not within *the poles of the deformed grains.*

4.2.3.7 Growth kinetics of the nuclei

By following the intensity of the diffraction spots arising from a nucleus as a function of annealing time it is possible to follow its growth. This was possible for nucleus 1 and nucleus 2, where a suitable diffraction spot was found at all intermediate annealing time steps. No diffraction spots were obtained from nucleus 3 at intermediate annealing times. For nucleus 1 and nucleus 2, the volume was determined from respectively a (002) and $(\bar{1}1\bar{1})$–reflection at the latest available annealing time step using equation 4.27.

At each time step, the intensity of the chosen reflection was determined by integrating the intensity within an area–of–interest (AI) centered on the reflection, and subtracting the background not due to the reflection. This was determined by integrating the intensity within an identical AI on four sides of the central AI, and the mean of these was defined to be the background.

Instead of applying equation 4.27 to find the size of the nuclei at every time step, the intensity of the reflection relative to the reference intensity (see above) was used to determine the size of the nucleus at all earlier time steps.

This was done because the intensity at the latest time step was considered less effected by whatever fluctuations might affect the integrated intensity of the reflection.

Estimating the uncertainties on the derived ECD was difficult since the intensities of the different reflections arising from the same nucleus could vary by nearly a factor 3. However, for the most intense reflections, the maximum error in the intensities is thought to be about a factor 2. Error bars have on purpose not been drawn on the nucleus growth curves in figure 4.23a–b, as their size would at best be quite arbitrary.

Nucleus 1

This nucleus was identified in sample A, where a time resolution of ≈6 minutes was obtained. Note that, because the sample edges of the hot specimen had to be realigned in situ *during* annealing, data was not acquired at early annealing times. The first exposure obtained during annealing was at 28.4 minutes after the annealing temperature had been reached.

Figures 4.21a–f show the evolution of the nucleus 1 (002)–reflection as a function of annealing time. Good intense diffraction spots were obtained throughout the dynamic study from the white square indicated on figure 4.12, and the integrated intensities of the diffraction spots were scaled directly with that obtained from the same diffraction spot in the GRAINDEX scan, where the nucleus was centered in the X–ray beam (see section 4.2.3.5).

We were able to follow the growth of the nucleus for a full additional hour. There was however considerable sample drift, which caused the nucleus to drift nearly completely out of the X–ray beam, so that only a very week signal was obtained from the otherwise intense (002)–reflection for the first 35–40 minutes. It was therefore not possible to reliably determine the integrated intensity of (002)–reflection, past the first annealing step, without making a considerable number of assumptions. It was therefore chosen to omit the additional data from the nucleus 1 kinetics curve (see figure 4.23a). However, for reasons of interest, the last recorded image of the reflection (after 106.5 minutes of annealing) has been included in figure 4.21 as figure 4.21f.

Nucleus 2

During annealing of sample C, only the red 2×2–grid shown on figure 4.14 was characterized, so as to improve the time resolution by a factor of four (≈8.5 minutes), but because the area (and possible tails) of the X–ray beam extended from the top left red grid area into the top white grid area, where

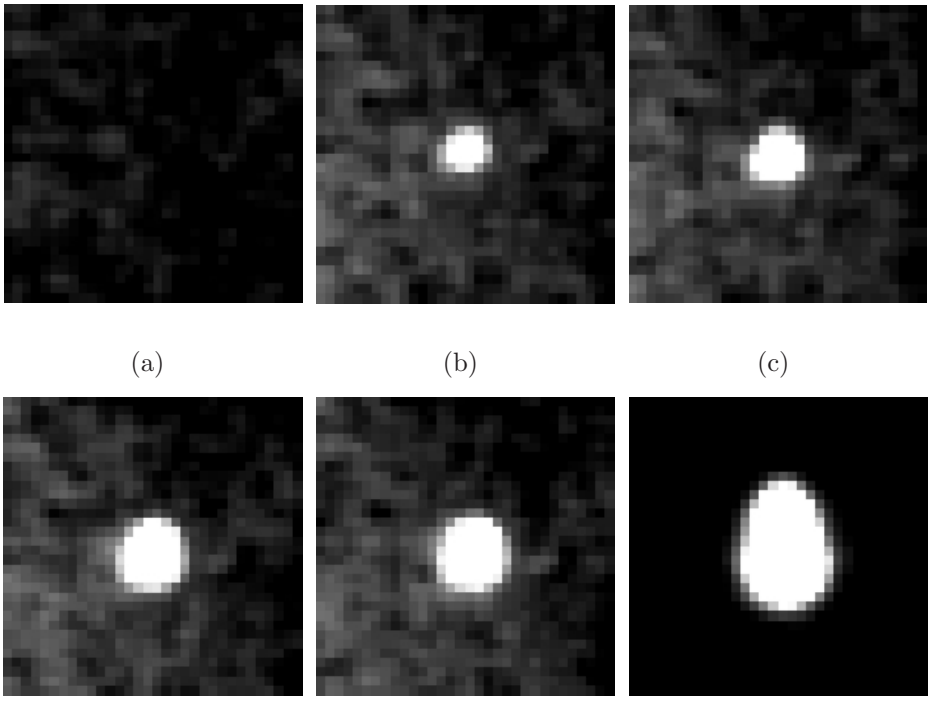

Figure 4.21: *Evolution of the nucleus 1* (002)*–reflection with annealing time:* ***(a)*** *0 min;* ***(b)*** *28.4 min;* ***(c)*** *34.1 min;* ***(d)*** *38.7 min;* ***(e)*** *43.3 min;* ***(f)*** *106.5 min.*

nucleus 2 was located, the nucleus also gave rise to (weak) diffraction spots in the top left red grid area.

Figures 4.22a–f show the time evolution of the nucleus 2 ($\bar{1}1\bar{1}$)–reflection as a function of annealing time. That we actually have dynamic data for this nucleus is due to the X–ray beam vs. grid area mismatch, which was described in the sample C–part of section 4.2.3.4. As can be seen from the images the contrast between the nucleus reflection and the surrounding background was minimal, and of the same order of magnitude.

It was therefore chosen not to use the full integrated intensity of the single usable reflection, which was found to fluctuate considerably. Rather, for the reflection, the highest measured single–pixel intensity was used to

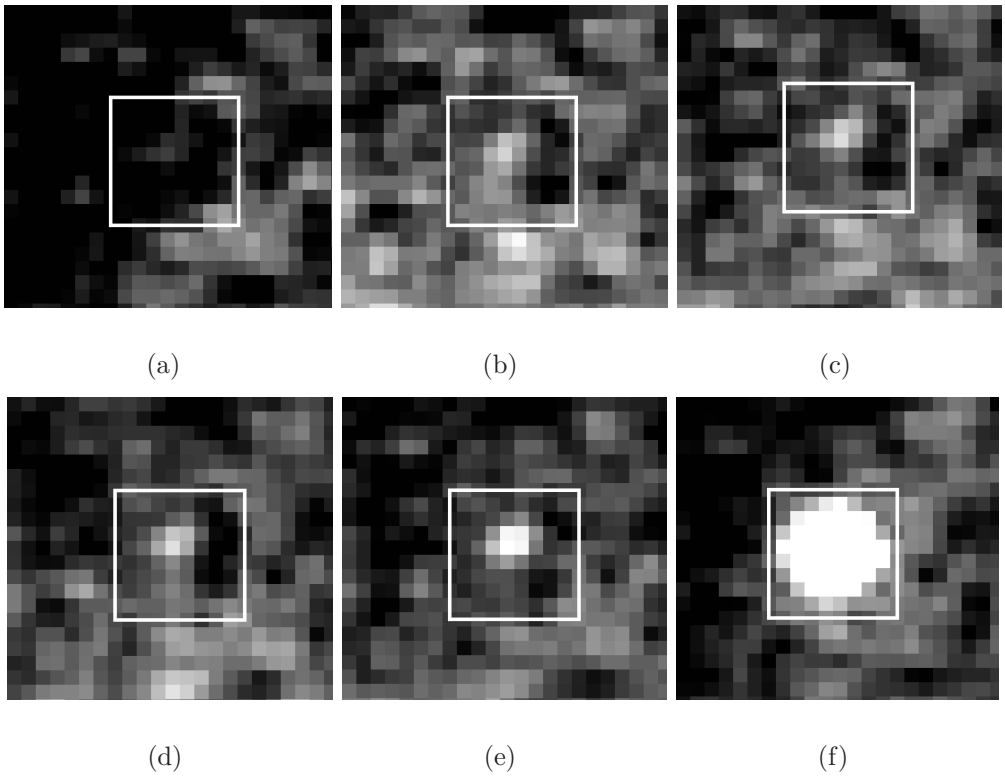

Figure 4.22: *Evolution of the nucleus 2* $(\bar{1}1\bar{1})$*–reflection with annealing time:* ***(a)*** *0 min;* ***(b)*** *2.5 min;* ***(c)*** *72 min;* ***(d)*** *124.5 min;* ***(e)*** *167.8 min;* ***(f)*** *180 min. Note that images* ***(a)*** *and* ***(f)*** *are obtained from the top* white *grid area, and* ***(b)–(e)*** *are obtained from the top left* red *grid area in figure 4.14.*

assign a size to the nucleus. This maximum pixel intensity was then scaled to the maximum pixel intensity observed in the same reflection in the white grid area, giving a rough intensity conversion factor for the maximum pixel intensity in the red and white grid areas ($I_{white} \approx 40 \cdot I_{red}$). The integrated intensity of the reflection could be reliably determined in the white grid area, and this was then scaled to the maximum pixel intensity. Thus, the maximum pixel intensity of the reflection in the red grid area was scaled linearly to an integrated intensity through the conversion factor. The resulting "integrated intensities", which were of course corrected for changes in the synchrotron ring current, were then be converted into volumes using equation 4.27.

4.3 Results

In this section we will focus on the results obtained from the 3DXRD nucleation experiment. Three samples were investigated, and to summarize the results: three nuclei were identified (one in sample A, and two in sample C), all of which were located within the bulk; the crystal orientations of the nuclei were determined, and compared to the parent microstructure; and lastly, growth curves were determined for two of the nuclei (see figure 4.23).

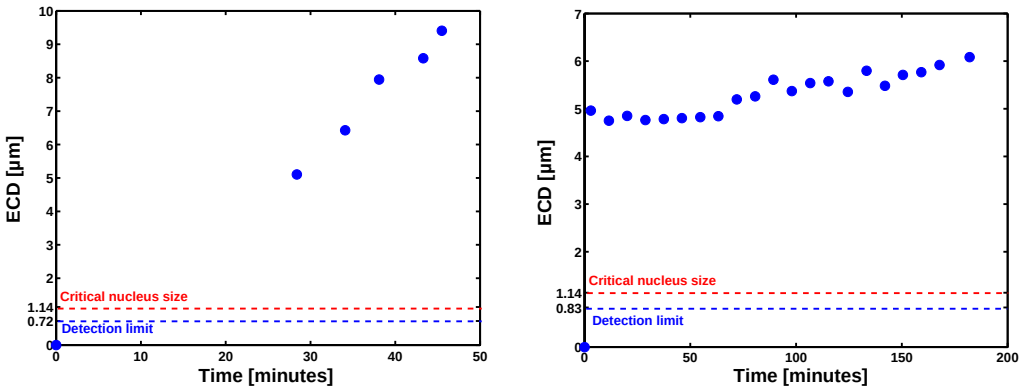

(a) (b)

Figure 4.23: *Nucleus growth curves. The equivalent circle diameter (ECD) of the nuclei are plotted as a function of annealing time. The annealing temperature was 290° C, and all values above ECD>0 were scaled from the intensity of an intense reference reflection:* ***(a)*** *nucleus 1;* ***(b)*** *nucleus 2.*
At t=0, the ECD of both nuclei was smaller than the detection limit (∼0.70 µm), and are plotted as ECD=0 µm. No error bars have been plotted on the growth curves for reasons discussed in section 4.2.3.7.

This section is divided into a subsection for the results obtained from each nucleus, and all begin with a short summary of the results obtained from that specific nucleus.

4.3.1 Nucleus 1

The (x, y, z)–position of nucleus 1 within the bulk of the sample was determined. The crystal orientation of this nucleus corresponded to a 1st order twin orientation of one of the deformed grains. Lastly, a growth curve was obtained for the nucleus, following its ECD from 5.1–9.4 μm during an annealing time space of 28.4–45.5 minutes (see fig. 4.23a).

The (x, y, z)–position of nucleus 1 was determined by the method detailed for sample A in section 4.2.3.4. From superscans, the CMS–positions of two $\{200\}$–reflections were found to be at ω_1=2.87° and ω_2=10.51°, and these were found to have respectively the following (y, z)–coordinates:

(y_1, z_1)=(0.803 mm, 137.460 mm) & (y_2, z_2)=(0.792 mm, 137.458 mm)

By inserting these coordinates into eq. 4.30, the distance from the nucleus to the centre–thickness in the (x, y)–plane is determined to be 83 μm, and because $\Delta y = y_2 - y_1$ is negative, it was also determined that the position is to the right of ω=0°, and therefore that it lies after the sample centre–thickness (see fig. 4.18). Since the sample centre–thickness is 150 μm from the surface in the x–direction, the nucleus was therefore located 150–83 μm=67 μm from the sample surface, thus making it a *bulk* nucleus.

The (x,y,z)–position of the nucleus was (0.233 mm, 0.799 mm, 137.456 mm), with negligible uncertainty, and from the EBSP study, the surface position of the triple junction was (y, z)=(0.769 mm, 137.460 mm). When determining the distance from the triple junction in the (y, z)–plane, we must take the EBSP step size of 20 μm into account, which infers an uncertainty of $\pm$10 μm on the (y, z)–position of the triple junction in the (y, z)–plane, giving an overall uncertainty of $\pm$14 μm. The nucleus was thus located 20$\pm$14 μm from the (y, z)–surface location of the triple junction in the (y, z)–plane.

From the set of diffraction images within an angular range of $\omega \in$[-45°,46°], an orientation was fitted to the experimental diffraction spots using GRAINDEX. The χ^2 of the least–squares fit was 0.24, and the completeness was 0.63, which corresponds to the successful indexing of 17 out of 27 expected reflections. The 10 missing reflections were all expected in areas covered by the poles of the deformed grains, and the fit was therefore considered to be a good representation of the orientation of the nucleus.

The orientation of the nucleus was found to be:

$$\mathbf{U}(\text{nucleus 1}) = \begin{bmatrix} 0.767 & -0.629 & -0.124 \\ -0.031 & 0.157 & -0.987 \\ 0.641 & 0.761 & 0.101 \end{bmatrix} \tag{4.32}$$

which is 41° from the 'cube', and 35° from the 'rolling' texture components (see appendix B for details).

By using the diffraction spot simulation routine described in section 4.2.3.6, the orientation of the nucleus was found to correspond to a 1st order twin orientation of one of the deformed grains, i.e., that the embryo nucleated with the orientation of one of the deformed grains, and subsequently twinned during its early growth. Before twinning, the orientation of the nucleus was:

$$\hat{\mathbf{U}}([1\bar{1}\bar{1}], -60°) = \begin{bmatrix} 0.384 & -0.890 & -0.246 \\ 0.690 & 0.454 & -0.564 \\ 0.641 & 0.047 & 0.788 \end{bmatrix} \tag{4.33}$$

where the crystal lattice of the nucleus is rotated -60° around the $[1\bar{1}\bar{1}]$–axis.

The centre–of–mass (CMS) orientation of the deformed grains was determined from the images of the recovered microstructure ($\omega \in [-45°, 46°]$) using GRAINDEX. Three individual grain CMS–orientations were identified with a completeness varying between 0.52 and 0.92. The CMS–orientation of the deformed nucleus–parent grain was:

$$\mathbf{U}(\text{parent grain}) = \begin{bmatrix} -0.231 & 0.390 & -0.891 \\ -0.560 & 0.695 & 0.450 \\ 0.795 & 0.604 & 0.058 \end{bmatrix} \tag{4.34}$$

By comparing the fitted orientation of the nucleus with the CMS–orientation of the deformed parent grain, it was determined that the pre–twinning nucleus was misoriented by 38° from the CMS–orientation of the grain.

On figure 4.24, the orientations of nucleus 1 and its 1st order twins are superimposed onto the {111}, {200}, and {220}–pole figures of the annealed (not deformed) microstructure. Note that it was chosen to use the annealed (i.e., recovered), rather than the deformed microstructure, as this allowed the ω–range to be increased from [-10°,11°] to [-45°,46°], and thus much more complete pole figures could be displayed. That a 1st order twin orientation (◯) of the nucleus lies within a pole in each pole figure is still evident.

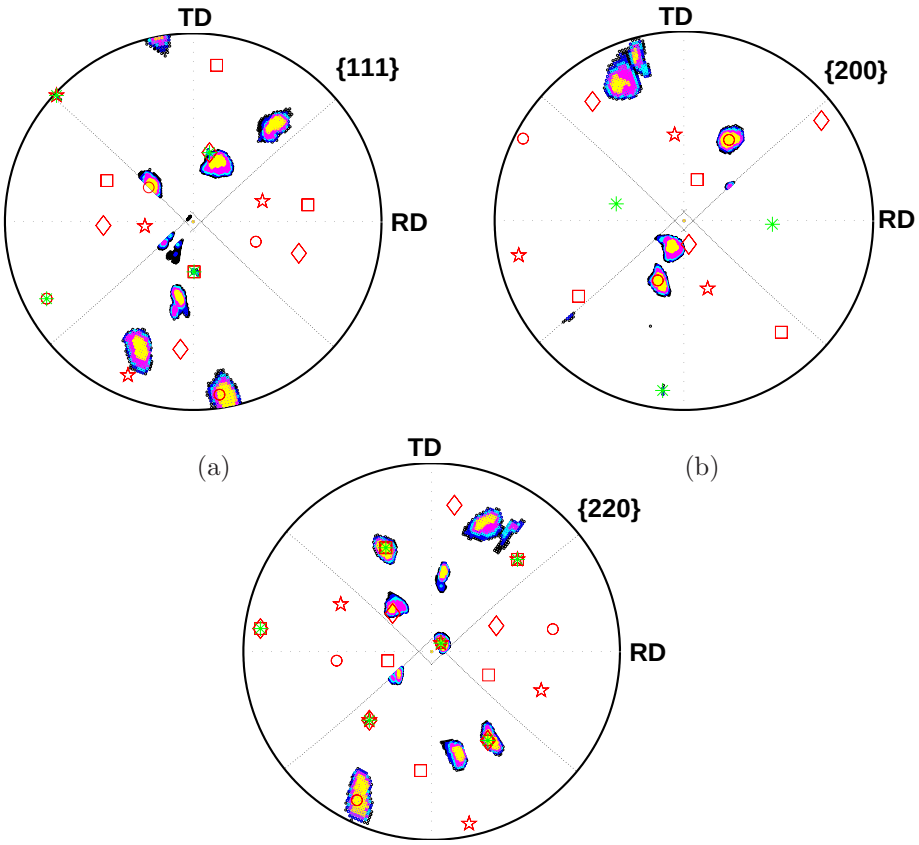

(a) (b) (c)

Figure 4.24: *Pole figures — nucleus 1 superimposed on the recovered microstructure. The green marker (✳) is the orientation of the nucleus, and the red markers (□, ◊, ◯, ★) are the 1st order twins of the nucleus orientation.*
*The ω–range was [-45°,46°], and the intensities are ordered by colour: [*black*=400,* blue*=1,000,* cyan*=2,500,* magenta*=5,000,* yellow*=10,000 counts]. Reflections used in the pole figures were:* ***(a)*** *{111};* ***(b)*** *{200}; and* ***(c)*** *{220}.*

4.3.2 Nucleus 2

Nucleus 2 was located within a specific volume in the *bulk* sized 40×40×164 μm. The crystal orientation of this nucleus *did not* correspond to the orientation of any of the deformed grains, nor a 1st order twin orientation of any of the deformed grains. Lastly, a growth curve was obtained for the nucleus, following its ECD from 4.8–6.1 μm during an annealing time space of 2.5–182.0 minutes (see fig. 4.23b).

The (y, z)–position of nucleus 2 was determined to be within the grid area, where the reflections had the highest intensity, which was the grid area centered at (y, z)=(0.716, 138.586). The maximum nucleus–to–centre–thickness distance was determined by the method detailed for sample C in section 4.2.3.3. The two outermost reflections, which were observed from nucleus 2, were at ω_1=-14°, and ω_2=21°, and by substitution into eq. 4.31 we find that R<82 μm, and thus that nucleus 2 is $150-82\,\mu m > 68\,\mu m$ from the sample surface. We may therefore conclude that nucleus 2 is a *bulk* nucleus.

The uncertainty on the (y, z)–position of the nucleus is set to half the grid node distance (±0.020 μm), and we may thus place nucleus 2 within the volume (0.150±0.082, 0.716±0.020, 138.586±0.020). In the (y, z)–plane, we have an uncertainty of ±14 μm on the position of the triple junction from section 4.3.1, and to this must be added the uncertainty ±28 μm on the position of the nucleus. In the (y, z)–plane, the nucleus was located 85±42 μm from the surface position of the triple junction.

From the set of diffraction images within an angular range of $\omega\in$[-20°,21°], an orientation was fitted to the experimental diffraction spots using GRAINDEX. The χ^2 of the fit was 0.15, and the completeness was 0.91, which corresponds to the successful indexing of 10 out of 11 expected diffraction spots, which is a very good fit of the nucleus orientation:

$$\mathbf{U}(\text{nucleus 2}) = \begin{bmatrix} -0.412 & 0.428 & 0.804 \\ 0.174 & -0.830 & 0.531 \\ 0.895 & 0.358 & 0.267 \end{bmatrix} \tag{4.35}$$

which is 40° from the 'cube', and 14° from the 'rolling' texture components.

When the diffraction spot simulation routine described in section 4.2.3.6 was utilized, the orientation of the nucleus was *neither* found to correspond to any of the deformed grains, or to a 1st order twin orientation of any of them. Nucleus 2 was therefore of special interest, because it exhibited a completely *new* orientation. Please note that twin–relations were not investigated to further than 1st order.

It was not possible to confidently determine the CMS–orientations of the deformed grains (or recovered grains for that matter) using GRAINDEX, due to considerable spot–overlap in the diffraction images, which yielded no less than 17 different individual grain orientations with completeness between 0.40 and 0.70. Of these orientations, no more than five could be discarded by manually inspecting the diffraction images.

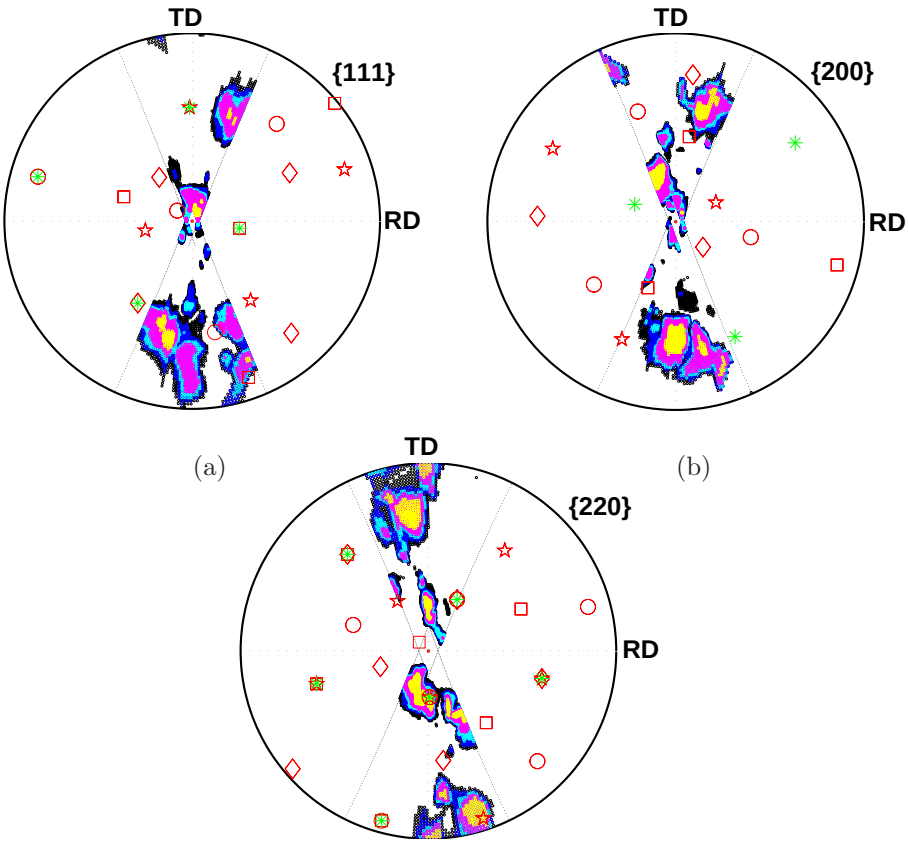

Figure 4.25: *Pole figures — nucleus 2 superimposed on the deformed microstructure. The green marker (✳) is the orientation of the nucleus, and the red markers (□, ◊, ◯, ★) are the 1st order twins of the nucleus orientation.*
*The ω–range was [-20°,21°], and the intensities were ordered by colour: [*black*=400,* blue*=1,000,* cyan*=2,500,* magenta*=5,000,* yellow*=10,000 counts]. Reflections used in the pole figures are:* ***(a)*** *{111};* ***(b)*** *{200}; and* ***(c)*** *{220}.*

On figure 4.25, the orientations of nucleus 2 and its 1st order twins are superimposed onto the {111}, {200}, and {220}–pole figures of the deformed microstructure. Note that for none of these orientations did all the reflections lie fully within the poles of the deformed grains.

4.3.3 Nucleus 3

Nucleus 3 was located within a specific volume in the *bulk* sized 40×40×164 μm. The crystal orientation of this nucleus corresponded to a 1st order twin orientation of one of the deformed grains. Lastly, its ECD was determined to 7.0 μm after 3.4 hours of annealing.

The (y, z)–position of nucleus 3 was determined to be within the grid area, where the reflections had the highest intensity, which was the grid area centered at (y, z)=(0.716, 138.706). The maximum nucleus–to–centre–thickness distance was determined by the method detailed for sample C in section 4.2.3.3. The two outermost reflections, which were observed from nucleus 3, were at ω_1=-20°, and ω_2=15°. By substitution into eq. 4.31 we find that R<82 μm, and thus that nucleus 3 is $150-82\,\mu m > 68\,\mu m$ from the sample surface. We may therefore conclude that nucleus 3 is a *bulk* nucleus.

The uncertainty in the (y, z)–position of the nucleus is set to half the grid node distance (±0.020 μm), and we may thus place nucleus 3 within the volume (0.150±0.082, 0.716±0.020, 138.706±0.020).
In the (y, z)–plane, we have from section 4.3.1, an uncertainty of ±14 μm on the position of the triple junction, and to this must be added the uncertainty ±28 μm on the position of the nucleus. In the (y, z)–plane, the nucleus was located 85±42 μm from the surface position of the triple junction.

From the set of diffraction images within an angular range of ω∈[-20°,21°], an orientation was fitted to the experimental diffraction spots using GRAINDEX. The χ^2 of the fit was 0.08, and the completeness was 0.53, which corresponds to the successful indexing of 8 out of 15 expected diffraction spots. 6 of the missing reflections were all expected in areas covered by the poles of the deformed grains, and the fit was therefore considered to be a good representation of the orientation of the nucleus.

$$\mathbf{U}(\text{nucleus 3}) = \begin{bmatrix} 0.955 & -0.236 & 0.181 \\ 0.223 & 0.167 & -0.960 \\ 0.196 & 0.957 & 0.212 \end{bmatrix} \tag{4.36}$$

which is 21° from the 'cube', and 26° from the 'rolling' texture components (see appendix B for details).

By using the diffraction spot simulation routine described in section 4.2.3.6, the orientation of the nucleus was found to correspond to a 1st order twin orientation of one of the deformed grains, i.e., that the embryo nucleated with the orientation of one of the deformed grains, and subsequently twinned during its early growth. Before twinning, the orientation of the nucleus was:

$$\hat{\mathbf{U}}([\bar{1}\bar{1}1], -60^\circ) = \begin{bmatrix} 0.595 & 0.540 & 0.596 \\ 0.733 & -0.060 & -0.677 \\ -0.330 & 0.839 & -0.431 \end{bmatrix} \tag{4.37}$$

where the crystal lattice of the nucleus is rotated -60° around the $[\bar{1}\bar{1}1]$–axis.

The centre–of–mass (CMS) orientations of the deformed grains were determined from the images of the recovered microstructure ($\omega \in [-20^\circ, 21^\circ]$) using GRAINDEX. Five individual grains were identified with completeness varying between 0.69 and 1.00. By utilizing the simulation routine, the nucleus orientation was found to originate from one of the grains, even though it was misoriented 32° from the CMS–orientation of the grain, which was:

$$\mathbf{U}(\text{parent grain}) = \begin{bmatrix} 0.572 & -0.597 & -0.563 \\ -0.070 & 0.685 & -0.722 \\ 0.779 & 0.506 & 0.371 \end{bmatrix} \tag{4.38}$$

On figure 4.26, the orientations of nucleus 3 and its 1st order twins are superimposed onto the {111}, {200}, and {220}–pole figures of the annealed (not deformed) microstructure. That a 1st order twin orientation (◊) of the nucleus lies within a pole in each pole figure is evident.

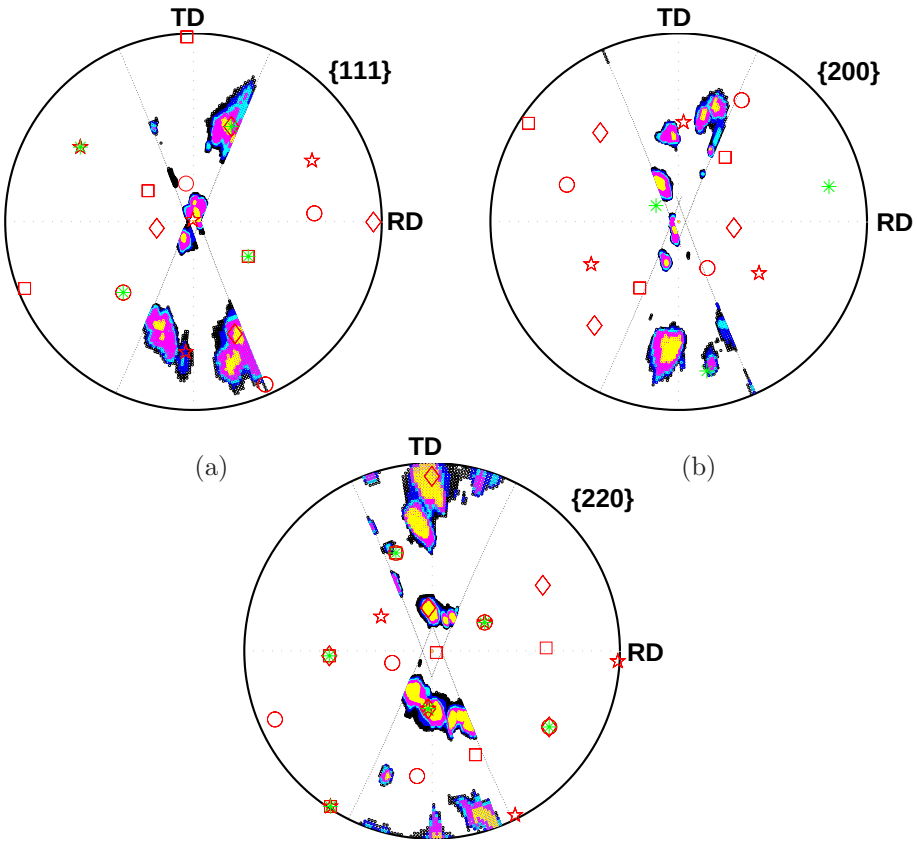

(a) (b) (c)

Figure 4.26: *Pole figures — nucleus 3 superimposed on the deformed microstructure. The green marker (✳) is the orientation of the nucleus, and the red markers (□, ◊, ◯, ★) are the 1st order twins of the nucleus orientation.*
*The ω–range was [-20°,21°], and the intensities were ordered by colour: [*black*=400,* blue*=1,000,* cyan*=2,500,* magenta*=5,000,* yellow*=10,000 counts]. Reflections used in the pole figures were:* ***(a)*** *{111};* ***(b)*** *{200}; and* ***(c)*** *{220}.*

4.4 Discussion and outlook

The main aim of the 3DXRD study was to investigate whether it was possible to relate the orientation of any identified nuclei with those orientations existing in the deformed microstructure at the nucleation site prior to annealing. The secondary aim was to investigate if the nuclei could be detected at the time when they nucleated, and if possible, follow their growth as a function of annealing time.

4.4.1 Discussion

Three nuclei were detected in the experimental diffraction images: two exhibited orientations corresponding to 1st order twin orientations (nucleus 1 and nucleus 3); and of particular interest, one exhibited an orientation neither corresponding to any of the deformed grains, nor a 1st order twin of any of them (nucleus 2). Orientations obtained through the use of GRAINDEX are generally accurate to within $\sim 1^{\circ}$.

The copper sample material was assumed to be free of large particles, as no particles were observed in the OIMs, and no diffraction spots from second phase particles sized above (>1 μm) the detection limit were observed in the X–ray diffraction images, which at a deformation of 20% rules out PSN according to Sandström (see section 1.2.6) [42]. Fine particles sized $\sim$0.1 μm could not be resolved in the diffraction images. However, according to Jones & Hansen any such dispersion of fine particles does not lead to PSN, but leads instead to a retardation of the nucleation of recrystallization [23].

The next question to be addressed must be whether it is possible that the nuclei grew from volumes, which were smaller than the detection limit. A TEM–study had shown that the minimum subgrain size was 1–2 μm, and further the classical critical nucleus size was found to be ECD_C>1.14 μm (see section 4.2.2.3), both of which were well above the detection limit of the experiment. We may therefore conclude that any subgrains present outside the poles would be detected in the diffraction images.

Lastly, there is the question of whether the orientation of nucleus 2 is twin–related to any of the deformed grains. In this study we have limited ourselves to comparing the orientation of the deformed grains with that of the nucleus and its 1st order twins. Based on the results of nucleus 2, it would seem that new orientations *do occur*. However, Haasen found up to 5th order twin–relationships while investigating nucleus–matrix orientation relationships in TEM [8, 39], so this could indicate that the above conclusion is in fact inconclusive. It should however be noted that no diffraction spots from any twin orientations were observed, which has two possible explanations: (i) either nucleus 2 does not have any twin–relation to the deformed/recovered microstructure, i.e., it is a new orientation; or alternatively, (ii) multiple twinning occurred so rapidly on the migrating high angle boundary of the nucleus that the intermediate twins are smaller than the detection limit. However, according to Leffers this is unlikely [114].

Other authors have reported nuclei with *new* orientations [3, 5, 6, 115], and have in each case noted a rotation about a <111>–axis with respect to one of the deformed parent grains. It was however not possible to determine any such relationship between the possible new orientation of nucleus 2 and the deformed grains. This was due to the fact that the X–ray beam was diffracted by all orientations lying within the volume traced out by the beam, while it would be necessary to know the exact orientations present at the nucleation site to determine whether the new orientation corresponded to a rotation about a <111>–axis.

It was possible to follow the kinetics of two of the three nuclei during annealing, and in one case the nucleus was detected after only 2.5 minutes of annealing at 290°C. The estimated error in the intensity of the most intense reflections is estimated to be a factor 2 at most. For the ECD, this gives a maximum relative error of 26%. The growth curves were plotted showing ECD as a function of time. However, given the fact that the nuclei most likely nucleated on triple junctions or grain boundaries, a more realistic nucleus shape would be saucer–like, which would result in a geometrically modified ECD. However, as it was not possible to obtain conclusive data indicating for or against a spherical nucleus shape (see section 4.1.4), determining this must be a task for the future.

4.4.2 Outlook

To summarize, a method which allows *in situ* studies of the nucleation of discontinuous recrystallization within diffracting bulk materials has been envisaged and realized. Depending on the data obtained, the following information about an observed bulk nucleus may be obtained: its deformed parent microstructure; its crystal orientation; its exact or approximate position; and its growth kinetics. To the knowledge of the author, this is the first technique to provide all this information, without the ambiguity of resorting to dynamic surface investigations.

As well as the scientific results obtained, this experiment should mainly be viewed as a feasibility study. In outlook, the method presented can be applied to almost any problem in nucleation, such as phase transitions and solidification, and should therefore find broad application. The spatial resolution of the deformed microstructure was rather crude in this study ($49\times49\times300$ μm^3), but this may be significantly improved at the discretion of the user, eg. by narrowing the X–ray beam and/or reducing the thickness of the sample, as has been successfully done by both Poulsen *et al.* and Gundlach *et al.* [4, 66].

In future experiments, the volume detection limit may if necessary be lowered significantly by a combination of several factors:
an additional undulator has been installed at ID–11 since the experiment, which means that the X–ray flux has been increased by a factor of 2–3 [97];
if the storage ring is run in normal (992 electron bunch) mode, the ring current is 200 mA (it was 90 mA during the experiment), and additionally, there are plans to upgrade the storage ring to running at 250 mA, which gives a relative flux increase of 2.2–2.8 [95];
the X–ray beam may be focused to a smaller size, eg. using a 25×25 μm^2 beam will increase the relative flux by a factor of 4;
and lastly, the detection limit may also be lowered by choosing to study a metal with a higher X–ray scattering factor (roughly proportional to Z), such as silver (Z=47) or gold (Z=79).

Lastly, a method which allows the actual nucleation mechanisms to be studied directly by 3DXRD is envisaged. This is done by locating and characterizing the strained zone surrounding elongated rigid interstitial particles of micrometre size *in situ* within the bulk of a deformed sample, because rigid particles are very likely nucleation sites (see section 1.2.6). Also, the strained zone around a rigid particle is generally misoriented relative to the surrounding microstructure, and may thus be distinguished from this with 3DXRD. By characterizing the strained zone surrounding a particle before and during annealing, there is a good chance that nucleation may be followed on the subgrain level, due to the relatively small size of the deformation zone ($\sim$10 μm), which may then be characterized in great detail, and with a X–ray beam of slightly larger size the annealing process may thus be followed with a single beam position.

The particle–containing sample should preferably be a deformed single or bi–crystal of small thickness, and consist of a metal with high stacking fault energy (such as aluminium), to avoid twinning as much as possible. Choosing a metal with a well–defined deformation microstructure will help as well. The initial detection of suitable particles can be performed with a large box beam, and a suitable particle may then be translated into the centre of rotation, after its precise position has been determined with a *superscan* on one of its reflections. Characterization of the strained zone around a particle may afterwards be performed with a X–ray beam focused to small size (eg. 10×10 μm^2).

This approach follows closely that of Gundlach *et al.* [66], but here a likely nucleation site is chosen for study, in the hope that nucleation will occur at that specific site, as opposed to simply following subgrain growth. If a bi–crystal is chosen the chances of nucleation occurring at the chosen particle may be further increased by choosing a particle situated at the grain boundary, due to the high local orientation gradients present at grain boundaries in deformed metals.

Chapter 5

Conclusions

In this PhD project the nucleation of recrystallization has been studied in a broad sense using various experimental techniques. This has lead to:

- Development of an experimental method, which allows reliable automatic line scans to be performed utilizing the EBSP technique. The program LSGRAINS represents a fast and efficient way of obtaining the recrystallization parameters V_V, S_V, and $<\lambda>$, which are important when studying recrystallization dynamics. The method has been compared to three different manual EBSP line scan methods and has been found to be in good agreement with these, and is now used for studies of recrystallization kinetics within the Metals–4D center.

- A reliable method by which serial sectioning of samples may be performed in steps down to 2 μm has been developed. Combined with OM or EBSP investigations of the sectioned surfaces, a full 3D reconstruction of the microstructure is possible with a spatial resolution of $\sim$2 μm. The method also allows polishing of samples down to a pre–specified target depth with an accuracy of 1–2 μm, and thus allows a direct comparison between surface and bulk sensitive techniques. Equally important is that this allows the two kinds of techniques to be combined within one experiment, so as to provide even more detailed information about the samples studied.

- 3DXRD has been proven to be a powerful tool for studying *in situ* bulk nucleation of recrystallization, yielding both crystallographic orientations as well as growth kinetics of individual bulk nuclei. Triple junctions have been proven to be likely nucleation sites, but also not all triple junctions lead to nucleation, which is in good agreement with previous surface and serial sectioning results.
  The first ever experiment using X–ray diffraction to study *in situ* bulk nucleation of recrystallization in a metal sample was carried out successfully. The deformed and annealed microstructures around triple junctions were characterized in three samples, from which three nuclei were identified, their crystal orientations were determined, and for two of them growth curves were determined as well.

- A nucleus emerging with a new orientation, not directly or 1st order twin–related to the deformed microstructure, has been observed growing. It is deemed very unlikely that its orientation should be the result of multiple twinning reactions, or that it grew from a cell smaller than the detection limit.

With the LSGRAINS program, obtaining experimental data on recrystallization dynamics is now a much faster and more efficient process. Several studies have already been performed or are in progress using this technique.

With the development of a reliable serial sectioning technique it has become possible to combine 3DXRD and microscopy, so that interesting microstructural features, such as nuclei, identified using 3DXRD may also be studied directly by microscopy by polishing the sample down to the depth of the feature. This should increase the knowledge gleaned from such experiments, as it will be possible to combine the strengths of the various microscopies.

Finally, it is the opinion of the author that with the various planned upgrades of the 3DXRD microscope and the experiment outlined in section 4.4.2, it will soon be possible to study *in situ* the nucleation of recrystallization on a scale and with a time resolution, which will allow the mechanism behind an observed nucleation event to be determined, thus leading to a breakthrough in the understanding of the nucleation of recrystallization.

Appendix A

Crystal orientations

The alignment between the sample geometry and the crystal lattice of a given crystal grain is called the crystal orientation of the grain...

There are several ways to quantitatively represent crystal orientations. However, to define crystal orientations we must first define the axes of the sample coordinate system. In this thesis we will focus on the rolling geometry, where the rolling axes and planes are derived from the deformation process (see figure A.1):

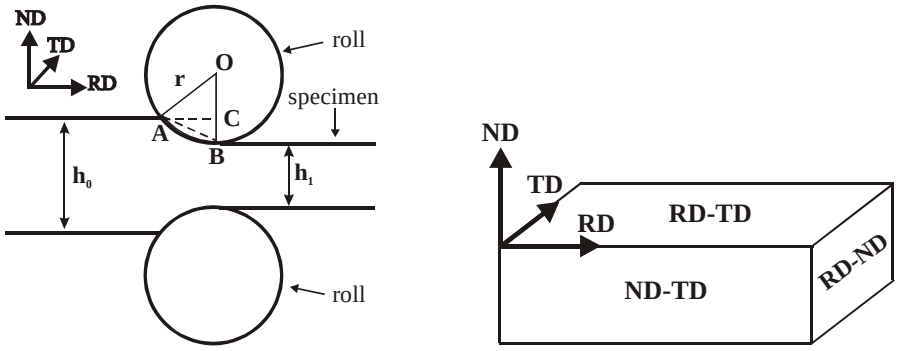

(a) (b)

Figure A.1: *The rolling geometry: the rolling direction (RD); the transverse direction (TD); and the normal direction (ND).* ***(a)*** *Rolling mill geometry: r is the radius of the rolls, and h_0 and h_1 are respectively the specimen thickness before and after rolling.* ***(b)*** *Rolling plane geometry: the rolling plane (ND–TD); the transverse plane (RD–ND); and the normal plane (RD–TD).*

Of course other deformation modes exist, eg. wire–drawing where only one axis is defined by the process, but since the samples used in this thesis have all been deformed by cold rolling the rolling geometry is used. For a more complete coverage of the topic of crystal orientations the author refers to Hansen *et al.* [13].

A frequently used way to represent the orientation of a crystal grain is to use the Miller indices (hkl)[uvw] to indicate which crystallographic planes lie in respectively the rolling plane (ND–TD) and along the perpendicular rolling direction (RD) [13]. The Miller indices {hkl}<uvw> indicate the family of crystallographic planes, which correspond to the same orientation. E.g. the 'cube' orientation has {100}<001>, which means that the axes of the unit cell are perfectly aligned with the rolling axes (see fig. A.1b). The main advantages of this representation is its brevity and that it may be plotted directly onto images of the microstructure, thus giving a visual and very intuitive understanding of an orientation.

An often used alternative to this representation is the Euler angles $(\varphi_1, \phi, \varphi_2)$, which are defined as the three rotations that will bring the sample coordinate system (x_s, y_s, z_s) to coincide with the crystal coordinate system (x_c, y_c, z_c). For a *cubic* lattice, the crystal coordinate system is spanned by the three lattice vectors ([100], [010], [001]). Here the Bunge definition of the Euler angles has been used [116]. First, (x_s, y_s, z_s) is rotated around z_s by the angle φ_1. Secondly, the rotated sample system (x'_s, y'_s, z'_s) is rotated around x'_s by the angle ϕ, which brings z'_s to coincide with z_c. Lastly, x'_s and y'_s are brought to coincide with x_c and y_c by a rotation of φ_2 around z'_s/z_c.

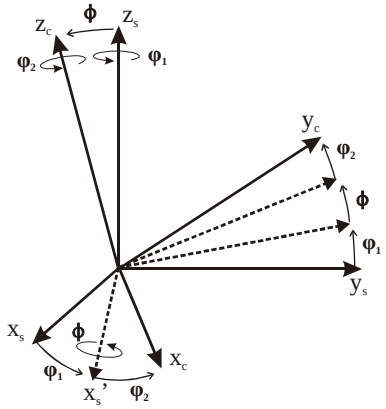

Figure A.2: *The Euler angles $\varphi_1 \in [0,2\pi]$, $\phi \in [0,\pi]$, and $\varphi_2 \in [0,2\pi]$ describe how the crystal coordinate system (x_c, y_c, z_c) may be rotated into the sample coordinate system (x_s, y_s, z_s).*

Generally, a 3×3 orientation matrix **U** is used to fix the crystal lattice to the sample geometry. This is a very useful representation, since it may be used directly to calculate the diffraction vector from an X–ray beam diffracted by a set of crystal planes in a crystal grain within a macroscopic polycrystalline sample (see section A.2) [13].
U may be calculated directly from a set of Miller indices (hkl)[uvw] [13]:

$$\mathbf{U}((\mathrm{HKL})[\mathrm{UVW}]) = \begin{bmatrix} \frac{\mathrm{U}}{\mathrm{N}} & \frac{\mathrm{V}}{\mathrm{N}} & \frac{\mathrm{W}}{\mathrm{N}} \\ \frac{\mathrm{KW-LV}}{\mathrm{MN}} & \frac{\mathrm{LU-HW}}{\mathrm{MN}} & \frac{\mathrm{HV-KU}}{\mathrm{MN}} \\ \frac{\mathrm{H}}{\mathrm{M}} & \frac{\mathrm{K}}{\mathrm{M}} & \frac{\mathrm{L}}{\mathrm{M}} \end{bmatrix} \tag{A.1}$$

where $\mathrm{M}=\sqrt{\mathrm{H}^2+\mathrm{K}^2+\mathrm{L}^2}$ and $\mathrm{N}=\sqrt{\mathrm{U}^2+\mathrm{V}^2+\mathrm{W}^2}$, or alternatively from the Euler angles $(\varphi_1, \phi, \varphi_2)$ [13]:

$$\mathbf{U}(\varphi_1, \phi, \varphi_2) = \begin{bmatrix} \cos\varphi_1 \cos\varphi_2 - \sin\varphi_1 \sin\varphi_2 \cos\phi & -\cos\varphi_1 \sin\varphi_2 - \sin\varphi_1 \cos\varphi_2 \cos\phi & \sin\varphi_1 \sin\phi \\ \sin\varphi_1 \cos\varphi_2 + \cos\varphi_1 \sin\varphi_2 \cos\phi & -\sin\varphi_1 \sin\varphi_2 + \cos\varphi_1 \cos\varphi_2 \cos\phi & -\cos\varphi_1 \sin\phi \\ \sin\varphi_2 \sin\phi & \cos\varphi_2 \sin\phi & \cos\phi \end{bmatrix} \tag{A.2}$$

A.1 Twin–orientations

Crystallographically, twinning amounts to a 60° rotation around a [111]–axis. The twin–orientations of an orientation are calculated by performing ±60° rotations around all eight <111>–axes. The resulting 16 **U**–matrices produce a total of 4 different twin–orientations when the symmetrically equivalent orientations (see below) are taken into account.

The orientation resulting from rotating an orientation **U** by an arbitrary angle θ around an arbitrary normalized axis vector $\hat{\mathbf{n}} = (\hat{n}_1, \hat{n}_2, \hat{n}_3)$ is:

$$\hat{\mathbf{U}}(\hat{\mathbf{n}}, \theta) = \mathbf{U}\,\mathbf{R}(\hat{\mathbf{n}}, \theta) \tag{A.3}$$

where **U** is the original orientation, $\hat{\mathbf{U}}(\hat{\mathbf{n}},\theta)$ is the new orientation, and the rotation matrix $\mathbf{R}(\hat{\mathbf{n}},\theta)$ is given by eq. A.4 [13]:

$$\mathbf{R}(\hat{\mathbf{n}}, \theta) = \begin{bmatrix} \hat{n}_1^2(1-\cos\theta) + \cos\theta & \hat{n}_1\hat{n}_2(1-\cos\theta) - \hat{n}_3\sin\theta & \hat{n}_1\hat{n}_3(1-\cos\theta) + \hat{n}_2\sin\theta \\ \hat{n}_1\hat{n}_2(1-\cos\theta) + \hat{n}_3\sin\theta & \hat{n}_2^2(1-\cos\theta) + \cos\theta & \hat{n}_2\hat{n}_3(1-\cos\theta) - \hat{n}_1\sin\theta \\ \hat{n}_1\hat{n}_3(1-\cos\theta) - \hat{n}_2\sin\theta & \hat{n}_2\hat{n}_3(1-\cos\theta) + \hat{n}_1\sin\theta & \hat{n}_3^2(1-\cos\theta) + \cos\theta \end{bmatrix} \tag{A.4}$$

where for a twin–orientation: $\theta = \pm 60°$; and $\hat{\mathbf{n}} = (\pm 1, \pm 1, \pm 1)/\sqrt{3}$.
Because $|\hat{n}|^2 = \hat{n}_1^2 + \hat{n}_2^2 + \hat{n}_3^2 = 1$, it is apparent from eq. A.4 that the rotation angle θ may be calculated directly from the *trace* of the rotation matrix $\mathbf{R}(\hat{\mathbf{n}},\theta)$:

$$\theta = \arccos\left(\frac{\mathrm{Trace}(\mathbf{R}(\hat{\mathbf{n}},\theta)) - 1}{2}\right) \tag{A.5}$$

Therefore, if two orientations are known, the misorientation angle θ between them may be determined by calculating $\mathbf{R}(\hat{\mathbf{n}},\theta)$ from eq. A.6 and inserting $\mathbf{R}(\hat{\mathbf{n}},\theta)$ into eq. A.5:

$$\mathbf{R}(\hat{\mathbf{n}},\theta) = \mathbf{U}^T\,\hat{\mathbf{U}}(\hat{\mathbf{n}},\theta) \tag{A.6}$$

where $\mathbf{U}^T$ is the transpose of $\mathbf{U}$.

However, it should be noted that because of the symmetry of the crystal lattice, the θ value given by eq. A.5 may not be the lowest misorientation angle between two orientations. This is found by calculating all symmetric equivalent orientations (24 in *fcc* crystals) of the first orientation, and determining the misorientation angle between each of these orientations and the second orientation. The one with the lowest misorientation angle is *chosen* as the misorientation angle between the two orientations.

The symmetric equivalents exist because it possible to perform symmetry operations (eg. rotations about an i–fold axis, or inversions about mirror planes), which result in exactly the same crystal lattice and therefore exactly the same orientation as before the symmetry operation was performed, but with a different $\mathbf{U}$–matrix [13].

A.2 The X–ray diffraction equation

In this section will determine the basic diffraction equation of the 3DXRD microscope. The derivation follows those of Nielsen and Lauridsen *et al.* [68, 94].

The experimental coordinate system (x_t, y_t, z_t), within which the experiment was performed, is tilted slightly from the laboratory coordinate system $(x_{lab}, y_{lab}, z_{lab})$. This is due to the fact that the initially horizontal X–ray beam leaves the monochromating–focusing optics at an angle. The transformation between the two coordinate systems is described by the following matrix operation:

$$\begin{pmatrix} x_t \\ y_t \\ z_t \end{pmatrix} = \begin{pmatrix} \cos(2\theta_m)\cos(2\theta_{ML}) & -\sin(2\theta_{ML}) & \sin(2\theta_m) \\ \sin(2\theta_{ML}) & \cos(2\theta_{ML}) & 0 \\ -\sin(2\theta_m) & 0 & \cos(2\theta_m) \end{pmatrix} \begin{pmatrix} x_{lab} \\ y_{lab} \\ z_{lab} \end{pmatrix} \tag{A.7}$$

where θ_m is the vertical diffraction angle from the monochromator crystal, and θ_{ML} is the horizontal diffraction angle from the multilayer.

Now that the tilted coordinated system is defined, we shall work exclusively in that. The vector $\mathbf{G}_t$ for elastic scattering of X–rays in the tilted system is given by (see fig. 4.3):

$$\mathbf{G}_t = \frac{2\pi}{\lambda} \begin{pmatrix} \cos(2\theta) - 1 \\ \sin(2\theta)\sin(\eta) \\ \sin(2\theta)\cos(\eta) \end{pmatrix} \tag{A.8}$$

When the sample is rotated, the positive sample rotation $\mathbf{\Omega}$ is in the anti–clockwise direction when one observes the sample from above (see fig. 4.3):

$$\mathbf{G}_\omega = \mathbf{G}_t\,\mathbf{\Omega} \tag{A.9}$$

$$\mathbf{\Omega} = \begin{pmatrix} \cos(\omega) & -\sin(\omega) & 0 \\ \sin(\omega) & \cos(\omega) & 0 \\ 0 & 0 & 1 \end{pmatrix} \tag{A.10}$$

The sample coordinate system (x_s, y_s, z_s) defines how the sample is mounted on the rotation stage with respect to the deformation axes of the sample. The setup of choice was x_s=TD, y_s=RD, and z_s=ND, which gives the $\mathbf{S}$–matrix (see fig. A.1a):

$$\mathbf{G}_\omega = \mathbf{S}\,\mathbf{G}_s \tag{A.11}$$

$$\mathbf{S} = \begin{pmatrix} 1 & 0 & 0 \\ 0 & 1 & 0 \\ 0 & 0 & 1 \end{pmatrix} \tag{A.12}$$

The Cartesian grain system (x_c, y_c, z_c) is related to the Cartesian crystal axes by making the crystal orientation transformation:

$$\mathbf{G}_s = \mathbf{U}\,\mathbf{G}_c \tag{A.13}$$

where $\mathbf{U}$ is the orthogonal matrix that relates the sample to the crystal coordinate system (see eq. A.1 and A.2). Lastly, the Miller indices (hkl), where the crystal scattering vector is calculated, are directly linked to the orthonormal crystal scattering axes $\mathbf{G}_c$ by the transformation matrix $\mathbf{B}$ [38]:

$$\mathbf{G}_c = \mathbf{B}\,\mathbf{G}_{hkl} \tag{A.14}$$

$$\mathbf{G}_{hkl} = (h, k, l) \tag{A.15}$$

$$\mathbf{B} = \begin{pmatrix} a^* & b^*\cos(\gamma^*) & c^*\cos(\beta^*) \\ 0 & b^*\sin(\gamma^*) & -c^*\sin(\beta^*)\cos(\alpha) \\ 0 & 0 & c^*\sin(\beta^*)\sin(\alpha) \end{pmatrix} \tag{A.16}$$

$$\cos(\alpha) = \frac{\cos(\beta^*)\cos(\gamma^*) - \cos(\alpha^*)}{\sin(\alpha^*)\sin(\beta^*)} \tag{A.17}$$

where $(a, b, c, \alpha, \beta, \gamma)$ and $(a^*, b^*, c^*, \alpha^*, \beta^*, \gamma^*)$ are respectively the lattice parameters in direct and reciprocal space. In the case of a *cubic* crystal we have $a^*{=}b^*{=}c^*{=}2\pi/a$ and $\alpha^*{=}\beta^*{=}\gamma^*{=}\pi/2$, which greatly simplifies $\mathbf{B}$ and simply adds a factor $2\pi/a$ in front of $\mathbf{G}_{hkl}$. When all transformations between the different coordinate systems are compounded, we get the basic diffraction equation for the scattering vector $\mathbf{G}_t$:

$$\mathbf{G}_t = \mathbf{\Omega}\,\mathbf{S}\,\mathbf{U}\,\mathbf{B}\,\mathbf{G}_{hkl} \tag{A.18}$$

which describes all scattering within the tilted laboratory coordinate system.

Appendix B

Crystallographic textures

When all possible crystallographic orientations do not occur with the same frequency in a polycrystalline material, and one or more preferred orientations exist, the material is said to have a *texture*. Texture is of major industrial importance, since the properties of a polycrystalline material will depend on the overall crystallographic orientation of the crystal grains and much effort is made to control it. The texture of a material is generally represented using either pole figures, which are quite visually intuitive, or orientation distribution functions, which quantify textures better. For further information about textures the author refers to Hatherley & Hutchinson [14].

In cold rolled *fcc* metals, the dominant texture components are:

'cube' {100}<001> — a texture component, which grows from volume fractions close to zero to high values during primary recrystallization.

'rolling' consisting of 'Brass' {110}<112>, 'S' {123}<624>, and 'Copper' {112}<111> — the dominant texture observed in cold rolled metals prior to annealing. This is due to the grains rotating in specific directions during plastic deformation.

'random' — Generally, any crystal grain not belonging to either of the above texture components is said to exhibit 'random' texture.

Depending on the application of the material other texture components (such as 'Goss' {110}<001>) may be of interest. Here we have used the first orientation notation presented in appendix A.

B.1 Pole figures

Pole figures are a way to visually represent the orientation of a single crystal or polycrystal with respect to directions given by the sample geometry and/or deformation method. The orientation of a single crystal grain in the sample can be represented by plotting a number of its crystal directions (eg. three {100} directions) at their appropriate angular positions relative to the reference direction.

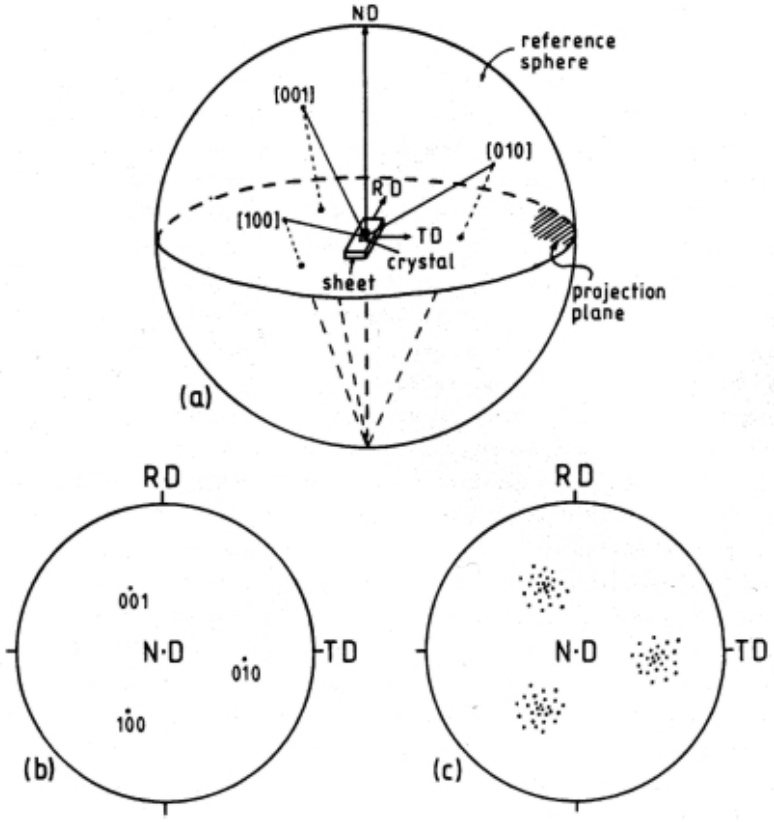

Figure B.1: *Pole figure of rolled sheet. The pole figure axes are the ND, RD, and TD directions, and the displayed plane normals are those of the {100} planes.* ***(a)*** *the stereographic projection of the {100} planes of a single crystal;* ***(b)*** *pole figure of an undeformed single crystal; and* ***(c)*** *pole figure of a deformed single crystal [14].*

To produce a pole figure, a single crystal is placed within an unit sphere,

who's axes are set equal to the axis of the imposed deformation (RD, TD, and ND). The intersections of the normal vectors of a set of crystal lattice planes (eg. {100}) with the surrounding unit sphere are determined (see fig. B.1a). The pole figure is the stereographic projection of these intersections.

In short, the stereographic projection consists of drawing lines from the intersection points on the northern hemisphere of the unit sphere to the south pole. The positions, where these lines cross the equatorial plane give a 2 dimensional representation of the orientation of the crystal, which is the *stereographic projection*.

In a pole figure the plane normals of one crystal grain will be spots with an orientation spread around them corresponding to the mosaic spread of the grain, so a perfect single crystal should give very distinct spots (see fig. B.1b), while a heavily deformed crystal grain with a large mosaic spread would produce a large spot centered around the average orientation of the grain (see fig. B.1c). The pole figure of a polycrystal will simply be the superposition of all the spots of all the grains onto the equatorial plane.

B.2 The orientation distribution function

When the texture of a polycrystal must be quantitatively described, this is generally well done using the orientation distribution function (ODF), which describes the volume fraction of crystal grains with a specific orientation in the 3 dimensional Euler angle space $(\varphi_1, \phi, \varphi_2)$, which is covered in appendix A. Shortly, the ODF is a function $f(g)$, which is defined in such a manner that $f(g)\,dg$ is the volume fraction of orientations within the orientation element dg, and that $f(g)$=1 for a random distribution of orientations. This is done by introducing the orientation volume element dg [13]:

$$dg = \frac{1}{8\pi^2}\,\sin\phi\,d\varphi_1\,d\phi\,d\varphi_2 \tag{B.1}$$

where the orientation distribution function $f(g)$ is defined by [13]:

$$\int f(g)\,dg = \int_0^{2\pi}\int_0^{\pi}\int_0^{2\pi} f(g)\,\frac{1}{8\pi^2}\,\sin\phi\,d\varphi_1\,d\phi\,d\varphi_2 = 1 \tag{B.2}$$

ODFs are generally plotted as a series of planes in Euler space, where one Euler angle (φ_1 or φ_2) is held constant in each plane.

Appendix C

Beamline specifics

Specific information on the X–ray source, monochromating–focusing optics, and the CCD–detector of beamline ID–11 has been placed in this appendix, as it is primarily thought to be of interest for dedicated X–ray scientists, and to be of less interest to the more general audience, with whom in mind this thesis has been written.

magnet period	23 mm (69 periods)
K_{max}	1.8995
field B_{max}	0.88 T
fundamental wavelength	1.70 Å
source size	57×10 μm^2 (H×V) FWHM (incl. source broadening)
source divergence	88×5 μrad^2 (H×V) FWHM
peak brilliance	$5{\cdot}10^{19}$ ph $s^{-1}mrad^{-2}mm^{-2}$, 0.1% BW, 0.1 A
peak tot. integ. flux	$2.5{\cdot}10^{16}$ ph s^{-1}, 0.1% BW, 0.1 A
power	3.8 kW (at 0.1 A SR current)
power density	114 Wmm^{-2}
beam size at 25 m	25×1.5 mm^2
total horizontal angular acceptance	2.2 mrad (FWHM)

Table C.1: *Specifics about the ID11 in–vacuum undulator. Properties are for a gap motor setting of 7.219 mm, which was used for the experiment. Note however, that fluxes given at a synchrotron ring current of 200 mA [97].*

Most of the information presented in these tables has already been presented in section 4.1, so they should mainly be viewed as a summary of the four standard devices used in the 3DXRD experiment.
No further explanation will be given here for the additional information available in these tables, but keen readers are recommended the book by Als–Nielsen & McMorrow for further reading [12].

CCD–chip size	1024×1024 pixels
effective pixel size	157×157 μm^2
Width of Point Spread Function	200–300 μm
effective active area	160×160 mm^2
Phosphor after–glow	$< 10^{-2}$ s
Dynamic range	14 bits
min. readout time	0.2 sec
sample to detector distance	330 mm

Table C.2: *Technical specifications for the 2D Frelon CCD–detector [97].*

energy	50 keV	80 keV
tunability	∼10%	∼10%
source–mono distance	51.2 m	51.2 m
mono–focus distance	2 m	2 m
reflection	(1 1 1)	(1 1 1)
asymmetry angle	0.8°	0.5°
bending radius	4 m	4 m
crystal thickness	2 mm	1 mm
energy bandwidth *(per 1 mm beam width)*	0.8%	0.8%
efficiency	90 %	90 %
focus size	1.5 μm	1.5 μm
focal length	2 m	2 m

Table C.3: *Specific information about the asymmetrically cut and cylindrically bent Si(111)–Laue crystals, used for monochromating and focusing the X–ray beam in the vertical direction [97].*

energy	50 & 80 keV
source–ML distance	52.5 m
ML–focus distance	1.4 m
ML materials	W & B_4C
number of periods	100
Γ–ratio	0.1455
central d–spacing	20 Å
gradient $\Delta d/d$	0.10
curvature (major rad.)	25 m
energy bandwidth	1.4 %
efficiency	50 %
focus size	4 μm

Table C.4: *Specific information about the elliptically shaped and laterally graded* W/B_4C*–multilayer, used to focus the X–ray beam in the horizontal direction [97].*

Appendix D

Publications

A1: A. W. Larsen and D. Juul Jensen. Automatic determination of recrystallization parameters in metals by EBSP line scans.
Materials Characterization, 51(4):271–282, 2003.

A2: A. W. Larsen, H. F. Poulsen, L. Margulies, C. Gundlach, Q. Xing, X. Huang and D. Juul Jensen. Nucleation of recrystallization observed in situ in the bulk of a deformed metal. *Scripta Materialia*, 53:553–557, 2005.

A3: A. W. Larsen. 'Logitech PM5D precision polishing and lapping system' user manual. Risø I–report, Risø–I–2051(EN), Risø National Laboratory, Roskilde, Denmark, September 2003.

A4: G. Winther, L. Margulies, H. F. Poulsen, S. Schmidt, A. W. Larsen, E. M. Lauridsen, S. F. Nielsen, and A. Terry.
Lattice rotations of individual bulk grains during deformation.
In *Textures of Materials, pts 1 and 2*, volume 408–4, pages 287–292, Roskilde, Denmark, 2002. Materials Science Forum.

A5: A. W. Larsen, C. Gundlach, H. F. Poulsen, L. Margulies, Q. Xing, and D. Juul Jensen. In–situ investigation of bulk nucleation by X–ray diffraction.
In *2. International conference on recrystallization and grain growth*, pages 81–86, Annecy, France, 2004. Trans Tech Publications Ltd.

A6: D. Juul Jensen, M. D. Lund, A. W. Larsen, and J. R. Bowen.
Recrystallization kinetics in the bulk and at the surface.
In *2. International conference on recrystallization and grain growth*, pages 147–151, Annecy, France, 2004. Trans Tech Publications Ltd.

A7: D. Juul Jensen and A. W. Larsen.
Orientations of recrystallization nuclei studied by 3DXRD.
In *Proceedings of the 14th International Conference on Textures of Materials*, pages 1285–1290, 2005. Materials Science Forum

Bibliography

[1] Instron. URL: http://www.instron.com.

[2] HKL Technology. URL: http://www.hkltechnology.com.

[3] T. J. Sabin, G. Winther, and D. Juul Jensen. Orientation relationships between recrystallized nuclei at triple junctions and deformed structures. *Acta Materialia*, 51:3999–4011, 2003.

[4] H. F. Poulsen, E. M. Lauridsen, S. Schmidt, L. Margulies, and J. H. Driver. 3D–characterisation of microstructure evolution during annealing of a deformed aluminum single crystal. *Acta Materialia*, 51(9):2517–2529, 2003.

[5] J. H. Driver, H. Paul, J-C. Glez, and C. Maurice. Relations between deformation substructure and nucleation in fcc crystals. In N. Hansen, D. Juul Jensen, T. Leffers, and B. Ralph, editors, *21st Risø International Symposium on Metallurgy and Materials Science*, pages 35–48, Roskilde, DK, 2000. Risø National Laboratory.

[6] F. Inoko, K. Kashihara, M. Tagami, and T. Okada. Relation between activated slip systems and nucleation of recrystallized grains in deformed single– and bi–crystals. In *2. International conference on recrystallization and grain growth*, pages 57–62, Annecy, France, 2004. Trans Tech Publications Ltd.

[7] F. J. Humphreys. Nucleation in recrystallization. In *2. International conference on recrystallization and grain growth*, pages 107–116, Annecy, France, 2004. Trans Tech Publications Ltd.

[8] P. Haasen. The generation of new orientations during primary recrystallization of single crystals. In T. Chandra, editor, *International*

conference on recrystallization in metallic materials, pages 17–26, Wollongong, Australia, 1990. TMS.

[9] R. T. DeHoff. Microstructural evolution during recrystallization. In N. Hansen, D. Juul Jensen, T. Leffers, and B. Ralph, editors, *7th Risø International Symposium on Metallurgy and Materials Science*, pages 35–52, Roskilde, DK, 1986. Risø National Laboratory.

[10] D. A. Porter and K. E. Easterling. *Phase Transformations in Metals and Alloys*. Chapman & Hall, London, UK, 2. edition, 1993.

[11] F. J. Humphreys and M. Hatherley. *Recrystallization and related annealing phenomena*. Pergamon, 1. edition, 1995.

[12] J. Als-Nielsen and D. McMorrow. *Elements of Modern X–ray physics*. John Wiley & Sons Ltd, Chichester, UK, 1. edition, 2001.

[13] J. Hansen, J. Pospiech, and K. Lücke. *Tables for Texture Analysis of Cubic Crystals*. Springer–Verlag, Berlin–Heidelberg, 1978.

[14] M. Hatherley and W. B. Hutchinson. *An introduction to textures in metals*. Chameleon Press Ltd., London, December 1979.

[15] P. Haasen. *Physical Metallurgy*. Cambridge University Press, Cambridge, UK, 3. edition, 1996.

[16] C. Vogel, C. Juhl, and E. Maahn. *Metallurgi for Ingeniører*. Akademisk Forlag, Denmark, 7. edition, 1995.

[17] R. E. Smallman. *Modern physical metallurgy*. Butterworths, London, UK, 2. edition, 1963.

[18] R. W. K. Honeycombe. *The Plastic Deformation of Metals*. Edward Arnold, 1985.

[19] N. Hansen. Deformation microstructures with a structural scale from the micrometre to the nanometre dimension. In N. Hansen et al., editors, *25th Risø International Symposium on Materials Science*, pages 13–32, Roskilde, DK, 2004. Risø National Laboratory.

[20] D. Hull and D. J. Bacon. *Introduction to dislocations*. Butterworth–Heinemann, Oxford, UK, 4. edition, 2001.

[21] H. F. Poulsen. *Three–Dimensional X–Ray Diffraction Microscopy*. Springer Tracts in Modern Physics. Springer, Berlin, Heidelberg, 1. edition, 2004.

[22] P. Cotterill and P. R. Mould. *Recrystallization and Grain Growth in Metals*. Surrey University Press, London, 1976.

[23] A. R. Jones and N. Hansen. Recovery changes leading to nucleation of recrystallization. In N. Hansen, A. R. Johns, and T. Leffers, editors, *1st Risø International Symposium on Metallurgy and Materials Science*, pages 13–25, Roskilde, DK, 1980. Risø National Laboratory.

[24] R. Doherty, D. A. Hughes, F. J. Humphreys, D. Juul Jensen, M. E. Kassner, W. E. King, T. R. McNelley, H. J. McQueen, and A. D. Rollet. Current issues in recrystallization: a review. *Materials Science and Engineering*, 238(A):219–274, 1997.

[25] C. M. Sellars. The influence of particles on recrystallization during thermomechanical processing. In N. Hansen, A. R. Johns, and T. Leffers, editors, *1st Risø International Symposium on Metallurgy and Materials Science*, pages 291–301, Roskilde, DK, 1980. Risø National Laboratory.

[26] C. M. Sellars. Modelling of structural evolution during hot working processes. In N. Hansen, D. Juul Jensen, T. Leffers, and B. Ralph, editors, *7th Risø International Symposium on Metallurgy and Materials Science*, pages 167–187, Roskilde, DK, 1986. Risø National Laboratory.

[27] C. M. Sellars and B. P. Wynne. Microstructural evolution — effects of microstructural and hot processing variables. In N. Hansen et al., editors, *25th Risø International Symposium on Materials Science*, pages 117–136, Roskilde, DK, 2004. Risø National Laboratory.

[28] V. Randle, B. Ralph, and N. Hansen. Grain growth in crystalline materials. In N. Hansen, D. Juul Jensen, T. Leffers, and B. Ralph, editors, *7th Risø International Symposium on Metallurgy and Materials Science*, pages 123–142, Roskilde, DK, 1986. Risø National Laboratory.

[29] M. E. Fine. *Introduction to phase transformations in condensed systems*. Macmillan Materials Science Series. The Macmillan Company, 1964.

[30] R. D. Doherty. Nucleation of recrystallization of single phase and dispersion hardened polycrystalline materials. In N. Hansen, A. R. Johns, and T. Leffers, editors, *1st Risø International Symposium on Metallurgy and Materials Science*, pages 57–69, Roskilde, DK, 1980. Risø National Laboratory.

[31] J. C. M. Li. Possibility of subgrain rotation during recrystallization. *Journal of Applied Physics*, 33(10):2958, 1962.

[32] R. D. Doherty and J. A. Szpunar. Kinetics of sub–grain coalescence — a reconsideration of the theory. *Acta Metallurgica*, 32(10):1789–1798, 1984.

[33] H. Hu. Nucleation of recrystallization for cube texture formation in fcc metals. In N. Hansen, A. R. Johns, and T. Leffers, editors, *7th Risø International Symposium on Metallurgy and Materials Science*, pages 75–92, Roskilde, DK, 1986. Risø National Laboratory.

[34] D. Juul Jensen. Orientation aspects of growth during recrystallization. Risø R–report Risø–R–978(EN), Risø National Laboratory, Roskilde, Denmark, April 1997.

[35] B. J. Duggan, M. Sindel, G. D. Köhlhoff, and K. Lücke. Oriented nucleation, oriented growth and twinning in cube texture formation. *Acta Metallurgica et Materialia*, 38(1):103–111, 1990.

[36] C. A. Verbraak. The application of the Rowland mechanism to the problem of the nucleation of secondary crystals in cube–texture copper. *Acta Metallurgica*, 8(2):65–70, 1960.

[37] B. J. Duggan, K. Lücke, G. D. Köhlhoff, and C. S. Lee. On the origin of cube texture in copper. *Acta Metallurgica et Materialia*, 41:1921–1927, 1993.

[38] C. Giacovazzo, H. L. Monaco, D. Viterbo, F. Scordari, G. Gilli, G. Zanotti, and M. Catti. *Fundamentals of crystallography*. Number 2 in IUCr texts on crystallography. Oxford University Press, Oxford, UK, 1. edition, 1995.

[39] P. Haasen. Direct observation of nucleation and formation of the recrystallization texture in deformed single crystals of Cu, Al, CuP. In

N. Hansen, D. Juul Jensen, T. Leffers, and B. Ralph, editors, *7th Risø International Symposium on Metallurgy and Materials Science*, pages 69–74, Roskilde, DK, 1986. Risø National Laboratory.

[40] S. Mahajan, C. S. Pande, M. A. Imam, and B. B. Rath. Formation of annealing twins in f.c.c. crystals. *Acta Mellurgica*, 45(6):2633–2638, 1997.

[41] F. J. Humphreys. Nucleation of recrystallization in metals and alloys with large particles. In N. Hansen, A. R. Johns, and T. Leffers, editors, *1st Risø International Symposium on Metallurgy and Materials Science*, pages 35–49, Roskilde, DK, 1980. Risø National Laboratory.

[42] R. Sandstöm. Criteria for nucleation of recrystallization around particles. In N. Hansen, A. R. Johns, and T. Leffers, editors, *1st Risø International Symposium on Metallurgy and Materials Science*, pages 45–49, Roskilde, DK, 1980. Risø National Laboratory.

[43] D. Tabor. *The hardness of metals*. Oxford University Press, 2000.

[44] A. R. Jones, B. Ralph, and N. Hansen. Subgrain coalescence and the nucleation of recrystallization at grain–boundaries in aluminum. In *Proc. Royal Soc. 368A*, pages 345–357. Royal Soc. London, 1979.

[45] E. Grant, D. Juul Jensen, and B. Ralph. A determination of the texture of a directionally solidified sample of high–purity copper. *Journal of Materials Science*, 21(5):1688–1692, 1986.

[46] D. J. Dingley and V. Randle. Microtexture determination by electron backscatter diffraction. *Journal of Materials Science*, 27(17):4545–4566, 1992.

[47] D. J. Dingley. Progressive steps in the development of electron backscatter diffraction and orientation microscopy. *Journal of Microscopy*, 213(3):214–224, 2004.

[48] H. S. Peiser, H. P. Rooksby, and A. J. C. Wilson, editors. *X–ray diffraction by polycrystalline materials*. Physics in Industry. Chapman & Hall, London, 1960.

[49] Neutron and synchrotron radiation for condensed matter studies. In J. Baruchel, J. L. Hodeau, M. S. Lehmann, J. R. Regnard, and C. Schlenker, editors, *Theory, Instruments and Methods + Applications to Solid State Physics and Chemistry*, volume 1+2. Springer–Verlag, Berlin Heidelberg, 1993, 1994.

[50] D. Juul Jensen and H. F. Poulsen. Recrystallization in 3D. In N. Hansen et al., editors, *Proceedings of the 21th Risø International Symposium on Materials Science: Recrystallization — fundamental aspects and relations to deformation microstructure*, pages 103–124, Roskilde, DK, 2000. Risø National Laboratory.

[51] URL: http://www.hardnesstesters.com.

[52] N. Hansen and R. A. Vandermeer. *Encyclopedia of condensed matter physics*, chapter Mechanical Properties: recovery, recrystallization and grain growth. 2004.

[53] T. Maitland. Electron backscatter diffraction. *Advanced Materials & Processes*, 162(5):34–36, 2004.

[54] V. Randle and B. Ralph. Application of electron back scattering to the measurement of grain misorientation texture. In *Institute of physics conference series*, volume 93, pages 231–232, Bristol, UK, 1988. IOP Publishing Ltd.

[55] D. J. Dingley, K. Z. Baba-Kishi, and V. Randle. *Atlas of backscattering Kikuchi diffraction patterns*. Inst of Physics Pub Inc, 1995.

[56] V. Randle and O. Engler. *Introduction to texture analysis: macrotexture, microtexture and orientation mapping*. CRC Pr I Llc, 2000.

[57] H. F. Poulsen. 3DXRD — a new probe for materials science, February 2004. Doctoral thesis at the Technical University of Denmark, Lyngby, DK.

[58] U. Lienert, H. F. Poulsen, and Å. Kvick. Mesoscale structural characterization within bulk materials by high-energy x-ray microdiffraction. *AIAA JOURNAL*, 39(5):919–923, May 2001.

[59] B. E. Warren. *X–ray diffraction*. Springer Tracts in Modern Physics. Dover Publication Inc., New York, 1. edition, 1990.

[60] A. C. Thompson, editor. *X–ray Data Booklet*. Lawrence Berkeley National Laboratory, Berkeley, USA, 2. edition, 2001.

[61] H. F. Poulsen, S. Garbe, T. Lorentzen, D. Juul Jensen, F. W. Poulsen, N. H. Andersen, T. Frello, R. Feidenhans'l, and H. Graafsma. Applications of high–energy synchrotron radiation for structural studies of polycrystalline materials. *Journal of Synchrotron Radiation*, 4:147–154, 1997.

[62] H. F. Poulsen, S. F. Nielsen, E. M. Lauridsen, S. Schmidt, R. M. Suter, U. Lienert, L. Margulies, T. Lorentzen, and D. Juul Jensen. Three–dimensional maps of grain boundaries and the stress state of individual grains in polycrystals. *Journal of Applied Crystallography*, 34:751–756, 2001.

[63] H. F. Poulsen and Xiaowei Fu. Generation of grain maps by an algebraic reconstruction technique. *Journal of Applied Crystallography*, 35:1062–1068, 2003.

[64] L. Margulies, G. Winther, and H. F. Poulsen. In situ measurement of grain rotation during deformation of polycrystals. *Science*, 291:2392–2394, 2001.

[65] E. M. Lauridsen, D. Juul Jensen, H. F. Poulsen, and U. Lienert. Kinetics of individual grains during recrystallization. *Scripta Materialia*, 43:561–566, 2000.

[66] C. Gundlach, W. Pantleon, E. M. Lauridsen, L. Margulies, R. D. Doherty, and H. F. Poulsen. Direct observation of subgrain evolution during recovery of cold-rolled aluminium. *Scripta Materialia*, 50(4):477–481, 2004.

[67] S. Schmidt, H. F. Poulsen, and G. B. M. Vaughan. Structural refinements of the individual grains within polycrystals and powders. *Journal of Applied Crystallography*, 36:326–332, 2003.

[68] S. F. Nielsen. *Synchrotron X–Ray Radiation and Deformation Studies*. PhD thesis, University of Copenhagen, DK, November 2000. Risø–R–1289(EN).

[69] S. Schmidt, S. F. Nielsen, L. Margulies, X. Huang, and D. Juul Jensen. Watching the growth of bulk grains during recrystallization of deformed metals. *Science*, 305:229–232, 2004.

[70] N. C. K. Lassen. *Automated determination of crystal orientations from electron backscattering patterns*. PhD thesis, Technical University of Copenhagen, Lyngby, DK, 1994. IMM–PHD–1994–3.

[71] J. Hjelen. Teksturudvikling i aluminium, studert ved elektronmikrodiffraksjon (EBSP) i scanning elektronmikroskop, 1990. Doctoral thesis at the University of Trondheim, Norway.

[72] N. C. Krieger Lassen, D. Juul Jensen, and K. Conradsen. Image procedures for analysis of electron back scattering patterns. *Scanning Microscopy*, 6(1):115–121, 1992.

[73] B. L. Adams. Orientation imaging spectroscopy: Application to measurement of grain boundary structure. *Mat. Sci. Eng.*, 166(A):59, 1993.

[74] R. A. Vandermeer. Edge–nucleated, growth controlled recrystallization in aluminium. *Transactions of the Metallurgical Society of Aime*, 215:577–588, August 1959.

[75] C. Y. Hung, G. Spanos, R. O. Rosenberg, and M-V. Kral. Three-dimensional observations of proeutectoid cementite precipitates at short isothermal transformation times. *Acta Materialia*, 50(15):3781–3788, 2002.

[76] T. Yokomizo, M. Enomoto, O. Umezawa, G. Spanos, and R. O. Rosenberg. Three-dimensional distribution, morphology, and nucleation site of intragranular ferrite formed in association with inclusions. *Materials Science and Engineering A*, 344(1–2):261–267, 2003.

[77] M. A. Wall, A. J. Schwartz, and L. Nguyen. A high–resolution serial sectionin speciment preparation technique for application to electron backscatter diffraction. *Ultramicroscopy*, 88:73–83, 2001.

[78] Koji Matsumaru and Atsushi Takata. Fabrication of porous metal bonded diamond grinding wheels for flat surface nanomachining. *MRS Bulletin*, pages 544–546, July 2001.

[79] Logitech Ltd. URL: http://www.logitech.uk.com.

[80] J. Reffs, J. Larsen, K. Hanneson, R. Nemholt, and U. Bhatti. 3D Visualisering af kornstruktur. RUC semester report RUC 2. semester NAT–BAS Hus 13.1, gruppe 7, Roskilde University, Roskilde, Denmark, Spring 2004.

[81] D. Juul Jensen and K. Hanneson. Comparison of microstuctures obtained by 3DXRD analysis and EBSP using serial sectioning. to be submitted in Metallurgical Transactions, 2004.

[82] X. Y. Lu, C. D. Cao, M. Kolbe B. Wei, and D. M. Herlach. Microstructure analysis of Co–Cu alloys undercooled prior to solidification. *Mat. Sci. Eng.*, 2004. article in press.

[83] H. Elias, editor. *Stereology*. Springer Verlag, New York, 1967.

[84] K. J. Kurzydlowski and B. Ralph, editors. *Stereology*. Springer Verlag, New York, 1967.

[85] J. W. Cahn and W. C. Hagel. *Decomposition of Austinite by Diffusional Processes*, chapter Theory of the Pearlite Reaction, pages 131–196. Interscience Publishers, 1 edition, 1962.

[86] R. T. Dehoff. The analysis of the evolution of particle size distribution during microstructural change. *Metallurgical Transactions*, 2:521–526, 1971.

[87] F. G. Yost. An extension of the Dehoff growth path analysis. *Metallurgical Transactions A*, 6A:1607–1611, 1975.

[88] N. C. K. Lassen, 2001. Personal communication.

[89] N. C. Krieger Lassen and D. Juul Jensen. Automatic recognition of recrystallized grains in partly recrystallized samples from crystal orientation maps. In *Proceedings of the twelfth International Conference of Textures of Materials*, volume 2, pages 854–859, Ottawa, CA, 1999. NRC Research Press.

[90] H. Jazaeri and F. J. Humphreys. Quantifying recrystallization by electron backscatter diffraction. *Journal of Microscopy*, 213(3):241–246, 2004.

[91] R. A. Vandermeer and D. Juul Jensen. Microstructural path and temperature dependence of recrystallization in commercial aluminium. *Acta Materialia*, 49:2083–2094, 2001.

[92] E. Knuth-Winterfeldt. *The Knuth–system of electropolishing*. H. Struers Chemiske Laboratorium, Copenhagen, Denmark, 5. edition, 1959.

[93] E. S. Andersen, P. Jespersgaard, and O. G. Østergaard. *Databog fysik kemi*. F & K Forlaget, 10. edition, 1986.

[94] E. M. Lauridsen, S. Schmidt, R. M. Suter, and H. F. Poulsen. Tracking: a method for structural characterization of grains in powders or polycrystals. *Journal of Applied Crystallography*, 34:744–750, 2001.

[95] ESRF Homepage:. http://www.esrf.fr.

[96] R. J. Dejus and M. S. del Rio. Xop: A graphical user interface for spectral calculations and x-ray optics utilities. In *Proceedings of the conference on Synchrotron Radiation Instrumentation '95*, volume 67. Rev. Sci. Instrum., 1996.

[97] ID11 Homepage:. http://www.esrf.fr/exp_facilities/ID11/handbook/welcome.html.

[98] Jonathan Wright, 2004. Private communication.

[99] C. Schulze, U. Lienert, M. Hanfland, M. Lorenzen, and F. Zontone. Microfocusing of hard X–rays with cylindrically bent crystal monocromators. *Journal of Synchrotron Radiation*, 5:77–81, 1998.

[100] C. B. Mammen. Meridional horizontal focusing by bent diamond Laue monochromator. University of Copenhagen, Denmark, 2001.

[101] C. B. Mammen, 2004. Private communication.

[102] C. B. Mammen, T. Ursby, M. Thunnissen, and J. Als-Nielsen. Bent diamond crystals and multilayer based optics at the new 5–station protein crystallography beamline 'cassiopeia' at MAX–lab. In T. Warwick

et al., editors, *Synchrotron Radiation Instrumentation: Eighth International Conference*, pages 808–811. American Institute of Physics, 2004.

[103] G. R. Speich and R. M. Fischer. Recrystallization in rapidly heated 3 1/4% silicon iron. In H. Margolin, editor, *Recrystallization, grain growth and textures*, pages 563–598, Metals Park, USA(OH), 1966. Amer. Soc. for Metals.

[104] J. H. Hubbel, Wm. J. Veigele, E. A. Briggs, R. T. Brown, D. T. Cromer, and R. J. Howerton. Atomic scattering factors, incoherent scattering functions, and photon scattering cross sections. *J. Phys. Chem. Ref. Data*, 4(3):471–538, 1975.

[105] O. V. Mishin, B. Bay, and D. Juul Jensen. Through–thickness texture gradients in cold–rolled aluminium. *Metallurgical and Materials Transactions A*, 31A:1653–1662, 2000.

[106] X. Huang, T. Leffers, and N. Hansen. Comparison between microstructural evolution in aluminium and copper deformed by cold rolling. In J. Bilde Sørensen et al., editors, *20th Risø International Symposium on Metallurgy and Materials Science*, pages 365–374, Roskilde, DK, 1999. Risø National Laboratory.

[107] X. Huang, 2004. Private communication.

[108] P. Gordon. Microcalorimetric investigation of recrystallization of copper. *Trans. AIME*, 203(9):1043–1052, 1955.

[109] J. R. Bowen, E. M. Lauridsen, and J. Teuber, 2004. Private communication.

[110] A. P. Hammersley, S. O. Svensson, M. Handfland, A. N. Fitch, and D. Häusermann. Two–dimensional detector software: From real detector to idealised image or two–theta scan. *High Pressure Research*, 14(4–6):235–248, 1996.

[111] A. P. Hammersley, S. O. Svensson, A. Thompson, H. Graafsma, A. Kvick, and J. P. Moy. Calibration and correction of distortion in 2–dimensional detector systems. *Review of Scientific Instruments*, 66(3):2729–2733, March 1995.

[112] C. Kittel. *Introduction to Solid State Physics*. John Wiley & Sons, 7. edition, 1996.

[113] O. V. Mishin, E. M. Lauridsen, N. C. Krieger Lassen, G. Brückner, T. Tschentscher, B. Bay, D. Juul Jensen, and H. F. Poulsen. Application of high–energy synchrtron radiation for texture studies. *Journal of Applied Chrystallography*, 33:364–371, 2000.

[114] T. Leffers, 2004. Personal communication.

[115] G. Wu, 2004. Personal communication.

[116] H. J. Bunge. *Texture analysis in materials science*. Butterworth, London, 1982.

[117] R. A. Vandermeer. The recrystallization characteristics of moderately deformed aluminum. *Metallurgical Transactions*, 1(5):819–826, 1970.

[118] A. T. English and W. A. Backofen. Recrystallization in hot–worked silicon iron. *Trans. Met. Soc. AIME*, 230:396–403, 1964.

[119] R.D. Doherty, A. R. Rollet, and D. J. Srolovitz. Structural evolution during recrystallization. In N. Hansen, D. Juul Jensen, T. Leffers, and B. Ralph, editors, *7th Risø International Symposium on Metallurgy and Materials Science*, pages 53–67, Roskilde, DK, 1986. Risø National Laboratory.

A1

ELSEVIER

Materials Characterization 51 (2003) 271–282

MATERIALS CHARACTERIZATION

Automatic determination of recrystallization parameters in metals by electron backscatter pattern line scans

Axel W. Larsen*, Dorte Juul Jensen

Center for Fundamental Research: Metal Structures in Four Dimensions, Risø National Laboratory, PO Box 49, 4000 Roskilde, Denmark

Received 14 December 2003; received in revised form 7 January 2004; accepted 14 January 2004

Abstract

In this paper, a new automatic procedure for determining critical recrystallization parameters, which are important when studying recrystallization kinetics, is presented. The method is based on electron backscatter patterns (EBSP) line scans using a scanning electron microscope, where three parallel lines are scanned. The concepts of equivalence and connectivity are used to group the data points into those originating in recrystallized grains and those originating in the deformed matrix. The computer program implementing the automatic procedure is tested in three different ways: three short scans are performed, where the calculations are also done by hand; the results of two long scans are compared to the direct observation of the microstructure seen in orientation image maps (OIMs) [Mater. Sci. Eng. A. 166 (1993) 59], and the results of scans from a series of samples are compared to statistical results obtained manually. A good correlation was achieved in all three cases.

Keywords: LSGRAINS; EBSP; Line scans; Recrystallization; Metals

1. Introduction

In the characterization of recrystallizing microstructures it is often important to determine the three parameters: the volume fraction recrystallized (V_V), the interfacial area separating recrystallized grains from the deformed matrix (S_V), and the mean recrystallized grain intercept length ($\langle\lambda\rangle$) [2].

For example, using the method of Cahn and Hagel, V_V and S_V are used for an exact determination of the average growth rate ($\langle G\rangle$) of the recrystallizing grains in the microstructure [3]:

$$\frac{dV_V}{dt} = \langle G\rangle S_V \quad (1)$$

An efficient way to determine these parameters is by the linear intercept method, which uses random line scans through the microstructure, and where the interfaces between recrystallized grains and the de-

* Corresponding author. Tel.: +45-46775783; fax: +45-46775758.

E-mail address: axel.wright.larsen@risoe.dk (A.W. Larsen).

URL: http://www.metals4d.dk.

1044-5803/$ - see front matter © 2004 Elsevier Inc. All rights reserved.
doi:10.1016/j.matchar.2004.01.001

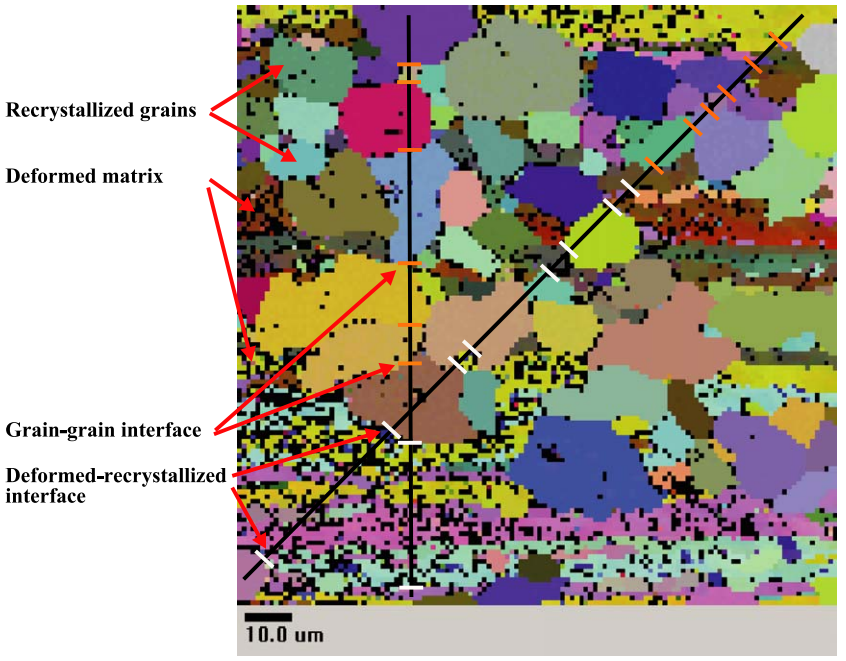

Fig. 1. EBSP OIM showing a recrystallizing microstructure is shown with two lines drawn through it [1]. Examples of recrystallized and deformed grains are identified by the red arrows, and where the drawn lines cross an interface this is marked orange for a recrystallized–recrystallized interface and white for a deformed–recrystallized interface.

formed matrix are noted (see Fig. 1) [4]. In this case V_V, S_V, and $\langle\lambda\rangle$ can be written as [3,5]:

$$V_V = \frac{L_{rex}}{L} \tag{2}$$

$$S_V = \frac{2n_{int}}{L} \tag{3}$$

$$\langle\lambda\rangle \equiv \frac{1}{N}\sum_{i=1}^{N}\lambda_i \tag{4}$$

where L is the total length of the scanned line, L_{rex} is the total length of the line in recrystallized material, n_{int} is the number of interfaces between recrystallized and deformed material crossed by the line, N is the number of grains intersected by the line, and λ_i is the intersect length of the ith grain.

If the orientations of the recrystallized grains are also determined, as it is possible by electron backscatter patterns (EBSP), V_V, S_V, and $\langle\lambda\rangle$ may be determined for the individual orientations. Therefore, the average growth rate for grains of different crystallographic orientations can also be determined, e.g., cube ($\langle 100\rangle$ $\{001\}$) oriented grains in fcc metals [6] or γ-fibre grains in bcc metals [7].

This approach to determining the parameters is adopted in the present work, where the EBSP technique is used. A previous technique, also based on EBSP, but scanning a *single* line was found to give an accurate determination of V_V and $\langle\lambda\rangle$, but S_V typically differed by one order of magnitude from the value obtained by manual scans (Krieger Lassen, private communication, 2001). In this paper, we present a new method based on scanning three parallel lines, the outer two of which are used solely as auxiliary lines to support the data points on the central line.

Alternatively, one may consider making the measurement by EBSP in full 2-D, which may even be a possibility as the EBSP data acquisition rate is constantly increasing (at present, up to 10–60 patterns/s).[1] However, as an efficient method for determination of

[1] Numbers from the homepages of: HKL Technology (http://www.hkltechnology.com), and TSL (http://www.edax.com/TSL/).

V_V, S_V, and $\langle\lambda\rangle$ is based on the linear intercept method, all the data points away from this line are redundant, and the measuring time is better spent measuring longer lines, which will intersect more grains than a 2-D scan, thus giving superior sampling statistics.

2. The procedure

The procedure is to scan along a line through the microstructure collecting EBSP orientation data at each step along the line. Going through the data, one of three specifications is allocated to every data point: recrystallized, deformed, or bad. Based on these specifications, it is determined which data points belong to which recrystallized grain and which data points belong to the deformed matrix.

This indexing is done using an algorithm called LSGRAINS, which has been specially developed for three-line scans (see Section 2.1): that is, a central line with two parallel auxiliary lines (an upper and a lower). Only the data points on the central line are considered "real" data points and are thus used to calculate V_V, S_V, and $\langle\lambda\rangle$. The data points on the auxiliary lines are *only* used to determine whether a data point on the central line is a part of a recrystallized grain or the deformed matrix, and to make sure that the correct orientation is attributed to a given data point in the case when this data point is incorrectly indexed (i.e., "bad").

The pivotal part of the algorithm is the concept of *equivalent* crystallographic orientation. Two data points are said to have equivalent orientation if their mutual misorientation is less than a user-specified limit—this is normally set to the resolution of the EBSP system (typically, 0.5–1.0°).

2.1. The three-line scan

The three-line scans (see Fig. 2) consist of three parallel lines: a central line with an upper and a lower auxiliary line. These auxiliary lines have the same step size as the central line, and are at the same distance to the central line as the step size. They function as a pair of reference lines for the central line, helping the algorithm determine whether a data point belongs to a recrystallized grain or the deformed matrix (Fig. 5 shows examples of real three-line scans).

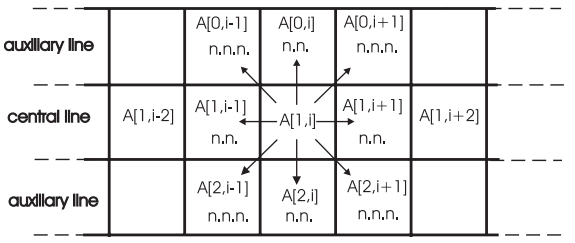

Fig. 2. The environment around the *i*th data point on the central line. The arrows indicate which neighboring data points are compared with the *i*th data point. If the *i*th and $(i-1)$ data points are both recrystallized and of the same orientation, then both data points belong to the same grain.

For a given data point, it is first determined whether the data point is "good" or "bad." Bad data points are data points with less correctly indexed EBSP Kikuchi bands than a user-preset limit [8]. If a data point is not bad (i.e., good) then it belongs to either the recrystallized or the deformed microstructure.

A *recrystallized* data point is a good data point (on the *central* line) that has the same crystallographic orientation as a user-specified minimum number of its neighboring data points on all three lines (see the arrows in Fig. 2), while a *deformed* data point is a good data point that does not satisfy this condition.

The single data point specifications are then compared from the start of the line and onwards, and built one on top of each other into a complete picture of the microstructure (recrystallized grains, deformed regions, and bad data points) along the *central* line, somewhat like beads on a string.

Additional routines, which will be described in detail in Sections 2.3 and 2.4, exist to improve the results based on geometry and growth kinetics. These corrections are applied in an iterative process. Finally, a routine orders the detected grains into groups according to which texture component they belong.

The corrections are to repair bad data points by (if possible) allocating the most representative orientation surrounding that specific data point, to eliminate too small deformed areas within/between recrystallized grains, to discard recrystallized grains without at least *one* high-angle boundary, and to discard too small recrystallized grains. An overview of the application of these corrections can be seen in Section 2.4.

2.2. The definition of a recrystallized grain

In order to identify recrystallized grains, it is essential to first precisely define what criteria we place on a grain.

A grain starts as a nucleus with a specific orientation. Theory has it that a nucleus must have a minimum size in order to overcome its surface tension and start growing [9,10]. Nuclei then grow by grain boundary migration into the deformed matrix, which is facilitated by high-angle boundaries of high mobility [2]. It is clear that our definition of grains in three-line scans must mirror these observations.

A data point must exhibit a minimum connectivity (i.e., number of good neighbors of equivalent crystallographic orientation); the grain must have a minimum intercept length; and at least one of its encompassing grain boundaries *must* be of high angle (generally, 15° for grain-deformed) to be considered recrystallized.

Using Fig. 3 as an example, we can see what the preset parameter "minimum data point connectivity" (pixcon) does. It is an integer that is equal to the number of neighboring data points *including* the central data point itself, which are of equivalent orientation to the central data point. Only properly indexed (i.e., good) data points have a connectivity. In Fig. 3, the data point called Equiv has three equivalent neighbors (shown by the solid arrows) and also counting itself, it therefore gets a connectivity of 4.

For pixcon ≥ 4, the three central good data points (coloured dark grey) within the grain boundaries on the central line are counted as being recrystallized. The leftmost data point has only a connectivity of 2; the second from the right is bad, and the rightmost data point has only a connectivity of 3. If the bad data point is repaired (see Section 2.3), the rightmost data point will have connectivity of 4, and will therefore also belong to the recrystallized grain.

If the distance between the two determined grain boundaries is less than the user-specified minimum intercept length λ_{min}, the grain will be rejected as too small. On Fig. 3 for (pixcon ≥ 4), the unrepaired grain satisfies $\lambda_{min} = 3$, and the repaired grain satisfies $\lambda_{min} = 5$.

If either one of the grain boundaries is of high angle, i.e., has a misorientation angle of more than the user-specified limit (generally, 15° for grain-deformed or 2° for grain–grain interfaces) the grain is accepted as being a recrystallized grain. For pixcon ≥ 4, it can be seen that this condition will not be fulfilled unless we perform the repair, as neither of the boundaries of the unrepaired grain will be of high angle.

2.3. Repairing bad data

In a data set some of the data points will yield fewer correctly indexed EBSP Kikuchi bands than the minimum specified by the user. For a minimum of five indexed Kikuchi bands, the bad data points generally number 2–20% of the data points, but this

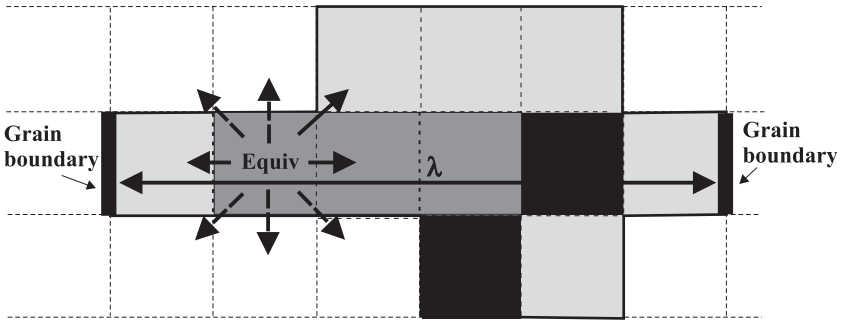

Fig. 3. Pixcon = 4, $\lambda_{min} = 2$ steps. A recrystallized grain is seen surrounded by the black line. Black squares indicate bad data points. The long line λ is the intercept length of the grain. The arrows around Equiv show which neighboring data points are tested for equivalence with the central data point (a solid arrow indicates equivalence; and a dashed arrow indicates nonequivalence). Thus, the data point has a connectivity of 4 (itself + 3 equiv. neighbors), and will thus be considered recrystallized. The dark grey area shows which data points initially satisfy a connectivity of 4.

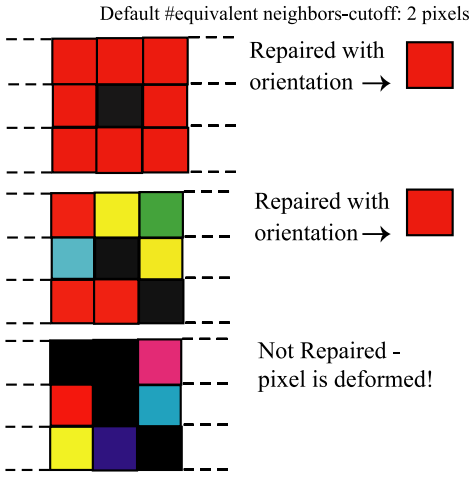

Fig. 4. Here is shown three different scenarios for repairing a bad data point. (Upper) Data point within a grain, (middle) data point outside a grain, and (lower) a nonreparable data point.

varies with the material, the quality of the polished surface, the grain/subgrain size, the length of the scan (microscope losing focus), and even the orientation of the backscattering grains.

The way we repair is by allocating the orientation (**G** matrix) of one of the neighboring data points to the bad data point. This is based on using the most common orientation amongst all the neighboring data points of the bad data point (see Fig. 2). Certain criteria exist for choosing this orientation. Firstly, a minimum number of user-specified neighbors *must* have equivalent orientations (normally, two or more). Secondly, if the bad data point lies next to a grain, preference is given to the orientation of that grain if it satisfies the first criteria. Some examples of repairing a bad data point are given in Fig. 4.

2.4. The algorithm

The algorithm goes through a series of iterations, which steadily refine the data processing by applying default and user-specified refining procedures.

The data are taken from a string and ordered in a $3 \times n_{\text{points}}$ array (see Figs. 2 and 5). The EBSP data file contains information such as Euler angles, *xyz* scan coordinates, the number of indexed EBSP Kikuchi bands, acquisition method, acquisition time, etc.

Before the first iteration, every data point $A[1,i]$ is checked to see if it satisfies the minimum number of successfully indexed EBSP Kikuchi bands (normally, 5). A data point that satisfies this condition is termed "good," and one that does not is termed "bad."

2.4.1. First iteration

Each good data point on the central line is checked for equivalence with all its good neighbors. This is done by checking how many of the neighboring data points are of equivalent orientation (i.e., their misorientation angle is less than the angular resolution of the EBSP system).

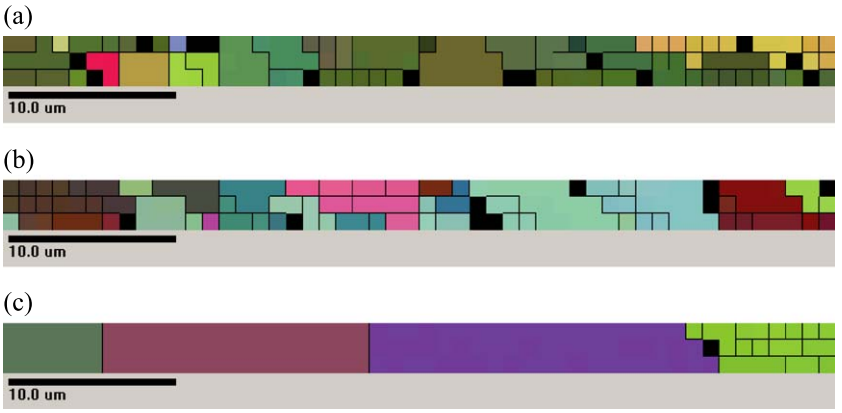

Fig. 5. Orientation plot of three-line scans (3 × 50 steps, 1-μm step size) of AA1050-aluminium sample at various annealing times. The black lines indicate a misorientation of $\Theta \geq 1.0°$ between neighboring data points, and black spots are bad data points. The samples were annealed in an oil bath at 250 °C for (a) 300, (b) 2000, and (c) 28,000 s, respectively.

If the number of equivalent data points is equal to or greater than the user-specified limit (normally, 5 or more), the data point is considered to belong to a recrystallized grain. Otherwise, it is considered to belong to the deformed matrix. The individual data points are allocated an ID number corresponding to their present status: "rex" (positive integer), "bad" (0), or "def" (-1).

2.4.2. Second iteration

Each bad (ID number = 0) data point on the central line is optionally run through a routine that attempts to allocate a new good orientation to that data point. This orientation is taken from the most common orientation amongst the neighboring data points (see Fig. 4), with preference for the orientation of neighboring grains. This is done by checking the neighbors for equivalence with each other. The orientations of the data points (on the line) to the left and right ($A[1, i-1]$ and $A[1, i+1]$) are checked first to see if they are "rex." This is to ensure that additional grains are not wrongly introduced into the data set.

If the most representative orientation is shared by a user-specified minimum number of equivalent data points (normally 2), the bad data point is termed good and given that orientation (**G** matrix). If not, the bad data point is termed "def" (ID number = -1).

2.4.3. Third iteration

The first iteration is done once more, but this time all data points are considered to be good or repaired; that is, data points are only recrystallized or deformed.

The data points are grouped into individual recrystallized grains, or the deformed matrix, and the location, type, and misorientation angle of each grain boundary is determined.

During this grouping, deformed data points belonging to a deformed region, with a smaller intercept length than a user-specified minimum length and bounded by recrystallized material, are automatically assumed to be measurement errors, and are added to the neighboring recrystallized grain(s).

2.4.4. Fourth iteration

Each grain is then checked to see if it has at least one high-angle boundary (normally, $\Theta \geq 15°$ for grain–deformed or $\Theta \geq 2°$ for grain–grain boundaries). Grains that cannot satisfy these criteria are rejected and treated as deformed material.

2.4.5. Fifth iteration

Each remaining grain is checked to see if it satisfies a user-specified minimum grain intersect length $\langle\lambda\rangle$ (normally, 1–3 times the step size). Grains that cannot satisfy this criterion are rejected and treated as cells in the deformed matrix.

2.5. Parameters

The following are the user-set parameters in the algorithm. These parameters have default settings, but the parameters need to be set and tested for each series of experiments if a different material is used. This can be done by comparing the algorithm's results with what is obtained from inspecting the orientation image map (OIM) of a three-line scan (see Section 3.1). Below is a list of the parameters, their capital letter codes, and their default values for aluminium.

min indexed bands: minimum number of correctly indexed Kikuchi bands from the EBSP (default: $M = 5$).

min data point connectivity: minimum number of equivalent data points around and including data point $A[1,i]$ (default: $C = 5$).

max misorientation: maximum allowed point-to-point misorientation between equivalent data points (default: $D = 1.0°$).

min boundary misorientation: minimum accepted misorientation across a "high" angle boundary (default: $X = 15.0°$ for grain-deformed, and $Y = 2.0°$ for grain–grain).

min grain intercept length: minimum accepted intercept length of a recrystallized grain *along* the line (default: $L = 3$ step lengths for 1 μm steps).

min deformed region intercept length: minimum accepted intercept length of a deformed region along the line (default: $I = 3$ step lengths for 1 μm steps).

min equivalent neighbors: minimum number of neighboring data points of equivalent orientation needed to repair a bad data point (default: $N = 2$ data points).

repair: try to repair bad data points (default: R = YES).

Table 1
Short line scans—3 × 200 data point line scans with a step size of 1 μm were performed on the 300-, 2000-, and 28,000-s samples

Time (s)	$V_{V,vis}$	$V_{V,auto}$	$S_{V,vis}$	$S_{V,auto}$	$\langle\lambda\rangle_{vis}$	$\langle\lambda\rangle_{auto}$
300	0.05	0.04	0.05	0.05	3.5	4.0
2000	0.04	0.04	0.04	0.04	3.5	4.0
28,000	0.66	0.67	0.11	0.11	14.6	14.8

The chosen parameters were $M=5$, $D=1.0°$, $C=5$, $L=3$, $I=1$, R = NO, B = YES, $Y=2°$, $X=15°$.

check boundaries: check the grain boundaries of each grain to see if it has at least one high-angle boundary.

In general, the stricter the requirements that are placed on data to be accepted as coming from recrystallized grains, the lower V_V will of course be. Discarding grains may cause S_V to either go up or down, generally depending on the degree of recrystallization in the scanned material. This is because the number of recrystallized–deformed interfaces depends on the local microstructure around the discarded grains, so discarding a grain may do anything in between removing or creating two interfaces. $\langle\lambda\rangle$ generally goes up with stricter requirements because only bigger and more developed grains are likely to satisfy stricter criteria.

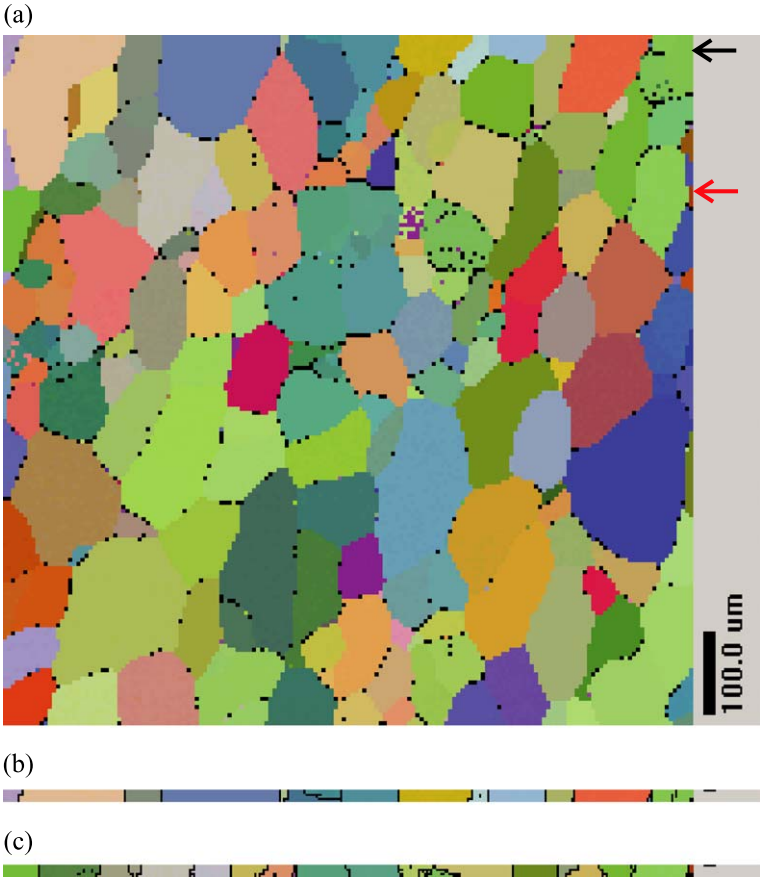

Fig. 6. (a) EBSP OIM (169 × 169 data points in 5 μm steps) of AA1050-aluminium, cold rolled 60%, and annealed for 1 h at 550 °C. The sample is fully recrystallized; note how the bad data points (the black spots) are largely constrained to the grain boundaries. Three-line scans were extracted from the topmost three lines and three lines one-fourth of the way down rows of the data file to use as three-line scans (3 × 169 steps). (b) Three topmost horizontal lines of the 2-D map (black arrow). (c) Three horizontal lines one-fourth of the way from the top of the 2-D map (red arrow).

Table 2
Extracted line scans—3 × 169 data point line scans with a step size of 5 μm were performed on the 300-, 2000-, and 28,000-s samples

Scan	$V_{V,OIM}$	$V_{V,auto}$	$S_{V,OIM}$	$S_{V,auto}$	$\langle\lambda\rangle_{OIM}$	$\langle\lambda\rangle_{auto}$
Middle	0.98	0.99	0.01	0.01	48.2	45.8
Top	1.00	1.00	0.00	0.00	59.6	59.6

The chosen parameters were: $M=5$, $D=1.0°$, $C=5$, $L=1$, $I=2$, R = YES, B = YES, $Y=2°$, $X=15°$.

It has been chosen *not* to include the quality factor (Q/A) as a parameter. Previous analysis based on Q/A has shown that Q/A goes up with increased deformation. However, from many investigations of recrystallizing aluminium and copper, it is our experience that many other factors affect Q/A, and that Q/A does not give a good measurement of V_V [11].

3. Validation

3.1. Experiment

To test the program it was run on three different types of scans.

(a) Three short (200 steps) 3 line scans were performed on three different samples, which had been annealed for different lengths of time. By performing short 3 line scans, the OIMs of the scans could to be printed on paper (see Fig. 5), allowing us to perform the same calculations as are performed by the algorithm on the orientation data by visual inspection and directly compare the results of the algorithm with the results it should produce if working properly. The calculations were performed by going through the data points on the central line and noting how many of the neighboring data points had orientations within 1° of the data point being inspected, as is clearly visible from the plots, where misorientations with $\Theta \geq 1°$ are marked by black lines. Additional plots were made with lines drawn for misorientations greater than 2° and 15° to allow the identification of boundaries of high angle. By choosing not to repair bad data points and not to ignore short deformed regions no error crept in that way. In addition, the visual inspections allowed us to determine whether a correctly functioning routine would misinterpret features within the microstructure. The results of the visually based and automatic calculations can be seen in Table 1.

(b) Two 3 line scans were extracted from the data file of a large 2-D scan of a fully recrystallized microstructure, where it was possible to identify the recrystallized grains by direct visual inspection of the OIM (which can be seen in Fig. 6). This allowed for a more direct comparison than in (a), and also allowed us to see that the program really could produce the crucial parameters $V_V=1.0$ and $S_V=0.0$ for a suitable data set. The results of the visual inspection and the automatic calculations can be seen in Table 2.

(c) A series of samples were annealed for different lengths of time were analyzed. Long (1000+ steps) 3 line scans were performed on these and data analysis was carried out with LSGRAINS. For comparison, manual line scans were also performed on the samples. This was done on both a statistical and a one-to-one basis. The statistical method consisted of comparing the results of *long* manual and automatic scans, where the scans were made long enough to include of the order of a hundred recrystallized grains to make the data sets from the two types of scans statistically comparable. The one-to-one comparisons consisted of scanning *precisely* the same line on the two samples manually and automatically. This allowed a direct comparison between the two methods, as it was possible to see what results were obtained

Table 3
Long line scans—3 × 1000+ data point line scans with a step size of 1 μm were performed on all the samples

Time (s)	$V_{V,man}$	$V_{V,auto}$	$S_{V,man}$	$S_{V,auto}$	$\langle\lambda\rangle_{man}$	$\langle\lambda\rangle_{auto}$
300	0.02	0.03	0.02	0.02	2.6	3.7
2000	0.07	0.05	0.05	0.03	3.5	4.3
11,000	0.22	0.22	0.09	0.08	5.8	7.1
20,000	0.60	0.89	0.06	0.05	14.2	12.8
28,000	0.21	0.43	0.05	0.09	6.9	8.5
38,000	0.37	0.43	0.05	0.08	13.5	14.5
55,000	0.78	0.93	0.03	0.03	23.8	16.7
72,000	0.96	0.64	0.02	0.10	18.1	13.1
86,400	0.87	0.89	0.05	0.05	16.7	15.2

The table shows the automatic vs. the manual results. The automatic results were based on the following choice of parameters: $M=5$, $D=1.0°$, $C=5$, $L=3$, $I=3$, R = YES, B = YES, $Y=2°$, $X=15°$.

from *exactly* the same microstructure. Manually scanning a sample corresponds to watching the EBSP on the SEM screen for changes while manually translating the sample translation stage. Deformed areas are characterized by a meandering EBSP, while the EBSP of a recrystallized grain is clear and does not move when the sample is translated. By noting down the changes in the EBSP, the grain boundaries between both recrystallized grains and between grains and deformed material are determined, giving the microstructure of the sample. The results of the long manual and automatic line scans can be seen in Table 3 and Fig. 7, while the results of the one-to-one comparisons can be seen in Table 4.

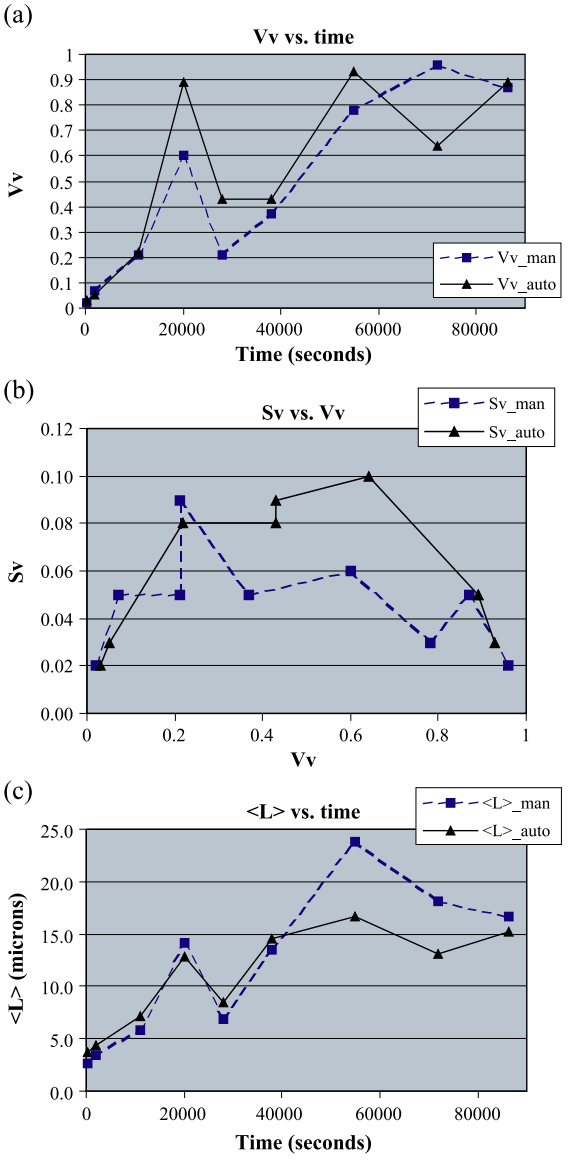

Fig. 7. The results from comparing long manual and automatic scans. (a) V_V vs. time, (b) S_V vs. V_V, (c) $\langle\lambda\rangle$ vs. time. Parameters are $M=5$, $D=1.0°$, $C=5$, $L=3$, $I=3$, R = YES, B = YES, $Y=2°$, $X=15°$.

Table 4
Directly compared manual and automatic line scans

Time (s)	L	$V_{V,man}$	$V_{V,auto}$	$S_{V,man}$	$S_{V,auto}$	$\langle\lambda\rangle_{man}$	$\langle\lambda\rangle_{auto}$
11,000	3	0.41	0.51	0.08	0.10	12.4	9.2
86,400	3	0.87	0.85	0.05	0.06	16.7	15.1
11,000	5	0.41	0.42	0.08	0.08	12.4	13.1
86,400	5	0.87	0.81	0.05	0.08	16.7	17.5

A step size of 1 μm was used, and the two samples were annealed for 11,000, and 86,400 s, respectively. The parameters were: $M=5$, $D=1.0°$, $C=5$, $L=3$ & 5, $I=3$, R = YES, B = YES, $Y=2°$, $X=15°$.

The same material was used for all tests of the algorithm. The material used in the studies was AA1050-aluminium (99.5% pure). This material is chosen because it has previously been used for extensive characterization and modelling [5]. In cases (a) and (c), the aluminium was cold rolled 90%, and then annealed in a 250 °C oil bath for 300, 2000, 11,000, 20,000, 28,000, 38,000, 55,000, 72,000, and 86,400 s. In case (b), the aluminium was cold rolled 60% and then annealed for 1 h in an air furnace at 550 °C, producing a fully recrystallized sample.

After annealing the RD-ND surface of the samples was mechanically and electrochemically polished to produce a surface suitable for EBSP measurements. For scans with a length of 1000+ μm a completely plane sample surface is very desirable. The samples were therefore mechanically lapped and polished on a Logitech[2] PM5D lapping and polishing machine using a PSM1 sample monitor, giving a height difference of only 1–2 μm across the sample surface [12]. The samples were electrochemically polished for 40 s at 12 V with an A2 electrolyte (12% H_2O, 70% ethanol, 10% ethylene glycol monobutyl ether, 7.8% HCl).

In all cases a JEOL JSM-840 scanning electron microscope with a LaB_6 filament was used to collect

[2] Logitech (http://www.logitech.uk.com/).

the EBSP data. The working distance was 22 mm, the electron beam current was 280 μA, and the voltage 20 kV.

The three short 3 line scans consisted of 3×200 data points with a step size of 1 μm, thus producing scans 200 μm long. The resulting scans can be seen in Fig. 5, where only the last 50 steps have been plotted to make the form of the data more obvious. The colors were generated by setting the red, green, and blue color levels proportional to the Euler angles, all black spots are bad points, and all point-to-point misorientations with $\Theta \geq 1.0^\circ$ are marked with black lines.

The two 3 line scans extracted from the already existing data file of a large (169×169 steps) 2-D scan had the dimensions 3×169. With a step size of 5 μm the total scan length was 840 μm. The full 2-D OIM and the two three-line scans extracted from it can be seen in Fig. 6.

Generally, the long 3 line scans have $3 \times 1000+$ data points in 1 μm steps, thus giving a line length of 1000+ μm. Great care was taken when mounting the samples because long line scans (1000+ μm) cover such a large horizontal distance that the sample surface will tend to move out of the microscope's focus if it is even slightly tapered. The solution to this problem was to align the firmly gripped samples in an optical microscope to get the scanning surface as horizontally flat as possible. When this is done, it is possible to perform line scans of lengths of the order of up to 10 mm with a 1 μm step size and down to 10% bad points (see Section 2.1).

3.2. Results

3.2.1. Short scans

To use a good nonsubjective test method, the three short scans (see Fig. 5) were analyzed visually and with LSGRAINS. *Exactly* the same criteria were used to define grains in the two procedures. The result of the short visual inspection and automatic line scans can be seen in Table 1.

The results show excellent agreement. The very slight scatter in V_V and $\langle\lambda\rangle$ comes from the slight uncertainty when measuring grain lengths on the paper printouts. Note that only grains intersected by all three lines were accepted as recrystallized grains by the algorithm. This indicates that the chance of accidentally indexing cells within the deformed matrix as recrystallized grains is very low.

3.2.2. Lines from large 2-D scans

Two 3 line scans were extracted from a large 2-D EBSP map. This 2-D map was done on a sample, which was fully recrystallized. The results are given in Table 2.

As in Section 3.2.1, the results show excellent agreement. The very slight scatter in V_V and $\langle\lambda\rangle$ again comes from the slight uncertainty when measuring grain lengths on the paper printouts. The choice of $L=1$ and $I=2$ is based on the step length of 5 μm, where small recrystallized grains with an intersect length of less than two step lengths (<10 μm) are very possible. Because of the poor indexing on the grain boundaries (see Fig. 6a), deformed areas less than two step lengths long are ignored.

3.2.3. Long scans

All of the comparisons between the manual and automatic long line scans were done along the rolling direction (RD) in the RD-ND plane. The long (1000+ data points) manual line scans were performed as described in Section 3.1. The number of grains intersected for each sample was in the range 64–251. The result of the long manual and automatic line scans can be seen in Table 3 as well as in Fig. 7.

As can be seen, there is some scatter in the data, but that is unavoidable due to the subjectivity of the manual method and that different parts of the microstructure are scanned.

The scatter is generally that the automatic method finds a higher V_V and S_V, indicating that maybe in the manual method some small recrystallized grains within the deformed matrix have been neglected (see Section 3.1).

It has to be noted that differences within the microstructure intersected by a single RD-ND section can be very big. Even for scans well above 1000 μm, the V_V measured along the line on the same surface can vary by as much as an order of magnitude, depending on how recrystallized the sample is. It is believed that this is responsible for the large difference between the manual and automatic results on the 72,000-s sample.

Also, there is an immense scatter between samples of different annealing times; for example, the 20,000-s

sample is found (in both the automatic and the manual scans) to be much more recrystallized than the 28,000-s sample.

The one-to-one comparisons between the manual and automatic scans (see Table 4) produces some quite interesting observations: For our standard choice of parameters (most notably, $L=3$), it is observed that the automatic method finds many more grains for the 11,000-s sample, while an excellent agreement is found for the 86,400-s sample. Upon choosing $L=5$, a near-perfect match is obtained for the 11,000-s sample, but the results for the 86,400-s sample dip below the manual results.

For $L=3$, it is noteworthy that for the 11,000-s sample the manual method overlooks many small grains within the deformed structure, which are seen by the automatic method. It is known that within some nuclei the crystallographic orientation can vary by up to 6° and that these internal misorientations decrease as recrystallization progresses [13]. This means that the EBSP pattern might be seen to wobble a bit while doing manual scans, causing the nuclei to be considered as deformed material, while they still satisfy the recrystallized grain criteria defined for the automatic method, and are thus included here. If these are also neglected in the automatic method (by setting $L=5$), the two methods match very well, but we conclude that the correct result must be to include the smaller recrystallized grains (thus, $L=3$).

For $L=5$, it is noteworthy that for the 86,400-s sample, the automatic method neglects small grains within the deformed structure, which are seen by the manual method. This indicates that in this case small recrystallized grains *are* observed using the manual method, and thus indicates that rejection of small grains in the manual method is less of a problem here. This agrees with the observation in Ref. [13] that the internal misorientations are reduced when the sample is annealed for a longer time.

Based on the arguments above, setting the parameter $L=3$ is assumed to give the correct description of the microstructure for the present sample.

4. Conclusions

A new automatic procedure for determining the critical recrystallization parameters V_V, S_V, and $\langle\lambda\rangle$ by EBSP line scans has been presented. The concept of grain connectivity is used and has proven to be a good method.

The procedure has been tested on aluminium, and we have obtained a fully satisfactory agreement with other available techniques. From the results presented in this paper we can conclude that the method correctly determines the values of V_V, S_V, and $\langle\lambda\rangle$, with the added advantage of being completely automatic (i.e., objective).

For samples in the latter stages of recrystallization (i.e., grains have grown to large sizes) considerable lengths can be covered relatively quickly by increasing the step size without sacrificing precision, as seen in case (b) in Section 3.1, where the distance 840 μm is covered in only 169 steps, each 5 μm long.

Acknowledgements

The authors would like to thank Roy Vandermeer and Brian Ralph for useful discussions and suggestions while writing this paper, and Preben Olesen for tremendous support when performing the many EBSP line scans necessary for this study.

The authors gratefully acknowledge the Danish Research Foundation for supporting the Center for Fundamental Research: Metal Structures in Four Dimensions, within which this work was performed.

References

[1] Adams BL. Orientation imaging spectroscopy: application to measurement of grain boundary structure. Mater Sci Eng, A 1993;166(A):59–66.

[2] Juul Jensen D. Orientation aspects of growth during recrystallization, Risø R-report Risø-R-978 (EN), Risø National Laboratory, Roskilde, Denmark; 1997 (April).

[3] Cahn JW, Hagel WC. Theory of the pearlite reaction. Decomposition of Austenite by Diffusional Processes. 1st ed. New York: Interscience Publishers; 1962. p. 131–96.

[4] Underwood EE. Surface area and length in volume. Quantitative Microscopy. New York: McGraw-Hill; 1968. p. 77–127.

[5] Vandermeer RA, Juul Jensen D. Microstructural path and temperature dependence of recrystallization in commercial aluminium. Acta Mater 2001;49:2083–94.

[6] Juul Jensen D. Growth of difference crystallographic orientations during recrystallization. Scr Metall Mater 1992;27:533–8.

[7] Magnusson H, Juul Jensen D, Hutchinsson B. Growth rates for different texture components during recrystallization of steel. Scr Mater 2000;44:435–41.
[8] Lassen NCK, Juul Jensen D, Conradsen K. Image procedures for analysis of electron back scattering patterns. Scanning Microsc 1992;6(1):115–21.
[9] Bay B, Hansen N. Recrystallization in commercially pure aluminum. Metall Trans 1984;15(A):287–97.
[10] Doherty RD. Nucleation of recrystallization of single phase and dispersion hardened polycrystalline materials. 1st Risø International Symposium on Metallurgy and Materials Science. Roskilde, Denmark: Risø National Laboratory; 1980. p. 57–69.
[11] Lassen NCK, Juul Jensen D. Automatic recognition of recrystallized grains in partly recrystallized samples from crystal orientation maps. Proceedings of the Twelfth International conference of Textures of Materials, vol. 2. Ottawa, Canada: NRC Research Press; 1999. p. 854–9.
[12] Larsen AW. 'Logitech PM5 precision polishing and lapping system" user manual. Risø I report Risø-I-2051(EN), Risø National Laboratory, Roskilde, Denmark; 2003 (September).
[13] Sabin TJ, Winther G, Juul Jensen D. Orientation relationships between recrystallized nuclei at triple junctions and deformed structures. Acta Mater 2003;51:3999–4011.

A2

Available online at www.sciencedirect.com
SCIENCE DIRECT®
Scripta Materialia 53 (2005) 553–557
Scripta MATERIALIA
www.actamat-journals.com

Nucleation of recrystallization observed in situ in the bulk of a deformed metal

Axel W. Larsen [a], Henning F. Poulsen [a], Lawrence Margulies [a,b], Carsten Gundlach [a], Qingfeng Xing [a], Xiaoxu Huang [a], Dorte Juul Jensen [a,*]

[a] *Center for Fundamental Research: Metal Structures in Four Dimensions, Risø National Laboratory, P.O. Box 49, Building 228, Frederiksborgvej 399, DK-4000 Roskilde, Denmark*
[b] *European Synchrotron Radiation Facility, BP 220, F-38043 Grenoble, France*

Received 31 January 2005; received in revised form 18 April 2005; accepted 22 April 2005
Available online 8 June 2005

Abstract

Nucleation of recrystallization is studied in situ in the bulk by three-dimensional X-ray diffraction. Copper samples cold rolled 20% are investigated. The crystallographic orientations near triple junction lines are characterized before, during and after annealing. Three nuclei are identified and it is shown that two nuclei are twin related to their parent grain and one nucleus has an orientation, which is neither present in the deformed parent grains nor first order twin related to any of them. Data on the nucleation kinetics is also presented.

Keywords: Nucleation of recrystallization; X-ray diffraction; Copper; Misorientation

1. Introduction

Nucleation is a much debated recrystallization process, whereby upon annealing nearly perfect nuclei form in a deformed material [1]. One reason for the debate is that it has been impossible to follow experimentally the nucleation process in situ, except at a sample surface.

It is characteristic of previous studies of nucleation, that these have been performed either on the surface of samples, which is not necessarily representative of the bulk of the sample, or have been statistical in nature. In the latter case, the bulk microstructure is characterized in deformed and annealed samples separately. It is therefore not possible to relate directly a nucleus to the specific deformation microstructure at the exact site where it formed. This "loss of evidence" [2] is important, as detailed quantitative analysis by electron microscopy has revealed that the deformed microstructure in metals is heavily subdivided into small, typically μm-sized volume elements of different crystallographic orientations [3]. Furthermore, the orientation of the original grain in a polycrystalline sample affects its subdivision, leading to heterogeneous deformation microstructures [4,5].

A currently much debated issue is the possible development of nuclei with new orientations compared to the deformed microstructure. Existing nucleation models such as strain induced boundary migration [6], nucleation in cube bands [7,8], and particle stimulated nucleation [9], all predict that orientation should be conserved. In contrast a number of electron microscopy (EM) investigations suggest that some fraction of the nuclei do appear with new orientations [10–20]. Such "odd nuclei" would have good growth potentials and are thus considered very important in the understanding of the recrystallization microstructures and texture

* Corresponding author. Tel.: +45 46 77 58 04; fax: +45 46 77 57 58.
E-mail address: dorte.juul.jensen@risoe.dk (D.J. Jensen).

1359-6462/$ - see front matter © 2005 Acta Materialia Inc. Published by Elsevier Ltd. All rights reserved.
doi:10.1016/j.scriptamat.2005.04.053

development. However, these EM studies can be questioned. In the case of in situ surface studies, the nucleus might have formed not at the surface characterized, but at a site below it. Also surface effects may lead to atypical types of nucleation. In the case of statistical studies, it is essential to note that nuclei are small as well as rare. To characterize a representative part of the deformed microstructure, it is necessary to measure volume fractions of the order of 10^{-8} or less with a sub-micron spatial resolution. That is not practical with existing EM methods.

These experimental limitations do not apply to three-dimensional X-ray diffraction (3DXRD) microscopy [21]—an emerging method based on the use of high energy X-rays generated by a synchrotron. 3DXRD enables characterization of the individual embedded grains in bulk crystalline samples as well as studies of the dynamics of the grains during processing [22–24]. In a recent publication, a variant of 3DXRD was demonstrated, whereby the microstructure of a channel-die deformed Al single crystal ($\varepsilon = 1.5$) could be characterized with respect to the existence of structural elements with "odd" orientations [25].

In this paper we extend this method to in situ studies of the microstructure evolution during annealing of deformed polycrystals. For the first time, a direct correlation between the orientation of the emerging nuclei and the parent microstructure is obtained in a polycrystalline sample.

2. Experimental

The material of choice is particle-free, 99.995% pure, oxygen-free, high conductivity copper. The initial material was prepared by cold rolling to 20% reduction in thickness and annealing for 8 h at 700 °C to give a microstructure with relatively coarse grains with an average size of 500 μm. This material was further cold-rolled to 20% reduction. The deformed material was characterized by transmission electron microscopy (TEM) using a JEOL-2000FX microscope operated at 200 keV. Similar to previous studies [26] the average distance between dislocation walls exhibiting a misorientation of 1° or more was 1–2 μm, depending on the orientation of the grain.

From this material three 10×10 mm^2 plates were cut, with the plate normal in the TD direction. These samples were thinned from both sides to a final thickness of 0.3 mm, using a Logitech PM5D polishing and lapping machine. Finally, the sample surfaces were electrochemically polished to remove any remnant surface scratches, which might act as unwanted surface nucleation sites.

The surface of each of the three samples (to be referred to as A, B and C) were inspected within a $\sim 1.8 \times 1.8$ mm^2 area by electron back-scattering pattern (EBSP) using a JEOL JSM-840 scanning electron microscope (see Fig. 1).

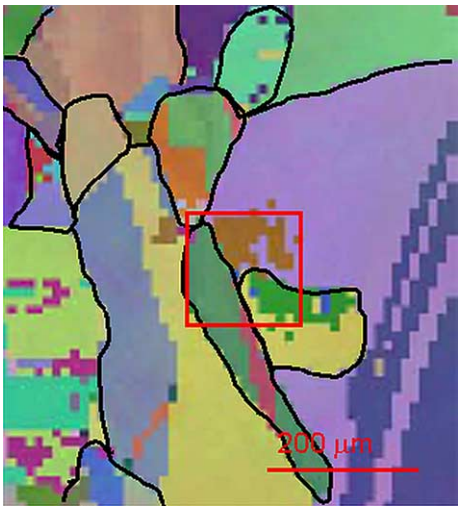

Fig. 1. An EBSP map of the surface of sample B. Deformed grains are outlined by black lines. The red square indicates the 160×160 μm^2 area in the vicinity of a triple junction, which was characterized in the X-ray diffraction study.

The experiment took place at beamline ID11 at ESRF, Grenoble, France. A sketch of the experimental set-up is shown in Fig. 2. The beam was monochromated and focused in two directions by means of a combination of a bent Laue Si crystal and a laterally graded multilayer [21]. The sample was positioned behind the focal spot. In combination with the use of an aperture this set-up resulted in the sample being illuminated by a nearly homogeneous 51 keV beam of dimensions 49×49 μm^2. Diffraction studies were performed in transmission mode by exposing a 14-bit FRELON CCD coupled by an image intensifier to a fluorescence screen of area 160×160 mm^2. Data acquisition times were typically 1 s.

To increase the volume characterized, exposures were made at a set of sample positions. For all samples these corresponded to the four points in a 2×2 (y,z)-grid, while for sample B a larger 4×4 (y,z)-grid was also used. In all cases, the distance between nodes was 40 μm. At each grid point, exposures were made for 22 equally spaced values of the rotation axis ω (see Fig. 2) within a range of 42°. To ensure an even sampling of integrated intensities, the sample was rotated by ±0.5° during each exposure. This corresponds to measurements of partial pole figures covering a fan of 42° around TD. As five reflections are recorded simultaneously on the detector this angular-range is sufficient to determine the crystallographic orientations of the evolving nuclei.

The data analysis methodology was described in Ref. [25]. In terms of image analysis, initially a background

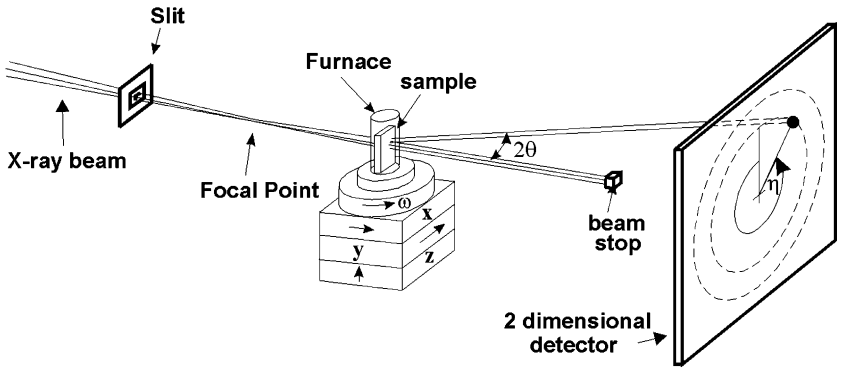

Fig. 2. Schematic diagram of the setup of the 3DXRD experiment, with indication of the angles 2θ, ω and η.

subtraction method was applied [27]. In the algorithm, a box of a given size is scanned across each image. The average and standard deviation of the pixel intensities within the box are determined as function of position. Positions with a small standard deviation are then defined to be in the background. The background level at each point is then determined by interpolation of the average values in the background areas. Images were spatially corrected by the program FIT2D [28].

For each nucleus, the orientation was determined with an accuracy of $\sim 1°$ by the multi-grain indexing algorithm, GRAINDEX [29]. In addition, the volume of the nucleus is readily found, as it is proportional to the integrated intensity of the associated diffraction spots. The proportionality constant was estimated from the integrated intensity of the diffracted signal from a reference Al powder with known thickness [21,25]. Furthermore, the (x, y, z) position of the nucleus can be estimated by trigonometry, based on information on when the nucleus "rotates out of the beam" during the ω-scan. To ensure the same volume was illuminated at all times, the position of the edges of the sample was repeatedly determined by scanning the sample.

The furnace provides a stable temperature of up to 500 °C, with a choice of working in a neutral atmosphere, and can rotate 360° about the z-axis. The sample is enclosed in a glass capillary tube with a thickness of 0.1 mm, giving rise to negligible absorption and minimizing diffuse scattering.

3. Results and discussion

Nucleation in three 300 μm thick plate shaped samples (A, B and C) was studied by the 3DXRD method. As a function of rotating the sample around the ω-axis, diffraction images were acquired with a highly efficient area-detector. Typical data from the as-deformed samples are shown in Fig. 3a. In the corresponding {111}, {200} and {220} partial pole figures, shown in Fig. 4, the orientations present are enclosed within broad poles associated with the three deformed grains at the triple

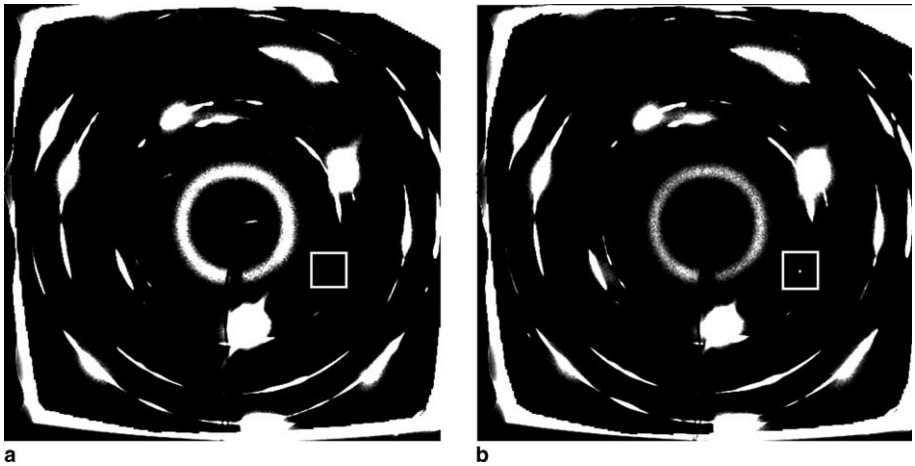

Fig. 3. Examples of 3DXRD images, acquired for sample B. A grey scale is used with white representing the more intense regions. The textured Debye–Scherrer rings of the {111}, {200}, {220}, {311} and {222} reflections are seen. The two images relate to the same position within the sample and represent (a) the as-deformed microstructure, and (b) the microstructure in the sample annealed for 3 h at 290 °C. The white box indicates the position of a diffraction spot, representing a nucleus.

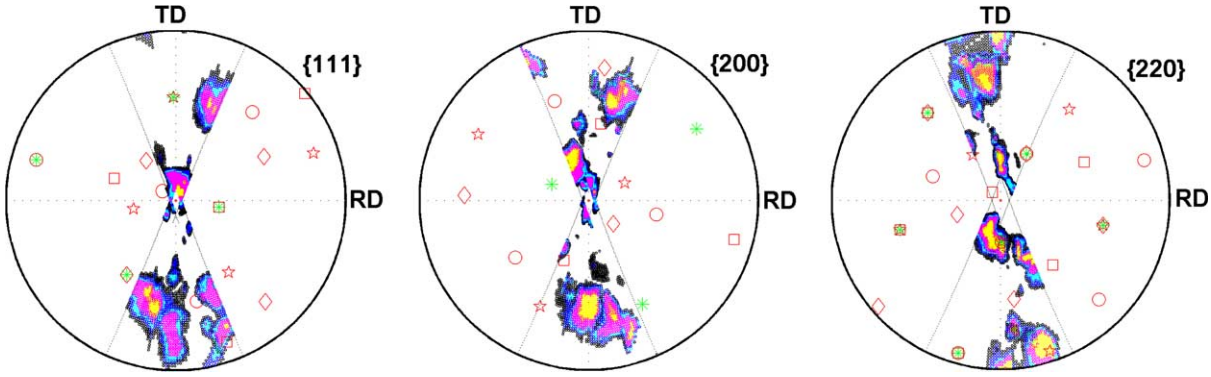

Fig. 4. Partial pole figures of sample B measured at the location of the nucleus with the new orientation. The orientations of the deformed microstructure are shown in colours with [black, blue, light blue, pink, yellow] corresponding to intensities of [400, 1000, 2500, 5000, 10,000] counts/s. The diffraction pattern from the sample after 3 h of annealing at 290 °C is very similar, except for the presence of three sharp diffraction spots, which are shown as green stars. The orientations of the associated four first order twins are marked by red symbols (squares, diamonds, circles, and stars). There is a small "invisible spot" in the centre of all pole figures.

junction. No smoothing has been applied. The individual elements in the deformed microstructure associated with these poles cannot be distinguished. Instead the virtue of the 3DXRD method in this case relates to characterization of the "empty" parts of the partial pole figures (i.e. within the measured ω-range of 42° but away from major poles). The boundary between the white and colored parts of the pole figures indicates the smallest volume elements that can be observed. This limit of 400 counts/s corresponds to an equivalent circle diameter (ECD) of 0.70 μm. In other words, all volume elements within an illuminated sample volume of $49 \times 49 \times 300$ μm^3 with an ECD larger than 0.7 μm will be recorded as a significant signal on the detector. It is characteristic of all three samples that large parts of the partial pole figures are empty, and furthermore that the intensities in the "tails" of the poles fall off rapidly with the distance to the centre of the pole.

The acquisition of such high-sensitivity pole figures was repeated with a frequency of ~10 min, while annealing the samples at 290 °C for 1–3 h. During this process, a few nuclei appeared, easily identifiable in the images as distinct point-like diffraction spots, see Fig. 3b. Based on the position and intensity of these spots 3DXRD specific analysis software was used to determine the orientation and position of the nuclei [21,25], as well as their volume as a function of annealing time.

Three nuclei were detected: one in sample A, two in sample B and zero in sample C—all positioned at least 65 μm from any surface. This result confirms that triple junctions are potential nucleation sites in this material, but also that not all junctions lead to nucleation, which is in good agreement with previous surface [20] and serial sectioning results [30].

The orientation of the sample A nucleus was identical to a first-order twin associated with an orientation close to the centre-of-mass of one of the poles. This nucleus grew to a size of ECD = 9.4 μm within 45 min. The orientation of one of the sample B nuclei was also identical to a first-order twin associated with an orientation close to the centre-of-mass of one of the poles. The results for the second nucleus in sample B, which is of the main interest here, is shown in Figs. 3 and 4. In this case six diffraction spots were observed in the "empty" parts of the partial pole figures (i.e. within the measured ω-range of 22° but away from the poles of the deformed parent grain), while another seven were on top of poles. From the six spots, the orientation of the nucleus was determined to be neither within the range of orientations found in the as-deformed sample, nor related to a first-order twin associated with any of the orientations in this range (see Fig. 4). This nucleus grew to a size of ECD = 6.1 μm within 3 h.

There are two explanations to why such a nucleus could be generated:

1. It emerged by reorientation of parts of the deformed structure.
2. It emerged from rare parts of the deformed microstructure associated with volume fractions of the order of 1.5×10^{-7}. All elements in the deformed microstructure associated with such hypothetical "odd orientations" have an ECD of less than 0.70 μm. This number corresponds to the lower limit of the size-distribution of elements as characterized by chord–length measurements in TEM [26]. Furthermore, they are substantially below the classical nucleation threshold [31], which in the present case is $ECD_{classic} > 1.1$ μm [1,32]. This explanation thus seems very unlikely.

A mechanism explaining how and why reorientation of parts of the deformed microstructure (explanation 1 above) should take place during the early stages of annealing has not been derived. The present result together with the previous observations of nuclei with

new orientations both at triple junction and away from them, however, strongly suggests that further detailed work should be devoted to the understanding of this. For the experimental part of such work, it appears the method presented here is an ideal tool. Uniquely, information on nucleation sites, orientation relationships and kinetics is obtained. The sensitivity of the method can be increased to ECD = 0.2 μm or better by improved focusing [33]. Statistics of nuclei characteristics can be extracted from repeated studies, which in turn is likely to give insight into the underlying mechanisms. Also, potential reorientations of emerging nuclei would be readily observable.

4. Conclusion

A unique method for in situ studies of nucleation in the bulk has been presented. The method is based on three-dimensional X-ray diffraction. It has been confirmed that volumes near triple junction lines are potential nucleation sites in 20% cold rolled copper. Three nuclei have been identified and followed during annealing at 290 °C. Analysis of orientation relationships with their deformed parent grains has revealed that nuclei may develop with orientations within the orientation distributions of the parent grains, being twin related here or with a new orientation that was not detected in the deformed parent grains.

Acknowledgments

The authors gratefully acknowledge the Danish National Research Foundation for supporting the Center for Fundamental Research: Metal Structures in Four Dimensions. This work was also partly supported the Danish Natural Science Research Council (via Dansync). The ESRF is acknowledged for provision of beam time. P. Nielsen and P. Olesen performed the pre-experiment sample scanning and testing.

References

[1] Humphreys FJ, Hatherly M. Recrystallization and related annealing phenomena. Oxford: Pergamon; 1995.
[2] Duggan B. Term suggest at international conference on textures of material. ICOTOM 11, 1996.
[3] Hansen N. Metall Mater Trans A 2001;32:2917.
[4] Driver JH, Juul Jensen D, Hansen N. Acta Metall Mater 1994;42:3105.
[5] Winther G. Acta Mater 2003;51:417.
[6] Bailey JE, Hirsch PB. Proc Roy Soc A 1962;267:11.
[7] Samajdar I, Doherty RD. Scr Metall Mater 1995;32:845.
[8] Vatne HE, Daaland O, Nes E. ICOTOM 10. Mater Sci Forum 1994;157–162:1087.
[9] Humphreys FJ, Fery M, Johnson C, Paillard P. In: Hansen N et al., editors. Proceedings of the 16th Risø international symposium on material science: Microstructural and crystallographic aspects of recrystallization. Roskilde, Denmark: Risø; 1995. p. 87.
[10] Wu GL, Godfrey A, Juul Jensen D, Liu Q. ICOTOM 14. Mater Sci Forum 2005;495–497:1309.
[11] Kikuchi S, Kimura E, Koiwa M. J Mater Sci 1992;27:4927.
[12] Juul Jensen D. In: Sakai T, Suzuki HG, editors. Proceedings of the 4th international conference on recrystallization and related phenomena, 1999;(JIM):3.
[13] Paul H, Driver JH, Maurice C, Jasienski Z. Acta Mater 2002;50:4339.
[14] Inoko F, Okada T, Tagami M, Kashihara K. In: Hansen N et al., editors. Proceedings of the 21st Risø international symposium on material science. Risø National Laboratory; 2000. p. 365.
[15] Godfrey A, Juul Jensen D, Hansen N. Acta Mater 2001;49:2429.
[16] Barett CS. Recrystallization texture of aluminium after compression. Metals Technol 1940:128–49.
[17] Driver JH, Paul H, Glez J-C, Maurice C. In: Hansen N et al., editors. Proceedings of the 21st Risø international symposium on material science. Risø National Laboratory; 2000. p. 35.
[18] Inoko F, Mima G. Scr Metall 1987;21(8):1039.
[19] Okada T, Huang X, Kashihara K, Inoko F, Wert JA. Acta Mater 2003;51:1827.
[20] Sabin TJ, Winther G, Juul Jensen D. Acta Mater 2003;51:3999.
[21] Poulsen HF. Three-dimensional X-ray diffraction microscopy. Berlin: Springer; 2004.
[22] Margulies L, Winther G, Poulsen HFI. Science 2001;291:2392.
[23] Offerman SE et al. Science 2002;298:1003.
[24] Schmidt S, Nielsen SF, Gundlach C, Magulies L, Huang X, Juul Jensen D. Science 2004;305:229.
[25] Poulsen HF, Lauridsen EM, Schmidt S, Margulies L, Driver JH. Acta Mater 2003;51:2517.
[26] Huang X, Leffers T, Hansen N. In: Bilde-Sørensen JB et al., editors. Proceedings of the 20th Risø international symposium on material science. Roskilde, Denmark: Risø National Laboratory; 1999. p. 365.
[27] Teuber J, Bowen J, Lauridsen EM, Private communication.
[28] Hammersley AP, Svensson SO, Hanfland M, Fitch AN, Häusermann D. High Pressure Res 1996;14:235.
[29] Lauridsen EM, Schmidt S, Suter RM, Poulsen HF. J Appl Cryst 2001;34:744.
[30] Vandermeer RA. Trans Metall Soc Aime 1959;215:577.
[31] Doherty R. In: Hansen N et al., editors. Proceedings of the 1st Risø international symposium on material science. Roskilde, Denmark: Risø National Laboratory; 1980. p. 57.
[32] Gordon P. Trans AIME 1955;203(9):1043.
[33] Ice GE, Chung JS, Tischler JZ, Lunt A, Assoufid L. Rev Sci Instrum 2000;71(7):2635.

A3

Risø-I-2051(EN)

'Logitech PM5D Precision Polishing and Lapping System' User Manual

Axel W. Larsen
Materials Research Department, Building 228

Risø National Laboratory, Roskilde
August 2003

Abstract This internal Risø report is a user manual for the 'Logitech PM5D precision polishing and lapping system'. It is not a 'stand alone' manual. It is assumed that the user has taken an introductory course to the PM5D system.
It includes: an introduction to the various components of the system; the necessary steps that must be taken before lapping/polishing can commence; how to operate that PM5D machine and do lapping and polishing on it; how to maintain the system in working order, as well as tips on how to achieve good polishing results are also found within.

Print: Pitney Bowes Management Services Denmark A/S, 2003

Contents

Preface

This manual is not thought as a booklet to teach prospective users how to use the 'Logitech PM5D precision polishing and lapping system'.
Rather, it should be seen as useful pre-reading before taking the introductory course, and after taking the course, the user should view it as a user reference manual while working with the PM5D system.
It is of course not possible to write a manual explaining everything about all aspects of using the PM5D system, but after the user has taken a introductory course, the manual should answer any questions he or she might have…

1 Introduction to the PM5D precision polishing and lapping system

WARNING: Please do not use this equipment until you have had a user course from one of the trained staff!!!

The Logitech PM5D polishing and lapping machine is built on the principle of an rotating lapping plate with a free standing and rotating sample holder on top. This sample holder is the PP5D Precision Polishing Jig with PSM1 sample monitoring system. The system includes the following pieces of equipment:

- PM5D Lapping and Polishing Machine with abrasive autofeed cylinder (see figure 1)
- PP5D Precision Polishing Jig with PSM1 sample monitoring system (see fig. 3)
- PJ2 two-position thin section bonding Jig (see fig. 2)
- Contact gauge with flat granite master plate.

The PM5D system allows control of the depth of material removal within 1-2 µm, and sample flatness to within 1-2 µm height difference across the sample.

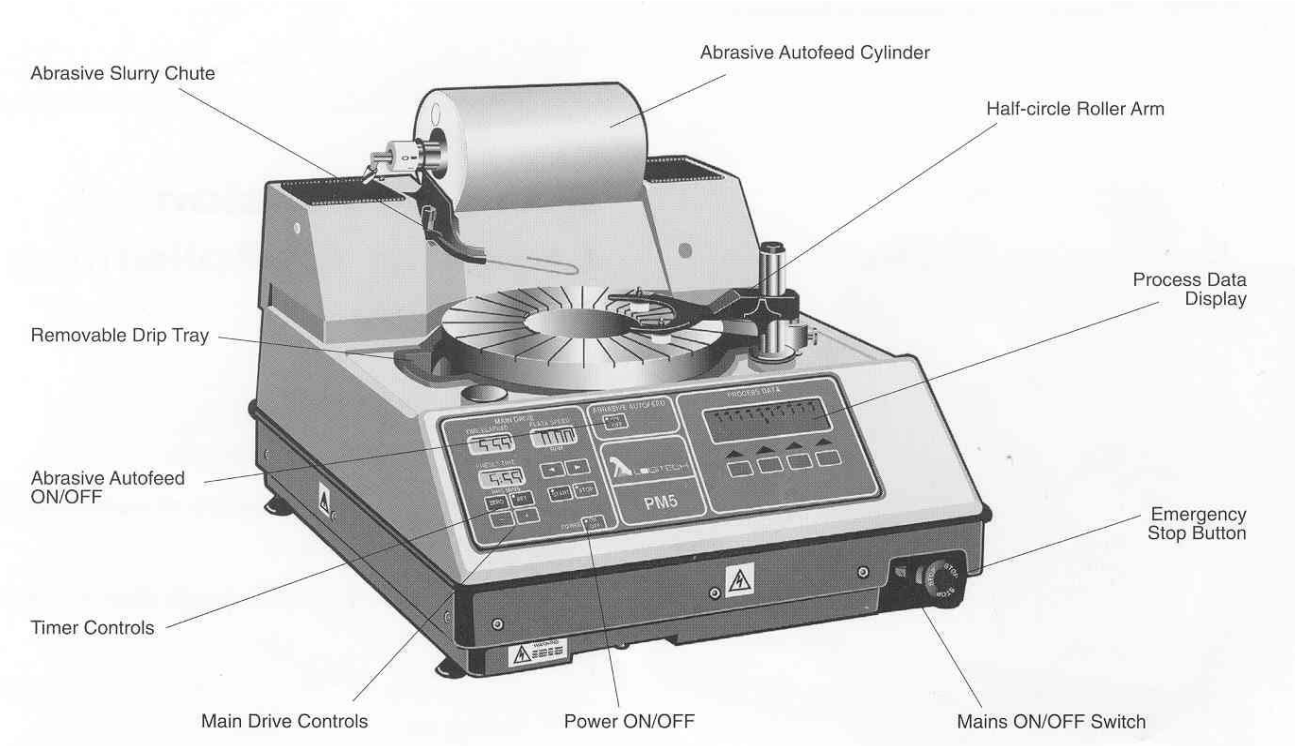

Figure 1. PM5D precision polishing and lapping machine.

2 Before getting started

This section includes the necessary steps, which must be performed before lapping and polishing can commence.

- Prepare the sample.
- Bonding the sample.
- Check (and correct) lapping plate flatness.
- Clean components when measuring and changing slurries during lapping and polishing.

2.1 Prepare the sample

Before processing make sure that the sides and edges of the sample are polished (by hand) to avoid small pieces chipping off the edges, causing scratching on the sample surface during polishing. Make sure that the sample is cleaned *well* with alcohol before starting the lapping.

2.2 Bonding the sample

The sample must be bonded onto the base plate of the PP5D polishing jig (see figure 2). This is normally done with a quartz wax. It has a melting point of 66-69º, which is well below the recovery and recrystallization temperature of *most* metals. The bonding is carried out with a hot plate (positioned opposite the PM5D machine), where a black line indicates the correct temperature, and the BJ2 two-position bonding jig.
Firstly, find a suitable amount of quartz wax and place this on the PP5D base plate. The base plate is then placed on the bonding jig, which is placed on the hot plate. Once the wax is fully melted, the sample is placed on the wax, and the spring driven piston is used (with a block in between) to press down and flatly bond the sample(s) to the base plate.
The metallurgy lab only has a very warm hot plate, so in the case of VERY heat sensitive samples, it is a good idea to find a less warm hot plate or use *dissolvable* glue instead. When the sample is bonded to the plate, use a scalpel to remove the excess wax/glue on the plate around the sample – this gives the most accurate height measurements afterwards.
Note that, size permitting, several samples of roughly the same height (within a few hundred micrometers) may be bonded to the base plate at the same time, allowing for the polishing of *several* samples at once!

In the case of samples mounted on a SEM sample stub, there is an alternative way to bond the sample. The SEM sample stub can be clamped to the base of the PP5D polishing jig with a special clamp. This method of bonding makes relatively easy serial sectioning possible if the area of interest is marked with hardness indents, so as to make the area of interest clearly identifiable.

Once bonded, any remaining sharp or ragged edges on the sample should be filed or cut with a scalpel. If this is not done, pieces of the edges can (and will) break off and cause scratching on the sample surface, as well as contaminate the polishing plate. If only a limited amount (i.e. a few hundred microns) of material is to be removed from the sample, pre-polishing the sample's edges (before bonding) by hand will do wonders for the resulting surface quality!

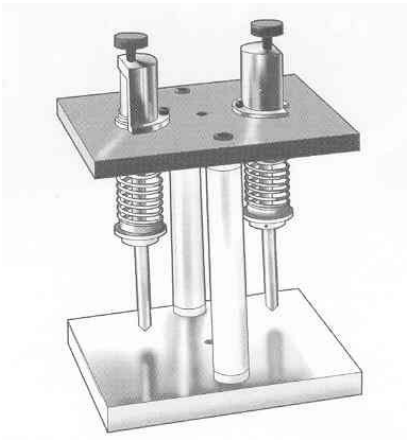

Figure 2. BJ2 two-position thin section bonding jig.

2.3 Check flatness of the lapping plate

For all moderately hard materials (i.e. metals, ceramics, composites etc.), the **lapping** takes place on cast iron lapping plates, which have a diameter of 30 cm. If the sample diameter is *bigger than 50 mm* across, the grooved lapping plate is used. Otherwise the non-grooved plate is used.
If the non-grooved lapping plate is used, the grooved test block is used; and if the grooved lapping plate is used, the non-grooved test block is used. To ensure that the lapping plate is perfectly flat. Let the relevant test block (grooved for flat plate, or flat for grooved plate) lap with a **static lapping arm** for 20 min at 70 rpm on a 9 µm Al_2O_3 slurry. This also removes the thin layer of rust that will often be on the cast iron plates.

The test block is then inspected with a contact gauge (which is first calibrated on the flat granite master plate) to determine whether it is concave/flat/convex. The test block surface will have the *opposite* deviation from flatness that the plate has test block → lapping plate: concave → convex, flat → flat, convex → concave
This inspection is carried out with a special contact gauge and the flat granite master plate, which is used to calibrate the contact gauge. If the lapping plate only deviates 1-2 µm from perfect flatness it is not a problem, but if it deviates more, the lapping plate will have to be corrected. **Remember to clean all surfaces with alcohol when measuring the test block!!!**
If the lapping plate is *concave*, move the sample arm so that the test block only just extends a few mm over the inner edge; and if the lapping plate is *convex*, move the sample arm so that the test block only just extends a few mm over the outer edge. Let the machine lap as before. The lapping plate will be corrected at a rate of about 1 µm/hr (at 70 rpm on a 9 µm Al_2O_3 slurry). This can be sped up by adding extra weight to the test block.

2.4 Clean components when necessary

Always clean all the components with water and/or alcohol when doing measurements and changing slurries. It is very important to avoid contamination, because this will normally result in scratching during the polishing process.
Use the differently labeled brushes when removing the different lapping and polishing slurries.

3 Machine operation

The machine works in three ways. In all three different ways the top left screen indicates the total lapping/polishing time that has passed:

- 100% user controlled. **manually** pressing 'ON/OFF'-button.
- the machine runs for a pre-specified period of **time** and then stops.
- the PSM1 unit can (for lapping) stop the machine when a pre-specified **thickness** of material has been taken off.

3.1 PM5D controls

The PM5D (see figure 1) has two main 'ON' switches + one on the membrane touch display, which must be turned on for the machine to function when the electric power has been turned on. The '*Emergency Stop*' button is a red knob on the lower right of the machine — if pressed, it immediately turns off all power to the machine, and it must be turned clockwise to reactivate the PM5D.
Right next to the emergency stop switch is the '*Mains Isolator*' switch, which will light up green when ON. Lastly, the 'ON/OFF'-button on the membrane touch display must be pressed.
When the display lights up the jig arm will do a self-test, after which you need to choose between static arm (lapping) or sweeping arm (polishing), and then press the button under <Systems check>. In the systems check you can adjust the position of the jig arm (static arm mode), or the outer positions of the jig arm (sweeping arm mode).

When the machine is first turned on, it will go through a systems check. Unless you know better, simply press the button under the arrow.
The machine starts when the '*START*' membrane button is pressed. The lapping plate will not start rotating until you press the '*Plate Speed Control*' keys, which increments the plate rotation speed in increments of ±1 rpm within the interval 0-70 rpm (NB! this speed is *not* stable if the chosen plate rotation speed is less than 10 rpm).
The slurry will not start dripping from the cylinder until the '*ABRASIVE AUTOFEED ON/OFF*' button is pressed, and the valve on the autofeed cylinder has been opened. If the slurry does not run properly down the drip wire onto the plate, use a finger to wet the wire.

3.2 Adjusting sample load

The downward load/pressure that the PP5D polishing jig exerts on the sample can be adjusted by rotating the collar behind the PSM1. The load on the sample can thus be varied from 0.1–2.7 kg. If the collar is rotated *clockwise*, the load is on the sample *increased*; and if the collar is rotated *anticlockwise*, the load on the sample is *decreased*.
Load is best adjusted by inspecting how much the sample protrudes from beneath the base ring of the polishing jig. For well-controlled lapping and polishing, the sample should protrude 0.1-1 mm, but if many hundred microns of material need to be lapped off, a larger sample load should be used (see sections 4 & 5).
It should be noted that too much sample load can result in *small* samples being forced through the lapping slurry, thus causing them to be scratched on the polishing plate.

3.3 Operation procedure

- Turn on machine (on all three buttons).
- Do systems check (static or sweeping arm).
- Place autofeed cylinder or SF1-container on machine and open valve.
- (if first use of the day) Run the machine with polishing block for 20 min with 9 µm Al_2O_3 at 70 rpm. Check (and correct) flatness.
- Adjust sample load.
- (if lapping) Turn on the PSM1 and the contact gauge. Reset the contact gauge and set a target depth on the PSM1. (if polishing) Press 'SET' on the PM5D to set the polishing time.
- Press '`START`', '`ABRASIVE AUTOFEED ON`', and '`PLATE SPEED CONTROL`' keys.
- When the slurry is spread out on the lapping plate, place the polishing jig on the plate, while restraining the sample base plate. Gently lower the specimen plate down onto the lapping/polishing plate in order to avoid damaging the sample.
- Stand the autofeed cylinder on its end, and wash everything thoroughly (very thoroughly if SF1 was used).
- Carefully clean all the components when changing lapping/polishing slurries, and clean the samples with water and/or alcohol as often as needed.

4 Lapping with the PP5D polishing jig with PSM1 sample monitor

Lapping is the wearing away of material by liquid abrasion from a free flowing liquid slurry. The sample aquaplanes on the slurry on the lapping plate.
Lapping causes sub-surface material damage down to a depth of approx. 3 times the diameter of the abrasive particles (i.e. a 9 µm abrasive will cause damage down to a depth of approx. 30 µm), and produces a non-reflective surface, with a surface roughness of several hundred nanometers (a 9 µm Al_2O_3 abrasive will result in a surface roughness of approx. 400 nm).
During **lapping** the sample holder arm is in **static mode**, and plate speed is 70 rpm.

4.1 Lapping slurries

The Risø PM5D system has two different lapping abrasives. They are on powder form and need to be mixed with **de-ionized** water (DI-water) in the ratio given:

3 µm Al_2O_3 (20% total slurry volume = 300 ml (full fill))
9 µm Al_2O_3 (10-15% total slurry volume = 150-225 ml (full fill))

DI-water must be used to avoid contamination, and the cylinder should only be filled up to the halfway-line (it contains **1.5 liters** of slurry). If refilling a non-empty cylinder, the above percentage indicates how much abrasive powder should be added. For example, 1 liter of '3 µm Al_2O_3' slurry comes from 200 ml of powder (20%) and 800 ml of DI-water

When the machine is stopped, stand the autofeed cylinders on their ends!
If the valve is kept closed, the slurry can remain in working order for months. If this is not done the Al_2O_3-abrasive has a tendency to solidify within the valve of the cylinder clogging it up, thereby stopping the flow of slurry to the lapping plate — this has already happened once!!!

Lapping allows *in situ* control of material removal. The digital contact gauge on the jig tells the depth of material taken off, and with the PSM1 installed the lapping process will be stopped once the specified depth has been reached. This is in general accurate within 1-2 µm, which can be checked with a contact gauge. In general, the majority of the material will be lapped with the 9 µm Al_2O_3, and only the last 30 µm (to be lapped) will be taken off with the 3 µm Al_2O_3, thus leaving only 10 µm sub-surface damage, which must then be removed during the polishing process. It is important to leave a bit of extra material for accidental overshooting, as the extra material may be taken off in the polishing process.
If *surface polishing* samples, the 9 µm-step may be omitted, thereby saving sample material and lapping time!

4.2 Material take-off rate

Depending on the material, the surface area being lapped, the PP5D sample load, and the lapping slurry being used, the material take-off rate can vary from 1 µm/min to 100 µm/min.
In general, the slower the lapping take-off rate, the better the depth control, but one must decide how long one wants to spend on the lapping stage, which does not dramatically effect the post-polishing surface. The take-off rate is controlled by increasing or decreasing the sample load (see section 3.2).

4.3 Using the PSM1 sample monitor

NB! The PSM1 only works properly during *lapping*!!!
Turn on the PSM1 by pressing the green button (see figure 3). If the PSM1 doesn't turn on (or only for a few seconds) the batteries are dead, and they should be replaced with the other set we have – please remember to recharge the old ones! The PSM1 will first display an error message "E7", which will disappear when the *contact gauge* on the polishing jig is turned on by pressing 'POWER'.
NB! Don't turn on the contact gauge without turning on the PSM1, as this will leech the internal battery in the contact gauge instead of using the rechargeable PSM1 batteries!
When the polishing jig is placed on the wet lapping surface, it should be allowed to rotate at least once to allow the slurry to get in under the sample and the ring of the polishing jig. The contact gauge is reset to 0 by pressing 'RESET'. If the error persists, check if the contact gauge is turned on. If this is the case, consult the Logitech PSM1 manual (which is found in the red plastic case next to the PM5D) for a complete list of error messages.
When the PSM1 and contact gauge are turned on, the PSM1 display should read 'P'. To set the desired amount of material to be removed (in microns), press the 'SET' button and use the '+'/'-' buttons to enter the desired value, followed by 'SET' once again - all this can be done in *advance* as long as the contact gauge is also turned on. When you are ready to start lapping, press 'RUN' and the PSM1 will start counting down to the desired depth on the screen. Before leaving the machine to lap by itself, take a moment to check that the PSM1 is actually counting down — in other words working properly!
When the sample gets within 20% of the desired depth the PSM1 will start beeping at an rate that increases as the specified depth comes closer. Finally, the PSM1 will stop the PM5D lapping machine using a continuous infrared signal when the desired depth is reached, and it will continue beeping after the machine has stopped! Please don't let the PSM1 stand in beeping mode for too long, as this will drain the batteries, and greatly annoy all other people in the metallurgy lab. To stop the beeping, press the red "Off" button on the PSM1, which turns it off. The contact gauge will turn off on its own.

Figure 3. PP5D precision polishing jig with PSM1 sample monitoring system.

5 Polishing with the PP5 polishing jig

Polishing is the removal of surface material by the grinding of small hard particles against the surface. It produces a reflective surface, with a surface roughness down to a few nanometers (or even lower if great care is taken).
During **polishing** the sample holder arm is in **sweeping mode**, and the plate speed is around 40 rpm.

In general, to get good results, keeping the working area as clean as possible and using a low sample loading weight is essential. If the resulting surface is to be used for EBSD analysis *without* additional to electro-chemical polishing, great care must be taken to ensure that the *entire* deformed surface layer from the lapping process (see previous section) is removed during the polishing.
Before starting, the edges of the samples should be visibly inspected for bits that might crack off, as these *will* cause surface scratching during the polishing process.

5.1 Polishing agents

The Risø PM5D system has two different polishing slurries:

1 µm synthetic polycrystalline diamond
1 µm colloidal silica (SF1)

When working with **soft** materials, such as annealed aluminium, **diamond** yields the best results. When working with **hard** materials, such as deformed nickel, **SF1** works very well, but this does vary from material to material. The SF1 solution does not seem to be very effective for polishing aluminium, but it gives very good results for materials such as cupper and steal.

Synthetic polycrystalline diamond (1 µm)

The diamond powder must be mixed with **ethane diol** polishing fluid. For standard research size samples 2 g diamond/cylinder fill will be a suitable concentration. It uses the expanded polyurethane (or the DP DUR) polishing cloths. The polishing cloths must be glued (they are self-adhesive) to the flat metal polishing plate. When applying the polishing cloth, make sure that the base plate is clean and that no air bubbles are left under the cloth.
The DP DUR cloths are both durable and chemically resistant, so the use of OPS (the finest mechanical polishing slurry available in the metallurgy lab) is also possible – if everything is cleaned quickly with water and washing up liquid *immediately* after polishing is finished.

SF1 colloidal silica (1 µm)

The SF1 colloidal silica is supplied in a **ready blended** SF1 polishing suspension, and it uses a (pink) hyprocel pellon polishing cloth. This cloth is a *permanent* polishing cloth, not to be confused with the expendable polishing cloths used with diamond polishing.
When using the SF1 suspension, it is **very important** to remember that the silica crystallizes **very quickly**, so about 5 minutes before stopping the plate it should be doused with DI-water to remove most of the SF1 . Immediately after removing the jig from the polishing plate, the sample and jig should be thoroughly rinsed with water, and be placed in a shallow bowl of DI-water with a soft cloth to soak for a while. The plate should be doused with plenty of DI-water and be kept rotating at 10-15 rpm, so the silica does not crystallize on the plate's surf
ace. In general, all components in contact with the SF1 solution should quickly be thoroughly cleaned after use, so as to avoid SF1 crystallizing on them.

5.2 Material take-off rate

Measuring material take-off while polishing is done in a somewhat different way than for lapping. Because the polishing plates are covered with a soft material, the sample penetrates somewhat into them making an accurate *in situ* sample take-off measurement with the PSM1 unit impossible!
Good quality polishing is generally a *slow* business, with a maximum material removal rate of 1 µm/min. The sample load should be as low as possible when polishing.
To get the polishing take-off rate. The sample thickness is measured with a contact gauge before polishing is begun and then again after 10-15 minutes of polishing. Dividing the amount of removed material with the polishing time gives the material removal rate (µm/min), which is used to calculate how long the sample must be polished for in order to reach the desired sample depth.
For this take-off "calibration" to be correct, it is very important *not to change* the polishing parameters: i.e. sample load; plate speed; and sample arm positions/speed. **Always err on the side of safety!!!**
A digital contact gauge can be found in the SOFC lap on the ground floor of Nordlab (building 227). Talk to Ebtisam Abdellahi (tel. 5750, e-mail: ebtisam.abdellahi@risoe.dk) about borrowing it. It is recommended to use this instead of our own mechanical contact gauge at the metallurgy lab.

6 Machine maintenance

Please leave the PM5D system in as good (or better) a state as you hope to find it!

When not in use, place the slurry cylinders up on their ends AND close the valve. This prolongs the lifetime of the slurry. If stored on its end and out of direct sunlight, the slurry in a cylinder can last up to a year.

Rinse and scrub all the removable components with DI-water and a brush. Give the machine a good clean, using some alcohol on the more difficult spots. Don't forget to clean the drip tray with a brush in the sink. Give the drip tube (the sink of the PM5D machine) a good rinse, using the water tube to the right of the machine. This is to prevent the slurry from drying in the tube and congesting it during and after use.

Whenever you're changing lapping/polishing slurries make sure to rinse the lapping plate and scrub the surface and gullies with a heavy brush. Also make sure that the slurry chute and drip wire are cleaned as well, since slurry contamination can cause scratching.

7 Final words

Please note that reading this manual is NO SUBSTITUTE for taking an introductory course on the PM5D system!!!

This course and copies of this manual, as well as the full Logitech PM5D system CD-ROM are available from Helmer Nilsson (tel. 5714, e-mail: helmer.nilsson@risoe.dk) & Axel Larsen (tel. 5787, e-mail: axel.wright.Larsen@risoe.dk).

Finally, if something goes disastrously wrong or badly malfunctions contact Helmer Nilsson (5714) or Axel Larsen (5787).

Bibliographic Data Sheet **Risø-I-2051(EN)**

Title and authors

'Logitech PM5D precision polishing and lapping system' user manual

Axel W. Larsen

ISBN	ISSN
xx-xxx-xxxx-x	xxxx-xxxx

Department or group	Date
Center for Fundamental Research: Metal Structures in Four Dimensions AFM	21.08.03

Groups own reg. number(s)	Project/contract No(s)

Sponsorship
Danish Research Foundation

Pages	Tables	Illustrations	References
13	0	3	0

Abstract (max. 2000 characters)

This internal Risø report is a user manual for the 'Logitech PM5D precision polishing and lapping system'. It is not a 'stand alone' manual. It is assumed that the user has taken an introductory course to the PM5D system.
It includes: an introduction to the various components of the system; the necessary steps that must be taken before lapping/polishing can commence; how to operate that PM5D machine and do lapping and polishing on it; how to maintain the system in working order, as well as tips on how to achieve good polishing results are also found within.

Information Service Department: 2 copies

A4

Mater. Sci. Forum vols. 408-412, 287-293

Lattice Rotations of Individual Bulk Grains during Deformation

G. Winther[1], L. Margulies[1,2], H.F. Poulsen[1], S. Schmidt[1], A.W. Larsen[1], E.M. Lauridsen[1], S.F. Nielsen[1] and A. Terry[2]

[1]Materials Research Department, Risø National Laboratory, DK-4000 Roskilde, Denmark

[2]ESRF, BP 220, F-38043 Grenoble Cedex, France

Keywords: polycrystal deformation; X-ray Diffraction; Synchrotron Radiation

Abstract. Three-dimensional X-ray diffraction has been applied to measure *in-situ* lattice rotations of individual grains deeply embedded in a 2 mm thick copper sample during 6% elongation. The tensile axis of seven grains initially close to <111> all rotated towards this orientation. This common rotation behaviour indicates a limited influence of grain interaction at low strains. Minor variations in the rotation of the tensile axis did not exceed the spread in the predictions by the classic Sachs and Taylor models.

Introduction

Polycrystal plasticity models for prediction of texture evolution during deformation are based on prediction of active slip systems in individual grains and calculation of the resulting grain rotation. Only bulk textures before and after deformation can be measured by standard techniques. The field has therefore been severely impeded by lack of data on the grain level. All models consequently rely on assumptions concerning the factors controlling the behaviour of individual grains. The earliest models, i.e. those proposed by Sachs [1] and Taylor [2], assume that the rotation of a grain is determined by its crystallographic orientation. Limitations of these models, especially when it comes to prediction of the rate of texture evolution, have lead to models which consider the detailed interaction between a grain and its neighbours as an important factor [3, 4].

Experimental studies of individual grains have mostly been limited to surfaces. A clever experiment where two metal surfaces were pressed tightly together during deformation to mimic bulk conditions has also been devised [5, 6]. It is however unclear to what extent these data are representative of true bulk grains.

Recently, *in-situ* studies of structural changes in individual grains deeply embedded in a polycrystal have become possible with the 3-Dimensional X-Ray Diffraction (3DXRD) microscope situated at the European Synchrotron Radiation Facility. The first application of this microscope to measure lattice rotations during straining was performed on four grains in a polycrystalline aluminium sample with 300 μm sized grains [7]. The number of measured grains was however too small to allow solid conclusions and the grain size was also rather large.

This paper presents data from a study of seven grains in copper with an average grain size of 35 μm. Only grains having the tensile axis close to the crystallographic <111> direction were monitored. In particular, some grains with nearly identical orientations were picked, in order to shed light on the relative importance of the initial crystallographic grain orientation and interaction with different neighbouring grains.

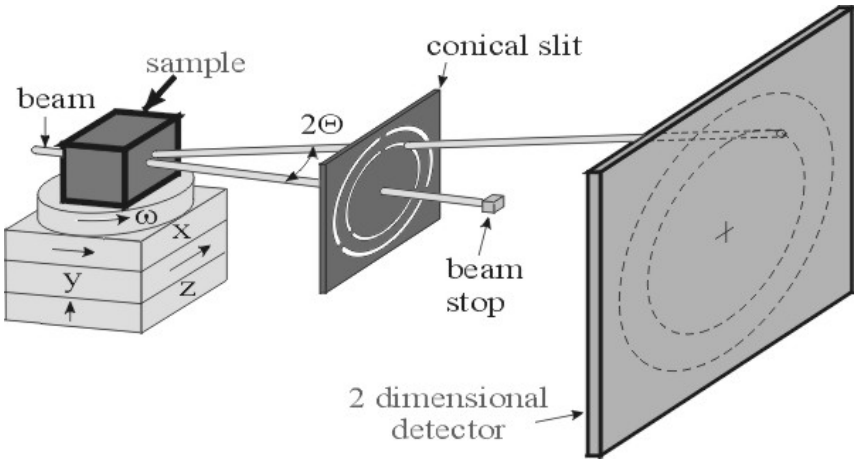

Fig. 1. Sketch of the experimental set-up, including definition of angles 2θ (Bragg angle) and ω (sample rotation).

Experimentals

The experimental set-up is sketched in Fig. 1. The material is 99% pure copper with an average grain size of 35 μm. Sample dimensions are 55 mm x 8 mm x 2 mm. The sample is mounted in a stress rig not shown in Fig. 1 so that tension can be carried out on-line. Data are acquired before deformation and after 0.5, 1, 2.5, 4, and 6% elongation. Dimensions of the X-ray beam are 13 x 6 μm^2 and the energy is 61.62 keV. Position and intensity of diffracted spots are recorded by the detector. At each deformation step an ω-range from –10° to +12° is scanned to obtain diffraction spots from different crystallographic planes in each grain in the sample volume probed.

A conical slit is placed between the sample and the detector. The conical slit contains 6 conically shaped openings, placed in accordance with the {111}, {200}, {220}, {222}, {331} and {422} reflections of copper. For each ring the conical slit ensures that only diffraction spots arising from a small intrinsic gauge volume are seen by the detector. For general information on the three dimensional X-ray microscope see refs. [8-13]. Specific information on its application to lattice rotations can be found in refs. [7] .

Indexing of the spots to derive the crystallographic orientation of individual grains is carried out as described in ref. [13]. For crystallographic reasons, the number of measured diffraction spots for each grain varies between 7 and 15 in the scanned ω-range. Typically, 2-3 of these are lost during straining because they rotate to positions outside the ω-range or overlap with other spots. To assure a uniform sampling for each grain crystallographic orientations are derived from a fixed set of 5 reflections.

Results

A total of 7 grains were found with initial orientations near the <111> corner. The measured grain rotations are plotted with respect to the tensile axis and one transverse axis in Fig. 2 and Fig. 3, respectively. The tensile axis of all grains rotates significantly towards the <111> orientation. The initial orientation of the transverse axis is not the same. The rotations in Fig. 3 therefore cannot be compared directly.

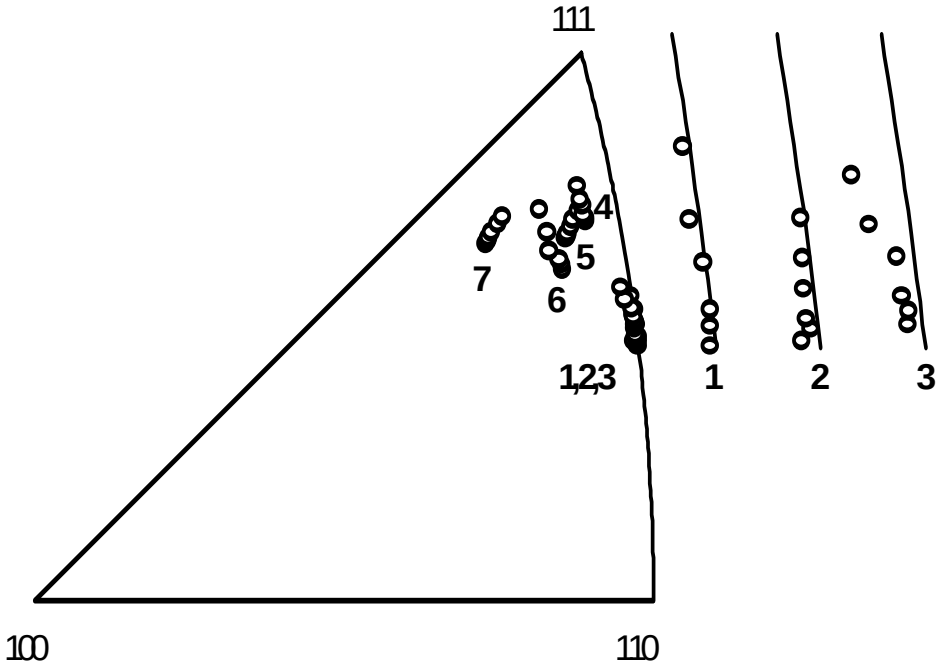

Fig. 2. Stereographic triangle showing the rotation of the tensile axis. All grains rotate towards the <111> corner. Enlargements of grains 1-3 relative to the <110>-<111> line are shown to the right.

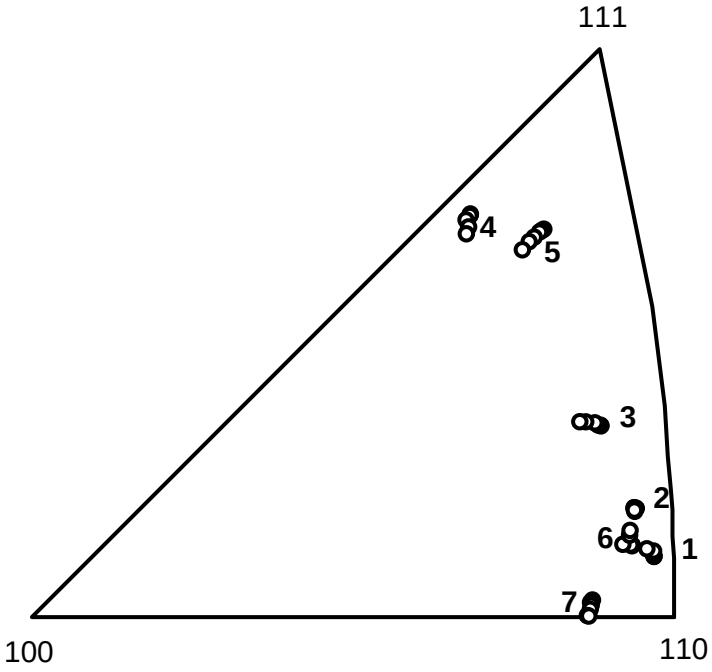

Fig. 3. Sterographic triangle showing the rotation of one of the transverse axis for all grains.

Discussion and modelling

The tendency for rotations towards <111>, i.e. the dominant component of tensile fcc textures, was also observed in the previous study of four aluminium grains. These data indicate that the interaction between an individual grain and its specific neighbours does not have a dominant influence on the rotation at least at low strains. The initial orientation spread of the present copper data is insufficient to judge the strength of the correlation between rotation behaviour and the initial crystallographic orientation of a grain. A more comprehensive investigation is currently being carried out.

Although the grains share a common main rotation direction, they do not rotate in completely the same way. The minor variations may be attributed to either grain interaction or to ambiguity in the activation of slip systems so that different slip system combinations accompanied by different rotations are equally likely.

One would expect grain interaction to be more dominant in polycrystals with small grain sizes than in large grained samples. The data available so far, which covers about a factor of ten in grain size, do not reveal significant grain size effects. The number of grains and the range of initial grain orientations studied are however too limited to reliably assess the effect of grain size.

Due to the fact that grain interaction does not seem to have a dominant influence on the rotations, the measured rotations are compared with predictions obtained with the Sachs and Taylor models. Measured and predicted rotations of the tensile axis are shown in Figs. 4 and 5. For the Taylor model all the different solutions with five active slip systems are shown. Linear combinations of these solutions are of course also valid. For the Sachs model the rotation was calculated as the antisymmetric part of the deformation tensor. The Sachs prediction always heads more towards the <100>-<111> line than the two Taylor predictions. The experimental data show that no grains rotate further towards the <100>-<111> line than the Sachs prediction and only a single grain rotates slightly more towards the <110>-<111> line than predicted by the Taylor model. The two models thus represent the extremes well and the experimental rotation paths span the orientation space between them.

There is a good correlation between the rotation direction and the magnitude of the rotation: Grains lying close to the Sachs prediction rotate faster than those lying close to the Taylor prediction. This is an indication of significant multislip in grains rotating more towards the <110>-<111> line as the rotation contribution from one slip system may be partly counterbalanced by contributions from other systems.

Comparison of the rotation of the transverse axis instead of the tensile axis does not give as clear a conclusion. Only in a few cases rotation of both tensile axis and transverse axis rotate consistently with respect to the model predictions. The best correlation between rotation of tensile and transverse axes is found for the three grains close to <221>. One of these grains almost perfectly follows the paths predicted by the Sachs model but rotates significantly less than predicted. Another of the grains follows the Taylor prediction closest to the <110>-<111> line nicely, both with respect to direction and distance. The third grain has a tensile axis which rotates as predicted by assuming double slip on the two equally stressed systems. The Taylor model predicts a tensile axis rotation in the same direction but too small. Neither of these models predicts the observed rotation of the transverse axis for this grain.

The conclusion is that the tensile axis of grains initially close to <111> appears to rotate in a reasonably well-behaved manner which lies in between the predictions of the Sachs and Taylor models while rotation of the transverse axis appears harder to predict.

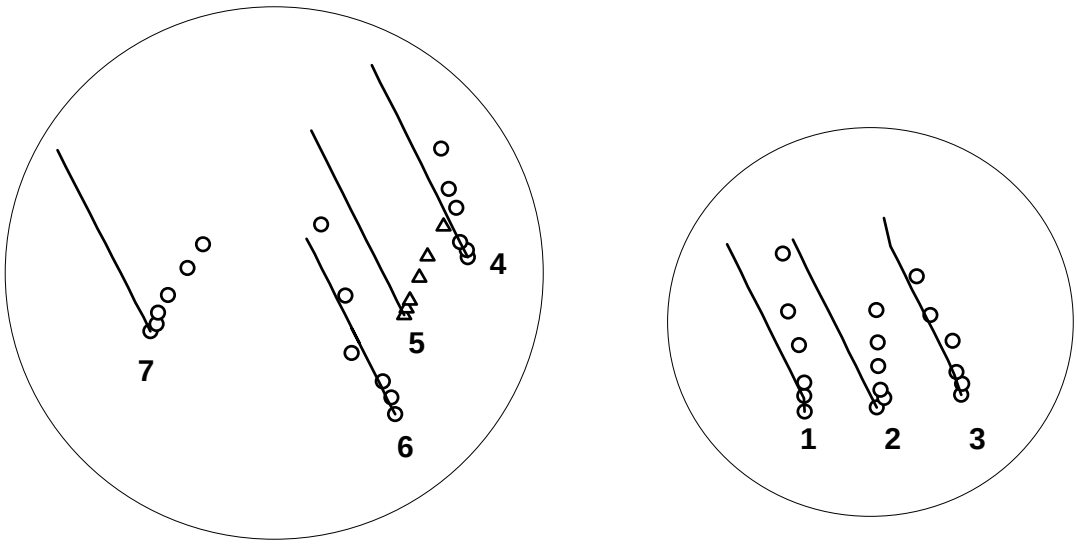

Fig. 4. Prediction with the Sachs model. To allow sufficient enlargement the stereographic triangle itself is not drawn. Grains 1-3 and 4-7 are shown separately.

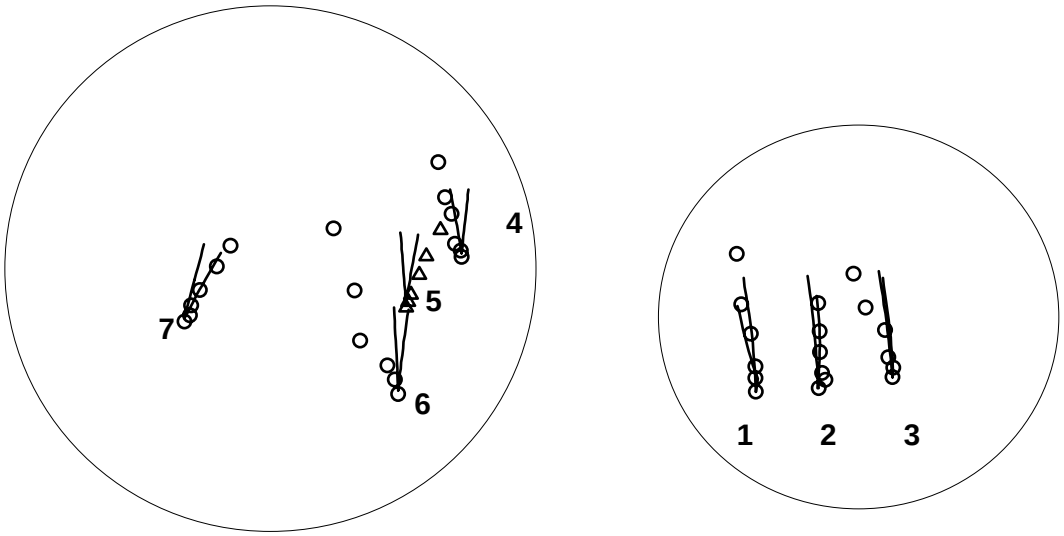

Fig. 5. Prediction with the Taylor model. To allow sufficient enlargement the stereographic triangle itself is not drawn. Grains 1-3 and 4-7 are shown separately. The two lines for each grain represent two different solutions with the Taylor model, each having five active slip systems.

Summary

- Three-dimensional X-ray diffraction has been applied to monitor lattice rotations of individual grains deeply embedded in a copper polycrystal during tensile straining.
- Seven grains with approximately the same orientation of the tensile axis (close to <111>) were studied.
- All grains exhibited the same main rotation of the tensile axis, indicating a limited influence of grain interaction.
- Variations in rotation of the tensile axis with respect to both direction and speed lie within the predictions of Sachs and Taylor.

Acknowledgments

The authors gratefully acknowledge the Danish National Research Foundation for supporting the Center for Fundamental Research: Metal Structures in Four Dimensions, within which this work was performed. Additional support for this work was provided by the Danish research council SNF (via Dansync). The authors thank P.B. Olesen, P. Nielsen, A. Goetz and M. Nicola for technical assistance, U. Lienert and R.V. Martins for help in setting up the experiment and N. Hansen and D. Juul Jensen for fruitful discussions.

References

[1] G. Sachs: Z. Ver. Deu. Ing. Vol. 72 (1928), p. 734
[2] G. J. Taylor: Journal of the Institute of Metals Vol. 62 (1938), p. 307
[3] U. F. Kocks, C. N. Tomé and H.-R. Wenk: Texture and anisotropy: Preferred orientations in polycrystals and their effect on materials properties (Cambridge University Press 1998)
[4] D. P. Mika and P. R. Dawson: Materials science and engineering A Vol. 257 (1998), p. 62
[5] C. S. Barrett and L. H. Levenson: TMS-AIME Vol. 137 (1940), p. 112
[6] R. Becker and S. Panchanadeeswaran: Acta metallurgica et materialia Vol. 43 (1995), p. 2701
[7] L. Margulies, G. Winther and H. F. Poulsen: Science Vol. 291 (2001), p. 2392
[8] D. Juul Jensen, Å. Kvick, E. M. Lauridsen, U. Lienert, L. Margulies, S. F. Nielsen and H. F. Poulsen: Materials research society symposium proceedings Vol. 590 (2000), p. 227
[9] U. Lienert, H. F. Poulsen and Å. Kvick: Proceedings of 40th conference of AIAA on structures, structural dynamics and materials, St. Louis, USA 1999
[10] U. Lienert, C. Schulze, V. Honkimäki, T. Tschentscher, S. Garbe, O. Hignette, A. Horsewell, M. Lingham, H. F. Poulsen, N. B. Thomsen and E. Ziegler: Journal of synchrotron radiation Vol. 5 (1998), p. 226
[11] S. F. Nielsen, A. Wolf, H. F. Poulsen, M. Ohler, U. Lienert and R. A. Owen: Journal of synchrotron radiation Vol. 7 (2000), p. 103
[12] H. F. Poulsen, S. F. Nielsen, E. M. Lauridsen, U. Lienert, R. M. Suter and D. J. Jensen: Journal of applied crystallography Vol. 34 (2001), p. 751
[13] E. M. Lauridsen, S. Schmidt, R. M. Suter and H. F. Poulsen: Journal of applied crystallography Vol. 34, p. 744

A5

Mater. Sci. Forum vols. 467-470, 81-86

In-Situ Investigation of Bulk Nucleation by X-Ray Diffraction

A.W. Larsen[1], C. Gundlach[1], H.F. Poulsen[1],
L. Margulies[1+2], Q. Xing[1], D. Juul Jensen[1]

[1] Center for Fundamental Research: Metal Structures in Four Dimensions,
Materials Research Department, Risoe National Laboratory, DK-4000 Roskilde, Denmark

[2] ID11, ESRF, 38043 Grenoble Cedex 9, France

Keywords: Nucleation, Triple junctions, 3DXRD, X-Ray Diffraction, Orientation measurements

Abstract. A new method for *in-situ* studies of nucleation in bulk metals based on high energy synchrotron radiation is presented. Copper samples cold rolled 20% are investigated. The crystallographic orientations near triple junctions are characterized using non-destructive 3DXRD microscopy before, during, and after annealing for 1 hour at 290°C. This method allows in-situ identification of new nuclei and the deformed material, which spawns the nuclei. Also, since data is acquired during annealing nucleation kinetics can be studied.

Introduction

Studies of bulk nucleation have always been hampered by the fact that it has been impossible to know the exact microstructure at the exact nucleation sites *before* the nuclei emerged.
It is possible to perform microscopic scanning electron microscopy (SEM) and transmission electron microscopy (TEM) studies of nucleation, where the starting structure is known [1,2]. But in both cases it is not possible to rule out surface effects. In SEM studies there is also the added problem of grains growing up from the hidden bulk sample below the surface.

With high X-ray energies (50 keV) a 10% transmission through a thickness of 25 mm of Al, 1.5 mm of Fe, and 1 mm of Cu is obtained, thus allowing non-destructive probing of the *bulk* of metal samples. By using samples of a suitable thickness it is possible to characterize the microstructure within a column through the sample, which is representative of the bulk microstructure. Depending on the X-ray beam spot size, the measurement time, and the material being investigated, a sub-micron volume resolution can be achieved.
Poulsen et al have shown that it is possible to perform in-situ studies of recovery in a deformed Al single crystal using 3DXRD microscopy [3].

Earlier studies of nucleation have shown that areas near triple junctions are likely sites for nucleation [2,4], so in this study we limit ourselves to volumes near triple junctions. The purpose of this paper is to explain in detail the experimental procedure and illustrate it's potentials, by showing the first results obtained with the method.

The 3DXRD microscope

The 3D X-ray diffraction (3DXRD) microscope[1] works in the X-ray energy regime of 40-100 keV [5]. It is installed in the second hutch of ID11, which is a high energy beamline at the ESRF[2] (Grenoble, France). The X-ray beam can be focused down to a 2x5 μm^2 spot, using double focusing

[1] http://www.risoe.dk/afm/synch/3dxrd.htm
[2] http://www.esrf.fr/exp_facilities/ID11/handbook/welcome.html

from a bent Laue Si-111 crystal and a bent multilayer, giving a maximum flux of $\Phi_0=1.5\cdot10^{10}$ (photons/sec/μm^2) on the sample with an energy bandwidth of 0.06-1%.
A schematic diagram of the 3DXRD microscope can be seen on Fig. 1.
The 3DXRD microscope allows static and dynamic studies of the microstructure of solid bulk samples. The high transmission and photon flux allows the reflections from individual crystallographic grains to be detected, and specialized software allows these reflections to be indexed back to the individual grains, thus allowing individual grains to be followed in-situ.
Slits placed right in front of the sample precisely define the spot size, and several different detectors of varying resolution are available. It is possible to mount a furnace (used in this study), a cryostat, a tensile stress rig, or a torsion device on the sample stage, thus allowing in-situ studies of phase transformations, annealing, and deformation.

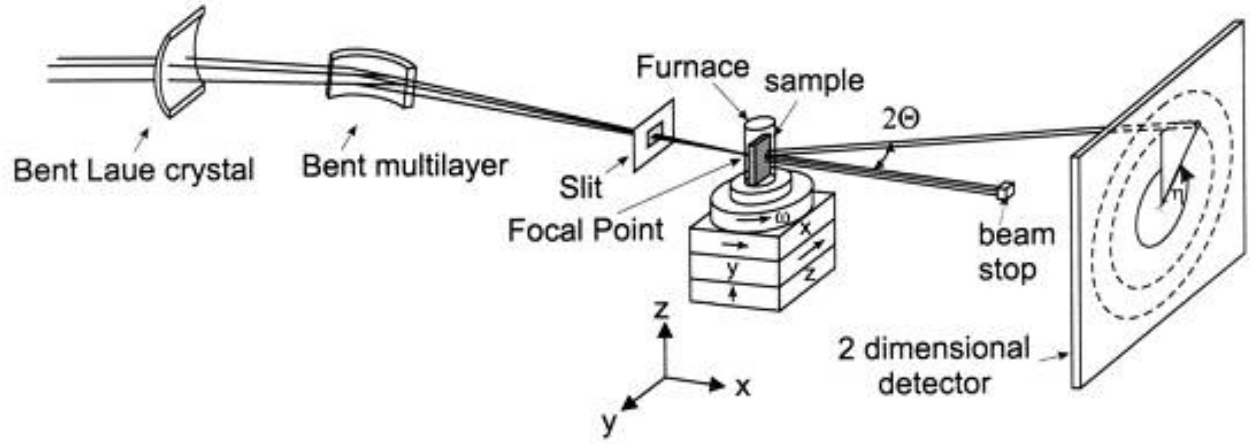

Figure 1: *Schematic diagram of the 3DXRD microscope. The 1×1 mm^2 white X-ray beam enters from the left, where it is monochromated and focused in the vertical plane using a bent Laue Si-111 crystal. Horizontal focusing is performed with a bent multilayer. A slit in front of the sample defines the size of the beam on the sample. The sample can be translated in the x, y, z-direction, ω is the sample rotation around the z-axis, and it is possible to tilt the sample around the x and y-direction.*

Sample preparation

The sample material is 99.995% Vol. pure copper, which is initially cold rolled 20%, and then annealed for 8 h at 700°C. This results in an inhomogeneous grain size distribution with an average grain size of about 500 μm. This starting material is additionally cold rolled 20% to a thickness of 25.6 mm. During cold rolling the *l/h* ratio is equal to 1.2, and the deformation is therefore expected to be uniform throughout the thickness of the material [6]. Here *l* is the cordal length of the contact area with the rolls, and *h* is the sample thickness.

From the rolled material a thin 10×10 mm^2 sample is cut out, and the sample surface (the RD/ND plane) is polished down to a thickness of 0.3 mm (see Fig. 2), using a Logitech PM5D polishing and lapping machine with a PSM1 sample monitor[3] [7], where polishing is performed from both sides. Lastly, the sample is electrochemically polished, with a D2-electrolyte[4] for 5 seconds at 10 V, to remove any remnant surface deformation or sub-micron scratching (i.e., surface nucleation sites).
An illustration of the sample geometry can be seen on Fig. 2.

[3] http://www.logitech.uk.com/
[4] D2: 500 ml H_2O, 250 ml H_3O_4P, 250 ml ethanol, 2 ml Vogel's Sparbeize, 50 ml propanol, and 5 g H_2N CO NH_2 (urea)

Initially, the surface microstructure of the sample is studied to determine the surface positions of the triple junctions within a chosen area on the surface. The surface microstructure of a 1.8×1.8 mm^2 area is characterized by electron backscatter patterns (EBSP), producing an orientation image map (OIM) of the area in studied [8,9]. A JEOL JSM-840 scanning electron microscope, with a LaB_6-filament is used to collect the data, and the step size is 20 µm. From the OIM, an area containing one or more well defined triple junctions is chosen for 3DXRD studies (see Fig. 2).

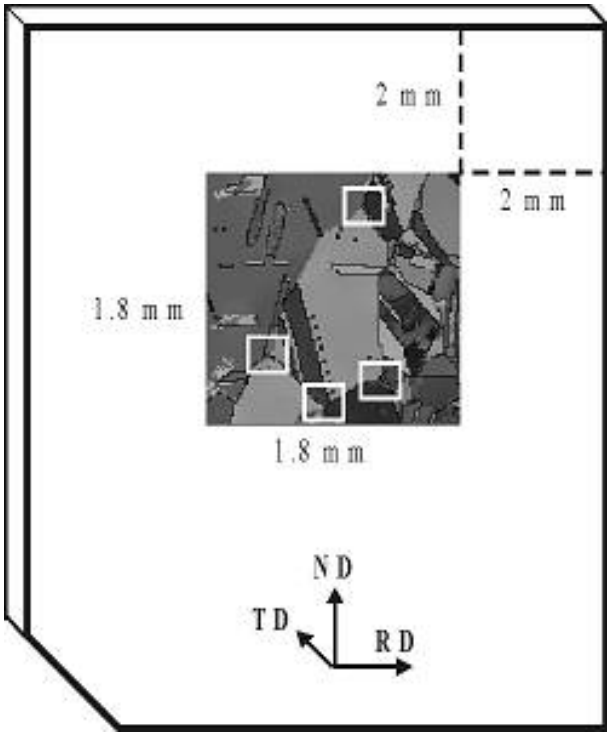

Figure 2: *Sample geometry. Side lengths are less than 10 mm, and thickness is 0.3 mm. The RD, ND, and TD-directions are respectively oriented along the y, z, and x-axis in the 3DXRD microscope (see Fig. 1).*
The upper right corner of the OIM is located 2 mm below the top edge and 2 mm to the left of the right edge. Note that the relative size of the OIM has been exagerated to make the microstructure more easily discernable. The white squares indicate the position of suitable triple junctions.

A TEM foil is taken parallel to the RD/ND plane, and prepared by electro polishing. From this the average distance between dislocation boundaries (the cord length) within the deformed material is determined using a JEOL-2000FX transmission electron microscope, operating at 200 kV. The average cord length is found to be about 0.5 µm, and the smallest length is ~0.15 µm.

3DXRD experiment

For the 3DXRD experiment, an energy of E=50.77 keV (λ=0.2442 Å) is chosen, giving a transmission of 50% through the 0.3 mm thick copper samples. A 1024×1024 pixel Frelon[5] CCD-detector was placed 333 mm from the sample, allowing for the simultaneous full recording of the four Debye-Scherrer rings of lowest multiplicity: [111], [200], [220], and [311].
The sample is mounted within a furnace (see Fig. 1), with the RD/ND plane perpendicular to the X-ray beam (see Fig. 2). It is possible to heat and cool the sample within the furnace, which consists of a 0.1 mm thick glass capillary tube with a thermocouple in the middle. This can be done in vacuum or in an argon atmosphere.

The approach is in detail to map a 100×100×300 $µm^3$ volume (grid area × sample thickness), centered on a triple junction in the as-deformed sample. The sample is then heated to 290°C, and data is continually collected from the same volume with a time resolution of 6 min. After 1 hour, the sample is cooled to room temperature, and the same 100×100×300 $µm^3$ volume is mapped

[5] http://www.esrf.fr/experiments/ISG/SpecialDetectors/AreaDiffraction.php

again. By comparing the post-annealed with the pre-annealed data, it is possible to locate new nuclei, and the microstructure from which it grew. If the new nuclei yields more than one diffraction spot, it is possible to determine the nuclei's maximum distance from the sample center by triangulating the positions of the diffraction spots.

To avoid spot-overlap (different sample volumes diffracting into the same position on the detector), it was decided to limit the number of grains intersected by the X-ray beam penetrating through the sample. The solution is to make the grain size and the sample thickness comparable, while keeping the sample thick enough for the microstructure to have true bulk properties. This lead to the chosen 0.3 mm sample thickness. Also, the sample is cold rolled 20%, only creating a moderate deformation and therefore only a moderate broadening of the poles. With this approach, it is typically possible to observe all the broadened reflections (poles) from the 3 grains at a triple junction *without* spot-overlap.

The time and ω resolutions are chosen as 1 second and 1° respectively. To make sure that the sensitivity of the 3DXRD microscope is high enough to detect the deformed cells, a small X-ray beam size is chosen: the beam is horizontally and vertically focused down to a 49x49 μm^2 spot.
To detect a cell, the diffracted intensity from that cell must be at least twice that of the background noise. A textureless aluminium foil of known thickness is used to calibrate the volume detection limit, and from that a volume detection limit of $(0.26\ \mu m)^3$ is determined for copper.

For the experiment, the microstructure of a 2×2 grid (100x100 μm^2 area), centered on a triple junction, which is chosen from the OIM, is characterized at different time steps. At each grid point a 1 second ±0.5° rocking curve scan is performed at ω positions from -20° to 20° in 1° increments. This angular range is sufficient to cover all crystallographic orientations.
The as-deformed triple junction is characterized at room temperature, after which the sample is heated to 290°C. When at temperature, identical 2×2 grid scans are continually performed at the same sample position. Each grid point contains 42 rocking curve scans (each taking ~2 seconds), and since there is 4 of these, it corresponds to a complete 2×2 grid scan roughly once every 6 minutes, thus allowing us to follow nucleation in-situ as a function of time with that time resolution.

The choice of a 49x49 μm^2 spot size is a compromise between spatial and time resolution. It is possible to focus the X-ray beam as far down as a 2x5 μm^2 spot, but since studying in-situ nucleation is a 'needle in the haystack' problem, a larger area would still have to be covered, requiring many more grid points, and the corresponding time resolution would make dynamical studies impossible.

Because the smallest observed cells (~0.15 μm) in the deformed structure are just smaller than the volume detection limit $(0.26\ \mu m)^3$, an additional high sensitivity measurement on an as-deformed sample is also performed. This measurement has a time and ω resolution of respectively 15 seconds and 0.5°, giving a volume detection limit of $(0.15\ \mu m)^3$, and thus allowing us to see the smallest length/cells observed in the TEM study.

Results

In the diffraction images from the as-deformed samples, the reflections are seen as elongated poles, as would is seen in the diffraction patterns from deformed crystals. Due to the moderate deformation (20%), even when all three grains diffract into the same image, the Debye-Scherrer rings are still *not* fully filled with reflections (see Fig. 3a). As heating progresses, nuclei are seen to appear as sharp diffraction spots with very low mosaic spread and intensity increasing with time (see Fig. 3b).
In Fig. 3, diffraction images from the same volume of the sample before and after annealing can be seen. In this case, the nucleus clearly forms with an old (already existing) orientation.
Triangulating the positions of the diffraction spots from the nuclei shows where the nuclei are inside the sample. It is therefore possible to determine whether a detected nucleus has formed in the sample bulk or on the sample surface.

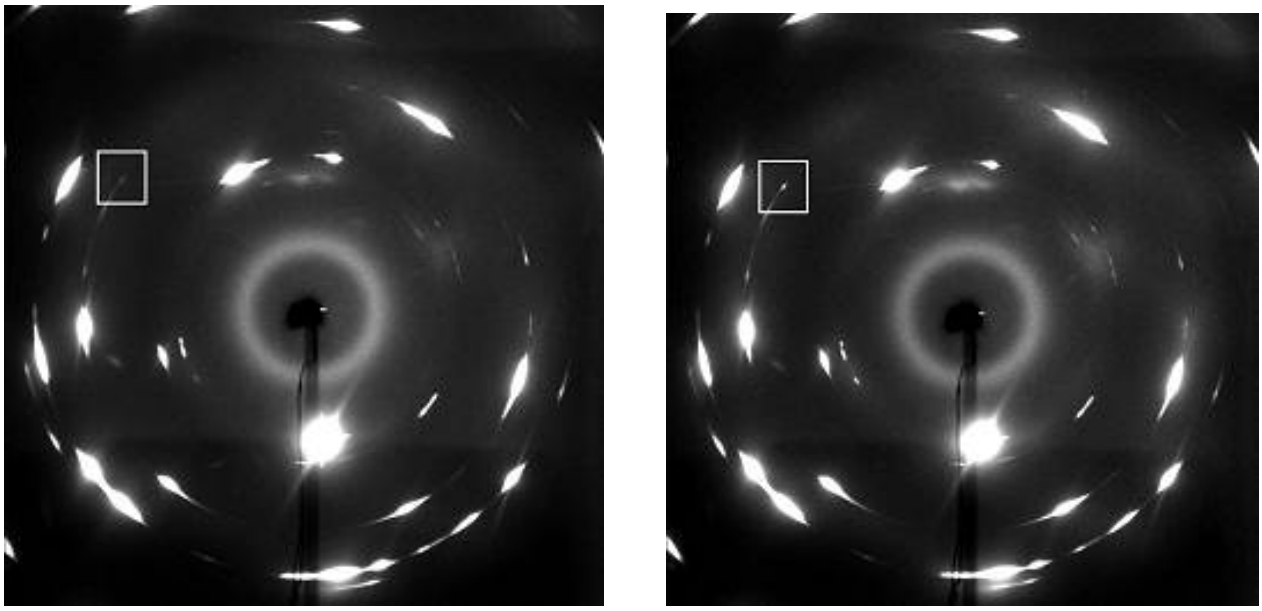

(a) **(b)**

Figure 3: *Example of experimental data. The two figures show the raw X-ray diffraction data as seen on the detector.* ***(a)*** *in the as-deformed state; and* ***(b)*** *after annealing for 3 hours at 290 ℃. The white square indicates where in the diffraction images a nucleus can be seen to appear.*

In general, the nuclei are observed primarily within the existing crystallographic orientations (the poles, see Fig. 3b), but some nuclei are also seen to form with orientations *not* previously found within the poles of the as-deformed sample.
In this case, the high sensitivity images of the as-deformed sample confirm that no diffraction spots are observed in the space between the crystallographic poles. This means that *before* the onset of annealing, no cells of volumes larger than $(0.15\ \mu m)^3$ have orientations outside the poles.
Further analysis will show if these new orientations are within annealing-twin orientations, results of grain rotations, or if they are indeed completely new orientations inherent to the annealing process itself.

Conclusion

A new method for in-situ studies of bulk nucleation has been presented. The method has allowed for the in-situ detection of new *bulk* nuclei, while they formed and therefore, the nucleation kinetics could be followed. It has been confirmed that triple junctions are good nucleation sites.
With this method, there is no 'lost evidence', i.e., the parent bulk microstructure is fully characterized *before* the nuclei form.
In the present preliminary investigation: Nuclei with crystallographic orientations corresponding to the orientations already observed in the deformed structure are seen (see Fig. 3); but some nuclei, which form with orientations not previously observed in the microstructure are seen as well.

Acknowledgements

The authors gratefully acknowledge the Danish Research Foundation for supporting the Center for Fundamental Research: Metal Structures in Four Dimensions, within which this work was performed.

References

[1] T.J. Sabin, G. Winther and D. Juul Jensen: *Orientation relationships between recrystallization nuclei at triple junctions and deformed structures* (Acta Mat. Vol. 51 (2003), p. 3999-4011)

[2] H. Hu: *Recovery and recrystallization in Metals* (Interscience, New York (1963), p. 311)

[3] H.F. Poulsen, E.M. Lauridsen, S. Schmidt, L. Margulies and J.H. Driver: *3D-characterisation of microstructure evolution during annealing of a aluminum single crystal of the S-orientation* (Acta Mat. Vol. 51 (2003), p. 2517-2529)

[4] R.A. Vandermeer and P. Gordon: *Edge-nucleated, growth controlled recrystallization in aluminum* (Met. Trans. Vol. 215 (1957), p. 577-588)

[5] H.F. Poulsen and D. Juul Jensen: *From 2D to 3D microtexture investigations*, 13. International conference on textures of materials (ICOTOM 13), Seoul (KR), 26-30 August 2002.
(*Mat. Sci. Forum* 408-412 (2002), p. 49-66)

[6] M. Holscher, D. Raabe and K. Lucke: *Relation between rolling textures and shear textures in fcc and bcc metals* (Acta Metall. Mater. Vol. 42:3 (1994), p. 879-886)

[7] A.W. Larsen: *'Logitech PM5D Precision Polishing and Lapping System' user manual* (Risø-I-2051(EN), Risoe National Laboratory, Roskilde, Denmark (2003))

[8] N.C.K. Lassen, D. Juul Jensen and K. Conradsen: *Image-processing procedures for analysis of electron back scattering patterns* (Scanning Microscopy Vol. 6:1 (1992), p. 115-121)

[9] B.L. Adams: *Orientation Imaging Microscopy: Application to measurement of grain boundary structure* (Mat. Sci. Eng. Vol. 166(A):59 (1993), p. 2517-2529)

A6

Mater. Sci. Forum vols. 467-470, 147-151

Recrystallization Kinetics in the Bulk and at the Surface

D. Juul Jensen[1], M.D. Lund[1+2], A.W. Larsen[1] and J.R. Bowen[1]

[1] Center for Fundamental Research: Metal Structures in Four Dimensions, Risø National Laboratory, Roskilde, Denmark

[2] Geological Institute, University of Copenhagen, Copenhagen, Denmark

Keywords: Growth rates, nuclei distribution, stereology, 3DXRD, EBSP

Abstract. Possible variations in recrystallization kinetics from the sample surface to the center have been investigated in 90% homogeneously cold rolled aluminium (AA1050). It was found that whereas the average growth rates are quite similar, the nucleation characteristics are different at the surface and in the bulk.

Introduction

In-situ investigations of recrystallization and grain growth near the surface of samples are relatively straightforward. Recently in particular the X-Ray Interface Continuous Tracking technique [1] has provided key results on grain boundary motion during grain growth but also results from in-situ SEM heating experiments are starting to appear [2, 3].

In-situ investigations of microstructural changes within the *bulk* of samples are much more complex. With 3 Dimensional X-Ray Diffraction (3DXRD) microscopy, it is possible to map the microstructure with a spatial resolution in the micrometer range and a time resolution of the order of minutes [4-8]. However, 3DXRD measurements can only be performed at high energy synchrotron sources, the measurements are typically not easy and the data analysis is demanding as the data sets almost always are very large and new software often has to be developed to treat the "state-of-the-art" data.

The purpose of the present work is to investigate recrystallization occurring near the surface and in the bulk of a rolled aluminium plate and to analyze if the nucleation characteristics and growth rates are similar at the two locations. It is well known that inhomogeneously rolled plates can exhibit quite large through-thickness differences [e.g. 9, 10]. Therefore, a plate rolled at intermediate draughts is chosen for the present work, and to be able to compare with previous work, it is rolled to a relatively high rolling reduction (90%).

In the investigation focus is on the *average* recrystallization behaviour. Therefore, stereological characterization of a series of partly recrystallized samples is chosen as the basis for the analysis instead of in-situ investigations, which more envisage the individualism of the various grains.

Experimental

Commercial purity aluminium (AA1050) heat treated to minimize the amount of iron in solid solution and with an initial grain size of 80 μm was used for the investigation. This starting material is similar to that used in a series of previous studies [e.g. 11 - 13]. The starting material was cold rolled to 90% reduction in thickness. In order to obtain a maximum degree of homogeneity through the sample thickness, the rolling was done at intermediate draughts [e.g. 9, 10] with l/h ratios in the range 1-2. Here l is the chord length of the contact arc with the rolls and h is the sample thickness.

From the rolled plate samples were cut out. These were paired in sets of two, which were kept together during the subsequent anneal at 280° in a molten tin bath. Annealing times ranged from 125 seconds to 6 hours, giving a series of partly recrystallized samples.

After the anneal, one of the two samples in each pair was sectioned to half thickness using a Logitech PM precision polishing and lapping system [14]. The other sample was just slightly polished to reveal the near surface microstructure.

All samples, both surface and bulk (half sample thickness), were inspected in the rolling plane by EBSP in a JEOL 840 SEM, to determine the following microstructural parameters:

V_v,	volume fraction of recrystallized material
S_v,	the grain boundary area density separating recrystallized grains from the deformed matrix.
$<\lambda>$	the mean intercept-free cord length of recrystallized grains.

In previous works these parameters have been determined by manual EBSP inspection [e.g. 12, 13]. In the present work an automatic method is used based on EBSP recordings of 3 parallel lines 1 μm apart. An example of such a 3 line EBSP scan is shown in Fig. 1. The two outer lines are used as auxiliary lines to support the analysis of the center line. It has been proven that for the present material, this automatic method is in good agreement with the manual inspections [15].

Fig. 1. Example of a section within a 3 line EBSP scan through a partly recrystallized structure. The step size is 1 μm and the distance between the lines is also 1 μm.

The length of the 3 line EBSP scans was in all cases 1000 μm, but in some cases several series of scans were performed on a sample to reduce the experimental scatter. This was in particular necessary for intermediate annealing times, where the microstructure is rather inhomogeneous; some large regions can be almost fully recrystallized, whereas others remain deformed.

Results and Discussion

The mean cord lengths of the recrystallizing grains are plotted as a function of annealing time in Fig. 2. Each 3 line EBSP scan is represented by one point. The figure shows that the grains on average grow to become 12-14 μm in the fully recrystallized state, which is in good agreement with our previous result of 14.8 μm [13]. The figure further reveals that the grain sizes in the bulk and at the surface are indistinguishable. Also when the complete grain size distributions are compared, there is no obvious difference between surface and bulk.

Figure 3 shows, how the volume fraction of recrystallized material evolves with time. A significant scatter is observed in particular for surface samples at about 50% recrystallization. Despite this scatter, the data show that the surface samples in general are more recrystallized than the bulk samples at a given annealing time. The difference is largest at short and intermediate annealing times.

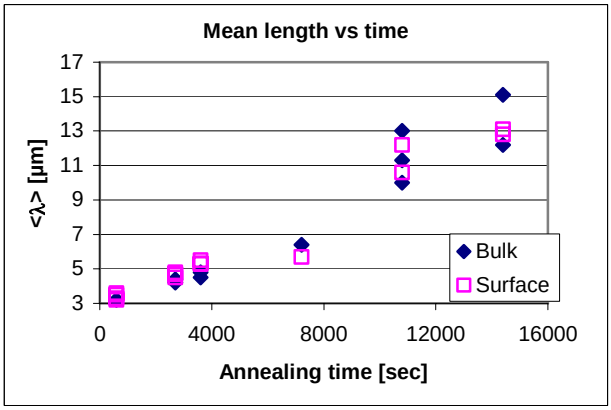

Fig. 2. Evolution in the grain size as a function of annealing time.

The evolution in free unimpinged surface area S_v is shown as a function of V_v in Fig. 4. For both the surface and bulk, the typical curve shape is observed with an initial increase in S_v at low V_v a maximum near V_v = 0.5 and then a decrease to S_v = 0 at V_v = 1.0. In the early stages of recrystallization new grains nucleate and grow, whereby the surface area S_v increases. Then the grains start to impinge and with increasing V_v a larger and larger fraction of the grain surface areas are neighboring other recrystallized grains (and not deformed matrix material) whereby S_v decreases.

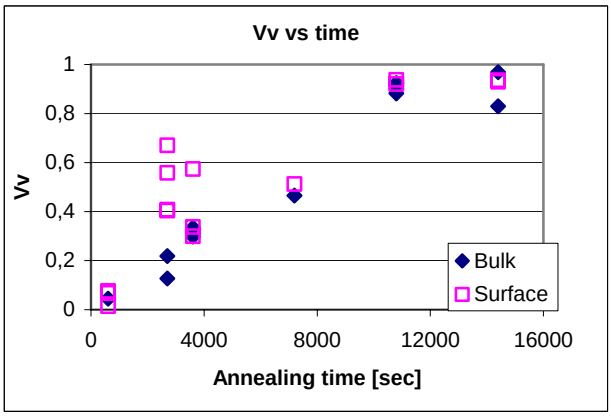

Fig 3. Evolution in the volume fraction of recrystallized material as a function of annealing time.

When the S_v results for the bulk and surface samples are compared (Fig. 4), it is seen that the S_v values for the surface samples are higher than those for the bulk, and the fitted maximum is at V_v = 0.5 for the surface, whereas it is at V_v = 0.47 for the bulk. A maximum S_v at lower V_v generally implies clustered nucleation, whereas a value near 0.5 is typical for a random distribution of the nuclei [16]. That the nuclei in the bulk are clustered is in good agreement with earlier more detailed investigations [13]. Here it was found by microstructural path modeling that linearly clustered nucleation fits the experimental data well [13]. That the present observations reveal more random nucleation near the surface may be an effect of some extra nucleation sites introduced by the proximity of the rolls.

From the measured S_v and V_v values the true average growth rate of the grains <G> can be calculated using the Cahn-Hagel approach:

$$\frac{dV_v}{dt} = \langle G \rangle S_v$$

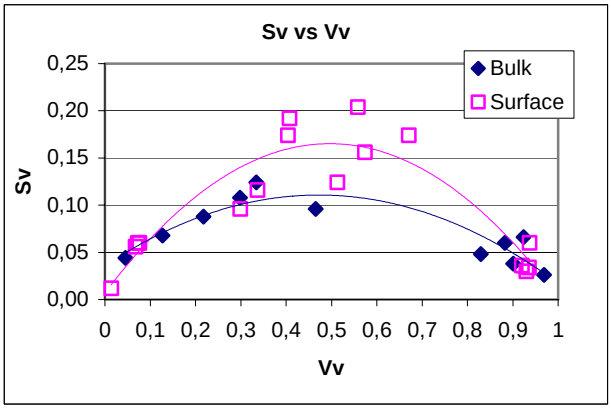

Fig. 4. Evolution in the free unimpinged surface area of the recrystallizing grains as a function of the volume fraction of recrystallized material.

The result is shown in Fig. 5. The curves show a transition: First the grains grow rapidly, but this high growth rate quickly reduces to a lower quite constant growth rate. This is in good agreement with the earlier observations [8]. No difference between bulk and surface is observed (see Fig. 5). So the differences observed for V_v and S_v "normalizes" out resulting in identical growth rates.

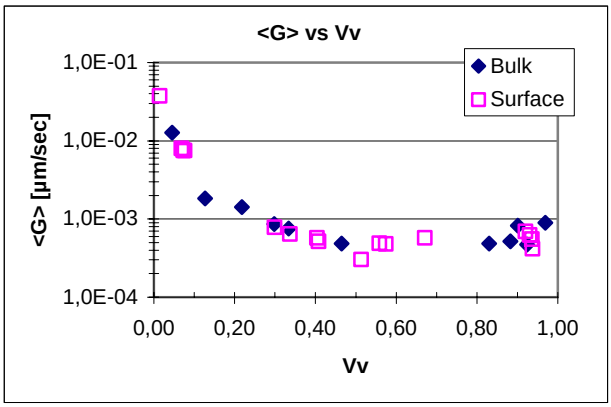

Fig. 5. The average growth rate determined by the Cahn-Hagel method as a function of the volume fraction of the volume fraction of recrystallized material.

Conclusions

The stereological parameters $<\lambda>$, V_v and S_v were used to evaluate possible differences in recrystallization near the surface of a 90% homogeneously cold rolled Al plate and in the bulk at the center of the plate. It was found that the average grain size and the recrystallization growth rate were identical at the two locations. The distribution of nuclei, however, appeared to be more random at the surface than in the bulk.

Acknowledgement

The authors gratefully acknowledge the Danish National Research Foundation for supporting the Center for Fundamental Research: Metal Structures in Four Dimensions, within which this work was performed.

References

[1] D.A. Molodov: *Grain Boundary Character – A key factor for Grain Boundary Control. Proc Recrystallization and Grain Growth*, ed. G. Gottstein and D.A. Molodov, Springer Berlin (2001), p. 21- 38

[2] I.M. Fielden, J. Cawley, J.M. Rodenburg: *Backscattered SEM Imaging of High Temperature Samples for Grain Growth Studies in Metals.* Proceedings of Physics Electron Microscopy and Analysis Group Conference, Ed. S. McVitie, in print.

[3] F.J. Humphreys, www2.umist.ac.uk/material/staff/academic/fjh/SEM-PSN.htm

[4] H.F. Poulsen and D. Juul Jensen: *From 2D to 3D microtexture investigations*, 13. International conference on textures of materials (ICOTOM 13), Seoul (KR), 26-30 August 2002. (Mat. Sci. Forum 408-412 (2002, p. 49-66)

[5] A.W. Larsen, C. Gundlach, H.F. Poulsen, L. Margulies, Q. Xing and D. Juul Jensen: *In situ Investigation of Bulk Nucleation by X-ray Diffraction* (In these Proceedings)

[6] S. Schmidt and D. Juul Jensen: *In-situ measurements of growth of nuclei within the bulk of deformed aluminium single crystals.* (In these Proceedings).

[7] R.A. Vandermeer, E.M. Lauridsen and D. Juul Jensen: *Growth Rate Distrubutions During Recrystallization of Copper* (In these Proceedings)

[8] H.F. Poulsen: *3DXRD – Mapping grains and their dynamics in 3 dimensions* (In these Proceedings)

[9] O.V. Mishin, B. Bay and D. Juul Jensen: *Through-Thickness Texture Gradients in Cold Rolled Aluminium* (Metall Mater Trans. A. Vol 31A (2000), p. 1653-1662).

[10] W. Truszkowski, J. Krol and B. Major: *On Penetration of Shear Texture into the Rolled Aluminium and Copper* (Metall Trans, Vol 13A (1982), p. 665-669).

[11] E.M. Lauridsen, H.F. Poulsen S.F. Nielsen and D. Juul Jensen: *Recrystallization Kinetics of Individual Bulk Grains in 90% Cold Rolled Aluminium* (Acta mater. vol. 51 (2003) p. 4423-4435).

[12] D. Juul Jensen: *Growth Rates and Misorientation Relationships Between Growing Nuclei/Grains and Surrounding Deformed Matrix During Recrystallization* (Acta Mater. Vol 43 (1995), p. 4117-4129).

[13] R.A. Vandermeer and D. Juul Jensen: *Microstructural Path and Temperature Dependence of Recrystallization in Commercial Pure Aluminium* (Acta Mater. Vol 49 (2001), p. 2083-2094).

[14] A.W. Larsen: *Logitech PM5D Precision Polishing and Lapping System' user manual* (Risø-I-2051(EN), Risø National Laboratory, Roskilde Denmark (2003))

[15] A.W. Larsen and D. Juul Jensen: *Automatic determination of recrystallization Parameters in metals by EBSP line scans, Materials Characterization.* in print.

[16] D. Juul Jensen and R.A. Vandermeer: Effect of Anisotropic Impingement on Recrystallization Texture, Microstructure and Kinetics (Proc. ICOTOM11, eds. Z. Liang et al. Int. Acad. Publisher Beijing (1996), p. 490-496)

[17]

A7

Mater. Sci. Forum vols. 495-497, 1285-1290

Orientations of recrystallization nuclei studied by 3DXRD

D. Juul Jensen[a] and A.W. Larsen[b]

Center for Fundamental Research; Metal Structures in Four Dimensions,
Risø National Laboratory, Roskilde Denmark

[a]dorte.juul.jensen@risoe.dk, [b]axel.wright.larsen@risoe.dk

Keywords: Nucleation, recrystallization,3DXRD, orientation relationships.

Abstract: recent results on nucleation of recrystallization are reported. This includes previously published data, obtained by EBSP and new results obtained by the 3 dimensional X-ray diffraction method. Focus is on the orientation relationship between nuclei and parent grains. It is demonstrated that nuclei may well form with orientations different from their parent grains.

Introduction

A critical point in the understanding of recrystallization textures is the development of crystallographic orientations of the nuclei. Here an issue, which has been debated much recently [eg. 1], is if nuclei have orientations identical to those of the deformation microstructures from which they originate or not. Traditional nucleation mechanisms like strain induced boundary migration [2] and particle stimulated nucleation [3] operate with nuclei orientations identical to the "parent" deformation microstructure. This is also what is commonly incorporated in recrystallization modeling. However, a number of studies have found recrystallization nuclei in orientations that were not expected from measurements on deformed structures. Some of these results are reviewed and discussed in this paper, and new in-situ results obtained by the 3 dimensional X-ray diffraction (3DXR) method are presented.

Electronmicroscopy Observations

Within recent years there have been a number of investigations into the local orientation is deformed metals and the development of recrystallization nuclei [4-22]. In these studies nuclei with orientations identical to the "parent" orientations in the deformed state are always observed. However, also nuclei of new orientations, which could not be directly identified in the deformed state, are generally reported. For example for recrystallization of deformed single crystals studied by TEM and EBSP before and after annealing, Godfrey et al. [17] found nuclei with orientations beyond and at the very far end of the orientation scatter observed in the deformed state in % channel die deformed (ε=1.5) S oriented aluminium crystals. Okada et al. [18] found new recrystallized grains which a twin relationship to crystal orientations present in the deformation microstructure in a 70% uni-axial tensioned aluminium single crystal. A twin relationship between a nucleus and its parent deformation microstructure may not sound too surprising even in aluminium [23], but in the paper by Okada et al. [18] the new twinned nucleus orientation is reported not to be a growth effect, but originating from a boundary dissociation process. Concerning the work by Godfrey et al. [17], nuclei with orientations at the far end of the deformation orientation scatter agree well with standard expectations as nuclei with such rare orientations compared to the deformed microstructure would have better growth potentials [24]. More interesting are the nuclei with orientations beyond the orientational scatter observed in the deformed state. Because of the indirect nature of the observation (measured separately before and after annealing, (it can, however, not be ruled out that these nuclei originated from volumes in the deformed microstructure with orientations rotated even further, which are just so rare that the (although very detailed) TEM and EBSP measurements did not record them.

Nuclei with new orientations are reported more frequently in deformed polycrystals. For example Sabin et al. [19] found that about half the nuclei in a 40% or coarse-grained aluminium

sample had orientations away from the parent deformed grains. In this work triple junctions were examined by EBSP before and after annealing. In Fig. 1 is shown a triple junction that produced two nuclei. One of these has the parent orientation whereas the other is rotated approximately 10° about a <111> pole from another parent grain. All nuclei with new orientations were observed to be rotating about a pole close to <111> relative to their parent grains [19]. As these results are based on surface observations, it could be that the nuclei grew upwards from deformed grains (with the nuclei orientations) positioned below the investigated surface. This was, however, concluded unlikely in [19], because such growth from below should not give only <111> rotations.

A smart way to avoid the uncertainty discussed above concerning "below-surface grains" possibly leading to nucleation of grains with orientations not seen at the surface is to work with columnar grained sample – i.e. samples where the surface grains extend through the entire sample thickness. Data from such an experiment is presented elsewhere in these proceedings and do reveal that also in this condition nuclei of new orientations may form [20].

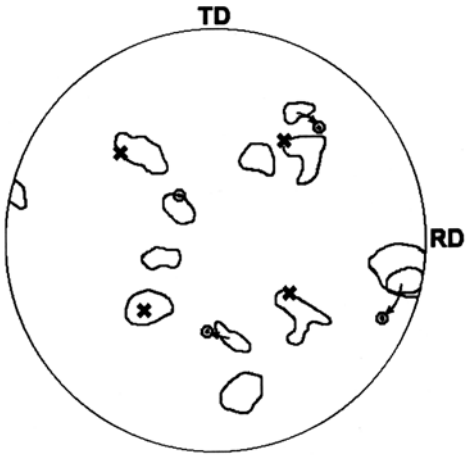

Fig. 1. {111} pole figure showing the orientation relationship between 2 nuclei and their parent deformed grains at a triple junction in 40% cold rolled aluminum annealed for 2.5 h at 300 °C. The contours indicate the extent of scatter in orientations from the deformed grains. The nucleus marked by "X" has the parent grain orientation, whereas the nucleus marked by "O" is rotated about 10° around a <111> pole from another grain [19].

3DXRD observations

The 3 dimensional X-ray diffraction (3DXRD) method allows in-situ studies of bulk microstructural changes non-destructively [21, 25, 26]. This method has been used for studies of nucleation. The channel die deformed aluminium single crystal discussed above in the work of Godfrey et al. [17] was characterized by 3DXRD before and after 5 minutes annealing at 300°C [21]. These 3DXRD measurements confirmed that new orientations could develop upon the annealing [21].

In the most recent 3DXRD experiment on nucleation a 20% cold rolled polycrystalline copper samples were studied in-situ while annealing. The orientations in volumes (100x100x300 μm^3) near selected triple junction lines were characterized in detail before annealing. For experimental details see [22]. Then while annealing at 290°C, data were continually collected from the same sample volume with a time resolution of 6 min. Examples of the diffraction images are shown in Fig. 2. The reflections from the deformed grains are seen as elongated poles whereas nuclei have sharp diffraction spots (see Fig. 2). By integrating the intensities within the diffraction spots from nuclei, their kinetics can be followed. Two examples are shown in Fig. 3. The nucleus in Fig 3a was only found after about 30 minutes annealing when it had a size of about 5 μm. In the following 30

minutes it grew fairly steadily to about 10 μm in size. On the contrary the nucleus shown in Fig. 3b very rapidly (within the first few minutes at temperature) grew to about 5 μm after which it only grew very little to about 6 μm in a following 3h anneal. This variety in growth kinetics agrees well

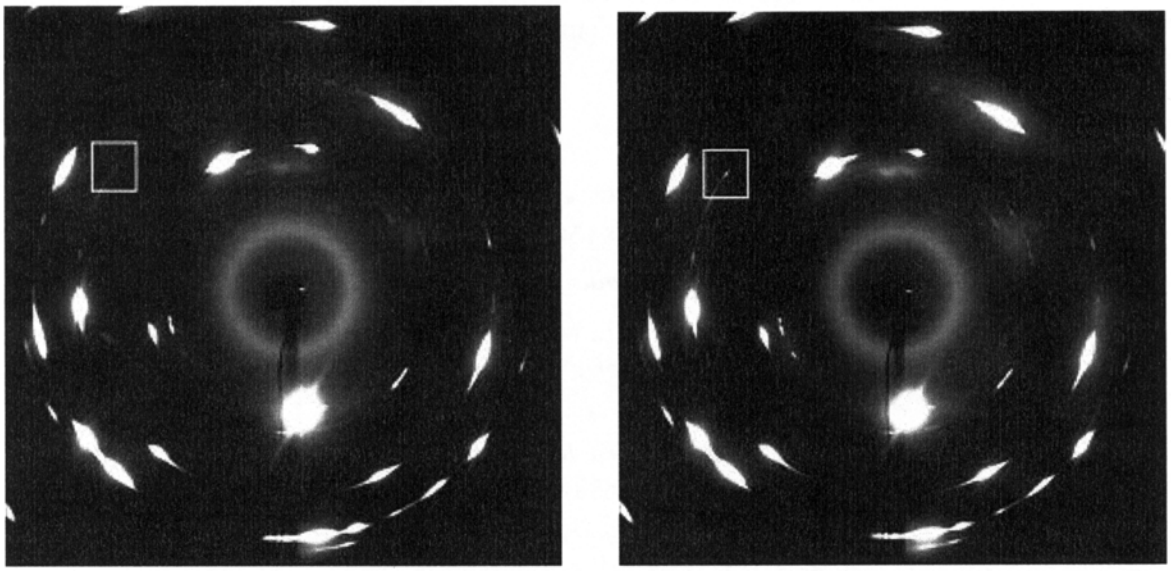

with previous 3DXRD observations of growth during recrystallization [27].
Fig. 2. Examples of signals recorded on the 3DXRD detector. a) Cu deformed 20%. b) as a) but annealed for3 hours at 290 °C. [22].

Also orientation relationships between nuclei and parent deformation structure were analyzed for 3 nuclei. It was found that 1 nucleus had an orientation within the deformation orientation spread, 1 was first order twin related to it and 1 had a new orientation. Focusing on the latter nucleus, one could speculate that it could have evolved from a surface imperfection. However, by a triangulation method using all recorded diffraction spots from the nucleus, was determined that the nucleus was at least 68 μm from the surface and thus is a true bulk nucleus. Another explanation could be that it originated from a small part of the deformation microstructure, which could not be differentiated from the background in the 3DXRD measurements. However, the experiment was set-up to record all volume elements larger than 0.7 μm. This value corresponds to the lower limit of cell sized recorded by TEM the deformed microstructure [28] and is significantly below the expected critical nucleation size which is calculated to be 1.1 μm for the present sample. This explanation thus seems very unlikely and it is believed that the nucleus has emerged by some reorientation of part of the deformed structure.

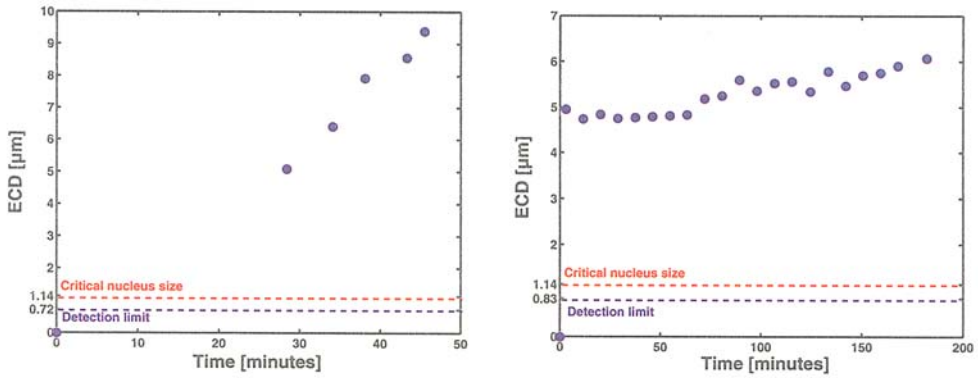

Fig. 3. 3DXRD results for the growth of individual nuclei. Sample and annealing conditions as given in Fig. 2.

Concluding remarks

Many independent studies using different experimental methods and different types of samples have shown that nuclei with crystallographic orientations different from those in the parent deformation microstructures can form during recrystallization. No realistic mechanism(s) explaining this phenomenon is yet available. The optimal experiment giving direct information to derivation of such a mechanism would be to characterize in detail and in 3D the deformation microstructure cell by cell and then follow its evaluation in-situ during recovery until nucleation occurs. The 3DXRD method offers potentials for this type of measurements in particular if the spatial resolution can be improved.

Acknowledgements

This work was supported by the Danish National Research Foundation through the “Center for Fundamental Research: Metal Structures in Four Dimensions” and by the Danish Natural Research Council via Dansync. Beam time at ESRF is also gratefully acknowledged.

Reference list

[1] Proc. Recrystallization and Grain Growth. Eds. B. Bacroix et al. (Trans Tech Publ. 2004).

[2] J.E. Bailey and P. B. Hirsch: Proc Roy. Soc. A. vol. 267 (1962), p. 11.

[3] F. J. Humphreys, M. Fery, C. Johnson and P. Paillard. (1995). In proc. 16th Risø Int. Symp. on Mat. Sci.: Microstructural and Crystallographic Aspects of Recrystallization, eds. N. Hansen et al. Risø, Roskilde, Denmark p. 87.

[4] M.G. Ardakani, F.J. Humphreys: Acta metall. mater Vol. 42. (1994), p. 763.

[5] K. Kashihara, M. Tagami, T. Okada, F. Inoko: Mater Trans JIM. Vol. 37 (1996) p. 572.

[6] T. Okada, W-Y. Liu, F. Inoko: Mater Trans JIM Vol. 40 (1999), p. 586.

[7] K. Kashihara, M. Tagami, T. Okada, F. Inoko: Mater Sci. Eng. A. Vol. 291 (2000), p. 207.

[8] T. Okada, K. Takechi, U. Takenaka, W-Y. Liu. M. Tagami, F. Inoko: Mater Trans JIM. Vol. 41 (2000), p. 470.

[9] X. Huang, J.A. Wert, H.F. Poulsen, N.C. Krieger Lassen, F. Inoko. In: Hansen. et Al., (Eds.), Proc. 21st Risø Int. Symp. 2000, p.359

[10] T. Okada, L. Ikeda, X. Huang, J.A. Wert, K. Kashihara, F. Inoko. Mater Trans. Vol. 42 (2001), p. 1938

[11] F. Inoko, G. Mima. Scripta metall. Vol. 21 (1987), p. 1039

[12] F. Inoko, T. Fujita, K. Akizono. Scripta metall. Vol. 21 (1987), p. 1399.

[13] F. Inoko, M. Kobayashi, S. Kawaguchi. Scripta metall. Vol. 21 (1987), p. 1405.

[14] Y.L. Liu, H. Hu, N. Hansen. Acta metall. mater. Vol. 42 (1995), p. 2395.

[15] J.H. Driver, H. Paul, J-C. Glez, C. Maurice. In: Hansen. et Al., (Eds.), Proc. 21st Risø Int. Symp. 2000, p. 35.

[16] S.R. Skjervold, N. Ryum. Acta mater. Vol. 44 (1996), p. 3407.

[17] A. Godfrey, D. Juul Jensen, & N. Hansen. Acta Mater. Vol. 49 (2001), p. 2429.

[18] T. Okada, X. Huang, K. Kashihara, F. Inoko and J.A. Wert: Acta mater. Vol. 51 (2003), p. 1827.

[19] T.J. Sabin, G. Winther and D. Juul Jensen: Acta Mater. Vol. 51. (2003), p. 3999.

[20] G. Wu and D. Juul Jensen. (2005) To be published in the Proceedings of ICOTOM 14.

[21] H.F. Poulsen, E.M. Lauridsen, S. Schmidt, L. Margulies and J.H. Driver: Acta Mater. Vol. 51 (2003), p. 2517.

[22] A.W. Larsen, C. Gundlach, H.F. Poulsen, L, Margulies, Q. Xing and D. Juul Jensen. In: Proc. Rex and Grain Growth 2nd, eds. B. Bacroix et al., Trans Tech Publ., p.

[23] P. Haasen (1986) In: Proc. 7th Risø Int. Symp. on Met. and Mat Sci.: Annealing Processes, eds. N. Hansen et al. Risø, Roskilde Denmark, p. 69.

[24] D. Juul Jensen: Acta Metall. Mater. Vol. 43 (1995), p. 4117.

[25] L. Margulies, G. Winther and H.F. Poulsen: I. Science. Vol. 291 (2001), p. 2392.

[26] S. Schmidt, S.F. Nielsen, C. Gundlach, L. Margulies, X. Huang and D. Juul Jensen: Science. Vol. 305 (2004), p. 229.

[27] E.M. Lauridsen, H.F. Poulsen, S.F. Nielsen and D. Juul Jensen: Acta Mater. Vol. 51 (2003), p. 4423.

[28] X. Huang, T. Leffers, N. Hansen (1999) Proc. 20th Risø Int. Symp. Mater. Sci. Eds: J. B. Bilde-Sørensen et al., Risø, Roskilde, Denmark. p. 365.

Mission

To promote an innovative and environmentally sustainable technological development within the areas of energy, industrial technology and bioproduction through research, innovation and advisory services.

Vision

Risø's research **shall extend the boundaries** for the understanding of nature's processes and interactions right down to the molecular nanoscale.

The results obtained shall **set new trends** for the development of sustainable technologies within the fields of energy, industrial technology and biotechnology.

The efforts made **shall benefit** Danish society and lead to the development of new multi-billion industries.